AN ANALYSIS OF LOW-MASS TRIGGERED STAR FORMATION IN H II REGION ENVIRONMENTS

by

Keely D. Snider

A Dissertation Presented in Partial Fulfillment
of the Requirements for the Degree
Doctor of Philosophy

ARIZONA STATE UNIVERSITY

December 2008

AN ANALYSIS OF LOW-MASS TRIGGERED STAR FORMATION

IN H II REGION ENVIRONMENTS

by

Keely D. Snider

has been approved

October 2008

Graduate Supervisory Committee:

John J. Hester, Chair
Steve Desch
Sumner Starrfield
Robert Marzke
Ariel Anbar

ACCEPTED BY THE GRADUATE COLLEGE

ABSTRACT

Most studies of low-mass star formation have focused on regions such as Taurus-Auriga where stars form in relative isolation, but this is likely not the dominant mode of low-mass star formation. Instead a majority of stars form in rich cluster environments with both high and low-mass stars, and the effects of the massive stars can influence how successive generations of low-mass stars form. This dissertation presents the results from four studies of specific H II regions using new data from the Spitzer Space Telescope along with a study of the overall surface distribution of Young Stellar Objects (YSOs) in the Galactic mid-plane using archival Spitzer data. Understanding the relationship between high and low-mass stars is very important in order to better understand how star formation proceeds in these rich environments. In each study YSOs are identified, and the spatial distribution of these objects are measured. The distributions show that there is a correlation between the locations where YSOs are forming and the locations of ionization fronts created by the nearby massive stars. Shock fronts traveling in advance of ionization fronts will compress the molecular gas and will likely trigger further generations of low-mass stars. The advancing ionization front will also have an affect on how the young protostars are formed. Spectral Energy Distribution (SED) fitting is performed on all candidate YSOs in order to determine best-fit physical properties for each source. These properties along with the distribution of the YSOs are used to calculate the amount of triggered star formation occurring in each region. Calculated triggered star formation

rates range from 14 - 58 percent of the total star formation rate, demonstrating that triggering of low-mass stars is occurring in multiple H II regions.

I dedicate this dissertation to my mother, Jolene Bevill, for always believing in me no matter which paths I choose to take.

ACKNOWLEDGMENTS

I would like acknowledge support for this work by the Arizona State University/NASA Space Grant, ASU Department of Physics and ASU School of Earth and Space Exploration, as well as support for this work provided by NASA through an award issued by JPL/Caltech, program PID 20726 for the *Spitzer Space Telescope*.

I would like to thank both my dissertation advisor, Jeff Hester, and the rest of my committee, Steve Desch, Sumner Starrfield, Ariel Anbar, and Robert Marzke, for all of their help and encouragement throughout this challenging process.

There have been a great number of very good friends and colleagues that I have made here at ASU. I want to thank all of them for their friendship and help along the way as we all traveled through the crazy, but often fun times of grad school together. I want to thank Amber Straughn, Russell Ryan, Joe Foy, Todd Veach, Seth Cohen, and Kirsten Chojnicki. I especially want to thank Allison Loll for the many years we spent together in classes, sharing an office, and all the other times she has supported me along the way.

I would like to thank my entire family for all of their support throughout my entire life. I'd especially like to thank my Uncle Ron and Aunt Melinda for always believing in me and for always being there for me. I'd like to thank my cousins Nate, Dave, and Ronnie for being like brothers to me. I'd especially like to thank my cousin Dave for sharing in the passion for astronomy with me when we were young, and for being my partner-in-crime when we went to Space Camp together all those many years ago. I want to thank my brother Devin for not only being a great, supportive

brother, but for also being a wonderful friend who can always make me laugh. I would like to thank my father, Tom, for always supporting me and for always being proud of me no matter what. Finally, I'd like to thank my mom, Jolene, and my step-father, Mike, for always being there for me and for believing in me always.

And most importantly, I would like to thank my husband, Steven, you have been my rock throughout this entire process, always supporting me and encouraging me. I would not have made it through this without you. Above all else, I am so glad that grad school brought us together. I can't imagine the last four years without you and I can't imagine the rest of my life without you either. Thank you for all of your love and support.

TABLE OF CONTENTS

Page

LIST OF FIGURES xii

LIST OF TABLES xvi

CHAPTER

1 INTRODUCTION 1

1.1 Overview of Star Formation in H II Regions 1

1.2 Overview of Low-Mass Protostars 8

1.3 Overview of This Dissertation 11

2 *SPITZER* OBSERVATIONS OF THE H II REGION NGC 2467: AN ANALYSIS OF LOW-MASS TRIGGERED STAR FORMATION 14

2.1 Outline 14

2.2 Introduction 14

2.3 Observations and Data Reduction 16

2.4 Results 19

2.5 Discussion 23

2.5.1 SED Model Fitting of YSOs 23

2.5.2 Mass Distribution of YSOs and Completeness 25

2.5.3 Comparison to *HST* Images 28

2.5.4 Spatial Distribution 31

2.5.4.1 Ionization Front Detection 34

CHAPTER Page

2.5.4.2 Distribution Tests 36

2.5.5 Estimates of Triggering and Star Formation Rates 43

2.6 Summary and Conclusions 50

3 *SPITZER* OBSERVATIONS OF THE H II REGION NGC 2175 75

3.1 Outline 75

3.2 Introduction 75

3.3 Observations and Data Reduction 78

3.4 Results 79

3.5 Discussion 83

3.5.1 SED Model Fitting of YSOs 83

3.5.2 Mass Distribution of YSOs and Completeness 85

3.5.3 Spatial Distribution of YSOs in NGC 2175 86

3.5.3.1 Ionization Front Detection 88

3.5.3.2 Statistical Distribution Tests 89

3.5.4 Estimates of Triggering and Star Formation Rates 91

4 *SPITZER* OBSERVATIONS OF THE H II REGION NGC 3324 124

4.1 Outline 124

4.2 Introduction 124

4.3 Observations and Data Reduction 127

4.4 Results 127

CHAPTER Page

4.5 Discussion 130
4.5.1 SED Model Fitting of YSOs 130
4.5.2 Mass Distribution of YSOs and Completeness 131
4.5.3 Spatial Distribution of YSOs in NGC 3324 132
4.5.4 Statistical Distribution Tests 135
4.5.5 Estimates of Triggering and Star Formation Rates 137

5 *SPITZER* OBSERVATIONS OF THE H II REGION M16 158
5.1 Outline 158
5.2 Introduction 158
5.3 Observations and Data Reduction 161
5.4 Results 163
5.5 Discussion 164
5.5.1 SED Model Fitting of YSOs 164
5.5.2 Mass Distribution of YSOs and Completeness 165
5.5.3 Comparison to *HST* Images 167
5.5.4 Spatial Distribution of YSOs in M16 170
5.5.5 Estimates of Triggering and Star Formation Rates 173

6 AN ANALYSIS OF YSO CLUSTERING ACROSS THE GALACTIC MID-PLANE USING GLIMPSE 204
6.1 Introduction 204

CHAPTER Page

6.2 Data Analysis 205

6.3 Discussion 207

6.3.1 Clustering of YSO Sources 208

6.3.2 Correlation of YSO Sources 209

7 CONCLUSION 227

REFERENCES 237

LIST OF FIGURES

Figure		Page
1.	3-color *Spitzer* Image of NGC 2467	61
2.	IRAC Color-Color Diagram for NGC 2467	62
3.	IRAC and MIPS Color-Color Diagram for NGC 2467	63
4.	2MASS & *Spitzer* Color-Color Diagram for NGC 2467	64
5.	Mass Distribution Function for YSOs in NGC 2467	65
6.	*HST* ACS F658N Hα image of NGC 2467	66
7.	3-color *HST* and *Spitzer* image of NGC 2467	67
8.	Ionization Front Locations for NGC 2467	68
9.	Distance Distribution of YSOs in NGC 2467	69
10.	Model Distribution for NGC 2467	70
11.	Random Probability Distribution for YSOs in NGC 2467	71
12.	NGC 2467 Distance Distribution of YSOs by Evolutionary Class	72
13.	Fraction of Detectable Sources vs. Age of Object for NGC 2467	73
14.	Fraction of Detectable Sources vs. Age of Region for NGC 2467	74
15.	3-Color DSS and *Spitzer* Image of NGC 2175	112
16.	3-Color *Spitzer* Image of NGC 2175	113
17.	IRAC Color-Color Diagram for NGC 2175	114
18.	IRAC and MIPS Color-Color Diagram for NGC 2175	115
19.	2MASS & *Spitzer* Color-Color Diagram for NGC 2175	116
20.	Mass Distribution Function for YSOs in NGC 2175	117

Figure Page

21. NGC 2175 Ionizaton Front Locations 118
22. Distance Distribution of YSOs in NGC 2175 119
23. Model Distribution for NGC 2175 120
24. Fractional Area of YSO Distribution for NGC 2175 121
25. Fraction of Detectable Sources vs. Age of Object for NGC 2175 . . . 122
26. Fraction of Detectable Sources vs. Age of Region for NGC 2175 . . . 123
27. 3-Color *Spitzer* Image of NGC 3324 146
28. IRAC Color-Color Diagram for NGC 3324 147
29. IRAC and MIPS Color-Color Diagram for NGC 3324 148
30. 2MASS & *Spitzer* Color-Color Diagram for NGC 3324 149
31. Mass Distribution Function for YSOs in NGC 3324 150
32. Ionization Front Locations for NGC 3324 151
33. Distance Distribution of YSOs in NGC 3324 152
34. *Spitzer* 5.8μm Image of NGC 3324 with Candidate YSOs 153
35. Model Distribution for NGC 3324 154
36. Random Probability Distribution for YSOs in NGC 3324 155
37. Fraction of Detectable Sources vs. Age of Object for NGC 3324 . . . 156
38. Fraction of Detectable Sources vs. Age of Region for NGC 3324 . . . 157
39. 3-Color *Spitzer* Image of M16 192
40. IRAC Color-Color Diagram for M16 193
41. IRAC and MIPS Color-Color Diagram for M16 194

Figure Page

42. 2MASS & *Spitzer* Color-Color Diagram 195
43. Mass Distribution Function for YSOs in M16 196
44. *HST* WFPC2 image of M16 197
45. Ionization Front Locations for M16 198
46. Distance Distribution of YSOs in M16 199
47. Model Distribution for M16 200
48. Random Probability Distribution for YSOs in M16 201
49. Fraction of Detectable Sources vs. Age of Object for M16 202
50. Fraction of Detectable Sources vs. Age of Region for M16 203
51. GLIMPSE Image of the Galactic Mid-Plane 212
52. Combined model SEDs from stellar and dust components 213
53. Sample of GLIMPSE IRAC Color-Color Plots 214
54. GLIMPSE Color Image of l=10-28 with YSO Contours 215
55. GLIMPSE Color Image of l=28-46 with YSO Contours 216
56. GLIMPSE Color Image of l=46-55 & l=307-316 with YSO Contours . 217
57. GLIMPSE Color Image of l=316-334 with YSO Contours 218
58. GLIMPSE Color Image of l=334-352 with YSO Contours 219
59. Location of YSOs in l=13-16 with YSO Contours 220
60. Location of YSOs in l=16-19 with YSO Contours 221
61. Location of YSOs in l=19-22 with YSO Contours 222
62. Color Image of l=13-16 with YSO Contours and H II Regions 223

Figure Page

63. Color Image of l=16-19 with YSO Contours and H II Regions 224

64. Color Image of l=49-52 with YSO Contours and H II Regions 225

65. Color Image of l=52-55 with YSO Contours and H II Regions 226

LIST OF TABLES

Table		Page
1.	*Spitzer* Photometry for YSOs in NGC 2467	54
2.	*Spitzer* Color Criteria for Protostellar Objects	56
3.	*Spitzer* IRAC Colors and 2MASS Photometry for NGC 2467	57
4.	Best-Fit Model Parameters for YSOs in NGC 2467	59
5.	*Spitzer* Photometry for YSOs in NGC 2175	95
6.	Best-Fit Model Parameters for YSOs in NGC 2175	105
7.	*Spitzer* Photometry for YSOs in NGC 3324	141
8.	Best-Fit Model Parameters for YSOs in NGC 3324	144
9.	*Spitzer* Photometry for YSOs in M16	177
10.	Best-Fit Model Parameters for YSOs in M16	186

1. INTRODUCTION

1.1. Overview of Star Formation in H II Regions

The Taurus-Auriga molecular cloud has long been studied as a typical site of low-mass star formation, partly due to its proximity (d $\sim$ 140 pc) to the Sun and also due to the ability of being able to study the formation of low-mass stars in isolation. On the other hand, low-mass star formation in crowded H II regions is not what is seen in Taurus-Auriga, just on a smaller scale. There are apparent differences in how star formation proceeds in these two types of environments. Unlike the relatively quiescent environment of Taurus-Auriga, environments around massive stars can evolve dramatically on relatively short timescales of only a few$\times 10^4$ yr. Protostars in Taurus-Auriga typically have large dusty disks and are buried deep within the molecular cloud in relative isolation (Padgett et al. 1999). Whereas, *Hubble Space Telescope* (*HST*) observations of protostellar objects in Orion show images of disks being photoevaporated away by the ultraviolet (UV) radiation from nearby massive stars (O'Dell et al. 1993; Bally et al. 2000). These varying environments should have large effects on the overall star formation of the stars and their disks. In order to better understand all modes of low-mass star formation it is important to study both modes independently.

Until recently, it was thought that our own Sun and Solar System formed in a similar, isolated, environment. However, recent meteoritic evidence (Tachibana & Huss 2003) has shown that live ^{60}Fe was abundantly present in the early solar system. This neutron-rich, short-lived radionuclide (SLR) cannot be formed at the required levels by spallation (Lee et al. 1998), but it is formed in abundance in core-collapse

supernova explosions. Supernova models are able to make most of the observed SLRs in reasonable abundances (Hester & Desch 2005; Wadhwa et al. 2007), and it is probable that many young low-mass stars will experience a nearby supernova explosion. The fact that our own Sun likely formed nearby to a massive star has impacted the study of low-mass star forming environments. In contrast to Adams & Myers (2001), who concluded that most low-mass star formation occurs in small isolated regions[1], Lada and Lada (2003) found that as many as 90% of all low-mass stars within 2 kpc of the Sun formed in rich clusters, with most of these clusters containing massive O and B stars. The Sun is constrained to have formed in an H II region. These statistics suggest that is a common mode of star formation.

Low-mass stars have been observed in the interiors of a number of H II regions, located between the molecular cloud and the ionizing massive stars. The young protostars and proplyds seen sitting in the interior of H II regions, like those seen in the Orion Nebula, did not form there. Instead, they had to form in the dense molecular gas and later be uncovered by the passing ionization fronts. The debate has been ongoing about the sequence of star formation in these regions. Are low-mass stars forming coevally with the high-mass stars; forming spontaneously throughout the region via cloud collapse and fragmentation and then just being exposed by the ionization fronts from the massive stars? Or are they being triggered by the expanding H II region created by nearby massive stars which compresses the molecular gas?

[1]They based this conclusion on statistics of open clusters, assumed to persist for hundreds of Myr. As Lada & Lada (2003) discuss, this approach neglects the 70% of clusters that disperse in 10 Myr or less.

One scenario of star formation in H II regions is based on coeval star formation. Different groups use isochronal fitting of young clusters and argue that a majority of the stars in a given cluster all have the same age and therefore there was one single star formation event in the cluster (Sleskick et al. 2008; Hillenbrand et al. 2007; Dahm & Hillenbrand 2007). Hillenbrand et al. suggest that arguments against this scenario are based on incorrect age estimates of both high and low-mass stars in many regions, with the greater ages of high-mass stars being overestimated and the younger ages of low-mass stars being underestimated. Better age estimates require seeing protostars young enough to still be embedded; in practice this requires the infrared capabilities of the *Spitzer Space Telescope*.

Different methods of triggering have been proposed for both high-mass and low-mass stars in these rich environments. In the past, most attention has focused on sequential star formation of massive stars in these types of regions, and assumed that most low-mass stars have formed spontaneously throughout the molecular cloud. Elmegreen & Lada (1977) proposed a model of ionization driven shock fronts into molecular clouds. In their "Collect and Collapse" scenario, a dense layer of gas piles up between the shock and ionization fronts; this layer becomes gravitationally unstable and dense gas clumps fragment and collapse. In this model, new massive stars form in the shocked gas cloud layers, whereas low-mass stars have formed spontaneously throughout the cloud. This has recently been seen observationally by Deharveng et al. (2005) and Zavagno et al. (2006) among others.

Another triggered star formation scenario is the radiatively-driven implosion model, where photoionizing ultra-violet (UV) radiation from massive stars feeds back into the environment of the nearby molecular cloud and interstellar medium (ISM) (Bertoldi 1989; Bertoldi & McKee 1990; Larosa 1983; Hester & Desch 2005). The shock front traveling in advance of the ionization front compresses the surface of the cloud until the cloud reaches critical density for collapse and then induced formation of low-mass stars occurs in the compressed edges of the cloud near the H II region. In this scenario, a random distribution of low-mass stars is not seen: the majority of embedded newly forming low-mass protostars are found in compressed gas between the shock and ionization fronts. Hester & Desch (2005) go on to propose that the Evaporating Gaseous Globule ("EGG") phase, originally proposed by Hester et al. (1996), occurs when the star-forming clump is overrun by the ionization front. The next phase in this hypothesized equence is the proplyd stage where the protostellar disk is truncated by photoevaporation. This has been seen in regions such as M16 (Hester et al. 1996), W3/W4 (Oey et al. 2005), RCW 49 (Whitney et al. 2004a), and M20 (Cernicharo et al. 1998; Hester et al. 1999).

Most O and B stars are observed in groups called OB associations (Blaauw 1964), but besides the O and B stars, young low-mass and intermediate-mass stars are also found in these groups. Studying OB associations can help to answer the questions of how star formation proceeds for different populations of stars, including both low and high-mass stars. Sequential star formation has been observed in a number of OB associations, including the Sco-Cen OB association and the Orion OB

association. Often, the sequential star formation observed in OB associations is on a larger scale than the triggering scenarios described above, which deal with the more localized interaction of neighboring massive stars to nearby high and low-mass stars. This sequential star formation process is seen with different subgroups within a given association having different ages, and it naturally arises that an age spread occurs among subgroups (Blaauw 1964). In the Sco-Cen OB association, sequential star formation has been observed and a few different mechanisms have been proposed for this region.

The Sco-Cen OB association (Sco OB2) has long been studied due to its proximity, as it is the closest OB association to the Sun (d $\sim$ 140 pc; de Zeeuw et al. 1999). There are a number of B stars in this region as well as a low-mass stellar population. Evidence for sequential star formation in Sco OB2 has been seen by a number of groups. The properties of the different subgroups have been studied by de Geus et al. (1989). They find that there is evidence for triggered sequential star formation in Sco OB2, but possibly not in the classical picture, where the sequence of star formation occurs in one direction. Ages of the subgroups in Sco OB2 were determined by de Geus et al. using HR-diagram isochronal fitting. The oldest subgroup, Upper-Cen Lupus, has a best-fit age of 14-15 Myr. The subgroup Lower-Cen Crux has a best-fit age of 11-12 Myr, and the youngest subgroup, Upper Sco, has a best-fit age of 5-6 Myr. No measurable age spread was seen in any of the individual subgroups, but the age spread from group to group suggests that a scenario of sequential star formation has taken place to form the entire Sco-Cen complex. Paradoxially, the oldest sub-

group, Upper-Cen Lup, is located in between the two younger subgroups. de Geus et al. suggest that it is possible that massive star formation began first in the middle of the molecular cloud and formed Upper-Cen Lupus, which in turn triggered star formation in two directions, forming Upper-Sco and Lower-Cen Crux.

Preibisch & Zinnecker (1999, 2001) have also looked at star formation in Upper Sco-Cen and found most of the stellar population has an average age of ∼5 Myr, with no measurable age spread found in this subgroup. They conclude that there was a burst of star formation with most stars being formed within a 1 - 2 Myr time period. They go on to suggest that there is evidence for triggered star formation of the entire complex from an external SN shock wave.

Sequential star formation of low-mass stars on a smaller scale has also been observed in some environments. Other recent evidence for sequential star formation has been seen in regions like BRC 37 by Ikeda et al. (2008). In this region there are two known O stars (09.5 V and O6 V), and a sequence of newly forming protostars in this bright-rimmed cometary globule has been observed. Six protostars, four that are low-mass, have been detected with a sequence of age seen pointing towards the ionizing O stars. The older YSOs have already been uncovered, while the youngest are still embedded. Ikeda et al. (2008) conclude that there is evidence for induced star formation from the ionization and shock fronts created by the O9.5 V star.

In another H II region, KR 140, the evidence for sequential star formation is less certain. Kerton et al. (2008) recently studied this region, which is near the W3/W4/W5 complex but appears to not be associated with it, and discovered a

non-uniform distribution of YSOs. Some of the population of YSOs appears to be distributed in the photodissociation region (PDR) in the immediate vicinity of ionization fronts, which would argue for a triggered star formation mechanism. However, a larger percentage of the discovered YSOs (60%) were found to lie outside the PDR. Therefore, Kerton et al. concluded that this supports a more spontaneous mechanism for low-mass star formation in this region. They did note that they saw a very young population of YSOs, $\sim 10^5$ yr, which suggests that there has been some recent star formation in this region and that the stellar population is not all coeval.

Evidence for sequential triggered star formation in the Orion star forming region has been observed by a number of groups (Sugitani et al. 1989; Cernicharo et al. 1992; Lee et al. 2005; Blaauw 1964). However, work by Hillenbrand (1997) cautions that there is not a clear picture of sequential high-mass star formation in the Ori OB association due to the Orion Ib subgroup being younger than Orion Ic. On the the other hand, there is evidence for the ionization front induced low-mass star formation scenario in the Orion OB association and in the Lac OB1 association (Lee et al. 2005; Lee & Chen 2007). The locations of bright-rimmed clouds (BRCs) near massive O stars suggests that these clouds were once part of larger molecular clouds that have now been photoionized by massive stars and are leading to further star formation in the BRCs (Lee et al. 2005; Sugitani et al. 1991). Lee et al. (2005) also showed that classical T Tauri stars (CTTSs) are preferentially seen between the O stars and six BRCs in Orion, with the youngest CTTSs being located closest to the BRCs. In the Orion and Lac OB associations, Lee et al. show evidence for compression of molecular

clouds by nearby massive stars and shaping of the clouds into BRCs or comet-shaped clouds. They also observe newly formed stars that line up between the massive stars and the parent molecular clouds in an age and evolutionary sequence. They find that no young stars are found to be embedded in molecular clouds far behind the ionization fronts. This suggests that "Collect and Collapse" star formation scenario of Elmegreen & Lada (1977), where only high-mass stars are triggered, and low-mass stars form spontaneously via cloud collapse, will not by itself explain what is seen in the OB associations observed by Lee & Chen.

Still, questions remain about how common triggered star formation is in particular H II region environments, and whether or not triggering is a dominant mechanism for low-mass star formation. The ability to detect low-mass protostars in the embedded phase can help to answer some of these questions about the amount of triggering that is occurring for low-mass stars in H II region environments.

1.2. Overview of Low-Mass Protostars

Young Stellar Objects (YSOs) have infrared excesses (above the stellar photospheric emission) due to a large infalling envelope in the early stages of formation, and an accretion disk in the later stages. Traditionally, YSOs have been separated into the "Class I, II, III" evolutionary stages, first defined by Adams, Lada, and Shu (1987), based on the shapes of their spectral energy distributions (SEDs). Objects with negative spectral indices (n = dlog(νF_ν) / dlog ν) in the near to mid-IR are considered to be protostars; objects with a near and mid-IR excess but with a positive or zero spectral index are thought to be embedded T Tauri stars. Soon after, an

additional class of objects, Class 0, was defined by Andre et al. (1993). Class 0 objects are the earliest stage of protostellar collapse, having SEDs that resemble blackbodies with a peak temperature ≤ 30 K (Andre et al. 1993). For Class 0 objects, most of the mass is in the infalling envelope and these sources can have strong bipolar molecular outflows (Whitney et al. 2003a).

The next youngest sources in the evolutionary sequence are the Class I YSOs. Protostars gain most of their mass in this stage due to accretion at average rates of 10^{-5} $M_{\odot}$ yr^{-1} (eg. Stahler 1988; Smith 1998). This is also typically a shorter stage in the lifetime of a protostar, lasting for approximately a few $\times$ 10^5 yr. Class I objects have large envelope masses that can have bipolar cavities which are evacuated by outflows. Class I objects also have a well-defined accretion disk. During the accretion phase optical emission from the central star is absorbed by dust in the accretion disk and then re-emitted in the infrared. The infrared emission from this process is seen as an excess in the SED above the stellar photosphere emission, with the peak occurring around 100 μm (Whitney et al. 2003a).

The Class II objects also tend to be characterized by excess infrared emission above the stellar photosphere, but the peak occurs in the near-IR. This SED profile is characteristic of a classical T Tauri star surrounded by an accretion disk. Mass infall from the cloud on to the central star has stopped at this point. Class II sources typically have ages of a few Myr (Strom et al. 1989). The final evolutionary stage includes the Class III sources, which are known as "weak-lined" T Tauri stars, and

they have SEDs that resemble a stellar photosphere. The Class III stage usually lasts for $\sim 10^7$ yr and ends with a zero-age main sequence star (ZAMS; Palla 1999).

Selecting sources from their *Spitzer* mid-IR colors can be a robust method for identifying nd classifying candidate YSOs (Allen et al. 2004; Whitney et al. 2003a, 2003b & 2004b), mainly because not all YSOs have an excess in the near-IR, but most show a steeper rise in their SEDs in the mid-IR wavelengths. However, there are still challenges in detecting YSOs in their mid-IR colors. In the mid-IR, protostars can have a wide range of colors depending on many characteristics of the specific system such as: geometry of the accretion disk, orientation of the system to our line of sight, mass and temperature of the central star, and mass of both the infalling envelope and accretion disk (Robitaille et al. 2006). However, selecting YSOs by their mid-IR colors can be done fairly well, especially for the younger Class I objects which typically have the largest color excesses. Also, the *Spitzer* [8.0]-[24] color can be good discriminator for YSOs due to the steeply rising SED of YSOs from 8 to 24 μm (Allen et al. 2004; Whitney et al. 2003a). Whenever possible we use all available colors of a source ranging from 2MASS to *Spitzer* IRAC and MIPS, including the [8.0]-[24] color, to identify it as a candidate YSO. Recent studies, including Poulton et al. 2008, Indebetouw et al. 2007, and Simon et al. 2007, have also successfully used a YSO SED-fitting tool from Robitaille et al. (2007) to identify and classify YSOs in multiple regions. The online SED fitter uses a grid of YSO models based on radiative transfer codes from Whitney et al. (2003a, 2003b,& 2004b). Therefore, YSOs can

be selected and confirmed by a variety of methods; one is color selection in multiple infrared color-color planes and a second is with SED fitting.

1.3. Overview of This Dissertation

The focus of this dissertation is to try to better understand the processes of low-mass star formation in H II region environments, environments that are different from those typically studied in the past for the formation of low-mass stars. New evidence has shown that, our own Sun likely did not form in an isolated environment but instead formed nearby a massive star that went supernova, and recent studies of embedded clusters have also shown that the majority of all low-mass stars form in these rich enviroments, not in isolation. Therefore, it is important to try to answer the many questions about how low-mass star formation proceeds in these environments and how it is different from low-mass star formation in regions like Taurus-Auriga. There are a number of predictions that can be made by each scenario. If the "Collect and Collapse" scenario is correct than most low-mass star formation in H II regions is spontaneous, and then one would expect to see a random distribution of low-mass stars, and the current population of low-mass stars would not be correlated with the locations of ionization fronts. If the ionization front-driven scenario is the more dominant mode of low-mass star formation in an H II region environment, then we should see a correlation between the ionization fronts and the locations of young protostars. We can test these different sets of predictions in order to better constrain how low-mass star formation is proceeding in the rich clusters and H II region environments.

In this dissertation, we present new *Spitzer Space Telescope* data on four H II regions. The in-depth analysis on each of these regions tries to characterize the overall environment in which stars are forming and quantify the amount of triggered star formation that may be occurring. We also look at a large scale picture of star formation across the Galaxy by measuring the surface distribution of YSOs throughout the midplane of the Galaxy. The techniques developed in this thesis help us to identify large numbers of YSOs in these various regions and to look at their overall distributions throughout the region. We initially select candidate YSOs in H II regions based on their mid-IR excesses shown in multiple color-color plots, and then the online SED fitting tool is used to confirm the candidate YSOs and to estimate their physical properties. Comparing the data from multiple regions is giving us new insight into how low-mass star formation is likely proceeding in H II region environments. We are also comparing the *Spitzer* data with other data, such as optical data from the *Hubble Space Telescope* and from other archives such as the Two-Micron All Sky Survey (2MASS) and the Digitized Sky Survey (DSS). This allows for identifying some of the youngest objects in these regions and learning not only about their distribution and formation, but also about the specific environments that they are forming in.

In Chapter 2, we present an in-depth analysis of the H II region NGC 2467. This region was our first test case for developing our selection of YSOs and for looking at the overall distribution of the YSOs. We also estimated the triggered star formation rate in this region and compared that to the overall star formation rate. These same techniques were applied to three other H II regions, NGC 2175, NGC 3324, and M16,

which are presented in Chapters 3-5. Finally, we use archival data from the *Spitzer* legacy survey, GLIMPSE, to look at the overall surface distribution of YSOs across the midplane of the Milky Way galaxy. These data and results are presented in Chapter 6. Finally, we present our conclusions in Chapter 7.

2. *SPITZER* OBSERVATIONS OF THE H II REGION NGC 2467: AN ANALYSIS OF LOW-MASS TRIGGERED STAR FORMATION

2.1. Outline

We present new *Spitzer Space Telescope* observations of the region NGC 2467, and use these observations to determine how the environment of an H II region affects the process of low-mass star formation. We use these observations to independently assess the relationship between low and high-mass star formation. We present IRAC (3.6, 4.5, 5.8, and 8.0 μm) and MIPS (24 μm) maps of this region, covering approximately 400 square arcminutes. The images presented here show a region of ionized gas pushing out into the surrounding molecular cloud, powered by an O6V star and two clusters of massive stars in the region. We have identified 45 sources that have infrared excesses in at least two mid-infrared colors. We present color-color diagrams of the sources and also quantify the spatial distribution of candidate Young Stellar Objects (YSOs) in the region. We find that the YSOs are not randomly distributed in NGC 2467; instead the majority of the sources are distributed along ionization fronts created by the massive stars in the region. Over 75% of the identified 45 YSO candidates are located near the edge of the H II region in gas that has been compressed by the expansion of the H II region. These *Spitzer* data support the hypothesis that a significant fraction of low-mass star formation in NGC 2467 is triggered by H II region expansion. At the current rate of star formation, we estimate at least 25-50% of the total population of YSOs formed by this process.

2.2. Introduction

The H II region NGC 2467, also known as Sharpless 311, is located at a distance of 4.1 kpc (Feinstein & Vazquez 1989). This region is dominated by one O6 Vn star,

HD 64315. The distance to the exciting star has also been determined to be 4.1 kpc. There are also two stellar clusters in the area, Haffner 19 (H19) and Haffner 18ab (H18ab), that contain one later type O and additional B stars, but most (∼70%) of the ionizing radiation comes from the O6 star. There has been some debate as to whether or not the H II region of NGC 2467 and the two clusters H18ab and H19 are actually associated. Photometric studies of the two clusters by Fitzgerald & Moffat (1974) concluded that H18 and H19 are located at a distance of ∼6 kpc. However, Pismis & Moreno (1976) argue that the photometric distance estimates for the clusters are too large. They used Fabry-Perot data to derive kinematic distances to all three components in the region of ∼4 kpc. Moreno-Corral et al. 2002 re-analyzed the Fabry-Perot data and concluded that NGC 2467 and H19 are at the same distance; however they claim that H18ab is farther away at a distance of ∼5 kpc. HI observations from Stacy & Jackson (1982) agree with kinematic observations from Pismis & Moreno, suggesting that H19, H18ab, and NGC 2467 are all associated and at approximately the same distance of 4 kpc. For purposes of our analysis, we assume a distance of 4.1 kpc to the entire H II region complex.

Using UBVRI broad-band data, Moreno-Corral et al. (2002) determined that there are approximately 34 B stars in the cluster H19, the most massive being a B1V star. They estimate the age of H19 to be ∼2 Myr. Fitzgerald & Moffat (1974) estimate the age of H18ab to only be 1 Myr, and Munari et al. (1998) obtained a best-fit age for H18ab of 2 Myr. Pismis and Moreno (1976) claim that the entire

H II region complex is very young, with an age around 2 - 3 Myr. We assume an average age in the region of 2 Myr.

Using *Hubble Space Telescope* (*HST*) Advanced Camera for Surveys (ACS) data, De Marco et al. (2006) identified a large number of cloud fragments in NGC 2467. The ionization front appears to be very near to many of these cloud fragments, suggesting that they have recently broken off from the molecular cloud and are being uncovered by the advancing ionization front. In the process these fragments are being photoevaporated and, thus NGC 2467 is an excellent candidate for a study of star formation in an H II region environment. We can try to answer questions about whether or not further generations of stars, specifically low-mass stars, will be formed due to the effects of the nearby O6V star and other massive stars in the region.

2.3. Observations and Data Reduction

The data for NGC 2467 were obtained by the *Spitzer Space Telescope* with the Infrared Array Camera (IRAC; Fazio et al. 2004) and by the Multiband Imaging Photometer for *Spitzer* (MIPS; Rieke et al. 2004) during Cycle #2 as part of the *Spitzer* program PID 20726. We have data in all four IRAC wavelength bands and in the 24 μm band with MIPS. The four IRAC bands are centered at 3.6, 4.5, 5.8, and 8.0 μm. The total mosaicked image size for NGC 2467 is $\sim$31$'$.7 $\times$ 16$'$.3 for IRAC and $\sim$20$'$.8 $\times$ 21$'$.3 for MIPS. The pixel scale is 1$''$.20 per pixel in all four IRAC bands and 2$''$.45 per pixel in the MIPS 24 μm band. The IRAC channel 1 and channel 3 bands coincide on the sky, as do the channel 2 and channel 4 bands, but there is an offset of 6$'$.73 between the center positions of the two pairs. The IRAC data for each frame

were exposed for 12 seconds, and the field was dithered five times resulting in a total exposure time of 60 seconds per pixel. For the 24 μm data, each frame was 10 seconds long with 4 cycles, resulting in a total exposure time of 560 seconds. The MIPS data were calibrated by the *Spitzer* Science Center (SSC) pipeline version S13.2.0, and the IRAC data were calibrated with the SSC pipeline version S14.0.0.

Mosaicked images were re-made by using the Basic Calibrated Data (BCDs) from the SSC pipeline in the MOPEX software program, version 030106. Within MOPEX, cosmic rays were rejected from the BCD images and detector artifacts were removed. Point sources were extracted from the mosaicked images by first identifying a small region with little background nebulosity present in both the 5.8 and 8.0 μm images. The 5.8 and 8.0 μm images have a much larger extent of nebulosity and therefore point sources are harder to identify above the emission compared with corresponding point sources in the other two IRAC frames. Point sources were selected in this low-background region by eye, and fluxes were measured for these specific sources using the *aper.pro* task in the IDLPHOT package in IDL. Using this same region, an artificial higher background was applied to it and again sources were identified by eye. This was done in order to help constrain the flux level needed to detect sources in the bright background regions of the dataset. We determined a maximum background threshold, comparable to the actual nebular background in the IRAC ch3 and ch4 bands, that we could apply and still detect sources above this background. Using only the sources still detected over the background level, we determined a minimum flux level of these sources and set this as the minimum flux threshold for reliable detection

of point sources. Having a higher background threshold ensures that we did not have a bias against detecting objects in the cluster.

Point sources were then extracted from all of the mosaicked images by selecting sources using the minimum flux threshold for reliable identification, described above. While this excluded some fainter sources in outlying low-brightness regions (sources that may have been identifiable, but are below the minimum flux threshold), the results more accurately represent the actual source distribution in the region of NGC 2467, helping to exclude faint background and foreground stars. There are also more detectable point sources in the IRAC ch1 and ch2 bands than there are in the longer wavelength IRAC bands (ch3 and ch4). However, for this analysis we are interested in selecting YSOs based on their mid-IR excess in *Spitzer* IRAC colors using all four bands, therefore we only select sources that can be detected in all IRAC channels.

The task *find.pro*, in IDLPHOT, was run on all mosaicked images with the new background threshold criteria set to extract all point sources. Aperture photometry was performed on the extracted sources using *aper.pro* in IDLPHOT. For the IRAC images, apertures of radii 3 pixels (3.″6) were used with a background sky annulus of 10-20 pixels (12-24″). For the 24 μm images, an aperture of 2.5 pixels (6″) was used with a sky annulus of 2.5-5.5 pixels (6-13″). Aperture corrections of 1.112, 1.113, 1.125, 1.218, and 1.698 and zero-magnitude fluxes of 280.9 Jy, 179.7 Jy, 115.0 Jy, 64.13 Jy, and 7.14 Jy, provided by the SSC, were applied for IRAC channels 1, 2, 3, 4, and MIPS 24 μm respectively. Magnitude errors were calculated for each source in each band using the standard method described by Everett & Howell (2001). Sky fluxes

were determined by the aperture photometry routine, and the gain and readnoise of each passband were provided by the SSC. Magnitudes and the associated errors of our sources are reported in Table 1.

2.4 Results

We found 186 sources in NGC 2467 that were detected in all four IRAC bands, and we found 23 MIPS 24 μm point sources. Color-color plots were generated from IRAC and MIPS fluxes using the [3.6]-[4.5], [5.8]-[8.0], [3.6]-[5.8] and the [8.0] - [24.0] colors. From these plots, we identified more than 50 sources with infrared excesses in one or more mid-IR colors. The infrared excesses of these sources indicate that they are a young population. The color criteria for the different protostellar objects are listed in Table 2. The IRAC color criteria are taken from Megeath et al. (2004) and are based on models from Allen et al. (2004) and Whitney et al. (2003a & 2004b). Possible Class II and Class I/0 protostars were also identified from the MIPS 24 μm sources based on color criteria from Reach et al. (2004). Similar methods were used by Rho et al. (2006) to identify protostars in the Trifid Nebula with *Spitzer*. In total, 46 possible protostellar candidates were identified in NGC 2467.

The Two-Micron All Sky Survey (2MASS) All-Sky Point Source Catalog (PSC) was used to find 2MASS counterparts to the *Spitzer* sources. There are 166 point sources that were detected in both surveys. There are 29 2MASS sources that show an infrared excess in 2MASS colors and 27 of them correspond to an IRAC YSO source. The overlap of 27 of the 2MASS infrared excess sources with the *Spitzer* detected YSOs validates the methods for selecting YSOs.

Background asymptotic giant branch stars (AGB) and extragalactic contaminants could be present in the data since they can have similar colors as YSOs. The 46 candidates were first checked by eye in all *Spitzer* images in an initial attempt to rule out any extended objects (galaxies) that might be present in the sample. None of the 46 protostellar candidates appeared to be an elongated or extended object. Color and magnitude criteria for both AGB stars and extragalactic contaminants from Harvey et al. (2006) were also used to attempt to reject these objects from the sample. The *Spitzer* color and magnitude criteria for AGB stars and extragalactic sources are also listed in Table 2. A few objects met the AGB criteria, but most were off-cloud sources. None of the selected 46 YSOs had a magnitude or color meeting the criteria for AGB stars. One of the selected YSOs matched the criterion of an extragalactic object. This source was not detected in the 2MASS bands, and was therefore discarded as a possible YSO. This left a total of 45 YSO candidates. Table 1 gives the IRAC and/or MIPS YSO classification, position, calculated *Spitzer* magnitudes and errors for the YSOs; Table 3 lists the IRAC colors that were used to classify the YSOs and the 2MASS magnitudes for the 45 possible YSOs found in NGC 2467.

Figure 1 shows a three-color image of NGC 2467; the IRAC 4.5 μm channel is in blue, the IRAC 8.0 μm channel is in green, and the MIPS 24 μm channel is in red. The IRAC and MIPS images show a region of ionized gas pushing out into the surrounding molecular cloud. Strong polycyclic aromatic hydrocarbon (PAH) emission can be seen in the 8.0 μm band. PAH emission is present throughout the photodissociation region (PDR) at 8.0 μm. PAH emission shows the locations of

edges and ionization fronts created by the O star. The MIPS 24 μm emission is concentrated in the area surrounding the central O6 star, indicating the presence of warm dust. The locations of the possible detected YSOs are shown in Figure 1, along with the locations of known OB stars in the region.

Figure 2 shows an IRAC color-color diagram of [3.6]-[4.5] vs. [5.8]-[8.0] for NGC 2467. The protostellar candidates are plotted in color in Figure 2; Class II sources are in green, Class I/II sources are in yellow, and Class I/0 sources are plotted in red. Figure 3 is a color-color diagram for the 23 detected point sources in the MIPS 24 μm band, with [3.6]-[5.8] vs. [8.0]-[24]. Of these, 18 MIPS sources were classified as protostars based on their colors. Class I/0 sources are plotted in red and Class II sources are shown in green. Of the 18 MIPS 24 μm sources that were found to have a mid-IR excess, all corresponded to an IRAC point source that also had a measured color excess in one or more IRAC colors. Sources that had a large color excess in the [8.0]-[24] color, but a [3.6]-[5.8] color less than zero, are defined by Reach et al. (2004) as sources with possible debris disks. Four 24 μm sources fell into this color regime. There are 45 sources from both the IRAC and MIPS color-color diagrams that had an infrared excess in at least two colors, and 18 sources had a measured color excess in four different colors.

Fourteen IRAC and 10 MIPS sources were found to have colors indicative of Class I/0 objects. Models of objects with these colors from Allen et al. (2004) and Whitney et al. (2003a, 2003b & 2004b) correspond to protostellar objects with infalling dusty envelopes. These are the youngest objects in the sample. Of the

10 MIPS Class I/0 sources, four corresponded to IRAC Class I/0 objects, and six corresponded to IRAC Class I/II sources. Thirteen IRAC and 8 MIPS sources were found to have colors indicative of Class II protostellar objects. The colors of these objects are characteristic of models of young low-mass stars with disks (Allen et al. 2004 and Whitney et al. 2003a, 2003b & 2004b). These objects are more evolved than the Class I/0 objects. Two MIPS Class II sources correspond to an IRAC Class II, and five of the MIPS Class II sources correspond with an IRAC Class I/II source. The other MIPS Class II source corresponds to an IRAC Class I/0 source. Eighteen other IRAC sources were classified as Class I/II objects based on their colors. The MIPS classification of YSOs overlapped fairly well with the IRAC classification. Cases where the sources did not correspond are mostly due to the fact that we only had two separate classifications of MIPS sources, but three possible classes for the IRAC sources.

Figure 4 shows a 2MASS & *Spitzer* color-color diagram of the 2MASS detected sources. The 29 sources to the right of the reddening vector are highlighted in blue, indicating an infrared excess in their 2MASS colors. The reddening vector due to interstellar extinction has a slope of 1.3 as defined by Tapia (1981). The corresponding IRAC YSO candidate sources are also identified; 27 of the 29 2MASS sources with an infrared excess correspond to YSOs selected from *Spitzer*. There is some separation of the IRAC classified sources seen in the 2MASS color-color diagram. A large fraction of the IRAC Class I/0 objects are the reddest sources in the K-[3.6] color. The IRAC

Class II objects lie in the middle range of color excess for the K-[3.6] color, but most have higher H-K colors than the Class I/II objects.

2.5. Discussion

2.5.1. *SED Model Fitting of YSOs*

We are interested in determining the masses and other physical properties of the detected YSOs. In order to look at the possible physical properties of each of the 45 YSO candidates, such as mass, age, and temperature, we used an online SED fitter from Robitaille et al. (2007). The fitter uses a grid of 2×10^4 YSO SED models based on radiative transfer codes from Whitney et al. (2003a, 2003b & 2004b) at 10 different inclination angles, giving 2×10^5 total SED models. There are 14 different model parameters, and in each model stellar mass, age, temperature, and radius are given along with other properties such as total luminosity, disk mass, and envelope accretion rate. Stellar mass ranges from 0.1-50 $M_\odot$, age ranges from 10^3 - 10^7 yr, temperature ranges from 2535 - 46000 K, and radius ranges from 0.4 - 780 $R_\odot$ in the models (see Robitaille et al. 2006 for more details on the total range of parameters).

The SED fitter from Robitaille et al. (2007) can help determine the uniqueness of a given fit based on the best-fit χ^2 value of a model and on the range of values for the various parameters in the model fits. For the youngest sources, the most important parameters are the envelope accretion rate, the disk/envelope inner radius, the stellar temperature, and the disk mass to a lesser extent. The disk properties mentioned above produce the mid-IR flux seen in the SEDs of the youngest sources. For the later evolutionary statges, once the envelope has mostly been dispersed, the important

physical parameters are disk inner radius, accretion rate, mass, and the amount of disk flaring (Robitaille et al. 2006). There is a correlation between age of a given source and the mass accretion rate. Older sources tend to have smaller envelope accretion rates; by the time the envelope accretion rate has fallen below 10^{-10} $M_{\odot}$ yr^{-1} the source tends to be older than 1 Myr, and is considered a disk only source (Robitaille et al. 2006). As mentioned above, the disk inner radius effects the mid-IR excess; at larger inner disk radii the IRAC colors become less red. The color excesses are, therefore, dependent on the size of the inner disk.

Numerous recent *Spitzer* studies have successfully used this fitter in identifying and classifying YSOs. Simon et al. (2007) used the online SED fitter to identify YSOs in the H II region NGC 346 in the Small Magellanic Cloud (SMC). Other recent work by Poulton et al. (2008) has used the SED fitter to model detected YSOs in the Rosette Nebula; they were able to identify over 750 YSOs and classify their evolutionary state. Seale and Looney (2008) used the SED fitter to look at the evolution of outflows produced by nearby YSOs. They found that the SED fitter from Robitaille et al. (2007) adequately matches the observed data from their sample of 27 YSOs.

For NGC 2467, the *Spitzer* and 2MASS fluxes for each candidate YSO were input into the SED fitter, along with a distance estimate for the region. All of our 45 candidate YSOs had at least four flux measurements, with the majority (39 out of 45) having seven or eight flux measurements. The fitter outputs a set of models for each source, and only models with χ^2-$\chi^2_{best} \leq 3$ (per data point) were used in our analysis in determining the best-fit properties of each candidate YSO (similar to

methods used by Robitaille et al. 2007 and Simon et al. 2007). We selected models that had ages less than 2 Myr, i.e. only models with ages that are within the assumed age of the region. We calculated the average mass only from models that were within 3 sigma of the total χ^2 from the best-fit. The corresponding model with the lowest χ^2 and mass closest to the weighted average mass was used. All of the candidate YSOs were checked with stellar photosphere models, and the total χ^2 of the stellar fit was compared to the χ^2 from the YSO fits; none of the candidate YSOs were better fit by a stellar photosphere model. This confirms our color selection criteria of YSOs for this region. The YSO best-fit parameters for each source are listed in Table 2.4. We found sources with masses ranging from 0.35 - 5.7 $M_{\odot}$ and ages ranging from 10^3 - $1{\times}10^6$ yr. There were at least seven sources that had a best-fit mass of less than 1 $M_{\odot}$, demonstrating that we are detecting some fraction of the low-mass star population.

2.5.2. *Mass Distribution of YSOs and Completeness*

A mass estimate for each of the candidate YSOs allows for an examination of the overall population of sources in this region. In order to look at the distribution of masses of YSOs in NGC 2467 and to estimate completeness, we used the best-fit model masses to determine a mass function for the 45 sources. We assumed a mass function of the following form:

$$\frac{dN}{dM} \propto M^{-\Gamma}. \tag{1}$$

Figure 5 shows a plot of log N vs log Best-Fit Mass. The masses of the 45 YSOs were grouped into 6 equally spaced mass bins, centered at 0.5, 1.5, 2.5, 3.5, 4.5, and 5.5 $M_{\odot}$. A least squares fit was performed on the data in order to obtain a line of best-fit to the YSO masses. This line was only fit to the higher mass bins (2.5 - 5.5 $M_{\odot}$), where the sample should be more complete. The best-fit line runs through four of the six mass bins, centered on 2.5, 3.5, 4.5 and 5.5 $M_{\odot}$. The best-fit line represents a mass function (MF) with a slope of 1.47 $\pm$ 0.04; this is comparable to the Salpeter (1955) initial mass function (IMF) value of 1.35 (also fit to the data in Figure 5). Given the best-fit slope of 1.47, the MF spectral index, Γ, is 2.47. Therefore our YSO mass distribution function has the following form:

$$\frac{dN}{dM} \propto M^{-2.47} \quad \text{or} \quad \frac{dN}{d(\log M)} \propto M^{-1.47}. \tag{2}$$

While, the YSO sample appears to be complete at the high mass end, there is a possibility that we are missing some higher mass sources. If this is the case, then the mass distribution would have a flatter slope, possibly closer to the observed mass spectrum seen in other star forming regions and molecular cloud complexes (see discussion in Elmegreen 2008 for more details). There is also the possibility that there is a turnover in the lower mass end of the spectrum, and that the lower mass sources, below 1 $M_{\odot}$, could be better fit by a log-normal mass function as shown by Chabrier (2003). However, due to the incompleteness in our YSO sample at the low-mass end, it is difficult to estimate how the mass spectrum might change. Therefore, for simplicity, we assume the same mass distribution as was calculated in the higher

mass bins down to a mass of 0.2 $M_\odot$. We can also assume that down to this detection threshold, $\sim$ 0.2 $M_\odot$, we would not be able to detect a separation between a Salpeter mass distribution or another form of the MF. The YSO mass spectrum in NGC 2467 appears to have a slope that is no steeper than what we measured, and the calculated MF is very close to the Salpeter IMF. In general, we are not concerned with determining the IMF for this region, per se, but rather to estimate the number of stars forming in this region. For simplicity, we therefore assume a Salpeter IMF (Γ = 2.35) to estimate the total number of stars in this region. There are approximately 20 known B8 and B9 stars in the region from cluster surveys of H19, H18, and SH-311 (Moreno-Corral et al. 2002). There are also two known O stars (O6 and O7) associated with the region. The number of B8/B9 stars was used to determine the IMF normalization constant; using the two known O stars also gives us a very similar normalization constant. The calculated average value of the normalization constant is 800. Using equation 3, we find that there should be approximately (5 $\pm$ 1)$\times 10^3$ stars (assuming Poisson statistics on the 20 stars used to calculate the normalization constant) between the mass range of 0.2-40 $M_\odot$ in NGC 2467:

$$N_{tot} = A \int_{M_1}^{M_2} M^{-2.35} dM = 8 \times 10^2 \int_{0.2M_\odot}^{40M_\odot} M^{-2.35} dM. \quad (3)$$

In order to address completeness, we estimate the total fraction of YSOs that should have been detected in this sample. Using the flux limits from *Spitzer*, we calculated the fraction of the total 200,000 SED models from Robitaille et al. (2006) that we would have been able to detect. Our calculated flux limits were based on our

three-sigma magnitude limits for the IRAC bands for our observations: 14.3, 14.1, 12.4, and 11.6 mag for IRAC 3.6, 4.5, 5.8, and 8.0μm, respectively. The SED models in the grid are based on sources at 1 kpc, so the model fluxes were scaled to 4 kpc, the assumed distance of our sources. The extinction to this region ranges from 1 - 3 magnitudes in A_V with an average extinction of A_V equal to 2 magnitudes (Moreno-Corral et al. 2002 and Munari et al. 1998); this average A_V was also accounted for in the flux limits. Finally, we only accounted for sources with masses less than 6 $M_\odot$ in our completeness estimate, because all of the YSOs had best-fit masses below this threshold, and we would have been able to detect any sources with masses greater than 6 $M_\odot$ in our sample. We found that with our flux limits we should have been able to detect 42% of all models in the grid. Completeness can also be estimated by another method using the mass function of the current YSO population. If the lower mass bins are scaled up the Salpeter best-fit line, we can get an estimated number of how many low-mass YSOs we did not detect. This results in a completeness estimate of 33%, comparable to the completeness estimate using the YSO SEDs.

2.5.3. *Comparison to HST Images*

The main motivation of our *Spitzer* proposal was to observe a select number of H II regions with *Spitzer* that had already been observed with *HST*. *HST* images provide us with detailed information about YSOs after they are in an ionized H II region environment, whereas *Spitzer* allows us to see both a larger view of the region and also to see protostars and their disks that are still embedded in the dense gas around the H II region.

The *HST* ACS images of NGC 2467 by De Marco et al. (2006) were combined with our *Spitzer* images in order to compare what is seen with the different wavelength regime and better resolution of *HST* with the larger field of view of the *Spitzer* images. The *HST* field is centered around the O6 V star, the brightest object in the *HST* ACS image, and a number of fragments, globules, and ionization front edges are also seen in these images. Five *Spitzer*-detected YSOs are located in the *HST* field: three Class I/II sources and two Class II sources. Including the five YSOs, only a total of eight point sources were detected in all four IRAC bands which fall in the ACS FOV. The *HST* ACS Hα image of NGC 2467 is shown in Figure 6; the five detected YSOs are labeled in the image by their YSO source number; the O6 V star is also labeled. Source #16 is classified as an IRAC Class I/II source and a MIPS Class I/O source, with a best-fit mass of 4.7$\pm$0.3 $M_{\odot}$ from our SED fitting. Source #'s 17 and 18 are IRAC Class I/II sources with masses of 3.9$\pm$0.9 $M_{\odot}$ and 4.3$\pm$0.5 $M_{\odot}$, respectively. Source #'s 33 and 34 are IRAC Class II sources with masses of 3.2$\pm$0.9 and 4.2$\pm$0.1 $M_{\odot}$, respectively.

Four out of the five YSOs in the *HST* field are seen sitting against dark clumps in the ACS image. These four sources are seen in projection immediately behind an ionization front. There appears to be one main ionization front that can be identified in the *HST* image, located to the bottom left of the image (see arrow in Figure 6). This location corresponds to a column of gas seen in the *Spitzer* images where a large number of YSOs are located. Figure 7 is a three-color *HST* and *Spitzer* image of the region with the *Spitzer* data scaled to the *HST* field of view. The ionization

front from the main column in the *Spitzer* bands is clearly outlined by the ionization front as seen in the F658N filter. Three YSOs appear to be in close proximity to this ionization front in the *HST* field. De Marco et al. (2006) make note of the many fragments that are being uncovered by the advancing ionization front. Two of the *Spitzer* sources (#'s 17 and 34) close to this ionization front appear to already have been uncovered and are now sitting in the interior of the H II region, while the third source, #16, near the ionization front is embedded in one of these fragments and should be uncovered by the advancing ionization front within a few$\times 10^4$ yr. Source #16 is somewhat hard to see in Figures 6 and 7, but when viewed at full resolution in the ACS image there is an identifiable point source present. One of the other YSOs, #18, appears to also be located in a denser clump of material that can be seen in the F656N *HST* image. The fifth YSO in the *HST* field is source #33; it is close to the O6 V star, and it also appears to be sitting inside the H II region.

One note of interest is that two of the Class I/II sources (#'s 16 and 18) are embedded in the densest clumps of gas, and are apparently still waiting to be uncovered by the advancing ionization front. In contrast, the two Class II sources that are presumably more evolved are located in the interior of the H II region, and have already been uncovered by the ionization front from the O6 star. Source #17 is a Class I/II and it is also located in the interior of the H II region, but it is very close, within 0.2 pc, to the edge of the ionization front and to a dense finger of gas. We interpret this as meaning that it has recently been uncovered by the ionization front. This shows that even in the *HST* field alone, without detailed analysis we already

see a progression of younger sources still embedded in the dense gas waiting to be uncovered by the advancing ionization front, and older Class II type sources sitting inside the ionized H II region having already been uncovered by the ionization front.

2.5.4. *Spatial Distribution*

As discussed in §1, there are two competing ideas for how low-mass star formation proceeds in H II region environments. Hillenbrand et al. (2007; White & Hillenbrand 2004) speculate that star formation in H II regions environments is coeval (low-mass and massive stars are all forming at the same time), and suggest that estimates of ages for low-mass stars have been underestimated and estimates of high-mass stars overestimated. Hillenbrand et al. use isochronal fitting to estimate the ages of sources in many star forming regions, and they find that there is no strong evidence for moderate age spreads in either young star forming regions or young open clusters. In contrast, Hester and Desch (2005) argue that star formation is ongoing over the lifetime of the region and that the dominant mode for low-mass star formation in these environments is triggering by H II region expansion. How can we logically test these two competing views of low-mass star formation? Our aim is to use the *Spitzer* observations of this region to try to answer this question or to try to determine if there is a combination of these two scenarios occurring in NGC 2467.

If there is no triggering occurring and most low-mass star formation is independent of the effects of the massive stars and H II region expansion, then we would expect that the spatial distribution of YSOs would not be correlated with compressed gas or ionization fronts. If this is the case, then we would expect to see clusters of

low-mass stars already forming in the outer regions around H II regions. On the other hand, if most low-mass star formation in H II regions is triggered, then we would expect to see the distribution of YSOs concentrated in the compressed gas and nearby to ionization fronts (see figures 8 & 9 from Hester & Desch 2005 for a more detailed explanation of these scenarios and the observational signtures of each).

Numerous observations of star forming regions have detected very young sources, many sitting at the tips of columns of gas close to massive stars. The work of Hester et al. (1996) using *HST* observations of M16 showed many YSOs sitting at the tips of the columns in the nebula, very close to being uncovered by the advancing ionization front from nearby massive stars. Work by Healy et al. (2004a) detected the presence of water maser emission from eight sources in M16. Water maser emission is known to be associated with protostars, and is a signpost for the earliest stages of star formation. Healy et al. (2004a) show that all eight water maser sources are located within 0.2 pc of an ionization front and conclude that they are not randomly distributed, demonstrating that triggered star formation may be occurring in M16. However, Indebetouw et al. (2007) on M16 and the associated young open cluster NGC 6611 have recently used *Spitzer* observations to look at a larger distribution of YSOs in this region. They find that the distribution of YSO candidates is clustered and conclude that the distribution of YSOs shows moderately distributed star formation, but not a large amount of evidence for triggering by the cluster NGC 6611. So controversy remains regarding triggering in M16. New *Spitzer* observations of other regions, on the other hand, are revealing clearer evidence of triggered star formation. *Spitzer*

observations of the cometary globule in IC 1396 (Reach et al. 2004) reveal many new protostars that have recently formed in the globule. The locations of the protostars, and their high concentration in such a small volume of gas, strongly suggest that their formation was triggered due to the nearby O star. *Spitzer* observations of RCW 49 (Whitney et al. 2004a) and the Trifid nebula (Rho et al. 2006) reveal similar results in each of those regions. These are a few of the examples of "anecdotal" evidence accumulating in favor of triggered star formation in H II regions.

There is also the possibility of solely high-mass triggered star formation in H II regions. As discussed in the introduction of this dissertation, models of high-mass triggered star formation in H II region environments have been proposed by Elmegreen & Lada (1977), along with recent observational studies that show evidence for high-mass triggered star formation via this scenario (Deharveng et al. 2005; Zavagno et al. 2006). But in the "Collect and Collapse" model low-mass star formation occurs spontaneouly throughout the region and is not affected by the massive stars. We are most interested in how low-mass star formation takes place in H II regions, but we have detected a number of intermediate mass YSOs (4 - 6 $M_{\odot}$), that may be late-type B stars, therefore we can address the possibility of triggered star formation in general occurring, or whether only high-mass stars are being triggered via a "Collect and Collapse" scenario. However, no sources above a mass of 5.7$M_{\odot}$ have been detected, and due to the small size of this cluster it is unlikely that any further generation of massive OB stars would have formed in this region.

We are interested in using our data to quantitatively distinguish between these possible scenarios (triggered vs. non-triggered, coeval star formation), or determine if there is a combination of these modes occurring. One possible way to do this is to look at the distribution of sources in the region; if they are all coeval then we would expect the YSOs to be distributed the same way as all other sources, including the more massive OB stars. We tested this by comparing the YSO distribution to the OB stellar population distribution and to the location of ionization fronts in NGC 2467. We are also interested in classifying the effect ionization fronts have on star formation; we tested this by measuring the distances of sources from ionization fronts in the region, and quantifying the degree of clustering of the YSO sources.

2.5.4.1 *Ionization Front Detection*

Ionization fronts were identified first coarsely, by examining the images by eye, and then more precisely by running the edge detection routine, *roberts.pro* in astrolib of IDL, on the *Spitzer* 5.8 and 8.0 μm band images. This routine performed gradient or directional filtering, selecting locations where the pixel values changed by a large amount from one pixel to the next in a given direction. Six areas in NGC 2467 had sharp edges visible in the smoothed image produced by the edge detection routine and these 6 areas were determined to contain possible ionization fronts. Once the six main ionization fronts were identified, they were mapped in xy coordinates using a routine in IDL that returns coordinate values; this routine yielded an x and y position along the length of each ionization front. The thickness of each ionization front outlined in

the images of NGC 2467 was assumed to be $\sim 10^{17}$ cm thick, comparable to typical thicknesses of ionization fronts (10^{16} - 10^{17} cm; Osterbrock 1989).

The main ionization front identified is around the column on the left of the image, as seen in Figure 1. The O6 V ionizing star is near this column of gas; it has an average projected distance of 3 pc away from the column. Ten protostellar sources were identified in projection on this column, the majority of them very near (1-18″) to the edge. Assuming a distance of 4.1 kpc to NGC 2467, these 10 sources are located at projected distances ranging from 0.02 to 0.35 pc from the edge of the ionization front. The second region with an ionization front and a strong clustering of sources is the central cluster in the middle of the image. This region is dominated by strong emission from a few B stars in H18ab, the most massive is a B1 V star. There are eight protostellar sources in close proximity to this region, with projected distances from the ionization front ranging from 0.12 to 0.73 pc.

The third most noticeable region is a possible Stromgren sphere towards the upper right of the image, excited by the B1 V star in the H19 cluster. The ionization front at the edge of the Stromgren sphere is clearly defined in the images of NGC 2467. There are five protostellar sources right on the edge of the ionization front, with projected distances from the ionization front ranging from 0.03 to 0.50 pc. There is also one other source slightly farther out, at a projected distance of 1.04 pc.

Three other ionization fronts were identified using the edge detection routines. Another five detected YSOs are located in close proximity to these three ionization fronts. Overall, 29 of the 45 identified YSOs appear strongly clustered around the

detected ionization fronts. Figure 8 shows the locations of all 45 YSOs and the identified ionization fronts (on the same scale as in Figure 1). The identified ionization fronts are outlined in red and over-plotted on the IRAC 8.0 μm image. This figure demonstrates that the majority of YSOs are most strongly concentrated around the ionization fronts, and they are not well correlated with the O and B star locations.

The histogram distribution of source distances shown in Figure 9 shows that there is a markedly higher frequency of sources near the ionization fronts. The projected distances of the 45 YSOs from the nearest ionization front ranges from 0.02 - 2.2 pc, with more than 60% (28 out of 45), of the sources falling within 0.6 pc of a detected ionization front, and 70% (32 out of 45 objects) falling within 1.0 pc of an ionization front. Our analysis is incapable of detecting face-on ionization fronts; therefore the other 13 sources, which are not seen in projection within 1.0 pc of an ionization front, may still be near ionization fronts as well.

2.5.4.2 *Distribution Tests*

The average projected distance of the edge-on ionization fronts in NGC 2467 is about 3 - 5 pc away from the OB stars. A simplified 3D-model[2] of a hemispherical ionization front which is on average 3 to 5 pc away from an O star was compared to the distribution of sources we see in NGC 2467. This model was used in order to determine if it is likely that the other YSOs not seen in projection within 1 pc from an ionization front are in fact closer to the ionization front than they actually appear to be. We were only able to detect parts of the ionization fronts that are moving edge-on to our line of sight. However, we would not be able to detect the part of

[2]A cylindrical bowl, with equal height and width was used to model the distribution.

the ionization front that is face-on. We therefore want to determine where this total predicted distribution of sources matches the observed distribution of YSOs in NGC 2467.

In order to calculate the predicted distribution of sources within a layer a given distance away from the ionization front, we calculated the ratio of the edge-on volume of this distribution (which we would be able to observe) to the total volume of this distribution. The thickness of the expected YSO distribution was measured from 0.1 to 2.2 pc. As the thickness of the distribution increased, the larger the percentage of expected observed sources within that distribution layer becomes. Varying the radius from 3 to 5 pc (the distance of ionization front to the OB star) only slightly changes the predicted fraction of sources at a given thickness. Using this model, we calculated that a distribution that is concentrated within a layer 0.5 pc away from an ionization front would show 68% of the sources within a projected distance of 0.5 pc from this layer when viewed in projection. For a distribution that is concentrated within 1 pc, we calculated that 70% or less of the sources should be seen in projection within 1 pc. However, for the actual distribution of YSOs in NGC 2467 almost 60% of them are seen in projection within 0.5 pc of an ionization front and over 70% are seen within 1 pc of an ionization front. Figure 10 shows the predicted fractions of sources for the 3D-hemispherical model centered at 3 and 5 pc versus thickness, along with the actual fraction of YSOs that are within the same distance (thickness) from an ionization front. The observed YSO distribution crosses the predicted model fractions at a distance between 0.9 and 1.0 pc. Above a distance of 1 pc, the YSO fraction

is greater than the expected distribution. This suggests that the overall distribution of YSOs in NGC 2467 is a population of sources that is concentrated within a layer that is 1.0 pc or less away from an ionization front.

A second statistical method was used in order to test the likelihood of this current distribution occurring. We calculated the probability of the YSO sources being randomly distributed versus the actual observed distribution. We calculated the fraction of the survey area that is within a given distance of the ionization fronts. If this were a random distribution then we would expect the fraction of YSOs located within a given distance of an ionization front to equal the fraction of the total survey that is within that distance. For example, only 4% of the survey area is within 0.2 pc of an ionization front, but 10 out of 45 YSOs (22%) are located within this distance. The probability of 22% of all randomly distributed YSOs falling within 0.2 pc of the ionization front by chance is only 0.001%. This was calculated using a Poisson probability distribution, which gives the probability of a specific number of YSOs (k) being distributed randomly, as shown by Equation 4:

$$Prob = \frac{\lambda^k e^{-\lambda}}{k!}. \tag{4}$$

The expected number of sources (λ) is equal to the fraction of the survey area within a given distance multiplied by the total number of sources (45) and k is equal to the observed number of YSOs within that distance. The results of this calculation are shown in Figure 11, where the probability of a random distribution from the Poisson Probability Function is plotted versus the distance of the total distribution

from the ionization fronts. The probability of a random distribution drops to as low as 10^{-12} at a distance of 0.5 pc from the ionization front, where 26 out of 45 YSOs are located within this distance, despite only 11% of the total survey area being within this distance. Looking at the likelihood of all 45 YSOs being located within a distance of 2.2 pc of the ionization fronts, we find the odds of this occurring by chance to be 10^{-6}. Therefore, we conclude that this is not a random distribution of sources. The data indicate that the locations of YSOs are strongly correlated with the location of the ionization fronts.

2.5.4.3 *Distance and Age with Evolutionary Class*

We also examined the distribution of YSOs for each specific evolutionary class in order to determine if there is any noticeable trend in distance from ionization fronts versus evolutionary class. The shock front will be traveling in advance of the ionization front, forming the embedded protostar before the ionization front uncovers it. If triggering is occurring in this region, then we would expect that we should see a trend of evolutionary class with distance, with the youngest forming sources (Class I/0s) being the most embedded YSOs compared to the older YSOs (Class II) more likely to have already been uncovered by the passing ionization front, and the Class I/II YSOs falling somewhere in between. For this analysis, we looked at the distance of each YSO from the ionization front in terms of those already uncovered versus those still embedded. YSOs that appear to be ahead of the ionization front and are still embedded are considered to have a negative distance from the ionization front. YSOs that are behind the passing ionization front and have already been uncovered

are given a positive distance. Figure 12 shows a histogram of the distance of the Class II and Class I/0 YSOs from the nearest ionization front, with positive distances for YSOs behind the front and negative distances for those ahead of the ionization front. In this plot it is fairly clear to see a dichotomy between the two different types of YSOs. The majority of the Class II YSOs have already been overrun by the passing ionization front (10 out of 13 with positive distances), while on the other hand a majority of the Class I/0 YSOs (10 out of 14 with negative distances) are still embedded in compressed molecular gas and have yet to be uncovered by the ionization front. The Class I/II YSOs, which are not plotted in Figure 12, fall in between these two distributions, with two-thirds (12 out of 18) located behind the front, and the other third still embedded in compressed gas ahead of the ionization front. This suggests that we see a trend of evolution with distance from an ionization front.

An argument against the triggered star formation scenario is that many of these objects may have been forming before the shock front (which travels in advance of the ionization front) passed over them. In this case, they are just being uncovered by the passing ionization front, and not triggered by the compression of the molecular gas due to the expanding shock front. This therefore partly becomes an age argument; if the majority of the sources have ages much greater than the timescale between the passage of the shock front and the ionization front, then it would be possible that they were forming before the shock front compressed the surrounding molecular gas.

The passage of the shock front is typically followed by the passage of the ionization front within a few$\times 10^5$ yr (Hester and Desch 2005; Sugitani et al. 2002).

For the 32 sources that fall within a projected distance of 1 pc or less from an ionization front, $\sim$70% have best-fit ages less than or equal to 10^5 yr and $\sim$80% have ages less than 3×10^5 yr. For all 45 YSOs, $\sim$65% have ages less than or comparable to the timescale between the passage of the shock front and the ionization front. Although the SED model best-fit ages may not be completely reliable, we can also use the calculated distances of the YSOs from the ionization fronts and can compare the time elapsed since the ionization front passed the YSOs (or will pass them) to their lifetimes. Assuming an ionization front speed of 0.5 - 2 km s^{-1} (Osterbrock 1989), sources at a distance of 0.5 pc from an ionization front are only 2.5×10^5 - 1×10^6 yr away from the nearest ionization front. YSOs that are closer than 0.5 pc were passed by the ionization front even more recently (or will be uncovered by the advancing ionization front even sooner). These timescales are comparable to the best-fit ages and expected lifetimes of Class 0, Class I, and Class II protostellar objects. We conclude that we are seeing very young objects that are still forming, many that are even younger than 10^5 yr. This demonstrates that when the majority of the YSOs formed in the last few$\times 10^5$ yr they likely formed in gas compressed by the shock front from the expanding H II region and are now forming very near to ionization fronts.

As just previously stated, most of the candidate YSOs are much younger than the age of the region (2 Myr), but a caveat to this analysis is that a few of the best-fit ages of the YSOs are close to a Myr old. Two YSOs (#'s 16 & 34) have best-fit

ages of 1.0 and 1.2 Myr old, and 12 YSOs have best-fit ages ranging from 3 - 9×10^5 yr old; therefore within that time period some of these sources could have possibly moved from where they first started forming to their present location. One way to circumvent this complication is to only look at the distribution of the youngest YSOs; 13 of the 14 Class I/0 YSOs have ages ranging from $1\times$ 10^3 - $1\times$ 10^5 yr, with only one Class I/0 YSO with an age of $\sim4\times10^5$ yr. Eight out of the 14 Class I/0 YSOs fall within a projected distance of 0.5 pc from an ionization front, and 10 of the 14 Class I/0 sources are within a projected distance of 1.0 pc from an ionization front. The one Class I/0 YSO with the oldest age is also the Class I/0 YSO that is farthest away ($\sim$ 2.2 pc) from an ionization front. At a speed of 2.5 km s^{-1}, this source could have easily moved a pc ($\sim50''$) or more during its 0.4 Myr lifetime, and could have conceivably been closer to an ionization front earlier on.

The most notable thing we see with the distribution of these sources is that they are strongly associated with the ionization fronts, and they are not randomly distributed. We also do not see clustering of YSOs around the OB stars, which seems to suggest that they are not correlated with the distribution of the OB stars themselves, but are instead more correlated with the ionization front locations. Also, we see no discernable separation in the distribution of the low-mass and the intermediate mass YSOs from the ionization fronts. It appears that low-mass sources are just as likely to be triggered by the expansion of the H II region as the more massive YSOs, and therefore in NGC 2467, we can rule out a solely high-mass triggered star formation scenario as suggested by the "Collect and Collapse" scenario. Overall, the

distribution of the candidate YSOs in this region suggests that a clear majority of the current protostars are forming in regions of gas that are being compressed from the advancing shock fronts.

2.5.5. *Estimates of Triggering and Star Formation Rates*

A final way to test the various scenarios for low-mass star formation is to estimate the amount of triggering that has occurred in NGC 2467 throughout the lifetime of the region. First, we estimate the total star formation rate (SFR) in NGC 2467. Using the Salpeter IMF, we determined that there should be a total of ∼5000 stellar sources ranging in mass from 0.2-40 $M_\odot$(see equation 3). We calculate the total mass in stars from the Salpeter mass distribution (Salpeter 1955), giving a total of 3500 $M_\odot$, as shown in equation 5. From there, we calculate the average SFR in NGC 2467 over the last 2 Myr, given by equation 6:

$$M_{tot} = \int_0^N M dN = A \int_{M_1}^{M_2} M^{-1.35} dM = 8 \times 10^2 \int_{0.2M_\odot}^{40M_\odot} M^{-1.35} dM \sim 3500\,\mathrm{M}_\odot \quad (5)$$

$$Average\ SFR = \frac{3500\,\mathrm{M}_\odot}{2Myr} = 1.75 \times 10^{-3}\ \ \mathrm{M}_\odot\,\mathrm{yr}^{-1} \quad (6)$$

In §2.5.2, we showed that we should be able to detect 42% of all YSO sources based on the grid of SED models from Robitaille et al. (2006); however this estimate diregarded the ages of the sources and of the region. Therefore, in order to calculate the total triggered star formation rate, we want to measure how the detection ability of individual sources would change with elapsed age in the region and age of the individual source. To do this, we took a population of stars given by the Salpeter

IMF, between our mass limits of 0.2 to 40$M_{\odot}$, and assumed a constant SFR equal to the average SFR from Equation 6 (1.75×10^{-3} $M_{\odot}$ yr^{-1}), and then used the Salpeter IMF to age that population of stars. We looked at the detection probabilities for this population of stars at timesteps every 10^5 yr. During each timestep we would take the population of stars at that specific age and of various masses (determined by the IMF), and determine the percentage of sources we should detect based on our *Spitzer* flux limits. The population of stars was aged from one timestep to the next, even as a new population of young stars was being added into the next timestep.

In Figure 13 we show the fraction of detectable objects versus age of the individual sources. In this plot, we see that the best range of ages to detect the YSOs is from 0 to 0.5 Myr, and the peak age is at 3×10^5 yr. After 0.5 Myr, the detection rate drops off dramatically. Within the first 0.5 Myr, the fraction of detected sources is near 50%, but by the time the YSOs reach an age of 2 Myr, the fraction that would be detected has fallen to less than 15%. This implies that the YSOs we are detecting likely have ages of a few$\times10^5$ yr, agreeing with best-fit ages from the SED fitter and timescales from the ionization fronts.

In Figure 14 we have plotted detection probability vs. elapsed age of the region, with probabilities being calculated every 10^5 yr. This plot shows the detection rate of YSOs integrated over the star formation history of the region. During the first 0.5 Myr the detection rate was almost 50%, which is comparable to the total completeness estimates of 42% that we found in §2.5.2; but as the age of the region increases and the population of stars ages, our detection rate decreased to only 27% by 2 Myr.

One other factor that could decrease our detection ability is the fact that once the ionization front overruns the newly forming protostar it will quickly begin to erode the protostellar disk. Johnstone, Hollenback and Bally (1998) calculated that the disk mass loss rate for low-mass stars due to nearby massive stars is $\sim 10^{-7}$ $M_{\odot}$ yr^{-1}. As discussed in §2.5.1, the mid-IR color excess of a YSO, and therefore the method for detecting a YSO, is due to physical properties of the inner disk. The photoevaporation from the ionization front will erode the envelope and the outer disk. This will cause the total luminosity of the source to decrease, therefore decreasing the detection fraction. Using the same SED models and method as above, we estimated what fraction of sources would still be detected if the total disk mass was decreased after the source was uncovered by an ionization front. Again, we only wanted to consider realistic models, therefore we only used models which had an initial disk mass of 10^{-8} $M_{\odot}$ or greater. The effect of different model disk masses on the detection calculations was tested by varying the lower limit of initial disk mass from 10^{-9} - 10^{-7} $M_{\odot}$. We found that the detection fractions only changed by a few percent between these different initial disk mass values, therefore the average value of 10^{-8} $M_{\odot}$ for the minimum disk mass was used. We assumed that the photoevaporation would last for timescales of 10^4 yr, and used the mass loss rate from Johnstone et al. (1998) to determine the new disk mass for each model.

If the initial disk mass of a source was less than 10^{-3} $M_{\odot}$, then that model was considered undetectable after the ionization front overruns the source, unless the initial flux values from the source were well above our flux limits, as was the case

with the more massive objects in the model grid. For example, Model #3004937 pertains to a 0.35 $M_{\odot}$ protostar with an initial disk mass of 5×10^{-4} $M_{\odot}$, and IRAC flux values slightly higher than our detection limits. But once the disk mass of this source is eroded down by the passing ionization front it will have a disk mass value close to zero and will have IRAC flux values below our detection limits. Therefore this is an example of a source that would only be detected during the time interval between its formation and when it is overrun by the ionization front. We found that the detection rate could drop from the initial 45% to as low as 20%, and again the best age range to detect these objects is around a few$\times10^5$ yr. These data are also shown in Figures 13 and 14.

In NGC 2467, YSOs are not distributed throughout the entire volume of the region, yet, while the lowest-mass YSOs will not be detectable for very long (because of the decrease in luminosity due to the loss of the disk and a decrease in luminosity with age in general), we should still expect to see YSOs (low and intermediate mass) throughout the entire region if this is a random distribution. However this is not what we see, the majority of detected YSOs, even the more massive ones, (that have larger flux values and would be seen both nearby and farther from the ionization front if located there), are located in close proximity to the ionization fronts. Also, the age distribution for even the more massive YSOs still peaks at a few $\times10^5$ yr, if older more massive YSOs were randomly distributed in the region they would be detectable, but we do not see them. Therefore, we can assume that we are seeing

the true distribution of YSOs in this region, and there is a correlation between the location of the ionization fronts and the formation of protostars in this region.

Another note of interest, as seen in Figures 13 and 14, is that while we assumed a constant star formation rate over the lifetime of the region the detection rate decreases with time. Haisch et al. (2001) showed that in young star forming clusters, the fraction of sources with disks decreases with age of the cluster. The results presented here seem to suggest that even though the same number of stars are being formed at each timestep, the total detection fraction is still decreasing, similar to the decrease in disk fraction measured by Haisch et al. (2001). Other recent studies have used the Haisch et al. result to justify that the star formation rate is dramatically decreasing with cluster age (Gounelle & Meibom 2008). However, it seems plausible that the star formation rates in young clusters may not be decreasing as dramatically after the first few Myr as claimed by Gounelle & Meibom (2008), only that the detectability of the total fraction of stars with disks decreases with time as demonstrated by Figures 13 and 14.

On the other hand, a recent study of disk survival in NGC 2244 using *Spitzer* data (Balog et al. 2007), has shown that it is possible that effects from high-mass stars on disk survival is only limited to distances of 0.5 pc or less from the high-mass stars, but they do note that compression of molecular gas from the effects of the H II region expansion is still likely as a triggering source in NGC 2244. Over half of the detected YSOs in NGC 2467 are within 0.5 pc of an ionization front, but only a few of the sources are within this distance from the actual ionizing source. If this is

the case, then the decrease in detection rate might mostly be dependent on the age of the source, and therefore in NGC 2467 the current detection rate might only be as low as 27%.

As shown in §2.5.4, we currently observe 45 YSOs, the majority of which have been influenced by the effects of H II region expansion. In order to look at the overall rate of triggered low-mass star formation, we need to estimate the average age of the current population of YSOs. From the SED model fitting, the 45 YSOs have best-fit ages that average to $\sim 2 \times 10^5$ yr. From the previous analysis, we show that best age to detect the YSOs is $\sim 3 \times 10^5$ yr. In §2.5.4.3, we also demonstrate that the due to the close proximity of a majority of the YSOs to the ionization fronts, the timescales are likely to be only a few$\times 10^5$ yr.

Multiple methods have shown that the 45 current YSOs likely have average ages of few$\times 10^5$ yr. While the actual detection fraction value might be somewhat uncertain, it is likely that it is at least below the 30% level, and under plausible assumptions about the distribution as discussed above, one might imagine that the detection fraction is even lower than 20%. Therefore, we assume that the detection rate for the current distribution of YSOs in NGC 2467 is in the range of 17 - 27%. If our ability to detect the current population of sources is at 20% compared to what it would have been during the first 0.5 Myr in the region, then this would also mean that the actual total number of current YSOs could be as much as five times larger. Therefore as shown in Equation 7, 45 detected YSOs with an average age of 2 - 3 $\times 10^5$ yr results in 6 - 13$\times 10^{-4}$ stars formed per yr that are triggered.

$$\frac{\#\ YSOs}{Avg.Age \times DetectionRate} = \frac{45}{(2-3\times10^5\ \mathrm{yr}) \times (0.17-0.27)} = 1.3{-}0.6{\times}10^{-3}\ \mathrm{stars\,yr^{-1}} \tag{7}$$

Using the Salpeter IMF this results in a triggered SFR of $\sim$ 4.2 - 9.0$\times10^{-4}$ $M_\odot$ yr^{-1}.

If this rate of triggered star formation has been constant over the age of the region then we would expect to have a total of 1200-2600 sources that have been triggered due to H II region expansion over the last 2 Myr in NGC 2467. Using the Salpeter IMF, we determined that there should be a total of $\sim$5000 stellar sources ranging in mass from 0.2-40 $M_\odot$. We therefore conclude that between 24 - 52% of the YSOs in NGC 2467 may have been formed due to triggering from H II region expansion.

There are a number of assumptions that have gone into this calculation: assuming a constant SFR, the determination of the current detection fraction, and an estimate of the average age of the YSOs from multiple methods, and while admittedly this is a somewhat simplified calculation, it does allow us to obtain some estimate for how much triggering is occurring in this region. This is a significant fraction ($\sim$25-50%) of the YSOs, a large enough value that triggering of further generations of YSOs cannot be ruled out as a mechanism for low-mass star formation in NGC 2467. Both the total SFR and the triggered SFR are average values over the last 2 Myr, but we would expect the entire process for triggered star formation to have been higher earlier on due to shocks moving at faster rates and densities being higher nearest to the O stars. Therefore, the estimates of 24 - 52% may represent lower limits

for the fraction of stars that would have been affected by triggering from H II region expansion. Although it is probable that not all of the low-mass stars in NGC 2467 have formed from triggering mechanisms, the evidence seems to suggest that some amount of triggering is occurring due to the expansion of the H II region. Even as a lower limit, 24 - 52% is a significant fraction of the total amount of star formation occurring in NGC 2467; therefore, this cannot be discarded as a possible mode of low-mass star formation.

2.6. Summary and Conclusions

The mid-IR data from *Spitzer* show that NGC 2467 is a region of active star formation. We detected a large number of sources with mid-IR excesses, which is evidence of the youth of the region. 45 YSOs were detected based on their *Spitzer* colors, and 27 of them also showed an infrared excess in their 2MASS colors. When comparing the YSOs and *Spitzer* images with *HST* ACS data, we found that 5 of the detected YSOs are in the *HST* field, and 4 of the 5 can be seen sitting against dark clumps, immediately behind an ionization front.

In order to determine the physical properties of each of the 45 YSO candidates, such as mass, age, and temperature, we used an online Spectral Energy Distribution (SED) fitter from Robitaille et al. (2007). We found best-fit masses ranging from 0.3 - 5.7 $M_{\odot}$. There were at least seven sources that had a best-fit mass of less than 1 $M_{\odot}$. Best-fit ages ranged from a few$\times 10^3$ - 10^5 yr for the Class I/0 sources, and 10^4 - 10^6 yr for the Class I/II and Class II sources. Using the masses from the model fitting, we calculated a mass function for the 45 objects. A slope of -1.47 was fit to the data,

this corresponds to an IMF mass spectral index of -2.47, which is comparable to a Salpeter IMF. Using a Salpeter IMF, we calculated that approximately 5000 stars ranging in mass from 0.2-40 $M_{\odot}$ have formed in this region throughout its lifetime. We estimate a completeness of 42%, however this fraction decreases with elapsed age of the region and with age of a given YSO. We estimate that the current detection rate could be as low as 17%, although more likely estimates place it at $\sim$27%.

In order to classify the effect ionization fronts have on star formation, we quantified the distance of sources from ionization fronts in the region and the amount of clustering for the YSO sources. The majority of these sources are located within close proximity to ionization fronts in the region created by massive stars. The distribution of YSOs is not correlated with the location of the OB stars themselves, rafter the sources are distributed along the ionization fronts.

Finally, we estimated the total current rate of star formation and a possible triggered star formation rate in NGC 2467. The estimated current total star formation rate is 1.75×10^{-3} $M_{\odot}$ yr^{-1}, with a triggered star formation rate equal to 0.42 - 0.90×10^{-3} $M_{\odot}$ yr^{-1}. Based on the distribution and age estimates of the current population of candidate YSOs, we estimate that between 24 - 52% of the YSOs forming in this region are due to triggering from the advance of ionization fronts created by nearby massive stars; this is likely a lower limit due to a probable higher triggered SFR in the past. It is probable that some of the low-mass stars in NGC 2467 have formed spontaneously throughout the lifetime of the region, but we are also seeing a population of very young objects that are currently forming in compressed

gas from the H II region expansion. While the data do not suggest that triggering is the only mode of low-mass star formation in this region, it does suggest that triggering is occurring in NGC 2467 and has contributed a substantial fraction to the overall star formation rate.

The environment created by the massive stars in this region is having a definite impact on the formation of further generations of stars. We find that newly forming low-mass stars are mostly forming in areas where the shock front driven in advance of the ionization front is compressing the molecular gas. The sources we are detecting with mid-IR excesses are very young sources, with the majority having ages less than a few $\times$ 10^5 yr, much younger than the age of the region and of the ages of the OB stars, which are around a few $\times$ 10^6 yr. Thus the sources we are finding are newly forming and are located in close proximity to the ionization fronts; they are not coeval with the OB stars. The 45 YSOs detected and the distribution of these sources suggest that NGC 2467 is a prime example of triggered star formation due to H II region expansion.

In the next chapters, using similar analysis methods on other *Spitzer* observed H II regions we will attempt to determine if the calculated triggered star formation rate remains consistent, or if there are variations from region to region. Although this is only one region, we can attempt to use the results from this region to predict what fraction of all low-mass stars may be triggered by H II region expansion. Lada and Lada (2003) have shown that as much as 70-90% of all low-mass stars form in rich clusters also containing massive stars, therefore if 24-52% of low-mass stars in rich

clusters are triggered, then as many as 17-47% of all low-mass stars may be formed by this mechanism.

TABLE 1

SPITZER PHOTOMETRY FOR YSOs IN NGC 2467

Source #	IRAC Class	R.A. J2000	Decl. J2000	[3.6]	[4.5]	[5.8]	[8.0]	[24]
1	I/0	7 52 34.45	-26 26 34.65	11.31 ± 0.03	10.84 ± 0.03	9.82 ± 0.09	8.38 ± 0.04	
2	I/0	7 52 34.43	-26 26 43.83	12.07 ± 0.05	11.52 ± 0.05	10.03 ± 0.10	8.55 ± 0.05	
3	I/0	7 52 36.77	-26 23 23.51	11.35 ± 0.03	10.76 ± 0.02	9.31 ± 0.05	7.80 ± 0.02	5.31 ± 0.18
4	I/0	7 52 38.00	-26 21 31.91	12.35 ± 0.05	11.65 ± 0.04	10.54 ± 0.12	9.22 ± 0.06	
5	I/0	7 52 36.44	-26 26 11.35	11.09 ± 0.02	10.52 ± 0.02	9.38 ± 0.06	8.07 ± 0.03	4.97 ± 0.12
6	I/0	7 52 39.99	-26 25 32.47	12.51 ± 0.06	11.97 ± 0.06	10.70 ± 0.12	9.12 ± 0.05	
7	I/0	7 52 44.41	-26 22 59.32	13.58 ± 0.17	12.60 ± 0.10	12.07 ± 0.52	11.11 ± 0.39	
8	I/0	7 52 45.29	-26 24 22.22	11.72 ± 0.05	11.17 ± 0.04	10.10 ± 0.14	8.79 ± 0.08	
9	I/0	7 52 45.00	-26 24 27.83	12.61 ± 0.10	10.44 ± 0.02	9.17 ± 0.06	8.38 ± 0.05	3.15 ± 0.02
10	I/0	7 52 46.68	-26 23 59.79	12.62 ± 0.09	10.96 ± 0.03	9.81 ± 0.08	8.65 ± 0.05	4.94 ± 0.07
11	I/0	7 52 47.87	-26 22 23.17	12.75 ± 0.08	12.23 ± 0.07	12.31 ± 0.64	10.48 ± 0.21	
12	I/0	7 52 52.82	-26 15 17.20	14.23 ± 0.29	13.10 ± 0.15	11.87 ± 0.44	10.17 ± 0.15	
13	I/0	7 52 51.65	-26 25 42.72	11.17 ± 0.02	10.49 ± 0.02	9.82 ± 0.05	7.96 ± 0.02	4.85 ± 0.03
14	I/0	7 53 01.60	-26 19 59.20	12.33 ± 0.04	11.84 ± 0.04	11.36 ± 0.20	10.24 ± 0.10	
15	I/II	7 52 16.33	-26 23 14.46	11.14 ± 0.02	11.06 ± 0.03	10.58 ± 0.14	9.05 ± 0.06	3.18 ± 0.02
16	I/II	7 52 20.15	-26 27 54.10	11.21 ± 0.03	11.20 ± 0.05	8.53 ± 0.03	6.78 ± 0.01	3.05 ± 0.04
17	I/II	7 52 21.33	-26 27 10.30	11.63 ± 0.04	11.62 ± 0.06	10.92 ± 0.23	9.74 ± 0.14	
18	I/II	7 52 24.04	-26 25 28.96	10.63 ± 0.02	10.61 ± 0.02	9.96 ± 0.08	8.78 ± 0.05	
19	I/II	7 52 27.53	-26 27 21.17	12.73 ± 0.09	12.56 ± 0.13	10.60 ± 0.14	8.81 ± 0.05	5.04 ± 0.09
20	I/II	7 52 31.64	-26 22 07.19	12.07 ± 0.04	11.90 ± 0.06	11.18 ± 0.24	9.99 ± 0.14	
21	I/II	7 52 35.54	-26 25 08.30	11.92 ± 0.04	11.71 ± 0.06	10.19 ± 0.10	8.67 ± 0.04	
22	I/II	7 52 36.38	-26 25 56.30	11.13 ± 0.02	10.83 ± 0.02	9.10 ± 0.03	7.47 ± 0.01	4.70 ± 0.10
23	I/II	7 52 38.58	-26 23 09.94	11.47 ± 0.03	11.37 ± 0.04	10.59 ± 0.13	9.32 ± 0.07	5.39 ± 0.11
24	I/II	7 52 43.16	-26 17 15.79	12.76 ± 0.07	12.50 ± 0.08	11.85 ± 0.40	10.33 ± 0.17	

Continued on next page...

TABLE 1 – Continued

Source #	IRAC Class	R.A. J2000	Decl. J2000	[3.6]	[4.5]	[5.8]	[8.0]	[24]
25	I/II	7 52 40.95	-26 23 48.73	11.28 ± 0.02	11.20 ± 0.03	9.80 ± 0.06	8.31 ± 0.03	5.31 ± 0.10
26	I/II	7 52 44.53	-26 17 26.95	11.68 ± 0.03	11.42 ± 0.03	10.30 ± 0.10	8.65 ± 0.04	4.31 ± 0.04
27	I/II	7 52 42.22	-26 22 51.03	12.55 ± 0.07	12.16 ± 0.07	11.51 ± 0.29	10.32 ± 0.17	
28	I/II	7 52 42.88	-26 24 12.95	10.98 ± 0.03	10.80 ± 0.03	9.39 ± 0.06	7.71 ± 0.02	2.19 ± 0.06
29	I/II	7 52 42.82	-26 25 45.80	11.09 ± 0.02	10.72 ± 0.02	10.21 ± 0.08	8.88 ± 0.04	5.05 ± 0.03
30	I/II	7 52 49.75	-26 16 33.06	11.11 ± 0.02	11.03 ± 0.03	10.39 ± 0.11	9.11 ± 0.05	
31	I/II	7 52 50.22	-26 18 07.62	12.61 ± 0.07	12.22 ± 0.08	10.12 ± 0.10	8.42 ± 0.04	3.75 ± 0.02
32	I/II	7 52 50.25	-26 26 40.30	11.39 ± 0.02	11.35 ± 0.03	10.95 ± 0.14	9.27 ± 0.05	5.42 ± 0.04
33	II	7 52 17.82	-26 25 20.77	11.17 ± 0.03	11.14 ± 0.04	11.40 ± 0.32	10.81 ± 0.35	2.68 ± 0.06
34	II	7 52 23.29	-26 26 50.30	10.24 ± 0.01	10.22 ± 0.02	10.05 ± 0.09	9.33 ± 0.08	
35	II	7 52 32.01	-26 22 37.26	12.49 ± 0.06	12.15 ± 0.07	11.58 ± 0.33	10.70 ± 0.26	
36	II	7 52 32.14	-26 22 30.21	11.99 ± 0.04	11.58 ± 0.04	11.20 ± 0.24	10.52 ± 0.23	
37	II	7 52 35.86	-26 21 58.04	10.79 ± 0.02	10.28 ± 0.02	9.94 ± 0.08	9.44 ± 0.09	
38	II	7 52 33.51	-26 26 47.88	9.05 ± 0.01	8.43 ± 0.01	7.67 ± 0.01	6.65 ± 0.01	3.15 ± 0.02
39	II	7 52 35.54	-26 25 44.39	11.92 ± 0.04	11.85 ± 0.06	11.90 ± 0.44	10.92 ± 0.32	4.45 ± 0.04
40	II	7 52 35.54	-26 26 34.36	9.21 ± 0.01	8.56 ± 0.01	7.92 ± 0.02	7.03 ± 0.01	4.74 ± 0.11
41	II	7 52 36.23	-26 25 48.15	12.02 ± 0.04	11.53 ± 0.04	11.19 ± 0.23	10.54 ± 0.22	
42	II	7 52 39.13	-26 23 21.85	10.63 ± 0.01	10.58 ± 0.02	10.19 ± 0.09	9.19 ± 0.06	
43	II	7 52 47.20	-26 15 58.44	10.59 ± 0.01	10.19 ± 0.02	9.63 ± 0.06	8.98 ± 0.05	
44	II	7 52 43.79	-26 24 21.94	10.94 ± 0.03	10.26 ± 0.02	9.53 ± 0.08	8.47 ± 0.06	
45	II	7 52 55.88	-26 22 39.50	11.21 ± 0.02	10.83 ± 0.02	10.54 ± 0.12	10.00 ± 0.12	

TABLE 2
COLOR CRITERIA FOR SELECTION OF PROTOSTELLAR OBJECTS

	IRAC	MIPS	AGB	Extra-Gal
Class I/0	[3.6]-[4.5] $\geq$ 0.8 or [5.8]-[8.0] $\geq$ 1.1 & [3.6]-[4.5] $\geq$ 0.4	[3.6]-[5.8] $\geq$ 1.4 and [8.0]-[24]: 2.0 - 6.0	[8.0]: 3 - 9 and [4.5]-[8.0] $\leq$ 1	[8.0] $\leq$ 14 - ([4.5]-[8.0])
Class I/II	[3.6]-[4.5] $\leq$ 0.4 and [5.8]-[8.0] $\geq$ 1.1			
Class II	[3.6]-[4.5] $\leq$ 0.8 and 0.4 $\leq$ [5.8]-[8.0] $\leq$ 1.1	[3.6]-[5.8] $\leq$ 1.4 and [8.0]-[24]: 2.0 - 6.0		

TABLE 3

NGC 2467 IRAC COLORS AND 2MASS PHOTOMETRY

Source #	[3.6]-[4.5]	[5.8]-[8.0]	J	H	K
1	0.47	1.44	14.58	13.42	12.61
2	0.56	1.47	16.54	15.34	14.17
3	0.60	1.51	16.54	14.66	13.42
4	0.70	1.32	15.74	14.65	13.87
5	0.57	1.31	15.31	13.88	12.85
6	0.54	1.59	14.66	13.89	13.32
7	0.98	0.96			
8	0.55	1.32	16.52	14.56	13.47
9	2.17	0.79			
10	1.66	1.16			
11	0.52	1.83	15.15	14.15	13.60
12	1.13	1.70			
13	0.67	1.85	14.56	13.81	12.85
14	0.49	1.12	14.98	14.14	13.66
15	0.08	1.53	11.37	11.28	11.15
16	0.01	1.75	14.66	14.52	14.48
17	0.00	1.18	12.12	11.82	11.77
18	0.02	1.18	11.13	10.79	10.73
19	0.16	1.79	15.21	14.81	14.42
20	0.16	1.19	13.53	12.98	12.57
21	0.21	1.53	14.75	13.71	13.16
22	0.30	1.63	15.67	14.24	12.53
23	0.09	1.28	12.19	11.89	11.68
24	0.26	1.51	14.89	14.30	13.83
25	0.08	1.49	12.54	12.09	11.83
26	0.26	1.65	12.00	11.94	11.98
27	0.39	1.18	15.20	13.79	13.23
28	0.19	1.68	11.46	11.36	11.31
29	0.37	1.32	14.44	13.64	12.79
30	0.08	1.27	11.85	11.33	11.14
31	0.39	1.70			
32	0.04	1.68	11.77	11.60	11.43
33	0.03	0.59	11.88	11.34	11.19
34	0.02	0.72	11.01	10.38	10.26
35	0.34	0.88	15.37	14.17	13.60
36	0.41	0.68	15.08	13.99	13.24
37	0.51	0.49	13.12	12.26	11.67
38	0.62	1.02	12.93	11.62	10.53

Continued on next page...

TABLE 3 – Continued

Source #	[3.6]-[4.5]	[5.8]-[8.0]	J	H	K
39	0.08	0.98	12.32	12.12	12.02
40	0.66	0.89	13.09	11.77	10.63
41	0.49	0.64	12.12	11.82	11.77
42	0.05	1.00	10.99	10.85	10.72
43	0.40	0.65	13.22	12.76	12.15
44	0.68	1.07			
45	0.38	0.54	13.51	12.71	12.18

TABLE 4

NGC 2467 YSO BEST-FIT PARAMETERS

Source #	Model #	Mass ($M_\odot$)	Age ($\times 10^5$ yr)	Radius ($R_\odot$)	Temp (K)	Log(d) (kpc)
1	3011772	2.10 ± 1.17	1.00	10.98	4340.0	0.61
2	3003476	3.59 ± 1.25	0.09	21.63	4298.0	0.62
3	3004748	1.92 ± 0.39	0.07	14.42	4180.0	0.62
4	3018503	0.62 ± 0.54	0.14	6.61	3816.0	0.62
5	3012434	1.35 ± 0.59	0.02	12.91	4050.0	0.60
6	3014174	0.99 ± 0.31	0.53	6.81	4103.0	0.60
7	3010612	0.93 ± 0.29	0.24	7.54	4027.0	0.61
8	3009627	2.46 ± 1.31	0.78	12.66	4359.0	0.60
9	3011577	1.23 ± 0.44	0.04	12.89	3995.0	0.62
10	3008298	1.52 ± 0.75	0.05	12.33	4124.0	0.61
11	3016995	0.63 ± 0.57	4.70	3.66	3936.0	0.61
12	3015705	0.35 ± 0.46	0.61	3.72	3489.0	0.60
13	3006942	2.52 ± 1.04	0.22	14.76	4305.0	0.62
14	3010799	1.43 ± 0.90	0.38	8.76	4226.0	0.62
15	3005834	2.37 ± 1.33	0.56	12.61	4343.0	0.60
16	3007424	4.70 ± 0.33	12.00	2.68	16000.0	0.62
17	3008715	3.94 ± 0.93	4.00	8.24	4903.0	0.60
18	3003892	4.31 ± 0.50	6.60	9.46	5762.0	0.60
19	3016713	1.16 ± 0.35	0.02	11.81	4008.0	0.60
20	3017850	2.50 ± 0.87	4.40	5.73	4700.0	0.62
21	3009574	1.98 ± 1.57	0.61	10.93	4313.0	0.60
22	3005274	5.73 ± 0.26	2.90	14.27	6109.0	0.61
23	3016205	3.80 ± 1.00	3.20	8.62	4807.0	0.60
24	3010603	1.10 ± 0.88	5.30	3.59	4314.0	0.60
25	3005254	2.55 ± 0.41	0.86	12.85	4369.0	0.61
26	3016360	1.88 ± 0.11	1.10	10.02	4321.0	0.62
27	3002399	0.89 ± 0.69	0.14	7.86	3989.0	0.60
28	3017155	2.44 ± 1.94	0.28	13.77	4319.0	0.60
29	3018885	1.92 ± 1.02	0.92	10.39	4318.0	0.60
30	3005897	2.17 ± 0.85	0.94	11.39	4341.0	0.60
31	3017257	1.23 ± 0.27	0.11	11.08	4057.0	0.62
32	3006533	4.21 ± 0.14	5.40	9.21	5209.0	0.60
33	3011105	3.15 ± 0.92	1.30	12.49	4502.0	0.62
34	3000825	4.17 ± 0.12	8.30	8.33	6482.0	0.60
35	3011935	0.83 ± 0.33	0.19	7.14	3976.0	0.61
36	3000455	1.28 ± 0.94	1.10	7.66	4214.0	0.60
37	3012794	4.21 ± 0.21	5.70	9.26	5268.0	0.60

Continued on next page...

TABLE 4 – Continued

Source #	Model #	Mass ($M_\odot$)	Age ($\times 10^5$ yr)	Radius ($R_\odot$)	Temp (K)	Log(d) (kpc)
38	3005266	5.12 ± 0.11	5.70	7.81	9534.0	0.61
39	3016265	3.81 ± 0.78	9.20	7.91	5612.0	0.60
40	3005266	5.12 ± 0.56	5.70	7.81	9534.0	0.62
41	3015096	1.40 ± 0.67	2.00	7.05	4292.0	0.61
42	3019036	3.62 ± 0.95	0.59	17.12	4414.0	0.62
43	3005949	3.99 ± 0.45	10.00	7.18	7158.0	0.62
44	3011228	2.90 ± 1.22	0.07	19.35	4246.0	0.62
45	3010779	2.55 ± 0.80	1.00	12.55	4386.0	0.62

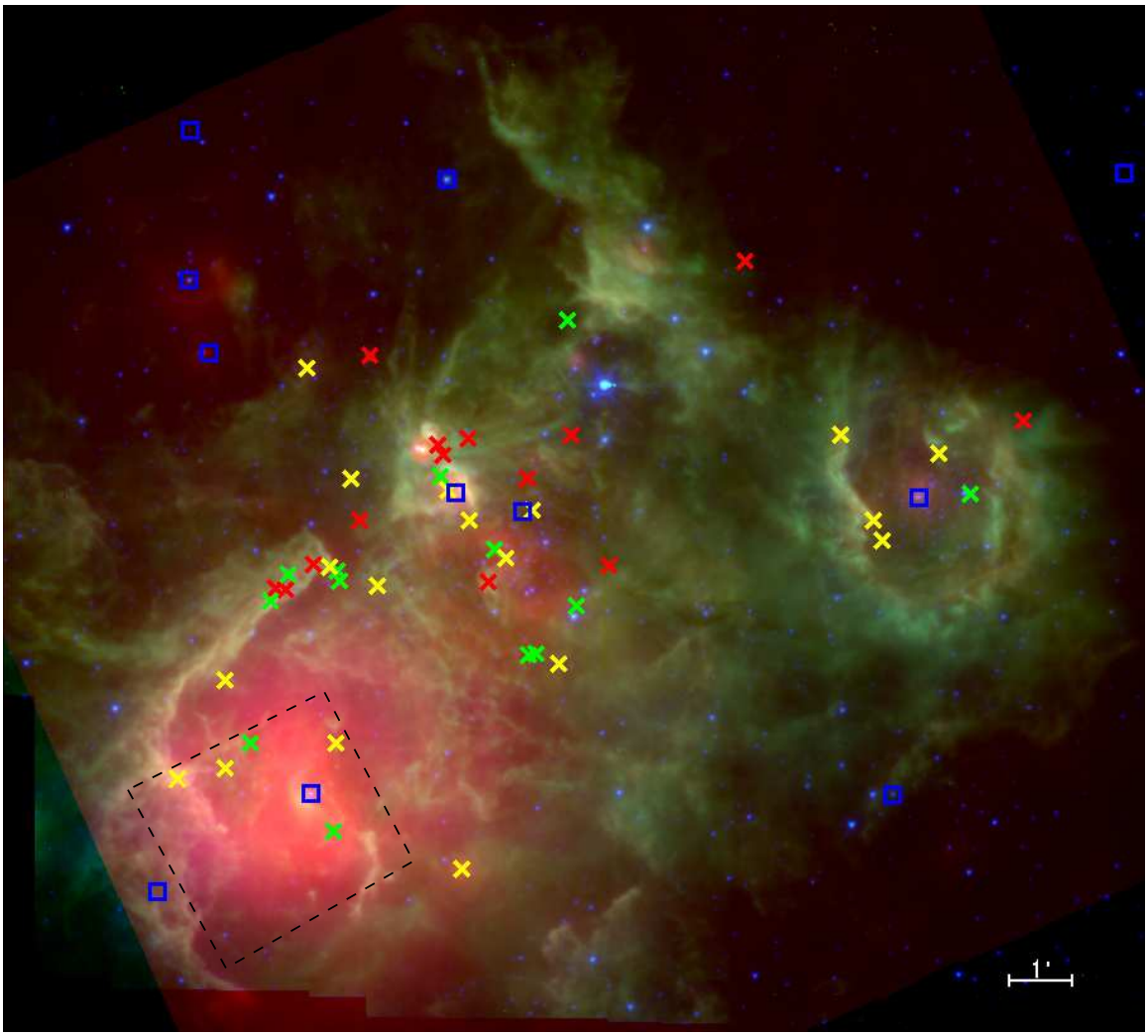

FIG. 1.—3-color *Spitzer* image of NGC 2467: Red is MIPS 24 μm, green is IRAC 8.0 μm, and blue is IRAC 4.5 μm. Red, yellow, and green Xs show locations of Class 0/I, Class I/II, and Class II protostars, respectively, and blue squares mark the locations of known OB stars in the region. The dashed line shows the location of the *HST* ACS FOV, as seen in Figures 6 and 7. A scale of $1'$ is labeled in the figure. This line corresponds to a distance of 1.2 pc given the assumed distance of 4.1 kpc to the region.

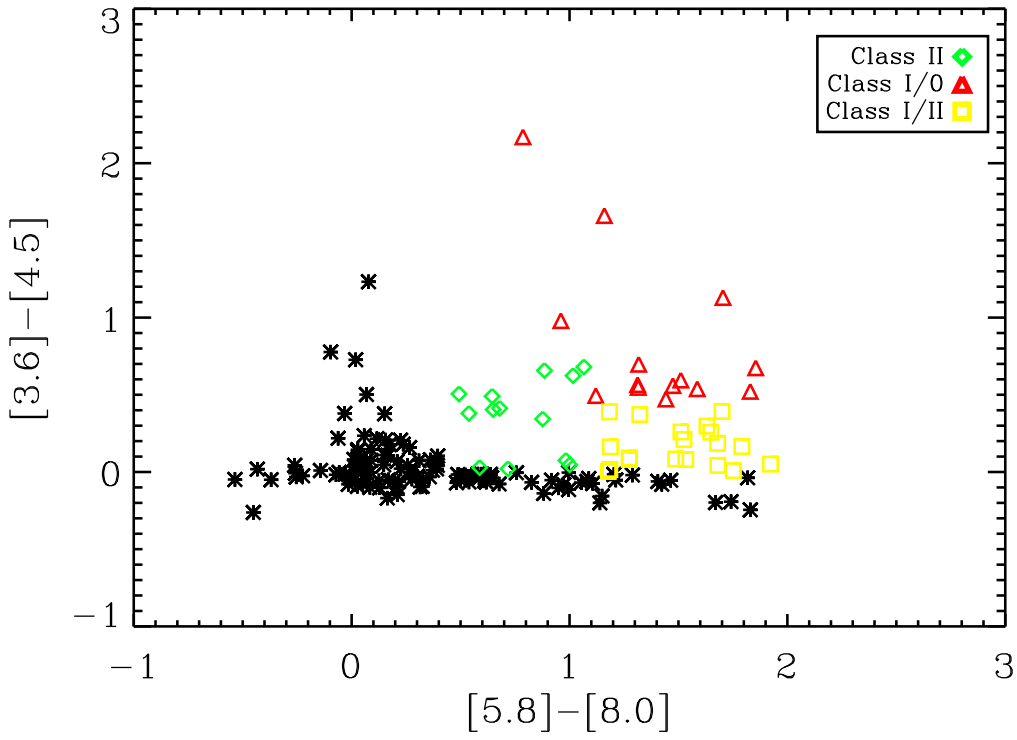

FIG. 2. —IRAC color-color diagram for NGC 2467, showing YSO classification of IRAC detected sources. Color criteria taken from Allen et al. (2004), and Whitney et al. (2003 & 2004b).

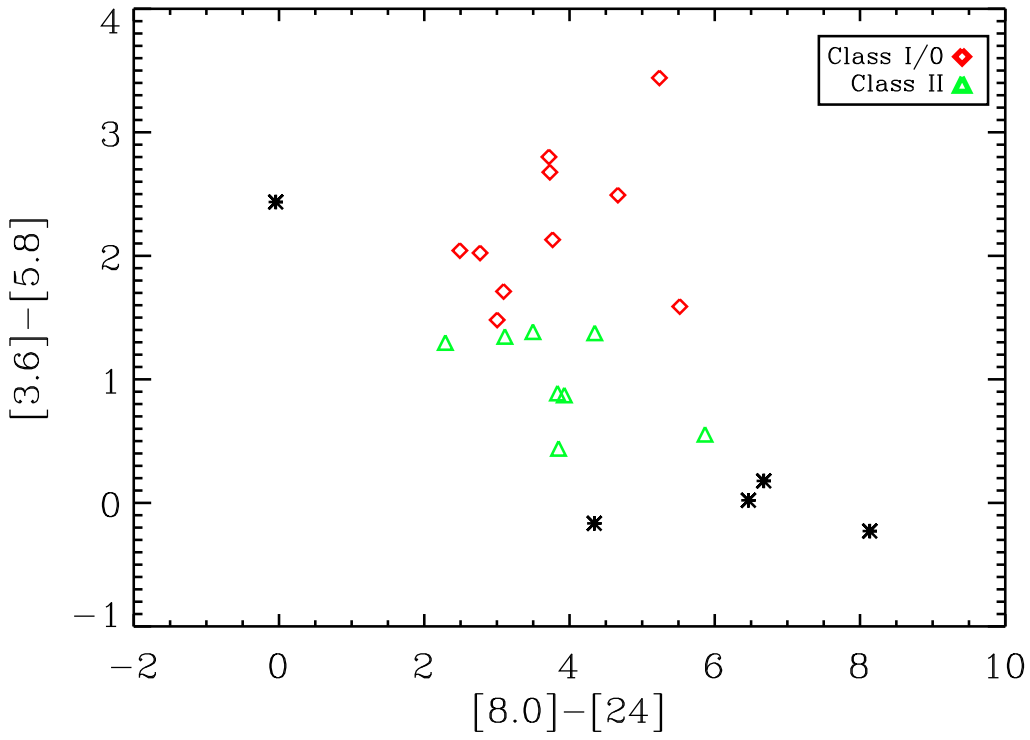

FIG. 3.—IRAC and MIPS color-color diagram for NGC 2467, showing YSO classification of the MIPS 24 μm detected sources. Color criteria taken from Whitney et al. (2003 & 2004b) and Reach et al. (2004).

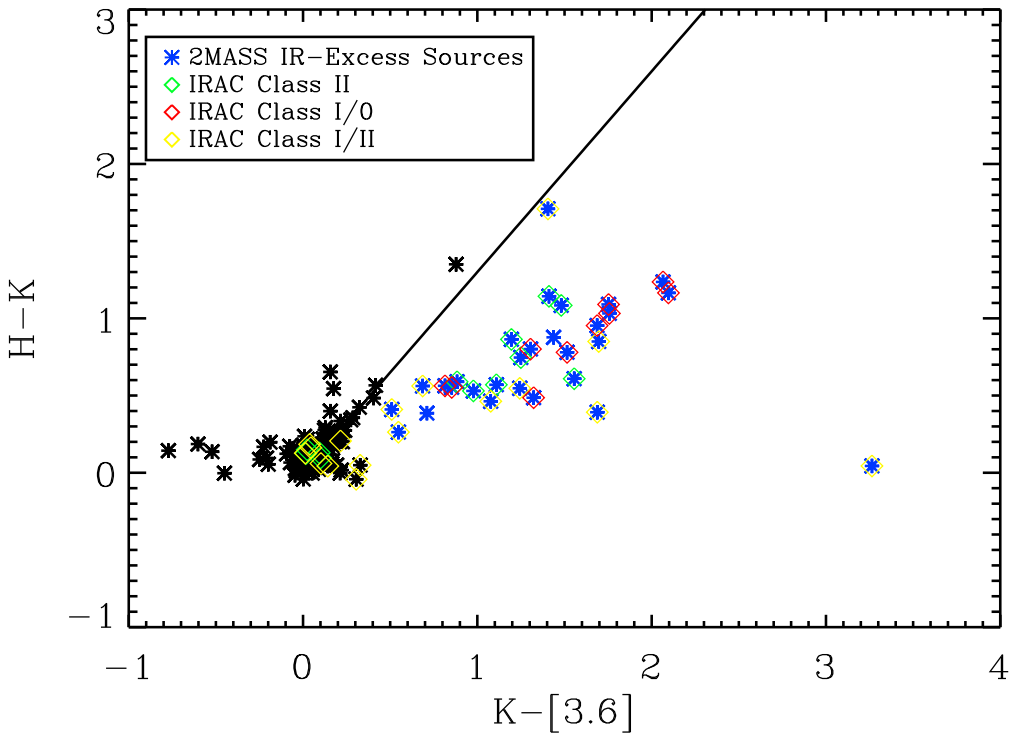

FIG. 4.—2MASS & *Spitzer* color-color diagram of the detected 2MASS sources in NGC 2467. Sources to the right of the reddening vector, which has a slope equal to 1.3, are sources with an infrared excess in the NIR. 27 out of the 29 sources with a 2MASS NIR-excess correspond to a *Spitzer* selected YSO candidate.

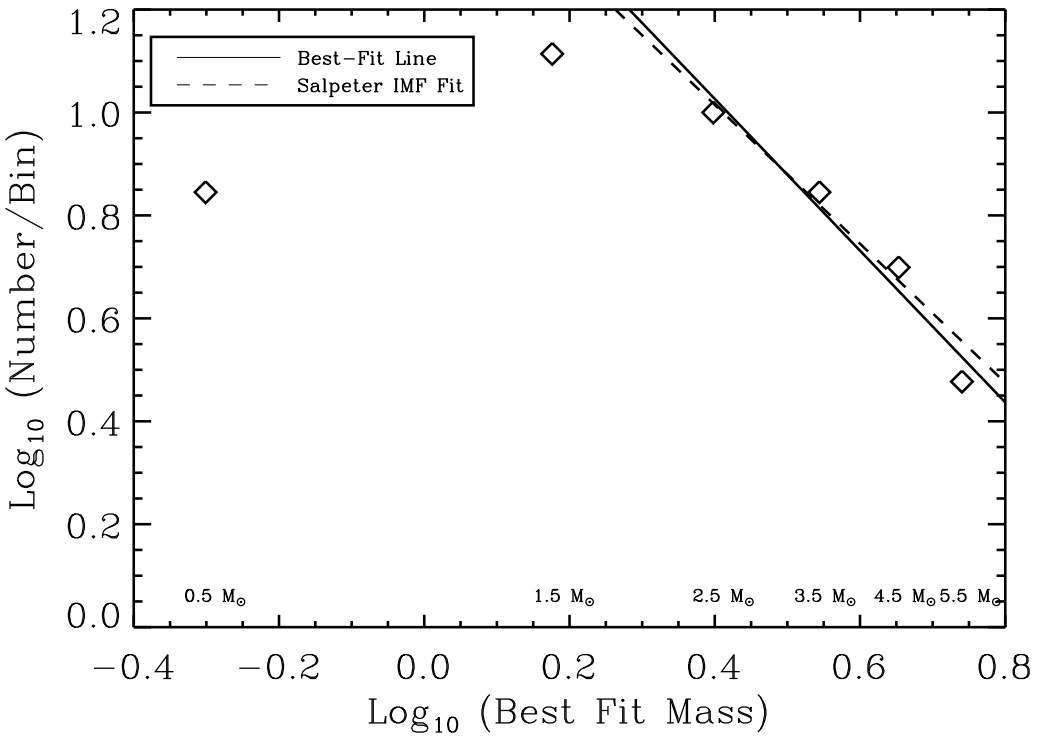

FIG. 5.—Mass distribution function for YSOs in NGC 2467. The solid line is the best-fit to our data, and corresponds to a slope of -1.47. The dashed line is for a Salpeter IMF with a slope of -1.35. Both lines were fit to the higher mass bins, where our sample is assumed to be more complete.

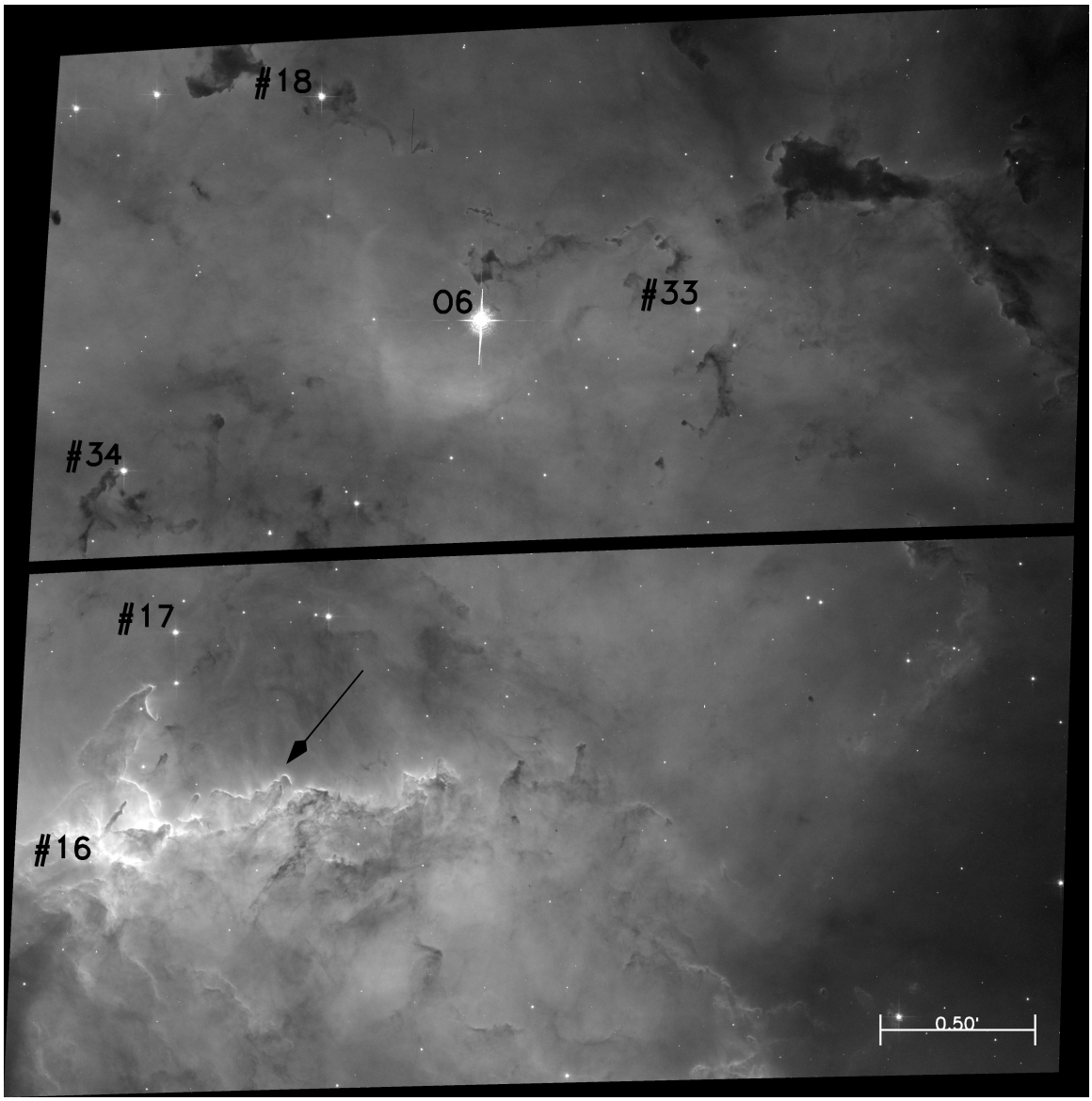

FIG. 6.—*HST* ACS F656N Hα image of NGC 2467, centered on the main O6 V ionizing star. The *HST* ACS image encompasses a total area of 4.2 × 4.2 pc, the scale bar on the image of 0.′5 corresponds to a distance of 0.6 pc. Detected YSOs in this image are labeled by their source number. There are three Class I/II sources, #16, #17, & #18, and there are two Class II sources, #33 & #18. Four of the five YSOs shown here are located in close proximity to ionization fronts, and are seen sitting against dark clumps in the ACS image. Part of the main ionization front can be seen in this image and is identified by the arrow.

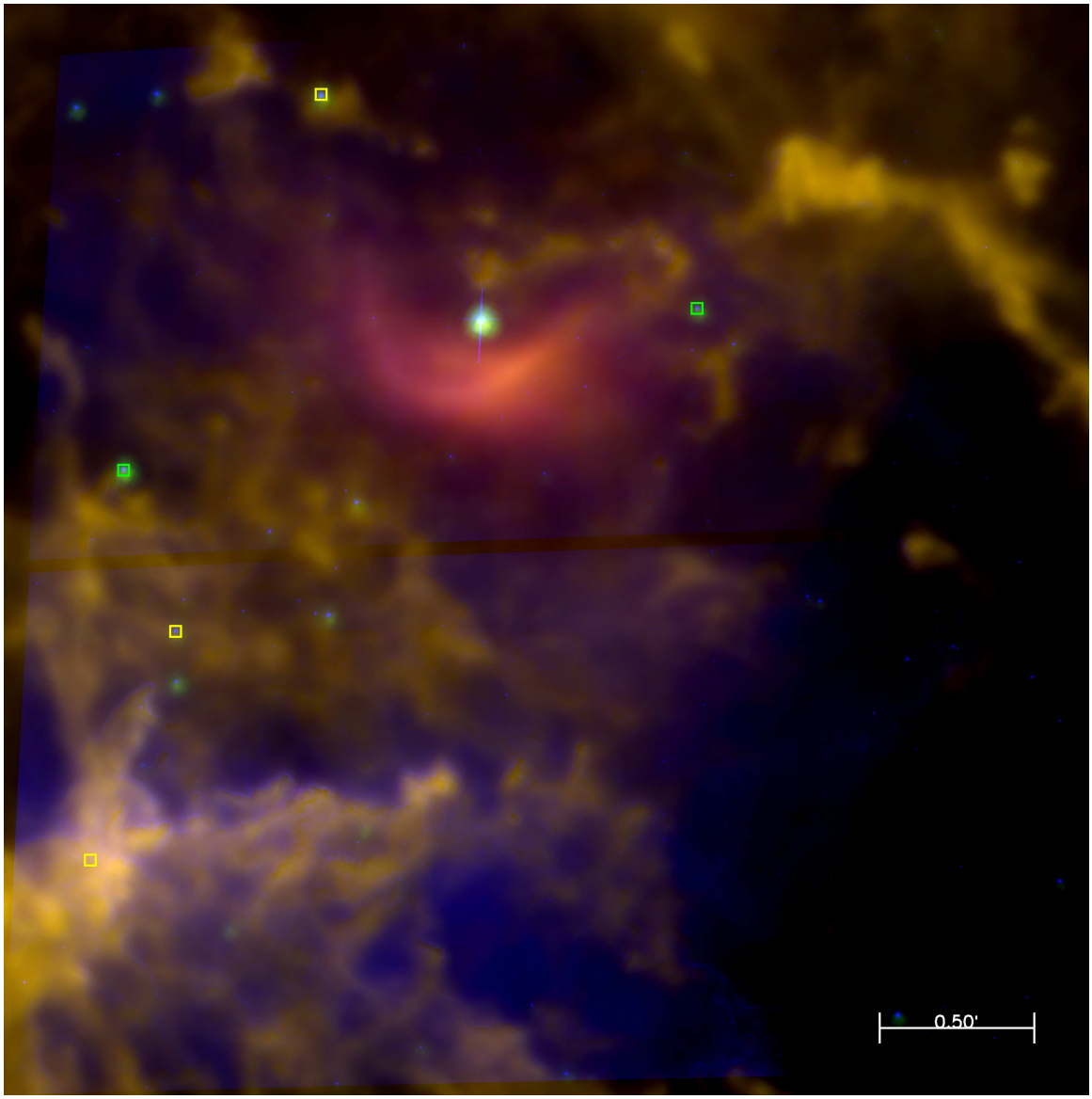

FIG. 7.—3-color image of NGC 2467, scale of the *HST* ACS image (total area equals 4.2 × 4.2 pc, with scale bar of 0′.5 equal to 0.6 pc). *Spitzer* IRAC channel 4 is in red, IRAC channel 3 is in green, and ACS F658N is in blue. Detected YSOs in the image are marked by yellow and green squares, for the Class I/II and Class II YSO sources.

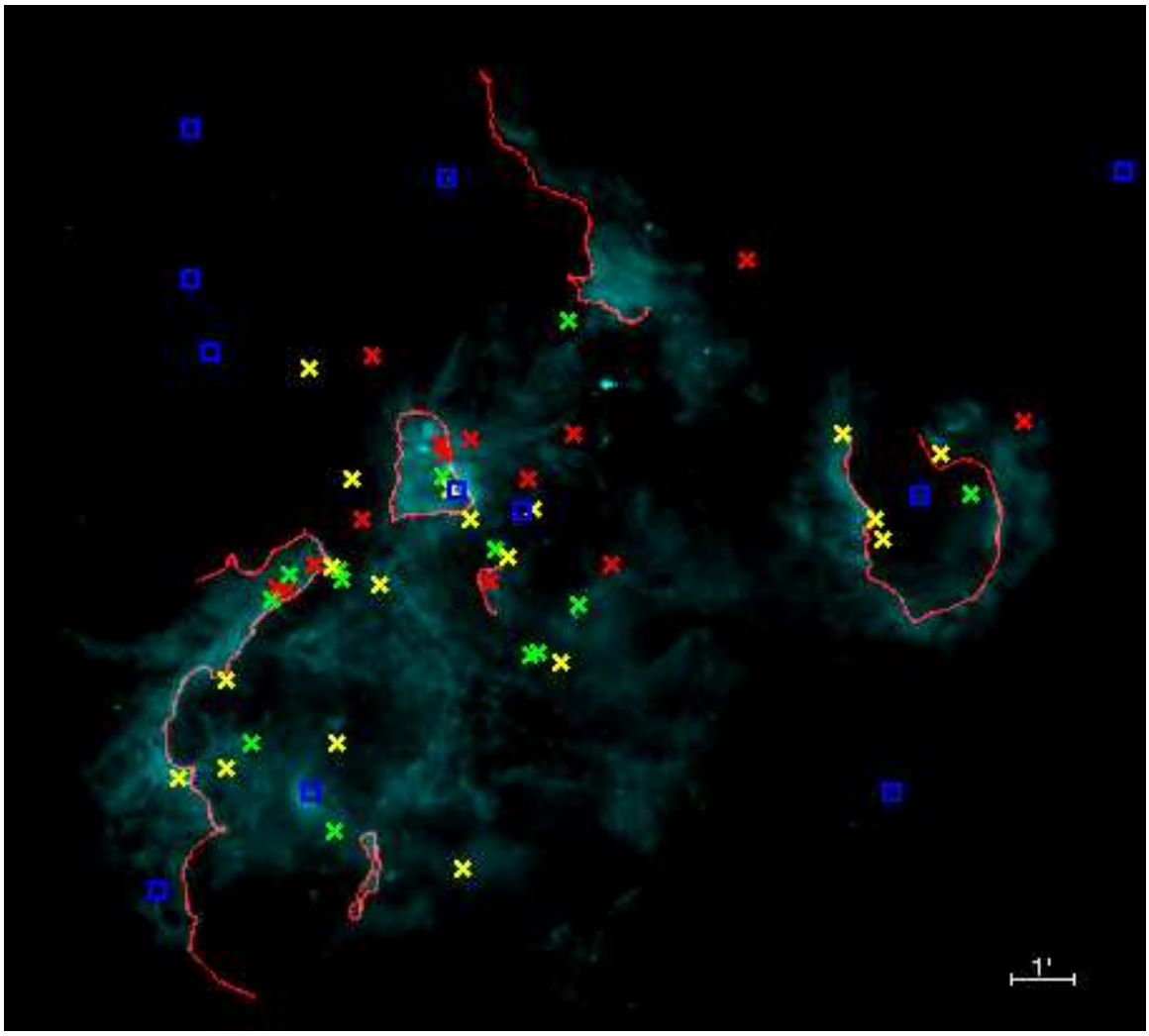

FIG. 8. —Locations of identified ionization fronts in NGC 2467, same scale as in Figure 1. Identified ionization fronts are outlined in red and are over-plotted on the IRAC 8.0 μm image. Red, yellow, and green Xs show locations of Class 0/I, Class I/II, and Class II protostars, blue squares mark the locations of known OB stars in the region. Line equal to $1'$ corresponds to a distance of 1.2 pc, given the assumed distance of 4.1 kpc to the region.

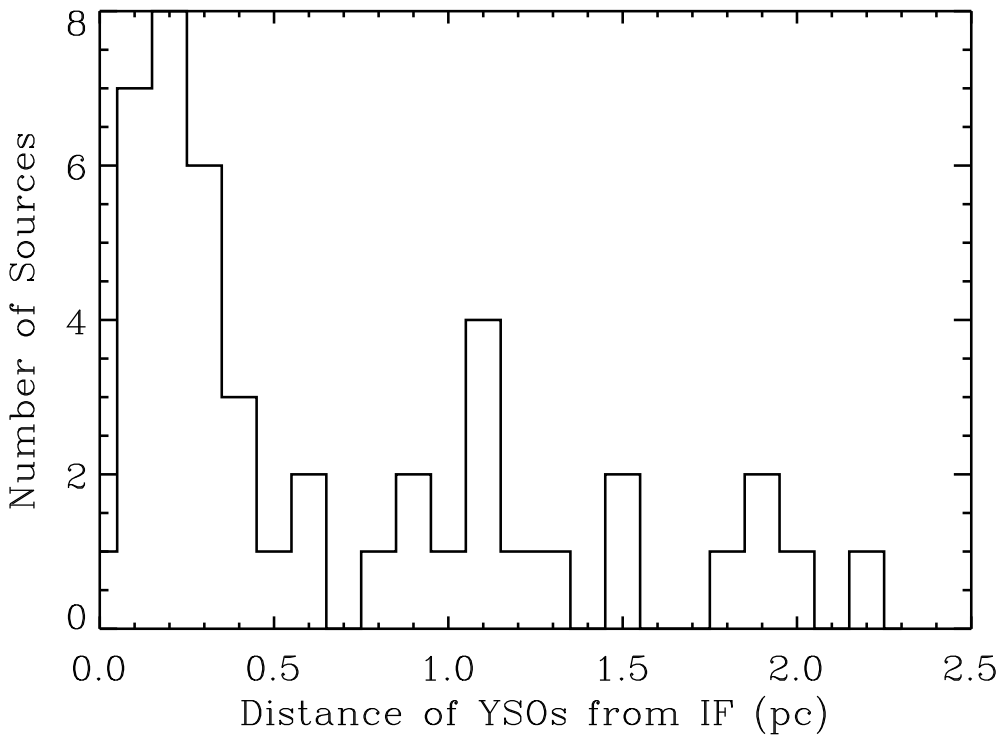

FIG. 9.—Distance distribution of YSOs in NGC 2467 from the nearest ionization front.

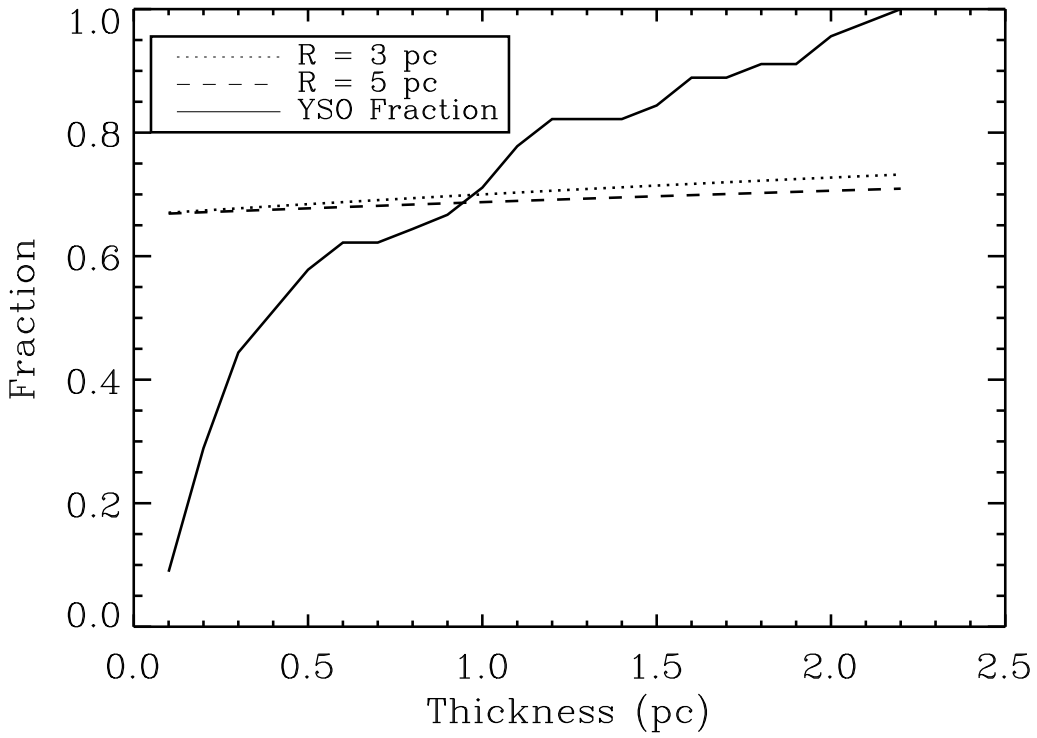

FIG. 10.—A simplified 3D hemispherical model of an ionization front is used to determine the expected number of observed sources that would be seen within the layer thickness when viewed in projection. Fraction of expected sources observed within a given thickness distribution from an ionization front, with ionization fronts centered at 3 and 5 pc away from an OB star shown by dashed lines. Actual distribution of YSOs in NGC 2467 shown by solid line. The expected distribution and the observed distribution cross at approximately 1 pc, indicating that the actual distribution of YSOs in NGC 2467 is a population of sources concentrated within 1 pc or less from the nearest ionization front.

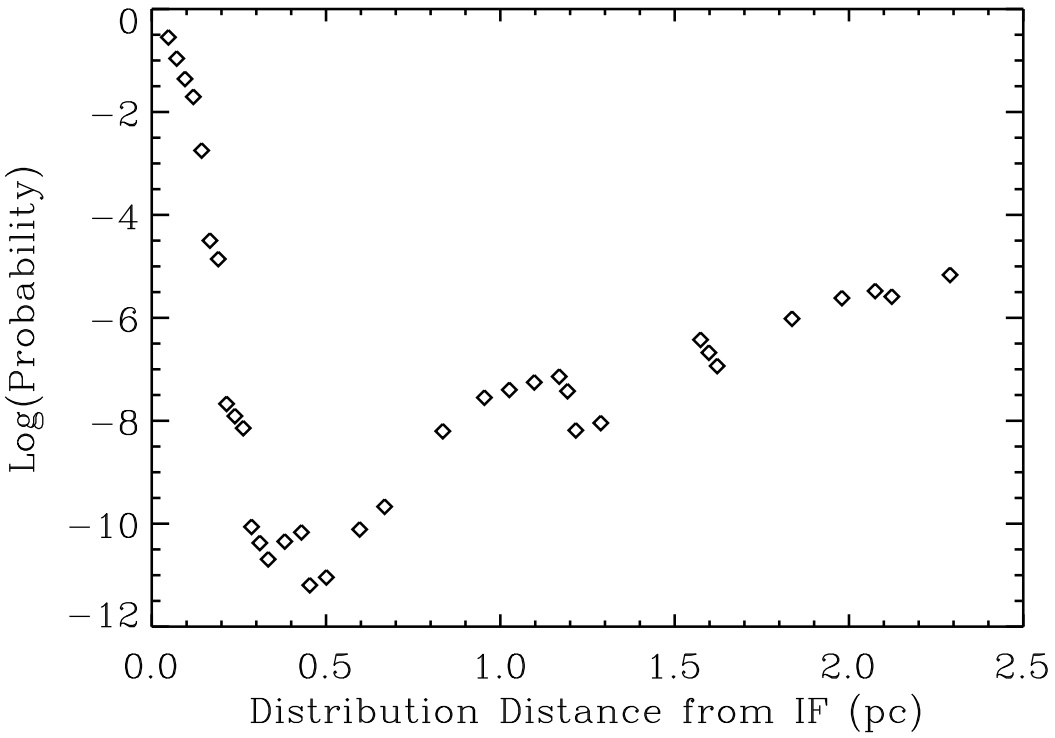

FIG. 11.—The probability of the distribution of YSOs being a random distribution is plotted versus distance. Using the Poisson probability function, the likelihood that the given distribution of YSOs is positioned within a given distance of an ionization front by chance is calculated. On average, the chance of this distribution occurring randomly is 10^{-5}.

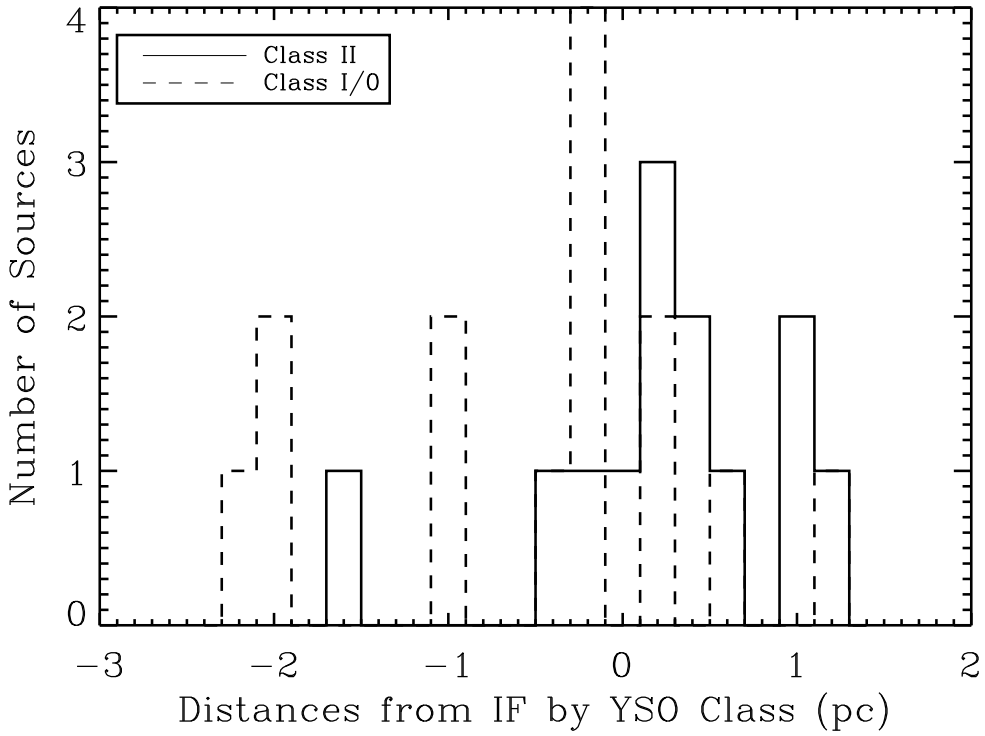

FIG. 12.—A histogram plot of the distances of Class II and Class I/0 YSOs from the nearest ionization front. Negative distances represent YSOs ahead of the ionization front, still embedded in compressed gas, positive distances for sources behind the ionization front that have already been overrun by the passing front. A separation between the two classes of protostellar objects can be seen, with a majority of the youngest YSOs (Class I/0) being located ahead of the ionization front in compressed gas, and a majority of the oldest objects (Class II) located behind the front.

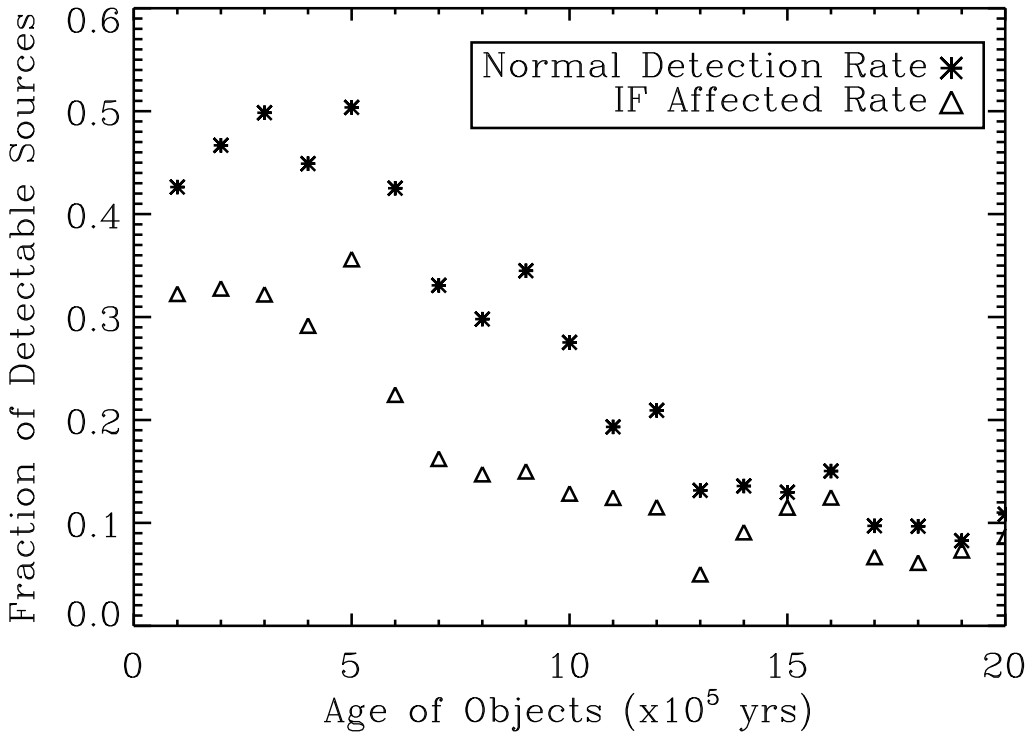

FIG. 13.—The fraction of detectable sources vs. age of the object. A population of stars given by a Salpeter IMF and a constant SFR (value equal to the calculated average SFR in NGC 2467) was aged over timesteps of 10^5 yr. The fraction of detectable sources based on our flux limits was calculated at each timestep, the normal detection rate is shown by the asterisk symbols. The detection rate was also calculated for sources uncovered by a passing ionization front. Disk erosion was assumed using models from Johnstone et al. (1998). The ionization front affected detection rate with object age is shown by the triangles. The data show that the best age range to detect the YSOs is around a few$\times 10^5$ yr.

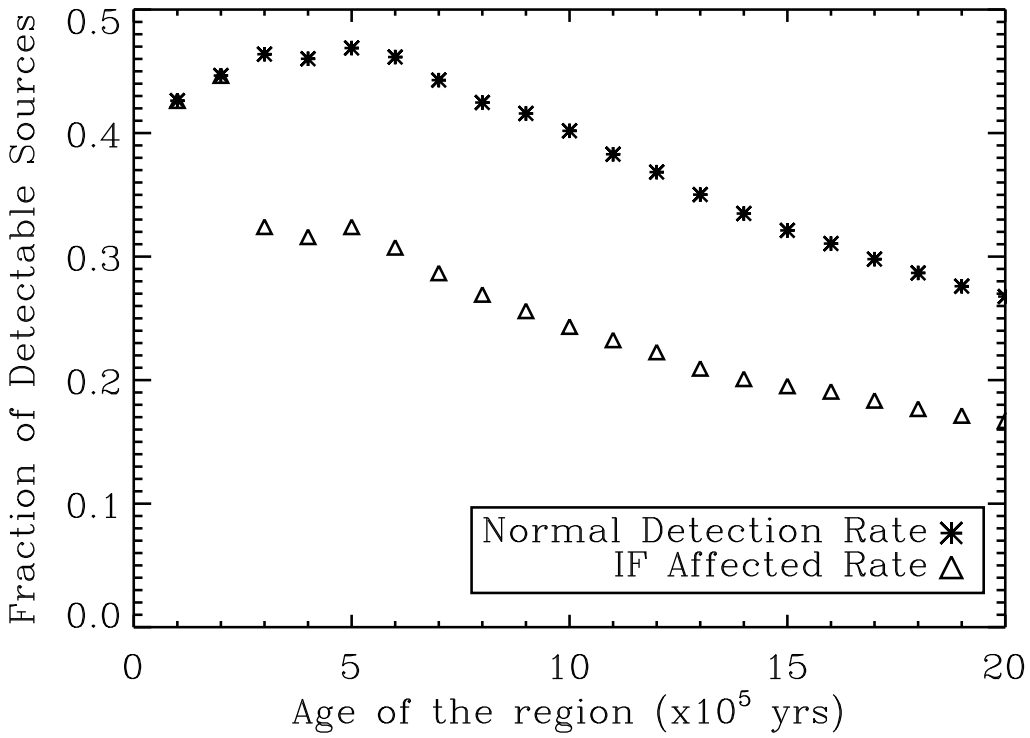

FIG. 14.—The fraction of detectable sources vs. age of the region, using the same methods as described for Figure 12. The normal detection fraction is shown by the asterisk symbols and the ionization affected fractions are shown by the triangles. The detection rate drops to below 20% by 2 Myr.

3. *SPITZER* OBSERVATIONS OF THE H II REGION NGC 2175

3.1. Outline

We present *Spitzer Space Telescope* observations of the H II region, NGC 2175. For this region, we present new MIPS (24 μm) data and use IRAC (3.6, 4.5, 5.8, and 8.0 μm) observations from the *Spitzer* GLIMPSE legacy survey, which covers approximately 1026 and 675 square arcminutes, respectively. In these images bright areas of emission can be seen in the mid-IR bands, some of which overlap with known concentrations of molecular gas and compact H II regions. These regions are bounded by ionization fronts created by the central O6.5 V ionizing star, HD 42088, and other massive OB stars in the region. Using the *Spitzer* data we have identified over 200 candidate Young Stellar Objects (YSOs). We present color-color diagrams of these objects, as well as look at the spatial distribution of the YSOs in this region. Based on best-fit ages and the spatial distribution of the YSOs, we conclude that triggering of low-mass stars in this region is occurring at a rate of approximately 40-60% of the total star formation rate.

3.2. Introduction

NGC 2175 is an excellent candidate for the study of low-mass star formation in a H II region environment. NGC 2175 is a young open cluster surrounded by the H II region Sharpless 252, also known as NGC 2174. The age of the cluster ranges from 1 - 2 Myr (Koempe et al. 1989; Grasdalen & Carrasco 1975), and the distance estimates of this region range from 2 - 2.6 kpc (Lada & Wooden 1979; Grasdalen & Carrasco 1975; Haikala 1995). In this dissertation we adopt a distance of 2.2 kpc to NGC 2175, taken from Haikala (1995).

Previous studies of NGC 2175 have shown the region to be a young H II region that can be modeled by a blister model (Fountain, Gary, & O'Dell 1983; Felli, Habing, & Israel 1977; and Grasdalen & Carrasco 1975). The central ionizing source is the O6.5 V star, HD 42088, which accounts for most of the ionizing radiation in the region and dominates the ultraviolet (UV) emission of the NGC 2175 cluster. A radio continuum study by Felli, Habing, & Israel (1977) revealed six compact thermal radio sources thought to be compact H II regions, some of which are still embedded in the surrounding molecular gas. ^{12}CO and ^{13}CO spectra observations by Lada & Wooden (1979) showed that the molecular cloud is separated into two distinct fragments with the O6.5 V star located between the two. The radial velocity of CO emission from both fragments is the same, $\sim$8 km s^{-1}, indicating that they are part of the same complex. The molecular cloud to the west is well bounded on one side by the ionization front from the O6.5 V star.

In Figure 15, we show the CO data from Lada & Wooden overplotted on B-band (blue) optical data from the Digitized Sky Survey (DSS), and *Spitzer* 4.5 (green) and 8.0 (red) μm bands. In this image, five of the compact H II regions are shown, (labeled A, B, C, E, & F). We have also overplotted known OB stars in the region (yellow squares), with the main ionizing O6.5 V star labeled as a yellow diamond. The boundary of the optical emission from the H II region also appears to correspond to the edge of the western molecular cloud fragment, as shown in both the CO and *Spitzer* data. Radio and CO data both suggest that there is an extended ionization front moving into this cloud (Felli, Habing, & Israel 1977; Lada & Wooden 1979).

The other cloud fragment, the eastern molecular cloud, also shows a sharp boundary in the CO data, but the radio and optical data are more patchy at this boundary. The lack of a sharp boundary at this location in these two datasets indicates that the molecular cloud is probably at the back edge of the H II region, and we are viewing it face-on, whereas we are viewing the western cloud fragment more edge-on to the ionization front (Lada & Wooden 1979; Fountain, Gary, & O'Dell 1983).

Many of the previous studies have shown evidence for sequential star formation of new high-mass stars. Lada & Wooden (1979) concluded that there is evidence for sequential OB star formation in this region. They showed that the optical H II region is in physical contact with the molecular cloud fragments from the CO data. From this, they demonstrated that a majority of the molecular material that is now in a dense ridge of material in the cloud fragments could have been swept up from a previous, more uniform molecular cloud by the expanding H II region. They go on to point out that most of the newly forming massive stars are associated with this ridge. Also, the locations of the compact H II region sources are in front of the ionization front, in areas where pressure from the ionization front due to HD 42088 has swept up material and led to triggered gravitational collapse.

The knowledge that there is evidence for triggered massive star formation makes this region in excellent candidate for further study of low-mass triggered star formation. With *Spitzer*, we can detect embedded low-mass protostars by their mid-IR excesses, and try to determine the sequence of their formation: have they formed spontaneously throughout the region or have they formed due to the influence of

nearby massive stars? YSOs have infrared excesses above the stellar photosphere due to a large infalling envelope in the initial stages, and an accretion disk in later stages. Using a similar process as in NGC 2467, we initially select candidate YSOs in NGC 2175 from *Spitzer* color-color plots, and use a Spectral Energy Distribution (SED) online fitter from Robitaille et al. (2007) to confirm their classification. Locations in the *Spitzer* color-color planes can be separated into the 'Class I, II, III" evolutionary stages. We will use this classification scheme to characterize the types of low-mass protostellar objects that can be found in NGC 2175.

3.3. Observations and Data Reduction

The data for NGC 2175 were obtained by the *Spitzer Space Telescope* with the Multiband Imaging Photometer for *Spitzer* (MIPS; Rieke et al. 2004) in the 24 μm band during Cycle #2 as part of the *Spitzer* program PID 20726, and with all four Infrared Array Camera (IRAC; Fazio et al. 2004) bands as part of the Galactic Legacy Infrared Mid-Plane Survey Extraordinaire (GLIMPSE; Benjamin et al. 2003). The total mosaicked image size in the 24 μm band is $27\farcm6 \times 38\farcm2$, the region of overlap with the IRAC bands from GLIMPSE is $\sim 25' \times 27'$. For the MIPS 24 μm data, each frame was exposed for three seconds with two cycles, for a total exposure time of 84 seconds. The IRAC GLIMPSE data for NGC 2175 had a total exposure time of 12 seconds. The MIPS data were calibrated by the *Spitzer* Science Center (SSC) pipeline version S14.4.0, and the IRAC data were calibrated with the SSC pipeline version S14.0.0.

For the IRAC data, mosaicked images were re-made by using the Basic Calibrated Data (BCDs) from the SSC pipeline in the MOPEX software program, version 030106. The SSC pipeline mosaic of the MIPS 24 μm band was used in our analysis. In order to extract point sources, we applied the same methods as for NGC 2467 (see §2.3). A threshold for point source extraction was determined based on the flux level of those sources that could still be detected above an artificial background. This was done in order to insure that only true point sources in high nebular background areas were being detected. This threshold was applied to all four IRAC bands for point source extraction, helping to extract the actual source distribution of objects in NGC 2175 and exclude numerous foreground and background stars.

Point source extraction was done using the task *find.pro* in the IDLPHOT package in Interactive Data Language (IDL). This task was run on all mosaicked images with the new background threshold criteria set to extract point sources. Aperture photometry was performed on the extracted sources using *aper.pro* in IDLPHOT. For the IRAC and 24 μm images, the same aperture sizes as were used on the NGC 2467 data were also used here. Aperture corrections of 1.112, 1.113, 1.125, 1.218, and 1.698 and zero-magnitude fluxes of 280.9 Jy, 179.7 Jy, 115.0 Jy, 64.13 Jy, and 7.14 Jy, provided by the SSC, were applied for IRAC channels 1, 2, 3, 4, and MIPS 24 μm, respectively.

3.4 Results

We found 1075 point sources in NGC 2175 that were detected in all four IRAC bands, along with 46 MIPS 24 μm point sources. In order to initially select candidate

YSOs, we generated color-color plots from the IRAC and MIPS point sources, using the [3.6]-[4.5], [5.8]-[8.0], [3.6]-[5.8] and [8.0] - [24.0] colors. From the IRAC color-color plots 338 candidate YSOs were identified. In the MIPS color-color plot, 44 YSOs were initially selected, 42 of which overlap with a IRAC candidate YSO source. All of these candidate YSOs have an infrared excess in at least one color which indicates they are a young population. The color criteria for the different protostellar objects are the same as in NGC 2467, and are listed in Table 2, except for the [5.8]-[8.0] minimum color value for the Class I/0 and Class II objects, which is 0.5 for NGC 2175 compared with 0.4 for NGC 2467. A larger [5.8]-[8.0] value of 0.5 was used in order to see a clear separation between Main Sequence sources and red sources in the color-color diagram. Also for the MIPS color criteria in NGC 2175, the [8.0]-[24] color in the MIPS Class II classification extends from 2.0 - 12.0 (vs. a value of 2.0 - 6.0 for NGC 2467). The IRAC color criteria are taken from Megeath et al. (2004) and are based on models from Allen et al. (2004) and Whitney et al. (2003a & 2004b), and the MIPS 24 μm candidate YSO sources are based on color criteria from Reach et al. (2004). In total, 340 possible protostellar candidates were initially identified in NGC 2175.

After the initial color-criteria identification, we checked the YSO source list against contaminant extragalactic sources and background AGB stars. We used the same color criteria method (see Table 2) to identify these possible sources as was used for sources in NGC 2467 (refer to §2.4). Only two Class II candidate YSOs in the initial YSO source list had colors matching those of possible AGB stars; these two sources were disregarded as possible YSO candidates. No candidate extragalactic

sources were identified among the protostellar objects. This left us with a total of 338 YSO candidates.

For NGC 2175, we identified 148 Class I/0 protostellar objects from the IRAC color-color plots and 41 Class I/0 sources from the MIPS color-color plot (39 of which overlapped with an IRAC YSO). 138 Class I/II objects and 50 Class II objects were also identified in the IRAC color-color plots. Three Class II YSOs were identified in the MIPS color-color plot, and all three overlapped with an IRAC YSO. The 338 candidate YSOs were run through an SED fitter to determine their properties and to also help confirm which of the candidates are actual YSOs; this process is discussed in detail in the next section (3.5.1). However, through that process, we ended up throwing out a total of 73 objects, and therefore only 265 sources were confirmed as likely YSOs. Those 265 sources are shown in Figure 16, which is a three-color *Spitzer* image of the region with the 265 identified YSOs overplotted; the IRAC 4.5 μm channel is in blue, the IRAC 8.0 μm channel is in green, and the MIPS 24 μm channel is in red. The candidate YSOs are labeled by X's and known OB stars in the region are marked by blue squares. In this image, three bright areas of emission can be seen, as well as a high concentration of candidate YSOs at each of these locations. The main O6.5 V ionizing star is located to the lower right of the image and a bright ridge of 24 μm emission can be seen just to the right of this star, possibly indicating the presence of warm dust in the interior of the H II region. Strong 24 μm emission is also seen in the three clusters and near other known OB stars in this region.

Figures 17 and 18 are the *Spitzer* color-color plots of the sources in NGC 2175. Figure 17 is the IRAC color-color diagram of [3.6]-[4.5] vs. [5.8]-[8.0]. In this figure the YSO candidates are plotted in color; Class I/0 sources are shown in red, Class I/II are in yellow, and Class II sources are in green. Figure 18 is a color-color diagram of the 46 detected MIPS 24 μm sources, with the [3.6]-[5.8] color plotted vs. the [8.0]-[24] color. The majority of these sources (44 out of 46) show a mid-IR excess in both colors. They are a classified into two groups Class II candidates shown in green and Class I/O objects plotted in red.

For both Figures 17 and 18, models of objects with these colors come from Allen et al. (2004) and Whitney et al. (2003a, 2003b, & 2004b); see §2.4 for more detail on the definition of the types of sources these models correspond to. The Class I/0 objects are the youngest and least evolved sources in the sample. Their large color excesses in both mid-IR colors are due to the objects having large infalling dusty envelopes at this stage in their evolution. Class II objects have smaller color excesses as they are typically more evolved and no longer have a large envelope; instead they are characteristic of low-mass protostars with accretion disks that are causing the infrared excess. The other candidate YSOs (Class I/II) fall in between these groups in terms of their protostellar evolution.

The final color-color plot we present is a 2MASS and *Spitzer* color-color diagram, shown in Figure 19. We used the 2MASS PSC to find 2MASS counterparts to the *Spitzer* detected sources. A majority of the *Spitzer* sources had a 2MASS counterpart. In Figure 19, we plot H-K vs. K-[3.6]; the reddening vector due to

interstellar extinction is overplotted. This line has slope of 1.3 as defined by Tapia (1981). 346 2MASS point sources are located to the right of this line, representing sources with 2MASS color excesses. Of these 346 sources with NIR color excesses, 191 overlap with a *Spitzer* YSO.

3.5. Discussion

3.5.1. *SED Model Fitting of YSOs*

Having selected a sample of candidate YSOs we used the YSO SED online fitter from Robitaille et al. (2007) to determine the physical properties of the detected YSOs. The different input and output parameters for the SED fitter were discussed in detail in §2.5.1. For NGC 2175, we use the *Spitzer* and 2MASS (when available) fluxes of each candidate YSO as input, as well as a distance estimate (2.2 $\pm$ 0.3 kpc; Haikala 1995) and average extinction to the region. For NGC 2175, A_V ranges from 1.2 - 5.8 mag, with an average value of $\sim$ 3.5 mag (Haikala 1995). The SED fitter also helps to confirm which candidates are actual young protostellar objects. The SED fitter uses a grid of 2×10^5 total SED models when fitting to a input source, and it also attempts to fit the best stellar photosphere model to the object. If a candidate YSO has a better stellar photospheric fit than any YSO SED fit, then it was thrown out as possible YSO. We also rejected any candidate YSOs that have a large χ^2 value (total χ^2 greater than 100 or χ^2 per data point greater than 12) for their best YSO fit, even if a stellar photospheric fit is also higher than this value. For NGC 2175, 73 of the initial 338 YSO candidates were discarded as possible protostellar objects, with the majority thrown out due to high best-fit χ^2 values; only two sources had a

better stellar photospheric fit than the best YSO fit. While we did throw out $\sim 22\%$ of our initial YSO candidates, this is mainly due to our conservative limits in terms of an acceptable best-fit χ^2 value. Since only two initial candidate YSOs were best-fit by a stellar photospheric model, this helps to confirm that our selection method of YSOs by their mid-IR colors is robust. The majority of sources that were thrown out were initially identified as Class I/II YSOs (57 of 73). This left us with 135 Class I/0 Objects, 81 Class I/II objects, and 49 Class II objects. The position, classification, and *Spitzer* magnitudes and errors for the 265 confirmed YSOs in NGC 2175 are listed in Table 5.

For each YSO, we had a set of output models which we used to determine the best-fit physical properties. In determining these properties, we selected only models that had ages less than the assumed age of the region, 2 Myr. To calculate the average mass of each YSO, we only used models within 3 σ of the total χ^2 from the best-fit model for that source. A weighted average mass was calculated for each source from the set of selected models, and the model with a mass closest to the weighted average mass and lowest χ^2 value was used. The best-fit model parameters for each selected YSO in NGC 2175 are listed in Table 6. We found YSOs with masses ranging from 0.25 - 6.9 $M_\odot$, and ages ranging from 1×10^3 - 2×10^6 yr. 44 YSOs had a best-fit mass less than 1 $M_\odot$ and another 77 objects had a best-fit mass between 1 - 2 $M_\odot$. This is almost half of the YSO selected population, demonstrating that we are detecting a population of newly forming low-mass stars in NGC 2175.

3.5.2. *Mass Distribution of YSOs and Completeness*

As was done for NGC 2467 in §2.5.2, we used the best-fit mass estimates for the YSOs in NGC 2175 to estimate completeness in the overall population of YSOs in this region. Using Equation 1, from §2.5.2, we calculated a mass function for the 265 YSO sources in NGC 2175. Figure 20 is a plot of log N vs log Best-Fit Mass. The masses of the 265 YSOs were grouped into seven equally spaced mass bins, centered at 0.5, 1.5, 2.5, 3.5, 4.5, 5.5, and 6.5 $M_{\odot}$. We performed a least squares fit to the data in the higher mass bins to obtain a line of best fit. This line runs from the mass bin centered at 2.5 $M_{\odot}$ through the 5.5 $M_{\odot}$ mass bin. The best-fit line has a slope of 1.65, slightly steeper than the Salpeter (1955) Initial Mass Function (IMF) slope of 1.35. Given the best-fit slope of 1.65, the IMF spectral index, Γ, is 2.65. Therefore the YSO mass distribution function for NGC 2175 has the following form:

$$\frac{dN}{dM} \propto M^{-2.65} \; or \; \frac{dN}{d(\log M)} \propto M^{-1.65}. \tag{8}$$

For NGC 2175, the largest mass bin centered at 6.5 $M_{\odot}$ appears to not be complete, as well as the two lowest mass bins (as is expected); however a few of the other higher mass bins could also be incomplete. If this is the case, then we would expect the addition of more sources in the highest mass bins would flatten the slope. We therefore conclude that the MF distribution of YSOs for NGC 2175 is no steeper than what we calculated, and may in fact be closer to Salpeter (1955). In order to estimate the total number of stars present in NGC 2175, we use the known numbers of massive stars to determine the IMF normalization constant. There are ~ 60 known B

stars and 3 O stars (O6 - O9) in the region. We used the number of B8/B9 stars (15) from Haikala (1995), as well as the number of O6-O9 stars to calculate an average IMF normalization constant. This resulted in an average normalization constant of 600. For NGC 2175, the IMF becomes:

$$N_{tot} = A \int_{M_1}^{M_2} M^{-2.65} dM = 6 \times 10^2 \int_{0.1M_\odot}^{40M_\odot} M^{-2.65} dM. \quad (9)$$

This results in 16 $\pm$ 2 $\times 10^3$ stars (assuming Poisson statistics on the 60 stars used to calculate the normalization constant) between the mass range of 0.1-40 $M_\odot$ in NGC 2175.

In order to address completeness, we followed the same methodology as in §2.5.2 for NGC 2467. Our calculated flux limits for NGC 2175 are based on our three-σ magnitude limits for the IRAC bands for our observations: 14.4, 13.9, 12.0, and 11.3 mag for IRAC 3.6, 4.5, 5.8, and 8.0μm, respectively. Using the model fluxes from the SED models of Robitaille et al. (2006), we scaled these fluxes from the default values at 1 kpc to 2 kpc, the distance of NGC 2175. We estimated the extinction in the region based on the average value, A_V=3.5 mag, from Haikala (1995). The extinction was accounted for in our calculations of the IRAC flux limits. Using these flux limit values, we determined that we should be able to detect 48% of the YSO models in the SED model grid. This calculation takes into account models at each inclination angle, therefore for a given source it would be possible that that source could be detectable only if it is inclined at a preferable viewing angle relative to our line of sight.

3.5.3. *Spatial Distribution of YSOs in NGC 2175*

As discussed in the introduction to this thesis and in §2.5.4, there are competing ideas for how low-mass stars form in H II region environments (triggered vs. coeval star formation). We have already shown, using the YSO distribution from NGC 2467, that it is likely that a majority of the YSOs are influenced by the nearby OB stars, and that triggering of low-mass protostars is occurring at a rate of 25-50% in NGC 2467. We now analyze the spatial distribution of the YSOs in NGC 2175. This region contains a larger number of massive stars and detected YSOs, so it is useful to compare our results for NGC 2175 to those of NGC 2467. Because there are a larger number of YSOs in this region, our statistics and analysis should be better. One might expect that we will see a more random distribution of these objects; on the other hand, if we still see a clustered distribution of YSOs nearby to the ionization fronts then this will add to the testable cases of triggered low-mass star formation in H II regions. We can also compare our current distribution of low-mass YSOs to previous work in this region on triggering of more massive stars.

For NGC 2175, we use our data to again try to distinguish between the two different low-mass star formation scenarios. We have mapped the detectable ionization fronts created by the massive stars and plotted the distribution of YSOs as a function of distance from the ionization fronts, as described in the next section. We will analyze how the detectable population of YSOs changes with advancing age of the sources and elapsed age of the region.

3.5.3.1 *Ionization Front Detection*

The same process was used to identify ionization fronts in NGC 2175 as was done with NGC 2467 (see §2.5.4.1, for a more detailed explanation). In NGC 2175 we only identified five main ionization fronts; these are shown in Figure 21, which shows the IRAC 8.0 μm band in green with the ionization fronts outlined in red. The 265 detected YSOs are also overplotted along with the OB stars in the region. Three of the ionization fronts are located around the bright clusters of emission that can be seen in the *Spitzer* images, and the fourth is located along a ridge of material immediately to the right (west) of the main ionized region created by HD 42088. Interestingly, there are only a few detected YSOs located along this ionization front. This is the extended ionization front along the western molecular cloud fragment that had previously been identified in other studies of this region. This ionization front is likely edge-on to the western molecular cloud. The compact H II region F is also located on the edge of the molecular material next to this ionization front. This is also the location of the *HST* WFPC-2 observations, the only *HST* observations of NGC 2175. There is only one YSO in the *HST* field of view, therefore we do not discuss at length the components of the *HST* images compared to the *Spitzer* images, but this ionization is very apparent in the *HST* images as well.

The other three detected ionization fronts are centered around three of the previously detected compact H II regions (A, C, and E), and there is strong clustering of YSOs at each of these locations. There are also a number of YSO sources around the edges of the compact H II region B, although no strong ionization fronts were

detected at this location. The fifth ionization front outlines an area between the compact H II regions E and C. There are a number of massive stars close to this ionization front, as well as a number of YSOs along the periphery of this ionization front.

Overall, almost 60% of the YSOs in this region fall within a projected distance of 1 pc from an ionization front. Figure 22 is a histogram plot of the distance of all 265 YSOs from the nearest ionization front. This plot shows that there is a higher frequency of YSO sources near an ionization front. For both the Class I/II and Class I/0 YSOs, over 60% are within a projected distance of 1 pc, whereas only 40% of the Class II YSOs are within 1 pc of an ionization front. This results in 57% of all YSOs located within 1 pc of the nearest ionization front. We also see strong clustering of YSOs around the ionization fronts, and not necessarily clustering around the OB stars themselves. In addition, there are only few detected YSOs located within the interior of the main H II region cavity, indicating that the low-mass stars are not forming spontaneously throughout the region, but are instead likely being triggered in areas of compressed gas due to the expansion of the H II region.

3.5.3.2 *Statistical Distribution Tests*

In NGC 2175 the distances of the OB stars from the detected ionization fronts ranges from about 0.5 - 3 pc. Following the same method as in §2.5.4.2, we calculated what the likely observed distribution of YSOs would be when viewed in projection, compared to the actual distribution we measure. We cannot detect ionization fronts that are face-on to our line of sight, and therefore some YSOs that are actually

located right along an ionization front could appear to be farther away from the nearest ionization front than they actually are. We model this scenario by using a 3D hemispherical bowl and projecting it onto the 2D plane of the sky. We then calculate what fraction of YSOs located within a given distance of the ionization front are actually measured to be within that projected distance on the sky. This is compared to our measured distribution of sources in order to determine the likely overall distribution of YSOs in this region.

In Figure 23, we show the predicted distribution of YSOs vs. the measured distribution of YSOs in NGC 2175. We plot the predicted fractions for four different hemispherical distributions (0.65, 1.0, 1.5,and 3.0 pc), where the size of the hemispherical ionization front varies depending on the distance of the ionization front from the ionizing OB star. If all YSOs are actually located within 1 pc of the nearest ionization front, then the model distributions predict that we should detect between 70 - 78 % of all YSOs within this distance in our 2D images; however for our actual distribution of YSOs we only detect 57% of the YSOs within 1 pc. This suggests that the YSOs in NGC 2175 are located within a distribution layer that is greater than 1 pc. Figure 23 shows the fraction of the measured distribution of YSOs crossing the model predicted distributions at a thickness between 2 - 2.6 pc, depending on the size of the model ionization front distribution. Therefore, we conclude that the overall distribution of YSOs in NGC 2175 is a population of sources that is concentrated within a layer that is 2.6 pc or less away from an ionization front, and at least 70% of the YSOs are located within a distance of 1 pc or less from an ionization front.

We also tested the statistical likelihood of the observed YSO distribution occurring by calculating the probability of the YSO sources being randomly distributed versus the actual observed distribution. Using the same method as in §2.5.4.2, we used a Poisson probability distribution to compare the distribution of the YSO sources to a random distribution. This resulted in an average probability of only 6% that the YSOs are randomly distributed when normalized around the area immediately surrounding the detected ionization fronts. If we include the total survey area then the likelihood of a random YSO distribution is even smaller.

One final way to demonstrate that this is not a random distribution of sources is shown in Figure 24. Here we plot the fraction of YSOs that fall on an ionization front versus the fraction of the area of the ionization fronts to the total survey area. If this distribution were random, then we would expect this plot to show a one-to-one correlation and have a slope equal to one. A line with slope equal to one is overplotted in this diagram and the fraction of YSOs versus the fractional area all fall above this line. For example, 10% of the YSOs should be distributed within 10% of the total survey area, but Figure 24 shows that 10% of the YSOs are actually contained within only 1.5% of the total area. By the time 10% of the total survey area is included we find that 43% of the YSOs are contained in this amount of area. Therefore, this is not a random distribution of sources.

3.5.4. *Estimates of Triggering and Star Formation Rates*

As with NGC 2467, we try to determine the rate of triggered low-mass star formation in NGC 2175 and compare that to the overall star formation rate in the

region. Using the MF we calculated in §3.5.2, we estimate the total mass in stars and take the assumed age of the region, 2 Myr, to determine the average SFR in NGC 2175:

$$M_{tot} = \int_0^N M dN = A \int_{M_1}^{M_2} M^{-1.65} dM = 6 \times 10^2 \int_{0.1M_\odot}^{40M_\odot} M^{-1.65} dM \sim 4000\,\mathrm{M}_\odot \tag{10}$$

$$Average\ SFR = \frac{4000\,\mathrm{M}_\odot}{2Myr} = 2 \times 10^{-3}\ \mathrm{M}_\odot\,\mathrm{yr}^{-1} \tag{11}$$

The average SFR calculated in NGC 2175 is slightly higher than the rate calculated for NGC 2467 (1.75×10^{-3} $\mathrm{M}_\odot$ yr^{-1}), which is not unexpected due to NGC 2175 being a more massive region and containing a larger number of massive OB stars. Using this calculated SFR for NGC 2175, we have determined how the detection ability of individual protostars changes with age of the sources and with elapsed age of the region. In §2.5.5, we showed that detection ability of YSOs in NGC 2467 can drop to as low as 20% at 2 Myr. We performed the same set of calculations for NGC 2175. We aged a population of sources given by our calculated MF, and at each timestep (10^5 yr) we calculated the fraction of YSO SED models would still be able to detect. The detection probability peaks at a YSO age of 3×10^5 yr, as shown by Figure 25. This figure demonstrates that the best age to detect newly forming protostellar objects is between the ages of 0.1 - 0.5 Myr; after that the detection fraction drops off dramatically. This implies that the YSOs we are detecting in NGC

2175 likely have ages of a few$\times 10^5$ yr, agreeing with the best-fit ages from the SED fitter, which have an average age of 2×10^5 yr.

Figure 26 plots the detection ability versus elapsed age of the region, and demonstrates that by the time the region has reached 2 Myr (the current age of NGC 2175), the detection ability is just slightly higher than 20%. We have also calculated how erosion of protostellar disks due to passing ionization fronts would affect the detectability of individual YSOs. These data are also shown in Figures 25 and 26, and the detection ability falls to about 15% when this effect is included.

We use the same formulation to calculate the amount of triggering of low-mass stars in NGC 2175 as we did with Equation 7 in §2.5.5 for NGC 2467. For NGC 2175, we detected 265 YSO candidates, and we showed in §3.5.3.2 that we can expect that approximately 70% of these 265 YSOs are located within 1 pc or less from an ionization front. YSOs located a distance of 1 pc (or less) from an ionization front have likely been influenced by the shock front, traveling in advance of the ionization front, and will be passed over by the ionization front within a few$\times 10^5$ yr (given an ionization front speed of 2 km s^{-1}). We therefore conclude that at least 70% of the YSOs in this region have been affected by the expansion of the H II region. We have also shown that our detection ability in NGC 2175 is currently at the 15-20% level, compared to what it was during the first 0.5 Myr in this region. The YSOs in this region have an average age of 2 - 3×10^5 yr, determined from SED fitting and from analysis of Figure 25. Therefore, as shown in Equation 12, 185 detected YSOs within

1 pc or less of an ionization front, and with an average age of 2 - 3 $\times 10^5$ yr results in 3 - 4.5$\times 10^{-3}$ stars formed per yr that are triggered.

$$\frac{\#\ YSOs}{Avg.Age \times DetectionRate} = \frac{185}{(2-3\times 10^5\ \text{yr}) \times 0.2} = 3{-}4.5{\times}10^{-3}\ \text{stars}\,\text{yr}^{-1} \quad (12)$$

Using the calculated MF from Equation 8, this results in a triggered SFR of $\sim$ 0.75 - 1.15$\times 10^{-3}$ $M_\odot$ yr^{-1}. Comparing that to our average total SFR in the region, the triggered SFR accounts for 38 - 58% of all of the star formation in NGC 2175. This is a slightly higher amount than was calculated in NGC 2467 (25-50%). Again, we are showing that while not all of the low-mass star formation is triggered, triggering does appear to be occurring, and it accounts for a significant fraction of the total star formation rate.

TABLE 5

SPITZER PHOTOMETRY FOR YSOs IN NGC 2175

Source #	YSO Class	R.A. J2000	Decl. J2000	[3.6]	[4.5]	[5.8]	[8.0]	[24]
1	I/0	06 09 59.92	20 30 07.35	11.68 ± 0.04	9.94 ± 0.01	8.91 ± 0.05	8.30 ± 0.05	3.98 ± 0.02
2	I/0	06 09 56.07	20 30 39.80	11.31 ± 0.04	10.88 ± 0.04	9.37 ± 0.08	7.79 ± 0.04	
3	I/0	06 09 52.84	20 31 01.90	10.94 ± 0.04	10.44 ± 0.03	9.03 ± 0.08	7.43 ± 0.04	
4	I/0	06 09 52.52	20 30 50.23	11.31 ± 0.05	10.58 ± 0.04	9.47 ± 0.13	8.11 ± 0.07	
5	I/0	06 09 52.50	20 31 04.11	11.94 ± 0.08	11.32 ± 0.06	9.48 ± 0.12	7.86 ± 0.05	
6	I/0	06 09 51.44	20 28 34.55	11.28 ± 0.02	10.30 ± 0.02	9.55 ± 0.05	8.09 ± 0.02	4.84 ± 0.03
7	I/0	06 09 51.88	20 30 38.69	12.08 ± 0.11	11.16 ± 0.06	10.52 ± 0.34	9.72 ± 0.30	
8	I/0	06 09 51.63	20 30 13.75	11.61 ± 0.07	10.78 ± 0.05	9.31 ± 0.12	7.34 ± 0.04	
9	I/0	06 09 51.52	20 30 32.00	11.62 ± 0.07	11.19 ± 0.06	9.07 ± 0.09	7.33 ± 0.03	
10	I/0	06 09 50.58	20 30 45.79	11.27 ± 0.03	10.78 ± 0.03	9.11 ± 0.06	7.73 ± 0.03	
11	I/0	06 09 50.36	20 31 39.36	11.51 ± 0.03	10.84 ± 0.03	9.39 ± 0.06	7.99 ± 0.03	
12	I/0	06 09 49.65	20 30 38.69	12.17 ± 0.06	11.47 ± 0.05	9.00 ± 0.05	7.36 ± 0.02	3.13 ± 0.03
13	I/0	06 09 49.12	20 30 49.42	11.56 ± 0.04	11.12 ± 0.04	9.70 ± 0.10	8.28 ± 0.05	
14	I/0	06 09 50.55	20 36 47.52	11.38 ± 0.02	10.92 ± 0.03	9.59 ± 0.05	8.06 ± 0.02	
15	I/0	06 09 48.74	20 30 55.40	11.52 ± 0.04	11.00 ± 0.03	9.80 ± 0.10	8.50 ± 0.06	
16	I/0	06 09 47.10	20 31 40.78	12.15 ± 0.06	11.71 ± 0.06	10.30 ± 0.15	9.00 ± 0.09	
17	I/0	06 09 42.62	20 34 48.36	9.94 ± 0.01	8.33 ± 0.00	7.09 ± 0.01	6.32 ± 0.01	3.10 ± 0.01
18	I/0	06 09 37.71	20 37 55.46	12.06 ± 0.05	11.59 ± 0.05	10.16 ± 0.12	8.62 ± 0.05	
19	I/0	06 09 34.12	20 32 39.98	9.14 ± 0.01	8.13 ± 0.00	7.20 ± 0.01	6.43 ± 0.01	1.92 ± 0.01
20	I/0	06 09 28.35	20 38 56.88	13.03 ± 0.13	12.44 ± 0.12	10.70 ± 0.23	9.26 ± 0.11	
21	I/0	06 09 27.70	20 39 07.14	12.50 ± 0.09	11.87 ± 0.07	9.89 ± 0.12	8.19 ± 0.04	
22	I/0	06 09 26.76	20 37 12.16	12.40 ± 0.07	11.96 ± 0.08	10.95 ± 0.25	9.31 ± 0.10	
23	I/0	06 09 27.49	20 40 42.17	12.71 ± 0.10	12.10 ± 0.07	9.74 ± 0.07	8.23 ± 0.04	
24	I/0	06 09 24.69	20 42 10.62	10.90 ± 0.01	10.02 ± 0.01	9.20 ± 0.03	8.04 ± 0.02	4.56 ± 0.02

Continued on next page...

TABLE 5 – Continued

Source #	YSO Class	R.A. J2000	Decl. J2000	[3.6]	[4.5]	[5.8]	[8.0]	[24]
25	I/0	06 09 23.16	20 38 32.87	12.55 ± 0.15	12.06 ± 0.13	10.34 ± 0.29	8.45 ± 0.10	
26	I/0	06 09 22.54	20 37 56.04	11.48 ± 0.04	11.03 ± 0.04	9.57 ± 0.10	8.03 ± 0.05	
27	I/0	06 09 22.81	20 39 27.28	12.05 ± 0.11	11.30 ± 0.09	11.02 ± 0.64	9.02 ± 0.19	
28	I/0	06 09 21.79	20 38 59.24	11.63 ± 0.08	11.12 ± 0.07	9.86 ± 0.22	8.48 ± 0.11	
29	I/0	06 09 21.30	20 38 09.78	12.13 ± 0.08	11.58 ± 0.07	10.17 ± 0.18	8.18 ± 0.05	
30	I/0	06 09 21.32	20 38 24.71	12.15 ± 0.11	11.55 ± 0.09	10.31 ± 0.28	8.78 ± 0.13	
31	I/0	06 09 20.96	20 37 34.51	13.08 ± 0.13	12.50 ± 0.12	10.82 ± 0.22	8.98 ± 0.07	
32	I/0	06 09 21.49	20 39 31.28	11.74 ± 0.09	11.07 ± 0.07	9.20 ± 0.12	7.68 ± 0.05	
33	I/0	06 09 20.88	20 38 20.93	14.22 ± 0.73	12.25 ± 0.16	10.93 ± 0.47	9.67 ± 0.28	
34	I/0	06 09 21.22	20 40 22.21	8.63 ± 0.01	7.97 ± 0.00	6.98 ± 0.01	5.79 ± 0.01	2.25 ± 0.05
35	I/0	06 09 20.44	20 38 31.23	11.72 ± 0.07	11.12 ± 0.06	8.78 ± 0.07	7.06 ± 0.03	
36	I/0	06 09 20.33	20 38 09.40	11.70 ± 0.05	11.05 ± 0.04	10.05 ± 0.17	8.22 ± 0.06	
37	I/0	06 09 20.01	20 39 54.16	12.82 ± 0.22	12.09 ± 0.16	9.45 ± 0.14	7.87 ± 0.06	
38	I/0	06 09 19.49	20 38 34.91	12.58 ± 0.15	12.05 ± 0.13	9.21 ± 0.09	7.47 ± 0.04	
39	I/0	06 09 18.97	20 38 43.25	11.42 ± 0.05	10.88 ± 0.04	9.14 ± 0.09	7.39 ± 0.03	
40	I/0	06 09 19.02	20 40 21.22	13.56 ± 0.26	12.43 ± 0.12	10.14 ± 0.15	8.94 ± 0.10	
41	I/0	06 09 18.88	20 40 04.00	11.84 ± 0.06	11.33 ± 0.05	9.04 ± 0.07	7.33 ± 0.03	
42	I/0	06 09 18.37	20 38 46.86	14.27 ± 0.65	13.00 ± 0.28	10.83 ± 0.37	9.05 ± 0.14	
43	I/0	06 09 17.70	20 39 54.10	13.45 ± 0.30	13.00 ± 0.28	11.08 ± 0.51	9.32 ± 0.19	
44	I/0	06 09 16.94	20 38 27.81	12.55 ± 0.08	12.09 ± 0.08	9.64 ± 0.07	7.77 ± 0.03	
45	I/0	06 09 13.76	20 27 25.29	12.38 ± 0.04	11.56 ± 0.04	9.62 ± 0.05	8.20 ± 0.03	
46	I/0	06 09 16.77	20 38 40.26	11.58 ± 0.03	11.13 ± 0.03	10.11 ± 0.12	8.64 ± 0.06	
47	I/0	06 09 16.69	20 38 35.94	10.78 ± 0.02	10.36 ± 0.02	9.41 ± 0.06	7.95 ± 0.03	
48	I/0	06 09 16.01	20 38 29.16	13.14 ± 0.13	12.14 ± 0.08	10.53 ± 0.16	8.82 ± 0.06	
49	I/0	06 09 15.45	20 39 33.04	12.24 ± 0.06	11.64 ± 0.05	9.82 ± 0.09	8.21 ± 0.04	
50	I/0	06 09 14.19	20 39 44.82	11.50 ± 0.03	11.06 ± 0.03	9.84 ± 0.08	8.45 ± 0.04	
51	I/0	06 09 07.00	20 42 04.68	11.39 ± 0.03	10.45 ± 0.02	9.83 ± 0.08	8.95 ± 0.07	

Continued on next page...

TABLE 5 – Continued

Source #	YSO Class	R.A. J2000	Decl. J2000	[3.6]	[4.5]	[5.8]	[8.0]	[24]
52	I/0	06 09 02.77	20 36 42.90	9.64 ± 0.01	8.96 ± 0.01	8.21 ± 0.02	6.55 ± 0.01	3.71 ± 0.01
53	I/0	06 09 03.53	20 41 34.34	11.66 ± 0.04	10.73 ± 0.02	10.12 ± 0.12	9.56 ± 0.13	4.61 ± 0.02
54	I/0	06 08 58.20	20 23 29.91	11.85 ± 0.03	11.00 ± 0.02	10.23 ± 0.09	9.29 ± 0.07	
55	I/0	06 08 58.48	20 29 36.77	12.50 ± 0.07	11.80 ± 0.06	9.54 ± 0.07	7.69 ± 0.02	
56	I/0	06 08 58.44	20 29 31.22	10.72 ± 0.02	9.77 ± 0.01	7.79 ± 0.02	6.09 ± 0.01	3.56 ± 0.02
57	I/0	06 08 57.67	20 29 35.98	12.68 ± 0.06	11.99 ± 0.06	10.78 ± 0.16	9.27 ± 0.07	
58	I/0	06 08 52.73	20 29 50.79	11.25 ± 0.02	10.08 ± 0.01	9.06 ± 0.03	8.08 ± 0.03	4.74 ± 0.02
59	I/0	06 08 55.10	20 40 23.48	11.94 ± 0.04	10.69 ± 0.03	9.72 ± 0.08	8.92 ± 0.08	4.24 ± 0.03
60	I/0	06 08 51.42	20 29 28.45	10.04 ± 0.01	9.11 ± 0.01	8.39 ± 0.02	7.74 ± 0.02	3.84 ± 0.02
61	I/0	06 08 49.72	20 29 55.24	11.79 ± 0.03	10.68 ± 0.02	9.63 ± 0.06	8.55 ± 0.04	
62	I/0	06 08 51.98	20 37 57.62	12.88 ± 0.12	12.10 ± 0.09	10.59 ± 0.20	9.10 ± 0.10	
63	I/0	06 08 48.67	20 29 31.57	11.42 ± 0.02	10.42 ± 0.02	9.72 ± 0.06	8.98 ± 0.06	
64	I/0	06 08 49.30	20 38 44.07	12.88 ± 0.12	12.45 ± 0.13	10.33 ± 0.16	8.60 ± 0.06	
65	I/0	06 08 48.77	20 38 53.72	11.31 ± 0.03	9.91 ± 0.01	8.93 ± 0.04	7.77 ± 0.03	2.46 ± 0.01
66	I/0	06 08 48.25	20 38 22.75	11.55 ± 0.03	10.53 ± 0.02	9.48 ± 0.07	8.37 ± 0.05	
67	I/0	06 08 45.59	20 29 34.68	12.45 ± 0.05	11.63 ± 0.04	10.87 ± 0.16	9.85 ± 0.13	
68	I/0	06 08 47.84	20 38 20.85	11.22 ± 0.03	9.75 ± 0.01	8.60 ± 0.03	7.53 ± 0.02	2.78 ± 0.01
69	I/0	06 08 47.79	20 37 43.19	12.22 ± 0.06	10.78 ± 0.03	9.57 ± 0.08	8.13 ± 0.04	3.96 ± 0.02
70	I/0	06 08 47.13	20 37 49.33	9.73 ± 0.01	8.80 ± 0.01	8.13 ± 0.02	7.35 ± 0.02	3.82 ± 0.03
71	I/0	06 08 47.11	20 38 29.35	11.33 ± 0.02	9.94 ± 0.01	8.90 ± 0.04	7.92 ± 0.03	4.38 ± 0.04
72	I/0	06 08 46.52	20 38 03.36	12.13 ± 0.05	10.69 ± 0.02	9.61 ± 0.07	8.58 ± 0.05	2.97 ± 0.01
73	I/0	06 08 46.06	20 37 18.47	12.82 ± 0.10	11.99 ± 0.07	11.10 ± 0.30	9.83 ± 0.18	
74	I/0	06 08 45.17	20 34 57.21	11.15 ± 0.02	10.34 ± 0.02	9.60 ± 0.08	8.99 ± 0.09	5.29 ± 0.03
75	I/0	06 08 45.36	20 35 48.41	12.30 ± 0.06	11.06 ± 0.03	9.86 ± 0.10	8.91 ± 0.08	5.28 ± 0.03
76	I/0	06 08 44.92	20 37 59.02	9.71 ± 0.01	8.44 ± 0.01	7.39 ± 0.01	6.27 ± 0.01	2.76 ± 0.01
77	I/0	06 08 43.93	20 34 25.79	12.65 ± 0.08	11.81 ± 0.06	10.53 ± 0.18	9.14 ± 0.10	
78	I/0	06 08 43.79	20 37 34.76	10.79 ± 0.01	9.81 ± 0.01	8.63 ± 0.03	7.63 ± 0.02	4.32 ± 0.03

Continued on next page...

TABLE 5 – Continued

Source #	YSO Class	R.A. J2000	Decl. J2000	[3.6]	[4.5]	[5.8]	[8.0]	[24]
79	I/0	06 08 43.10	20 36 55.48	11.56 ± 0.03	11.02 ± 0.03	10.03 ± 0.09	8.71 ± 0.05	
80	I/0	06 08 42.88	20 36 07.68	13.48 ± 0.15	12.50 ± 0.10	10.76 ± 0.16	9.11 ± 0.07	
81	I/0	06 08 42.93	20 36 38.46	9.34 ± 0.01	8.51 ± 0.01	7.39 ± 0.01	6.49 ± 0.01	3.91 ± 0.02
82	I/0	06 08 43.22	20 38 11.21	13.90 ± 0.21	12.30 ± 0.07	10.75 ± 0.17	9.38 ± 0.10	
83	I/0	06 08 41.76	20 36 32.97	13.39 ± 0.13	11.73 ± 0.05	10.52 ± 0.14	9.35 ± 0.09	
84	I/0	06 08 42.30	20 38 48.63	12.17 ± 0.04	11.04 ± 0.03	10.17 ± 0.10	9.21 ± 0.08	5.08 ± 0.03
85	I/0	06 08 39.42	20 32 06.57	13.10 ± 0.12	12.66 ± 0.12	11.04 ± 0.27	9.33 ± 0.11	
86	I/0	06 08 38.81	20 31 55.97	11.17 ± 0.02	10.06 ± 0.01	8.94 ± 0.04	7.74 ± 0.03	4.46 ± 0.02
87	I/0	06 08 40.70	20 38 52.35	13.60 ± 0.15	12.86 ± 0.12	11.04 ± 0.22	9.28 ± 0.09	
88	I/0	06 08 40.17	20 38 43.56	12.42 ± 0.06	11.89 ± 0.05	9.74 ± 0.07	7.87 ± 0.02	4.67 ± 0.03
89	I/0	06 08 39.68	20 38 15.96	11.93 ± 0.04	10.36 ± 0.02	9.05 ± 0.04	7.90 ± 0.02	2.61 ± 0.01
90	I/0	06 08 39.49	20 38 03.18	12.82 ± 0.09	11.33 ± 0.03	10.33 ± 0.12	9.57 ± 0.11	
91	I/0	06 08 38.59	20 37 13.32	12.51 ± 0.05	11.43 ± 0.03	10.48 ± 0.12	9.60 ± 0.11	
92	I/0	06 08 36.83	20 35 15.75	14.19 ± 0.33	12.52 ± 0.10	10.76 ± 0.19	9.28 ± 0.10	
93	I/0	06 08 36.28	20 34 26.23	12.60 ± 0.09	11.83 ± 0.07	10.89 ± 0.29	9.56 ± 0.16	
94	I/0	06 08 36.59	20 37 11.05	11.84 ± 0.04	10.72 ± 0.02	9.73 ± 0.07	8.91 ± 0.06	5.07 ± 0.03
95	I/0	06 08 36.98	20 39 21.99	11.46 ± 0.03	10.89 ± 0.02	9.58 ± 0.06	8.04 ± 0.03	
96	I/0	06 08 37.05	20 39 18.43	11.36 ± 0.02	10.83 ± 0.02	9.48 ± 0.05	7.99 ± 0.02	
97	I/0	06 08 36.56	20 38 58.67	11.27 ± 0.03	10.38 ± 0.02	9.48 ± 0.05	8.47 ± 0.04	
98	I/0	06 08 36.31	20 38 18.69	12.23 ± 0.05	11.82 ± 0.05	10.34 ± 0.12	8.83 ± 0.06	
99	I/0	06 08 36.41	20 38 49.95	11.54 ± 0.03	10.75 ± 0.03	9.78 ± 0.07	8.54 ± 0.04	
100	I/0	06 08 35.35	20 35 10.95	11.43 ± 0.03	10.65 ± 0.02	9.69 ± 0.07	8.57 ± 0.05	
101	I/0	06 08 35.25	20 35 05.55	10.16 ± 0.01	9.15 ± 0.01	8.39 ± 0.03	7.61 ± 0.02	
102	I/0	06 08 33.02	20 27 29.06	13.56 ± 0.12	11.59 ± 0.04	10.06 ± 0.07	8.75 ± 0.04	4.35 ± 0.02
103	I/0	06 08 34.72	20 34 28.63	13.14 ± 0.15	12.65 ± 0.14	10.64 ± 0.23	9.00 ± 0.10	
104	I/0	06 08 35.77	20 38 58.28	10.79 ± 0.02	9.73 ± 0.01	9.04 ± 0.04	8.08 ± 0.03	
105	I/0	06 08 35.59	20 39 19.77	10.70 ± 0.02	9.81 ± 0.01	8.54 ± 0.03	7.32 ± 0.02	

Continued on next page...

TABLE 5 – Continued

Source #	YSO Class	R.A. J2000	Decl. J2000	[3.6]	[4.5]	[5.8]	[8.0]	[24]
106	I/0	06 08 35.44	20 39 03.72	10.84 ± 0.01	9.57 ± 0.01	8.22 ± 0.02	6.91 ± 0.01	
107	I/0	06 08 35.14	20 39 04.48	10.75 ± 0.02	9.55 ± 0.01	7.94 ± 0.02	6.66 ± 0.01	
108	I/0	06 08 31.50	20 26 40.78	10.78 ± 0.01	9.80 ± 0.01	8.97 ± 0.03	8.13 ± 0.02	
109	I/0	06 08 34.88	20 38 51.64	12.48 ± 0.10	11.97 ± 0.09	8.85 ± 0.03	7.11 ± 0.01	
110	I/0	06 08 31.43	20 26 35.13	12.89 ± 0.07	11.68 ± 0.04	10.82 ± 0.14	9.84 ± 0.11	
111	I/0	06 08 30.72	20 26 29.70	11.56 ± 0.02	10.71 ± 0.02	10.08 ± 0.07	9.43 ± 0.07	
112	I/0	06 08 32.10	20 31 48.08	11.64 ± 0.03	10.87 ± 0.02	10.27 ± 0.12	8.99 ± 0.07	
113	I/0	06 08 31.77	20 31 41.88	8.17 ± 0.00	7.35 ± 0.00	6.07 ± 0.00	5.43 ± 0.00	1.90 ± 0.01
114	I/0	06 08 31.79	20 34 11.72	11.98 ± 0.04	11.31 ± 0.04	9.66 ± 0.06	8.17 ± 0.03	
115	I/0	06 08 32.71	20 39 06.80	11.63 ± 0.07	10.80 ± 0.05	8.49 ± 0.05	7.29 ± 0.03	
116	I/0	06 08 32.38	20 40 30.32	11.68 ± 0.03	10.67 ± 0.02	9.39 ± 0.04	8.19 ± 0.03	4.49 ± 0.02
117	I/0	06 08 31.71	20 38 58.87	11.96 ± 0.09	11.15 ± 0.06	10.22 ± 0.24	8.54 ± 0.09	
118	I/0	06 08 31.65	20 39 21.69	10.34 ± 0.02	9.62 ± 0.02	8.36 ± 0.04	6.41 ± 0.01	
119	I/0	06 08 31.30	20 38 58.74	11.71 ± 0.07	10.85 ± 0.04	10.19 ± 0.24	8.60 ± 0.10	
120	I/0	06 08 30.97	20 38 08.93	11.18 ± 0.02	10.32 ± 0.02	9.64 ± 0.07	8.52 ± 0.05	
121	I/0	06 08 31.64	20 41 22.50	10.46 ± 0.01	9.61 ± 0.01	8.77 ± 0.02	7.66 ± 0.02	4.21 ± 0.02
122	I/0	06 08 30.81	20 38 40.50	12.47 ± 0.12	11.97 ± 0.10	9.80 ± 0.14	8.13 ± 0.06	
123	I/0	06 08 29.79	20 38 40.23	12.32 ± 0.04	11.43 ± 0.04	9.49 ± 0.05	8.61 ± 0.06	2.81 ± 0.02
124	I/0	06 08 29.50	20 38 01.74	11.77 ± 0.04	10.75 ± 0.02	9.77 ± 0.08	8.71 ± 0.06	4.31 ± 0.02
125	I/0	06 08 29.32	20 38 17.03	11.76 ± 0.03	10.97 ± 0.03	9.74 ± 0.08	8.36 ± 0.04	
126	I/0	06 08 29.15	20 38 02.45	13.04 ± 0.10	12.38 ± 0.09	10.60 ± 0.16	9.01 ± 0.07	
127	I/0	06 08 29.63	20 42 07.93	11.99 ± 0.03	10.93 ± 0.02	10.18 ± 0.07	9.16 ± 0.06	
128	I/0	06 08 27.53	20 37 43.58	12.51 ± 0.06	11.84 ± 0.05	11.00 ± 0.23	9.75 ± 0.14	
129	I/0	06 08 27.51	20 37 47.90	12.07 ± 0.04	11.58 ± 0.04	10.85 ± 0.20	9.70 ± 0.14	
130	I/0	06 08 25.39	20 34 10.24	11.57 ± 0.03	10.23 ± 0.01	9.23 ± 0.04	8.34 ± 0.03	
131	I/0	06 08 18.07	20 36 31.44	8.94 ± 0.00	7.52 ± 0.00	5.74 ± 0.00	4.98 ± 0.00	1.21 ± 0.01
132	I/0	06 08 15.90	20 32 39.58	10.81 ± 0.01	9.67 ± 0.01	8.58 ± 0.02	7.37 ± 0.01	3.43 ± 0.02

Continued on next page...

TABLE 5 – Continued

Source #	YSO Class	R.A. J2000	Decl. J2000	[3.6]	[4.5]	[5.8]	[8.0]	[24]
133	I/0	06 08 15.57	20 31 39.79	12.75 ± 0.06	11.59 ± 0.03	10.67 ± 0.11	9.67 ± 0.08	
134	I/0	06 08 51.36	20 30 46.27	13.52 ± 0.15	11.97 ± 0.06	11.65 ± 0.25	11.47 ± 0.33	4.36 ± 0.02
135	I/0	06 08 49.55	20 29 31.64	11.52 ± 0.03		9.65 ± 0.06	8.75 ± 0.05	5.15 ± 0.03
136	I/II	06 09 58.56	20 30 04.49	12.53 ± 0.09	12.49 ± 0.13	10.99 ± 0.31	9.36 ± 0.13	
137	I/II	06 09 54.17	20 30 28.03	12.08 ± 0.11	12.23 ± 0.19	9.06 ± 0.09	7.30 ± 0.03	
138	I/II	06 09 53.38	20 30 25.52	11.35 ± 0.06	11.04 ± 0.06	9.12 ± 0.10	7.65 ± 0.05	
139	I/II	06 09 52.78	20 30 10.68	10.02 ± 0.02	9.62 ± 0.02	9.22 ± 0.11	7.47 ± 0.04	
140	I/II	06 09 52.63	20 30 16.44	9.08 ± 0.01	8.72 ± 0.01	8.18 ± 0.04	6.74 ± 0.02	
141	I/II	06 09 52.50	20 30 09.07	10.19 ± 0.02	9.81 ± 0.02	8.39 ± 0.05	6.54 ± 0.02	
142	I/II	06 09 49.70	20 31 27.34	12.13 ± 0.07	11.96 ± 0.08	10.30 ± 0.17	8.74 ± 0.08	
143	I/II	06 09 48.37	20 30 32.21	12.37 ± 0.07	12.15 ± 0.08	10.26 ± 0.12	8.77 ± 0.06	
144	I/II	06 09 45.77	20 31 28.38	11.15 ± 0.03	11.14 ± 0.04	10.17 ± 0.13	8.97 ± 0.08	
145	I/II	06 09 41.29	20 35 32.57	12.51 ± 0.06	12.15 ± 0.07	10.80 ± 0.16	9.35 ± 0.08	
146	I/II	06 09 39.37	20 34 28.61	12.51 ± 0.06	12.19 ± 0.07	10.96 ± 0.17	9.39 ± 0.08	
147	I/II	06 09 38.54	20 31 46.89	11.68 ± 0.03	11.78 ± 0.05	10.92 ± 0.18	9.73 ± 0.11	
148	I/II	06 09 36.87	20 35 54.78	12.17 ± 0.05	11.95 ± 0.06	10.70 ± 0.16	9.03 ± 0.06	
149	I/II	06 09 35.41	20 39 47.02	12.26 ± 0.05	12.31 ± 0.08	10.96 ± 0.20	9.43 ± 0.10	
150	I/II	06 09 27.19	20 30 32.26	11.80 ± 0.03	11.48 ± 0.03	10.96 ± 0.15	9.86 ± 0.10	
151	I/II	06 09 28.21	20 38 36.46	12.78 ± 0.10	12.65 ± 0.14	10.72 ± 0.23	9.21 ± 0.10	
152	I/II	06 09 25.86	20 38 56.07	10.48 ± 0.02	10.42 ± 0.03	9.76 ± 0.16	8.59 ± 0.10	
153	I/II	06 09 25.35	20 37 10.59	12.39 ± 0.07	12.28 ± 0.10	10.48 ± 0.17	8.57 ± 0.05	
154	I/II	06 09 24.97	20 41 43.93	12.11 ± 0.04	11.80 ± 0.05	10.38 ± 0.11	8.73 ± 0.06	
155	I/II	06 09 23.76	20 39 05.03	11.75 ± 0.08	11.69 ± 0.12	9.56 ± 0.16	7.74 ± 0.06	
156	I/II	06 09 23.71	20 38 43.49	13.16 ± 0.28	12.87 ± 0.32	10.54 ± 0.37	9.03 ± 0.17	
157	I/II	06 09 23.49	20 41 29.41	11.81 ± 0.03	11.75 ± 0.04	10.54 ± 0.14	9.13 ± 0.08	
158	I/II	06 09 22.69	20 38 38.17	11.55 ± 0.06	11.31 ± 0.08	9.01 ± 0.09	7.19 ± 0.03	
159	I/II	06 09 22.12	20 38 11.88	11.61 ± 0.05	11.67 ± 0.07	9.25 ± 0.08	7.46 ± 0.03	

Continued on next page...

TABLE 5 – Continued

Source #	YSO Class	R.A. J2000	Decl. J2000	[3.6]	[4.5]	[5.8]	[8.0]	[24]
160	I/II	06 09 21.80	20 38 46.56	12.20 ± 0.12	11.80 ± 0.12	9.29 ± 0.12	7.52 ± 0.05	
161	I/II	06 09 21.95	20 39 30.10	8.87 ± 0.01	8.57 ± 0.01	7.90 ± 0.04	6.47 ± 0.02	
162	I/II	06 09 21.85	20 39 20.08	11.95 ± 0.10	11.68 ± 0.13	9.21 ± 0.12	7.40 ± 0.04	
163	I/II	06 09 22.02	20 40 45.13	11.77 ± 0.06	11.40 ± 0.05	9.35 ± 0.09	7.70 ± 0.04	
164	I/II	06 09 21.86	20 39 57.42	11.99 ± 0.11	11.83 ± 0.14	10.87 ± 0.55	9.17 ± 0.21	
165	I/II	06 09 21.58	20 40 15.39	11.93 ± 0.09	11.83 ± 0.12	9.85 ± 0.19	8.42 ± 0.09	
166	I/II	06 09 21.25	20 39 51.08	11.85 ± 0.09	11.63 ± 0.11	9.56 ± 0.16	8.05 ± 0.07	
167	I/II	06 09 20.59	20 37 39.51	12.28 ± 0.07	12.17 ± 0.09	10.08 ± 0.12	8.22 ± 0.04	
168	I/II	06 09 20.75	20 39 29.83	11.31 ± 0.06	10.92 ± 0.06	8.99 ± 0.10	7.35 ± 0.04	
169	I/II	06 09 20.75	20 39 19.50	11.75 ± 0.09	11.87 ± 0.15	9.02 ± 0.11	7.35 ± 0.04	
170	I/II	06 09 20.95	20 40 27.53	11.25 ± 0.04	10.98 ± 0.05	9.55 ± 0.13	7.68 ± 0.04	
171	I/II	06 09 20.81	20 40 36.75	11.86 ± 0.06	11.48 ± 0.05	9.68 ± 0.11	7.99 ± 0.04	
172	I/II	06 09 20.60	20 40 03.38	12.43 ± 0.15	12.05 ± 0.16	9.52 ± 0.15	7.98 ± 0.07	
173	I/II	06 09 19.83	20 40 32.69	12.36 ± 0.05	12.38 ± 0.09	9.87 ± 0.10	8.10 ± 0.04	
174	I/II	06 09 19.75	20 39 58.70	12.70 ± 0.18	12.44 ± 0.22	9.82 ± 0.20	8.06 ± 0.07	
175	I/II	06 09 19.03	20 38 03.05	11.45 ± 0.03	11.20 ± 0.04	9.38 ± 0.08	7.64 ± 0.03	
176	I/II	06 09 19.21	20 38 55.70	11.35 ± 0.05	10.95 ± 0.05	9.38 ± 0.11	7.84 ± 0.05	
177	I/II	06 09 17.81	20 39 13.63	11.29 ± 0.03	11.13 ± 0.05	9.51 ± 0.10	7.77 ± 0.04	
178	I/II	06 09 17.16	20 40 35.39	12.18 ± 0.05	11.93 ± 0.06	9.64 ± 0.07	7.89 ± 0.03	
179	I/II	06 09 05.60	20 29 49.51	10.93 ± 0.02	10.93 ± 0.03	10.06 ± 0.08	8.69 ± 0.04	
180	I/II	06 09 03.12	20 30 04.13	11.97 ± 0.05	12.01 ± 0.07	10.79 ± 0.21	9.12 ± 0.09	
181	I/II	06 09 05.03	20 43 16.91	11.60 ± 0.02	11.55 ± 0.03	10.99 ± 0.16	9.67 ± 0.09	
182	I/II	06 08 58.61	20 28 07.10	10.89 ± 0.02	10.73 ± 0.02	10.07 ± 0.10	8.85 ± 0.06	
183	I/II	06 09 01.02	20 38 00.88	10.76 ± 0.02	10.75 ± 0.03	10.30 ± 0.13	9.13 ± 0.09	
184	I/II	06 08 59.45	20 35 05.52	12.87 ± 0.10	12.67 ± 0.13	10.56 ± 0.16	8.64 ± 0.05	4.74 ± 0.02
185	I/II	06 09 01.03	20 41 21.51	12.62 ± 0.10	12.67 ± 0.16	10.82 ± 0.27	9.02 ± 0.09	
186	I/II	06 08 59.55	20 40 24.68	10.72 ± 0.02	10.69 ± 0.03	9.78 ± 0.09	8.54 ± 0.05	

Continued on next page...

TABLE 5 – Continued

Source #	YSO Class	R.A. J2000	Decl. J2000	[3.6]	[4.5]	[5.8]	[8.0]	[24]
187	I/II	06 08 59.15	20 41 22.64	11.98 ± 0.06	11.91 ± 0.08	10.35 ± 0.18	8.53 ± 0.06	
188	I/II	06 08 51.13	20 28 31.93	11.94 ± 0.03	11.77 ± 0.05	10.94 ± 0.18	9.55 ± 0.10	
189	I/II	06 08 51.65	20 31 58.54	12.28 ± 0.06	12.29 ± 0.09	10.51 ± 0.16	8.88 ± 0.07	
190	I/II	06 08 52.62	20 37 28.36	12.10 ± 0.06	11.91 ± 0.08	10.52 ± 0.18	9.02 ± 0.08	
191	I/II	06 08 50.52	20 32 21.08	12.61 ± 0.09	12.32 ± 0.10	10.51 ± 0.19	8.93 ± 0.08	
192	I/II	06 08 49.65	20 31 48.06	11.93 ± 0.05	11.88 ± 0.06	10.86 ± 0.26	9.44 ± 0.14	
193	I/II	06 08 51.75	20 41 05.59	11.74 ± 0.04	11.63 ± 0.05	10.59 ± 0.17	9.35 ± 0.10	
194	I/II	06 08 50.77	20 39 10.99	12.56 ± 0.09	12.40 ± 0.12	10.92 ± 0.29	9.66 ± 0.18	
195	I/II	06 08 48.89	20 39 10.25	12.11 ± 0.05	12.07 ± 0.08	11.01 ± 0.30	9.55 ± 0.15	
196	I/II	06 08 47.23	20 34 29.66	13.12 ± 0.15	12.87 ± 0.17	10.82 ± 0.26	9.22 ± 0.12	
197	I/II	06 08 46.83	20 37 32.12	12.72 ± 0.10	12.42 ± 0.11	10.68 ± 0.20	8.95 ± 0.08	
198	I/II	06 08 43.02	20 30 54.66	10.33 ± 0.01	10.14 ± 0.01	9.76 ± 0.08	8.57 ± 0.05	3.98 ± 0.02
199	I/II	06 08 42.34	20 30 45.17	11.05 ± 0.02	10.83 ± 0.02	9.94 ± 0.09	8.60 ± 0.05	
200	I/II	06 08 42.18	20 31 33.68	12.93 ± 0.10	12.72 ± 0.12	10.31 ± 0.14	8.57 ± 0.05	
201	I/II	06 08 41.07	20 30 18.04	11.33 ± 0.03	10.99 ± 0.03	10.36 ± 0.13	9.04 ± 0.08	
202	I/II	06 08 40.03	20 35 11.16	12.80 ± 0.08	12.63 ± 0.11	10.95 ± 0.22	9.33 ± 0.10	
203	I/II	06 08 38.54	20 32 05.35	12.71 ± 0.09	12.45 ± 0.10	10.26 ± 0.14	8.56 ± 0.06	
204	I/II	06 08 37.85	20 34 52.00	12.44 ± 0.07	12.29 ± 0.09	10.55 ± 0.18	8.80 ± 0.07	
205	I/II	06 08 35.73	20 32 20.82	11.65 ± 0.03	11.75 ± 0.05	10.18 ± 0.12	8.55 ± 0.05	
206	I/II	06 08 35.42	20 37 22.85	12.47 ± 0.06	12.45 ± 0.09	10.33 ± 0.12	8.65 ± 0.05	
207	I/II	06 08 34.86	20 38 22.64	12.73 ± 0.10	12.60 ± 0.12	10.51 ± 0.19	8.88 ± 0.08	
208	I/II	06 08 33.21	20 32 59.46	12.18 ± 0.05	12.01 ± 0.07	11.00 ± 0.25	9.49 ± 0.12	
209	I/II	06 08 33.61	20 38 44.43	12.39 ± 0.11	12.22 ± 0.14	9.60 ± 0.11	7.66 ± 0.03	
210	I/II	06 08 33.15	20 38 27.80	12.29 ± 0.07	11.97 ± 0.07	9.74 ± 0.10	7.92 ± 0.04	
211	I/II	06 08 32.59	20 38 27.14	11.75 ± 0.05	11.61 ± 0.06	9.79 ± 0.13	8.01 ± 0.05	
212	I/II	06 08 32.04	20 39 18.39	9.10 ± 0.01	8.72 ± 0.01	7.73 ± 0.03	5.83 ± 0.01	
213	I/II	06 08 30.59	20 38 58.64	11.70 ± 0.06	11.35 ± 0.07	9.03 ± 0.08	7.33 ± 0.03	

Continued on next page...

TABLE 5 – Continued

Source #	YSO Class	R.A. J2000	Decl. J2000	[3.6]	[4.5]	[5.8]	[8.0]	[24]
214	I/II	06 08 28.85	20 40 21.60	11.53 ± 0.03	11.50 ± 0.04	10.44 ± 0.13	9.01 ± 0.06	
215	I/II	06 08 25.66	20 35 40.90	11.95 ± 0.04	11.59 ± 0.04	10.69 ± 0.17	9.42 ± 0.10	
216	I/II	06 08 09.50	20 41 13.34	11.18 ± 0.02	11.00 ± 0.02	10.53 ± 0.11	9.43 ± 0.07	
217	II	06 10 00.62	20 36 55.37	11.22 ± 0.02	11.41 ± 0.03	10.92 ± 0.15	9.98 ± 0.12	
218	II	06 09 55.34	20 33 34.60	9.72 ± 0.01	9.23 ± 0.01	8.98 ± 0.03	8.00 ± 0.02	4.91 ± 0.02
219	II	06 09 53.38	20 31 20.45	11.92 ± 0.08	11.60 ± 0.08	10.77 ± 0.38	10.13 ± 0.40	
220	II	06 09 52.24	20 30 49.87	11.26 ± 0.05	10.52 ± 0.04	9.97 ± 0.20	9.25 ± 0.19	
221	II	06 09 50.23	20 36 22.98	10.95 ± 0.02	11.03 ± 0.03	10.45 ± 0.11	9.40 ± 0.07	
222	II	06 09 45.69	20 31 33.99	10.74 ± 0.02	10.82 ± 0.03	10.32 ± 0.14	9.44 ± 0.12	
223	II	06 09 43.55	20 28 42.30	9.98 ± 0.01	9.94 ± 0.01	9.74 ± 0.06	9.01 ± 0.05	
224	II	06 09 44.71	20 34 12.10	11.47 ± 0.02	11.51 ± 0.04	10.96 ± 0.16	10.08 ± 0.14	
225	II	06 09 41.77	20 31 24.48	11.46 ± 0.03	10.97 ± 0.03	10.53 ± 0.16	9.92 ± 0.18	
226	II	06 09 37.39	20 38 01.64	11.71 ± 0.04	11.54 ± 0.05	10.75 ± 0.19	9.83 ± 0.16	
227	II	06 09 33.88	20 32 31.78	11.26 ± 0.02	10.83 ± 0.02	10.44 ± 0.11	9.46 ± 0.08	
228	II	06 09 33.77	20 32 45.43	12.29 ± 0.04	11.57 ± 0.04	10.99 ± 0.17	10.05 ± 0.13	
229	II	06 09 30.30	20 39 32.66	12.66 ± 0.08	12.23 ± 0.08	10.70 ± 0.19	9.98 ± 0.19	
230	II	06 09 30.18	20 41 14.15	11.54 ± 0.03	11.39 ± 0.04	11.02 ± 0.20	10.22 ± 0.21	
231	II	06 09 24.26	20 38 13.59	12.43 ± 0.10	12.29 ± 0.13	10.91 ± 0.35	10.18 ± 0.34	
232	II	06 09 23.43	20 38 02.35	11.02 ± 0.03	10.38 ± 0.03	9.89 ± 0.14	9.14 ± 0.13	
233	II	06 09 04.64	20 32 22.53	11.07 ± 0.02	11.05 ± 0.03	10.87 ± 0.18	10.14 ± 0.17	
234	II	06 09 06.88	20 42 16.22	11.92 ± 0.04	11.51 ± 0.04	10.79 ± 0.18	9.89 ± 0.16	
235	II	06 09 06.14	20 42 13.99	11.30 ± 0.02	10.57 ± 0.02	10.04 ± 0.10	9.35 ± 0.10	
236	II	06 09 02.45	20 39 47.61	11.15 ± 0.03	11.12 ± 0.04	10.64 ± 0.18	9.99 ± 0.19	
237	II	06 08 58.85	20 28 09.86	9.77 ± 0.01	9.80 ± 0.01	9.47 ± 0.06	8.53 ± 0.04	
238	II	06 08 56.89	20 28 27.85	10.65 ± 0.01	10.39 ± 0.02	9.88 ± 0.09	9.13 ± 0.08	
239	II	06 08 57.97	20 35 47.94	11.56 ± 0.03	11.59 ± 0.06	10.95 ± 0.23	9.92 ± 0.17	
240	II	06 08 55.44	20 30 46.98	10.45 ± 0.01	9.76 ± 0.01	9.23 ± 0.05	8.34 ± 0.04	

Continued on next page...

TABLE 5 – Continued

Source #	YSO Class	R.A. J2000	Decl. J2000	[3.6]	[4.5]	[5.8]	[8.0]	[24]
241	II	06 08 54.40	20 28 47.99	11.76 ± 0.03	11.18 ± 0.03	10.91 ± 0.19	10.34 ± 0.22	
242	II	06 08 53.76	20 28 46.15	12.11 ± 0.04	11.45 ± 0.04	10.53 ± 0.13	9.56 ± 0.10	
243	II	06 08 51.57	20 35 36.68	11.44 ± 0.03	11.07 ± 0.03	10.55 ± 0.18	9.61 ± 0.14	
244	II	06 08 48.53	20 29 26.16	11.72 ± 0.03	11.03 ± 0.02	10.48 ± 0.12	9.69 ± 0.11	
245	II	06 08 49.15	20 32 44.48	11.94 ± 0.05	11.68 ± 0.06	10.88 ± 0.26	9.85 ± 0.20	
246	II	06 08 47.71	20 29 05.65	10.63 ± 0.01	10.05 ± 0.01	9.65 ± 0.06	8.94 ± 0.05	
247	II	06 08 46.70	20 37 41.89	11.19 ± 0.03	10.59 ± 0.02	9.93 ± 0.10	8.88 ± 0.08	
248	II	06 08 42.37	20 30 13.68	11.30 ± 0.02	11.32 ± 0.03	10.95 ± 0.22	10.22 ± 0.22	
249	II	06 08 43.18	20 33 59.98	11.15 ± 0.02	10.43 ± 0.02	9.81 ± 0.09	8.83 ± 0.07	4.43 ± 0.02
250	II	06 08 41.45	20 38 35.62	12.41 ± 0.05	11.83 ± 0.05	10.93 ± 0.19	9.84 ± 0.14	
251	II	06 08 38.93	20 33 08.22	10.76 ± 0.02	10.21 ± 0.02	9.53 ± 0.07	8.60 ± 0.05	
252	II	06 08 36.77	20 29 42.92	11.97 ± 0.04	11.44 ± 0.03	10.96 ± 0.19	9.90 ± 0.14	
253	II	06 08 36.04	20 31 22.44	12.71 ± 0.06	12.18 ± 0.06	11.09 ± 0.20	10.44 ± 0.24	
254	II	06 08 38.21	20 39 22.89	11.72 ± 0.03	11.09 ± 0.03	10.44 ± 0.12	9.67 ± 0.12	
255	II	06 08 35.63	20 34 17.15	11.05 ± 0.02	10.83 ± 0.03	10.36 ± 0.19	9.27 ± 0.13	
256	II	06 08 35.37	20 36 04.14	8.20 ± 0.01	7.48 ± 0.01	6.22 ± 0.01	5.43 ± 0.01	1.83 ± 0.01
257	II	06 08 31.72	20 25 31.31	11.73 ± 0.03	11.16 ± 0.03	10.94 ± 0.17	10.08 ± 0.14	
258	II	06 08 34.88	20 37 56.57	12.11 ± 0.06	11.69 ± 0.05	10.98 ± 0.26	10.07 ± 0.22	
259	II	06 08 33.00	20 33 42.17	11.76 ± 0.04	11.15 ± 0.04	10.27 ± 0.15	9.44 ± 0.13	
260	II	06 08 31.78	20 33 34.56	10.03 ± 0.01	9.86 ± 0.01	9.62 ± 0.06	8.77 ± 0.05	
261	II	06 08 33.27	20 40 38.62	11.45 ± 0.02	10.89 ± 0.02	10.21 ± 0.08	9.32 ± 0.08	
262	II	06 08 27.72	20 36 47.42	11.42 ± 0.03	10.75 ± 0.02	10.24 ± 0.13	9.39 ± 0.11	
263	II	06 08 28.65	20 41 03.18	10.87 ± 0.01	10.19 ± 0.01	9.55 ± 0.05	8.58 ± 0.04	
264	II	06 08 26.65	20 36 37.39	12.41 ± 0.07	11.86 ± 0.05	11.01 ± 0.25	10.05 ± 0.19	
265	II	06 08 24.19	20 36 27.41	11.73 ± 0.03	11.61 ± 0.04	10.85 ± 0.18	10.10 ± 0.18	

TABLE 6

NGC 2175 YSO BEST-FIT PARAMETERS

Source #	Model #	χ^2	Mass ($M_\odot$)	Age ($\times 10^5$ yr)	Temp (K)	Radius ($R_\odot$)	Log(d) (kpc)
1	3006919	71.2	4.15 ± 1.21	0.47	4421	19.45	0.30
2	3020123	26.3	3.11 ± 1.31	0.02	4225	21.92	0.34
3	3005590	24.5	2.69 ± 0.78	1.16	4408	12.70	0.38
4	3007513	69.7	2.73 ± 1.74	0.19	4296	16.34	0.34
5	3005590	85.0	2.69 ± 1.46	1.16	4408	12.70	0.30
6	3008321	68.9	0.90 ± 0.21	0.02	3936	9.42	0.35
7	3008605	5.3	0.73 ± 0.44	1.98	3994	4.93	0.35
8	3005565	36.5	5.67 ± 0.98	4.65	11900	6.96	0.38
9	3002183	91.3	1.63 ± 0.26	1.09	4281	9.08	0.33
10	3012148	48.4	3.31 ± 0.98	0.02	4227	23.27	0.30
11	3003798	74.4	3.65 ± 1.21	0.89	4447	16.23	0.30
12	3000931	107.0	1.25 ± 0.47	0.09	4036	11.91	0.31
13	3008880	36.6	3.09 ± 1.76	0.02	4221	21.92	0.30
14	3007508	120.3	1.37 ± 1.34	1.04	4234	8.04	0.32
15	3011853	9.5	1.11 ± 0.87	0.05	4061	9.71	0.37
16	3003809	17.0	1.79 ± 1.27	1.89	4369	8.17	0.31
17	3017697	101.8	3.00 ± 1.24	0.03	4229	20.88	0.28
18	3009124	14.3	2.24 ± 1.22	0.10	4195	16.58	0.38
19	3014125	97.0	5.33 ± 0.75	0.37	4446	23.71	0.30
20	3019854	9.3	0.90 ± 0.37	0.01	3934	9.50	0.34
21	3018872	37.4	1.10 ± 0.92	0.11	4089	8.84	0.34
22	3006938	9.2	1.02 ± 0.66	0.20	4051	8.54	0.37
23	3003476	41.5	3.59 ± 2.04	0.09	4298	21.63	0.38
24	3016440	73.6	3.17 ± 1.46	2.14	4639	9.26	0.38
25	3004674	17.2	1.78 ± 1.03	0.05	4156	14.12	0.30
26	3013081	12.5	2.42 ± 0.56	0.17	4271	15.31	0.38
27	3001308	21.6	1.31 ± 0.89	0.37	4178	8.71	0.38
28	3007348	10.8	4.28 ± 1.21	0.10	4284	26.59	0.38
29	3009694	18.8	5.30 ± 1.63	2.20	4944	16.23	0.31
30	3006583	10.4	1.64 ± 0.77	0.69	4272	9.41	0.30
31	3006432	14.0	0.99 ± 0.69	0.05	3927	11.36	0.32
32	3008111	9.1	2.03 ± 1.03	0.09	4186	15.09	0.31
33	3012732	28.1	2.56 ± 2.04	0.62	4359	13.27	0.34
34	3005095	114.2	4.65 ± 0.75	6.69	7591	8.49	0.30
35	3006097	129.7	4.96 ± 1.92	0.04	4199	36.02	0.32
36	3015204	13.5	2.22 ± 1.58	2.96	4574	6.61	0.32
37	3009134	3.4	5.63 ± 1.70	0.24	4420	26.19	0.30

Continued on next page...

TABLE 6 – Continued

Source #	Model #	χ^2	Mass ($M_\odot$)	Age ($\times 10^5$ yr)	Temp (K)	Radius ($R_\odot$)	Log(d) (kpc)
38	3013121	44.2	4.42 ± 1.40	0.01	4125	37.82	0.36
39	3003476	83.9	3.59 ± 2.53	0.09	4298	21.63	0.31
40	3003473	14.3	2.85 ± 1.43	0.40	4365	14.74	0.30
41	3003476	57.1	3.59 ± 0.35	0.09	4298	21.63	0.30
42	3006432	11.7	0.99 ± 0.80	0.05	3927	11.36	0.36
43	3002367	5.5	0.92 ± 0.73	0.57	4080	6.32	0.33
44	3009134	19.7	5.63 ± 1.13	0.24	4420	26.19	0.30
45	3008780	23.0	1.56 ± 1.07	0.02	4093	13.92	0.30
46	3009871	116.9	3.36 ± 1.46	1.69	4593	10.90	0.38
47	3011153	25.2	2.31 ± 1.48	0.15	4242	15.36	0.32
48	3015461	2.3	2.21 ± 1.24	0.35	4312	12.50	0.31
49	3017133	36.2	2.00 ± 0.15	0.54	4313	11.10	0.38
50	3005205	29.5	1.21 ± 0.88	1.14	4194	7.35	0.34
51	3007755	21.6	1.46 ± 0.65	1.34	4264	8.17	0.37
52	3001971	107.1	4.03 ± 0.12	19.3	14500	2.39	0.38
53	3018582	20.0	1.02 ± 0.49	1.65	4146	6.33	0.30
54	3019987	9.0	1.73 ± 0.96	0.40	4276	10.10	0.34
55	3009134	9.2	5.63 ± 1.44	0.24	4420	26.19	0.30
56	3002150	127.3	2.01 ± 0.63	0.03	4129	17.11	0.30
57	3010798	2.6	0.92 ± 0.78	0.79	4090	6.12	0.38
58	3009456	10.9	0.91 ± 0.19	0.02	3934	9.60	0.38
59	3017342	17.7	1.74 ± 1.60	0.21	4241	11.03	0.36
60	3006919	59.2	4.15 ± 0.80	0.47	4421	19.45	0.38
61	3007489	19.1	1.24 ± 0.56	0.20	4105	9.88	0.34
62	3010263	3.2	0.92 ± 0.52	0.02	3926	10.09	0.38
63	3004220	7.1	2.34 ± 0.97	1.55	4426	10.29	0.32
64	3002444	32.7	0.66 ± 0.52	0.06	3817	7.57	0.32
65	3002045	52.3	1.47 ± 0.46	0.03	4126	11.78	0.32
66	3009627	9.7	2.46 ± 1.75	0.78	4359	12.66	0.36
67	3000728	1.9	0.75 ± 0.35	0.67	3990	5.35	0.31
68	3016881	90.6	1.01 ± 0.09	0.19	4032	8.80	0.34
69	3010673	4.2	0.47 ± 0.38	0.02	3648	6.38	0.30
70	3011335	32.3	4.11 ± 0.49	1.58	4631	12.88	0.34
71	3008423	44.3	1.16 ± 0.26	0.02	4004	12.01	0.30
72	3000522	39.9	1.46 ± 0.37	0.05	4138	11.32	0.38
73	3011453	13.1	0.90 ± 0.71	0.45	4063	6.36	0.38
74	3012341	119.2	2.33 ± 0.83	2.07	4504	8.43	0.30
75	3012678	33.4	0.64 ± 0.41	0.01	3784	8.14	0.34
76	3000186	61.4	1.67 ± 1.65	0.03	4144	13.32	0.38
77	3010516	5.7	1.43 ± 0.83	0.80	4241	8.43	0.30

Continued on next page...

TABLE 6 – Continued

Source #	Model #	χ^2	Mass ($M_\odot$)	Age ($\times 10^5$ yr)	Temp (K)	Radius ($R_\odot$)	Log(d) (kpc)
78	3003961	94.3	0.90 ± 0.45	0.02	3934	9.58	0.32
79	3014453	4.4	5.39 ± 1.69	0.03	4171	41.14	0.36
80	3018872	1.6	1.10 ± 0.93	0.11	4089	8.84	0.38
81	3018691	37.2	1.03 ± 0.15	0.05	3974	10.89	0.33
82	3016315	0.7	0.67 ± 0.29	0.05	3818	7.80	0.37
83	3003943	2.5	0.55 ± 0.20	0.03	3730	6.95	0.31
84	3013350	15.5	0.37 ± 0.23	0.19	3518	4.90	0.35
85	3013343	4.0	1.29 ± 1.12	0.21	4119	10.02	0.31
86	3009456	39.0	0.91 ± 0.32	0.02	3934	9.60	0.33
87	3004674	13.3	1.78 ± 1.18	0.05	4156	14.12	0.36
88	3006503	101.5	3.25 ± 0.50	14.43	5633	6.19	0.29
89	3018492	21.0	1.42 ± 0.22	0.12	4173	9.93	0.32
90	3012541	8.3	1.79 ± 0.90	0.83	4296	9.93	0.38
91	3002808	7.9	2.11 ± 1.31	0.93	4335	11.16	0.30
92	3004159	1.1	1.53 ± 0.71	0.12	4165	11.27	0.34
93	3014129	4.8	0.73 ± 0.46	0.71	3981	5.26	0.36
94	3007755	32.3	1.46 ± 1.30	1.34	4264	8.17	0.30
95	3003798	49.6	3.65 ± 0.76	0.89	4447	16.23	0.34
96	3013081	55.5	2.42 ± 0.81	0.17	4271	15.31	0.32
97	3003561	2.4	1.56 ± 1.00	0.22	4204	10.43	0.35
98	3016727	25.7	1.82 ± 1.14	0.85	4302	10.06	0.30
99	3006424	17.8	0.82 ± 0.60	0.10	3944	7.71	0.38
100	3008940	21.8	1.00 ± 0.87	0.16	4008	9.26	0.35
101	3006471	17.3	3.46 ± 0.85	0.62	4410	16.45	0.30
102	3017660	10.8	0.24 ± 0.08	0.03	3182	5.16	0.30
103	3018872	13.0	1.10 ± 0.98	0.11	4089	8.84	0.38
104	3016826	56.6	2.16 ± 0.92	0.15	4230	14.78	0.30
105	3003621	15.2	5.32 ± 1.87	0.04	4195	38.73	0.30
106	3010464	0.8	1.65 ± 1.05	0.04	4143	13.19	0.30
107	3014455	5.8	5.18 ± 1.88	0.09	4286	31.62	0.30
108	3016826	13.8	2.16 ± 0.97	0.15	4230	14.78	0.30
109	3015498	31.8	6.47 ± 1.86	0.02	4153	49.85	0.30
110	3016282	1.2	0.97 ± 0.88	0.26	4038	7.92	0.35
111	3010799	17.0	1.43 ± 1.04	0.38	4226	8.76	0.31
112	3011361	26.4	2.78 ± 1.22	2.30	4601	8.40	0.35
113	3016505	95.4	6.11 ± 1.07	1.83	5313	20.99	0.38
114	3004159	133.9	1.53 ± 0.82	0.12	4165	11.27	0.38
115	3017419	65.9	6.92 ± 2.78	0.09	4297	40.21	0.38
116	3014612	82.8	0.60 ± 0.19	0.01	3757	7.75	0.34
117	3007384	54.0	2.35 ± 1.74	0.74	4347	12.31	0.30

Continued on next page...

TABLE 6 – Continued

Source #	Model #	χ^2	Mass ($M_\odot$)	Age ($\times 10^5$ yr)	Temp (K)	Radius ($R_\odot$)	Log(d) (kpc)
118	3003476	11.9	3.59 ± 0.98	0.09	4298	21.63	0.34
119	3005036	3.9	0.97 ± 0.90	0.19	4016	8.51	0.35
120	3006088	15.6	1.49 ± 0.60	0.10	4162	10.94	0.36
121	3016440	12.2	3.17 ± 0.08	2.14	4639	9.26	0.38
122	3018872	28.4	1.10 ± 0.94	0.11	4089	8.84	0.32
123	3011396	75.7	2.63 ± 0.88	1.74	4504	9.91	0.35
124	3006618	4.7	1.76 ± 1.44	1.38	4318	9.22	0.35
125	3006948	31.1	2.51 ± 1.34	0.75	4361	12.87	0.38
126	3012868	18.8	0.86 ± 0.73	0.49	4047	6.09	0.30
127	3019480	19.1	0.96 ± 0.56	0.64	4102	6.49	0.30
128	3003895	17.3	1.16 ± 0.89	2.32	4221	6.28	0.36
129	3010531	5.5	0.74 ± 0.32	1.39	4000	5.08	0.31
130	3014061	13.6	1.43 ± 0.59	0.26	4211	9.15	0.32
131	3010566	130.2	0.38 ± 0.10	0.02	3497	6.05	0.38
132	3006405	58.4	0.88 ± 0.50	0.02	3930	9.13	0.31
133	3011453	0.7	0.90 ± 0.49	0.45	4063	6.36	0.30
134	3003577	28.6	1.63 ± 0.74	2.33	4389	6.77	0.29
135	3012982	22.5	1.79 ± 0.75	1.21	4311	9.59	0.35
136	3011352	10.8	1.05 ± 1.11	0.17	4058	8.73	0.34
137	3013136	84.5	4.94 ± 0.43	7.02	11950	5.67	0.32
138	3005888	70.2	2.54 ± 0.93	0.02	4131	21.84	0.37
139	3017051	24.1	1.77 ± 0.79	0.68	4292	10.00	0.33
140	3008917	36.5	4.72 ± 0.70	1.73	4709	13.59	0.32
141	3009134	25.3	5.63 ± 0.86	0.24	4420	26.19	0.38
142	3009124	14.3	2.24 ± 1.42	0.10	4195	16.58	0.34
143	3001421	20.2	2.42 ± 2.19	0.37	4333	13.22	0.38
144	3011069	27.8	3.42 ± 0.66	4.50	4850	6.90	0.36
145	3011722	14.3	1.12 ± 0.77	1.43	4178	6.81	0.31
146	3009974	11.3	1.25 ± 0.63	0.01	3961	14.39	0.36
147	3007961	33.5	3.11 ± 0.56	6.35	4888	5.69	0.38
148	3017868	29.3	1.19 ± 0.71	1.69	4207	6.99	0.34
149	3000773	133.1	3.47 ± 0.78	0.45	4400	16.88	0.30
150	3010269	19.1	4.10 ± 2.12	0.59	4429	18.90	0.38
151	3007513	15.4	2.73 ± 1.09	0.19	4296	16.34	0.32
152	3017718	6.3	3.03 ± 0.81	1.92	4592	9.57	0.35
153	3015782	18.1	1.31 ± 0.62	0.60	4207	8.09	0.36
154	3009124	19.4	2.24 ± 1.27	0.10	4195	16.58	0.34
155	3020123	57.7	3.11 ± 1.46	0.02	4225	21.92	0.36
156	3005481	9.7	2.26 ± 1.53	0.14	4232	15.48	0.38
157	3007866	33.1	4.59 ± 1.18	13.14	15760	2.65	0.36

Continued on next page...

TABLE 6 – Continued

Source #	Model #	χ^2	Mass ($M_\odot$)	Age ($\times 10^5$ yr)	Temp (K)	Radius ($R_\odot$)	Log(d) (kpc)
158	3002183	69.0	1.63 ± 0.25	1.09	4281	9.08	0.30
159	3011127	79.0	6.08 ± 1.43	0.54	4532	23.66	0.34
160	3006097	57.2	4.96 ± 2.00	0.04	4199	36.02	0.34
161	3002412	9.9	4.76 ± 0.66	0.83	4490	19.64	0.38
162	3013136	79.7	4.94 ± 0.27	7.02	11950	5.67	0.34
163	3017133	99.5	2.00 ± 0.27	0.54	4313	11.10	0.30
164	3007866	2.7	4.59 ± 1.63	13.14	15760	2.65	0.32
165	3003441	55.0	2.42 ± 0.95	1.60	4441	10.28	0.31
166	3019058	35.0	5.75 ± 1.92	0.40	4476	24.12	0.38
167	3002914	43.3	0.92 ± 0.88	0.41	4064	6.66	0.32
168	3003476	49.9	3.59 ± 0.14	0.09	4298	21.63	0.37
169	3009134	85.1	5.63 ± 0.07	0.24	4420	26.19	0.34
170	3004847	52.7	5.88 ± 1.72	0.53	4517	23.24	0.38
171	3013081	42.2	2.42 ± 1.01	0.17	4271	15.31	0.30
172	3015461	39.4	2.21 ± 1.26	0.35	4312	12.50	0.30
173	3003476	82.0	3.59 ± 0.05	0.09	4298	21.63	0.38
174	3009134	5.9	5.63 ± 0.86	0.24	4420	26.19	0.36
175	3000590	85.5	2.08 ± 0.04	0.72	4324	11.25	0.34
176	3006221	22.3	3.19 ± 1.52	0.13	4320	18.35	0.34
177	3006503	61.3	3.25 ± 1.49	14.43	5633	6.19	0.38
178	3003476	67.2	3.59 ± 0.06	0.09	4298	21.63	0.37
179	3006465	28.2	2.40 ± 0.75	1.84	4485	9.25	0.37
180	3007866	20.4	4.59 ± 1.27	13.14	15760	2.65	0.38
181	3011811	19.1	4.73 ± 0.06	17.02	15960	2.58	0.34
182	3016596	9.1	4.22 ± 0.28	10.70	11120	4.95	0.33
183	3016659	11.4	3.23 ± 0.78	2.56	4691	8.52	0.34
184	3007923	103.6	0.64 ± 0.30	0.01	3779	8.13	0.37
185	3008962	41.9	4.34 ± 1.03	1.64	4660	13.17	0.32
186	3012258	24.1	2.46 ± 0.63	1.02	4372	12.27	0.33
187	3016180	24.7	2.21 ± 2.26	2.06	4483	8.26	0.35
188	3013888	8.8	4.62 ± 0.29	14.16	15780	2.57	0.34
189	3008721	24.1	2.55 ± 2.01	0.55	4355	13.34	0.38
190	3006583	26.9	1.64 ± 1.11	0.69	4272	9.41	0.37
191	3007376	18.3	1.19 ± 0.92	0.19	4100	9.40	0.30
192	3018043	21.7	1.77 ± 0.68	3.18	4494	5.71	0.38
193	3014085	10.8	1.22 ± 0.78	0.84	4191	7.52	0.34
194	3002977	11.9	0.92 ± 0.48	0.81	4092	6.11	0.30
195	3010132	10.3	2.25 ± 0.36	8.16	4746	4.18	0.34
196	3004889	17.5	1.11 ± 1.05	0.18	4100	8.48	0.33
197	3003175	20.4	2.19 ± 1.52	1.07	4354	11.26	0.32

Continued on next page...

TABLE 6 – Continued

Source #	Model #	χ^2	Mass ($M_\odot$)	Age ($\times 10^5$ yr)	Temp (K)	Radius ($R_\odot$)	Log(d) (kpc)
198	3017718	131.7	3.03 ± 0.64	1.92	4592	9.57	0.33
199	3012258	13.7	2.46 ± 0.93	1.02	4372	12.27	0.32
200	3018872	46.1	1.10 ± 0.72	0.11	4089	8.84	0.36
201	3009659	15.2	1.63 ± 1.13	0.40	4258	9.71	0.30
202	3006432	14.6	0.99 ± 1.16	0.05	3927	11.36	0.38
203	3001421	17.9	2.42 ± 1.06	0.37	4333	13.22	0.34
204	3013081	38.7	2.42 ± 1.22	0.17	4271	15.31	0.38
205	3008987	65.0	3.25 ± 0.80	11.20	5213	5.62	0.38
206	3015782	53.4	1.31 ± 0.69	0.60	4207	8.09	0.38
207	3007376	33.2	1.19 ± 0.95	0.19	4100	9.40	0.30
208	3008942	5.4	1.07 ± 0.33	1.65	4165	6.49	0.37
209	3007102	52.2	5.35 ± 1.20	8.55	17040	2.98	0.38
210	3003476	49.7	3.59 ± 0.05	0.09	4298	21.63	0.33
211	3013081	44.7	2.42 ± 0.45	0.17	4271	15.31	0.30
212	3009964	26.5	3.88 ± 1.14	0.24	4378	19.81	0.37
213	3003476	59.9	3.59 ± 0.91	0.09	4298	21.63	0.32
214	3007866	62.3	4.59 ± 0.96	13.14	15760	2.65	0.32
215	3008500	6.0	1.47 ± 1.28	0.67	4244	8.67	0.34
216	3012445	12.7	2.93 ± 0.73	5.54	4818	5.69	0.31
217	3018483	11.6	2.86 ± 0.89	4.21	4747	6.29	0.34
218	3010453	28.7	3.99 ± 0.55	9.67	6580	7.71	0.38
219	3009034	1.9	0.78 ± 0.32	3.35	4048	4.68	0.33
220	3015954	13.1	2.05 ± 0.96	2.26	4480	7.53	0.34
221	3008466	17.6	2.67 ± 0.84	2.78	4635	7.43	0.30
222	3014616	12.5	3.59 ± 0.21	11.59	5827	7.21	0.34
223	3019444	11.1	4.63 ± 0.98	1.41	4631	14.91	0.34
224	3018195	31.6	3.16 ± 0.45	7.27	4937	5.54	0.33
225	3018005	4.1	2.06 ± 0.92	2.54	4507	6.99	0.33
226	3001226	11.4	0.98 ± 0.42	0.51	4097	6.81	0.30
227	3019806	7.0	2.10 ± 0.94	6.49	4682	4.42	0.31
228	3001085	6.2	0.97 ± 0.54	2.74	4156	5.48	0.31
229	3019987	10.9	1.73 ± 1.37	0.40	4276	10.10	0.32
230	3000437	4.8	2.11 ± 0.97	2.70	4530	6.81	0.30
231	3010438	10.1	0.93 ± 0.64	5.72	4217	3.31	0.30
232	3010282	8.6	3.15 ± 1.00	10.80	5102	5.18	0.30
233	3014123	25.6	3.25 ± 0.23	16.97	6459	5.95	0.35
234	3009772	6.9	1.49 ± 0.90	3.90	4449	4.75	0.35
235	3013492	4.1	1.75 ± 0.77	1.83	4359	8.21	0.35
236	3015939	8.1	2.81 ± 0.88	2.72	4649	7.70	0.31
237	3017509	31.8	4.65 ± 0.18	2.40	4820	11.92	0.33

Continued on next page...

TABLE 6 – Continued

Source #	Model #	χ^2	Mass ($M_\odot$)	Age ($\times 10^5$ yr)	Temp (K)	Radius ($R_\odot$)	Log(d) (kpc)
238	3015251	27.0	3.62 ± 0.95	0.55	4411	17.23	0.38
239	3001834	12.2	2.70 ± 0.48	4.39	4734	5.98	0.38
240	3017083	2.5	2.96 ± 0.70	24.58	7902	4.39	0.38
241	3000059	8.7	1.78 ± 0.92	3.33	4504	5.58	0.36
242	3009191	4.4	0.77 ± 0.28	0.54	4000	5.60	0.32
243	3010225	2.4	1.66 ± 0.83	6.14	4553	4.01	0.31
244	3010757	4.1	1.51 ± 0.90	2.50	4373	6.29	0.33
245	3014085	5.3	1.22 ± 0.80	0.84	4191	7.52	0.36
246	3014322	9.9	2.10 ± 0.94	1.06	4343	10.96	0.35
247	3018233	8.3	2.71 ± 1.03	5.06	4762	5.64	0.33
248	3008088	14.3	2.96 ± 0.29	17.99	5535	5.24	0.30
249	3013836	7.5	0.31 ± 0.36	0.35	3387	3.88	0.30
250	3003917	6.7	0.61 ± 0.47	0.41	3853	5.27	0.38
251	3003210	9.4	1.89 ± 0.84	0.59	4302	10.56	0.38
252	3019106	7.1	1.34 ± 0.75	3.48	4373	4.90	0.38
253	3020113	5.0	1.08 ± 0.78	0.42	4134	7.21	0.32
254	3009426	0.9	0.94 ± 0.42	0.58	4086	6.41	0.32
255	3001242	8.5	1.67 ± 0.69	0.72	4280	9.53	0.30
256	3005266	126.5	5.12 ± 0.52	5.70	9534	7.81	0.38
257	3013157	6.9	1.26 ± 0.57	1.74	4224	7.21	0.38
258	3000755	8.7	1.46 ± 0.93	5.14	4467	4.10	0.37
259	3011370	9.8	0.92 ± 0.35	1.04	4098	6.05	0.35
260	3001337	14.6	3.43 ± 0.86	16.78	8284	5.15	0.31
261	3016004	8.9	2.41 ± 0.85	4.57	4689	5.54	0.31
262	3018501	14.1	1.93 ± 0.88	4.72	4597	4.87	0.31
263	3008989	8.7	1.65 ± 0.83	1.84	4335	8.06	0.38
264	3003499	0.8	0.84 ± 0.31	1.88	4068	5.45	0.31
265	3005159	7.5	1.28 ± 0.86	2.54	4280	6.22	0.35

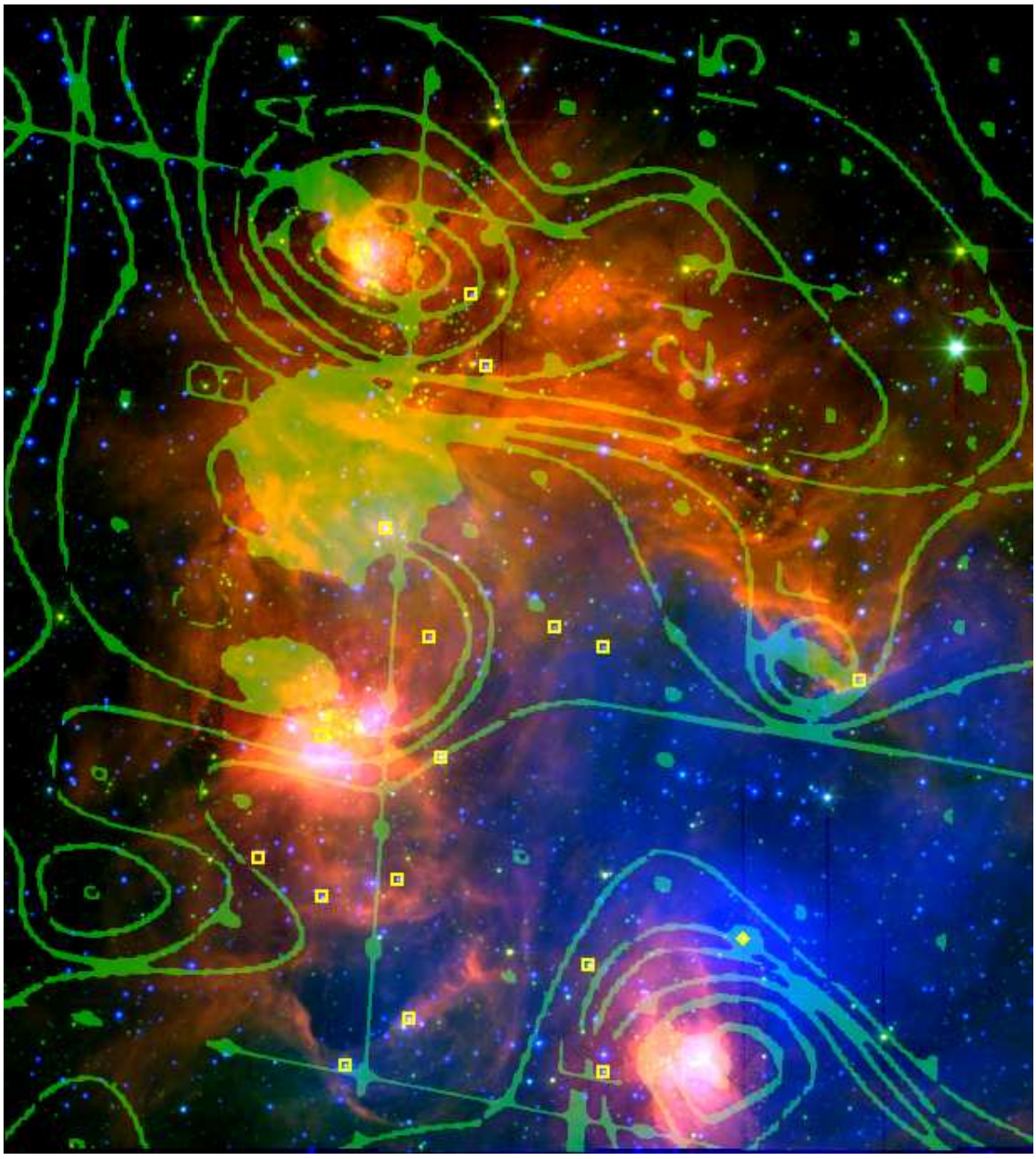

FIG. 15. —3-color Digitized Sky Survey (DSS) optical and *Spitzer* image of NGC 2175, with CO observations from Lada & Wooden overplotted (1978): Red is IRAC 8.0 μm, green is IRAC 4.5 μm, and blue is DSS B-band. Yellow squares mark the locations of known OB stars in the region, with the main ionizing source HD 42088 marked by a yellow diamond.

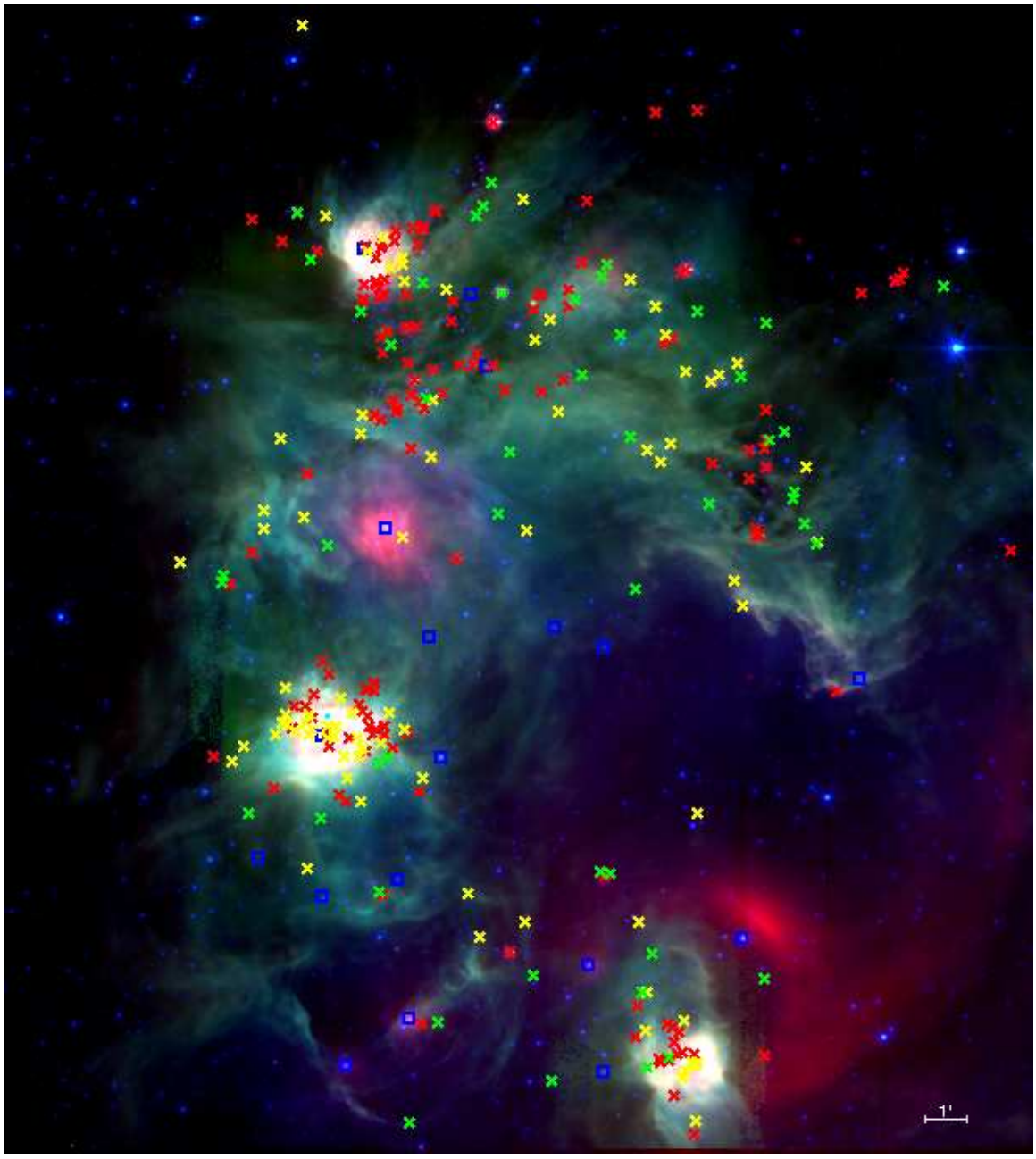

FIG. 16.—3-color *Spitzer* image of NGC 2175: Red is MIPS 24 μm, green is IRAC 8.0 μm, and blue is IRAC 4.5 μm. Red, yellow, and green Xs show locations of the 265 Class 0/I, Class I/II, and Class II protostars, and blue squares mark the locations of known OB stars in the region.

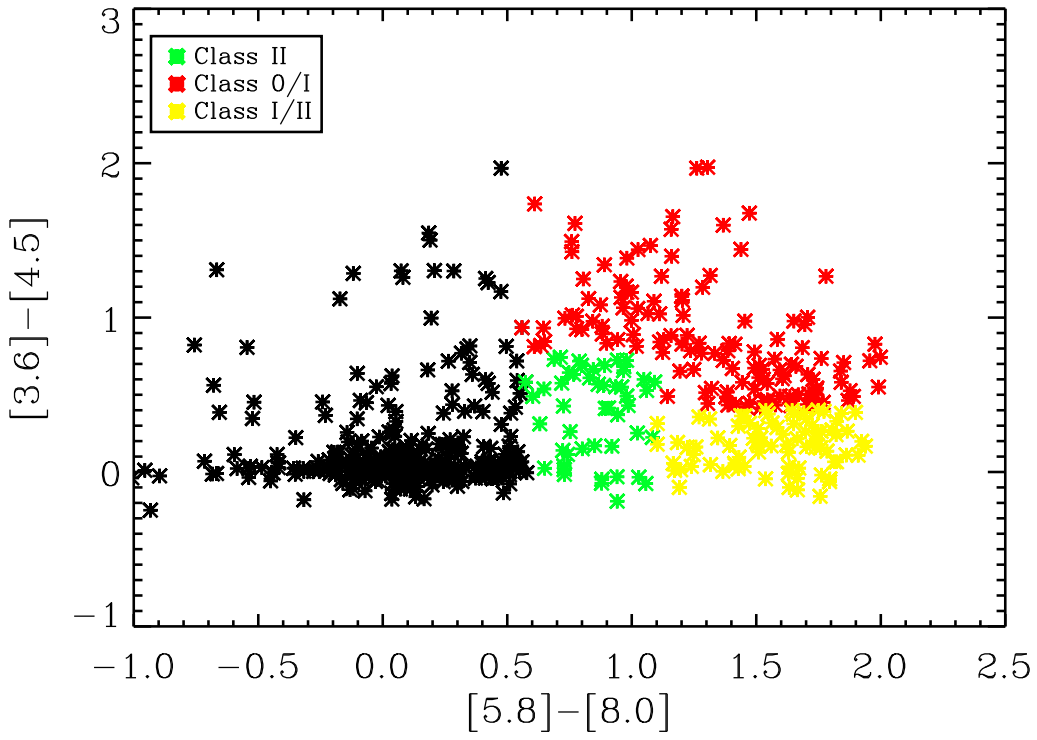

FIG. 17.—IRAC color-color diagram for NGC 2175, showing YSO classification of IRAC detected sources. Color criteria taken from Allen et al. (2004), and Whitney et al. (2003 & 2004b).

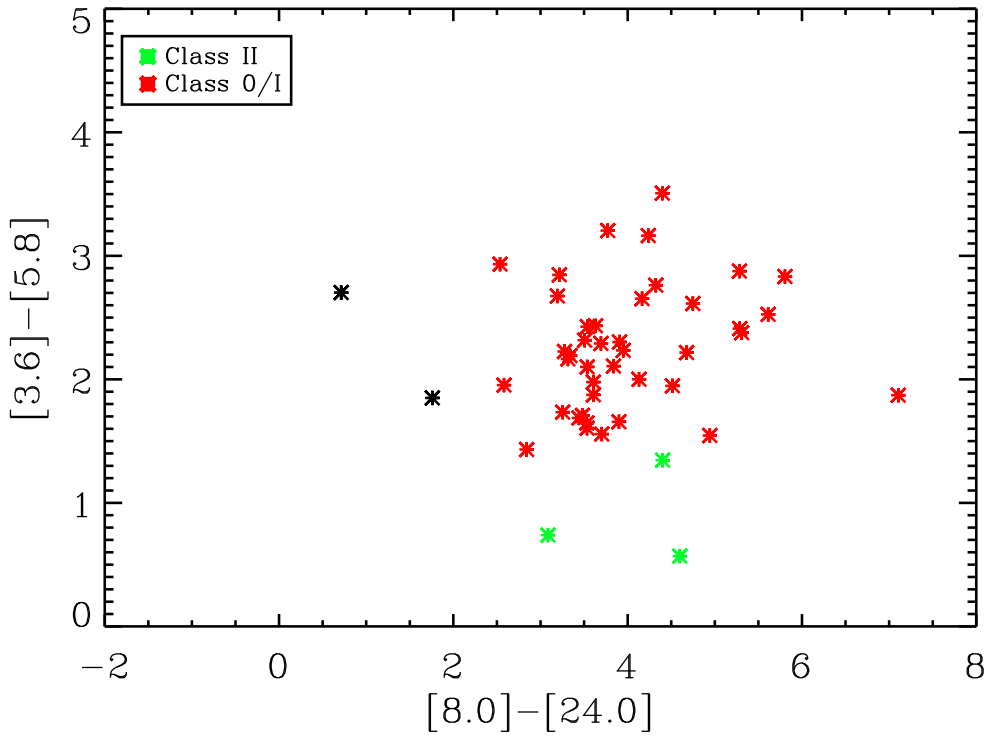

FIG. 18.—IRAC and MIPS color-color diagram for NGC 2175, showing YSO classification of the MIPS 24 μm detected sources. Color criteria taken from Whitney et al. (2003 & 2004b) and Reach et al. (2004).

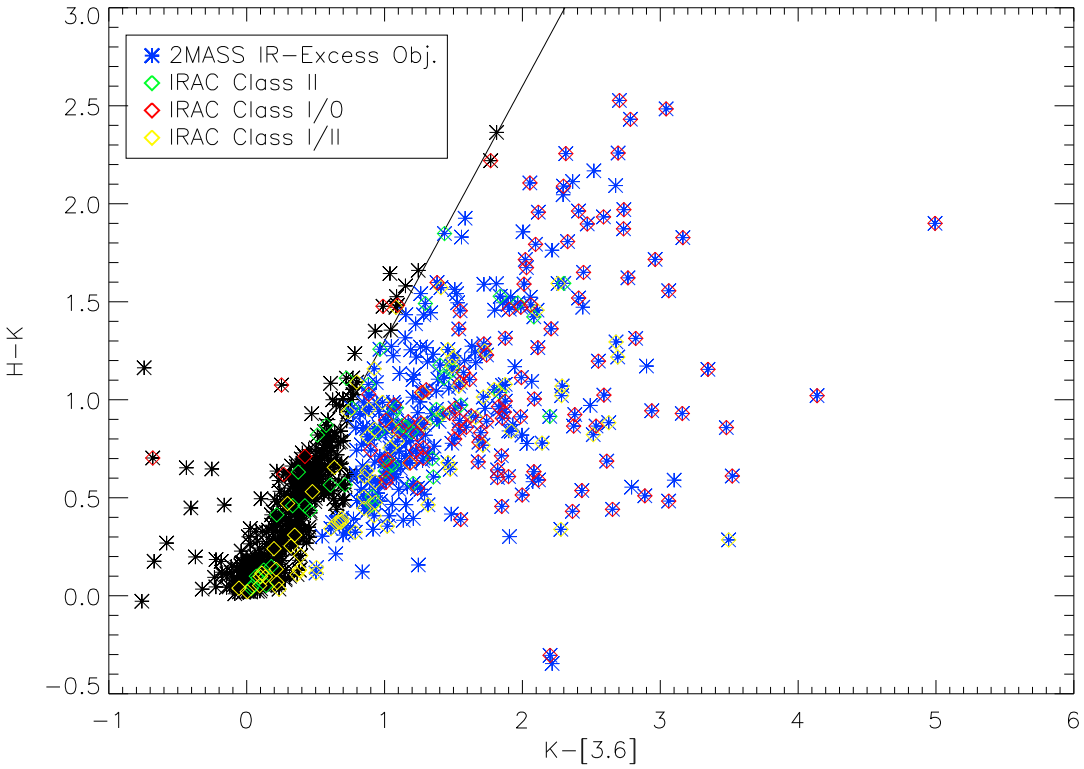

FIG. 19.—2MASS & *Spitzer* color-color diagram of the detected 2MASS sources in NGC 2175. Sources to the right of the reddening vector, which has a slope equal to 1.3, are sources with an infrared excess in the NIR. 191 out of the 346 sources with a 2MASS NIR-excess correspond to a *Spitzer* selected YSO candidate.

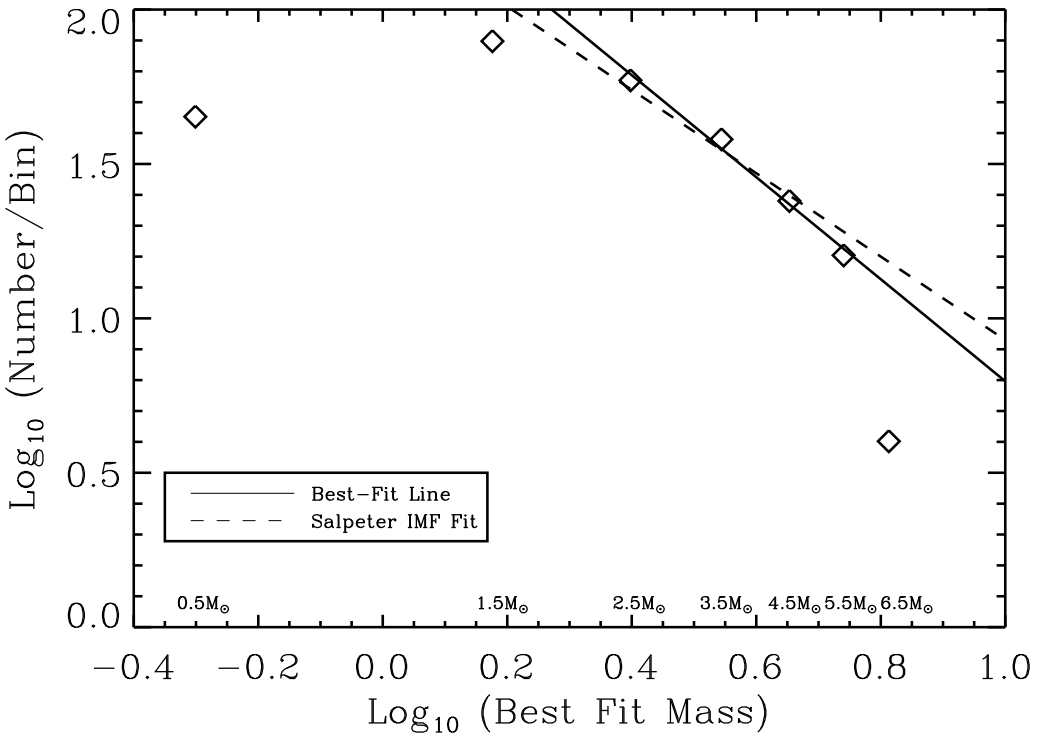

FIG. 20.—Mass distribution function for YSOs in NGC 2175. The solid line is the best-fit to our data, and corresponds to a slope of -1.65. The dashed line is for a Salpeter (1955) IMF with a slope of -1.35. Both lines were fit to the higher mass bins, where our sample is assumed to be complete.

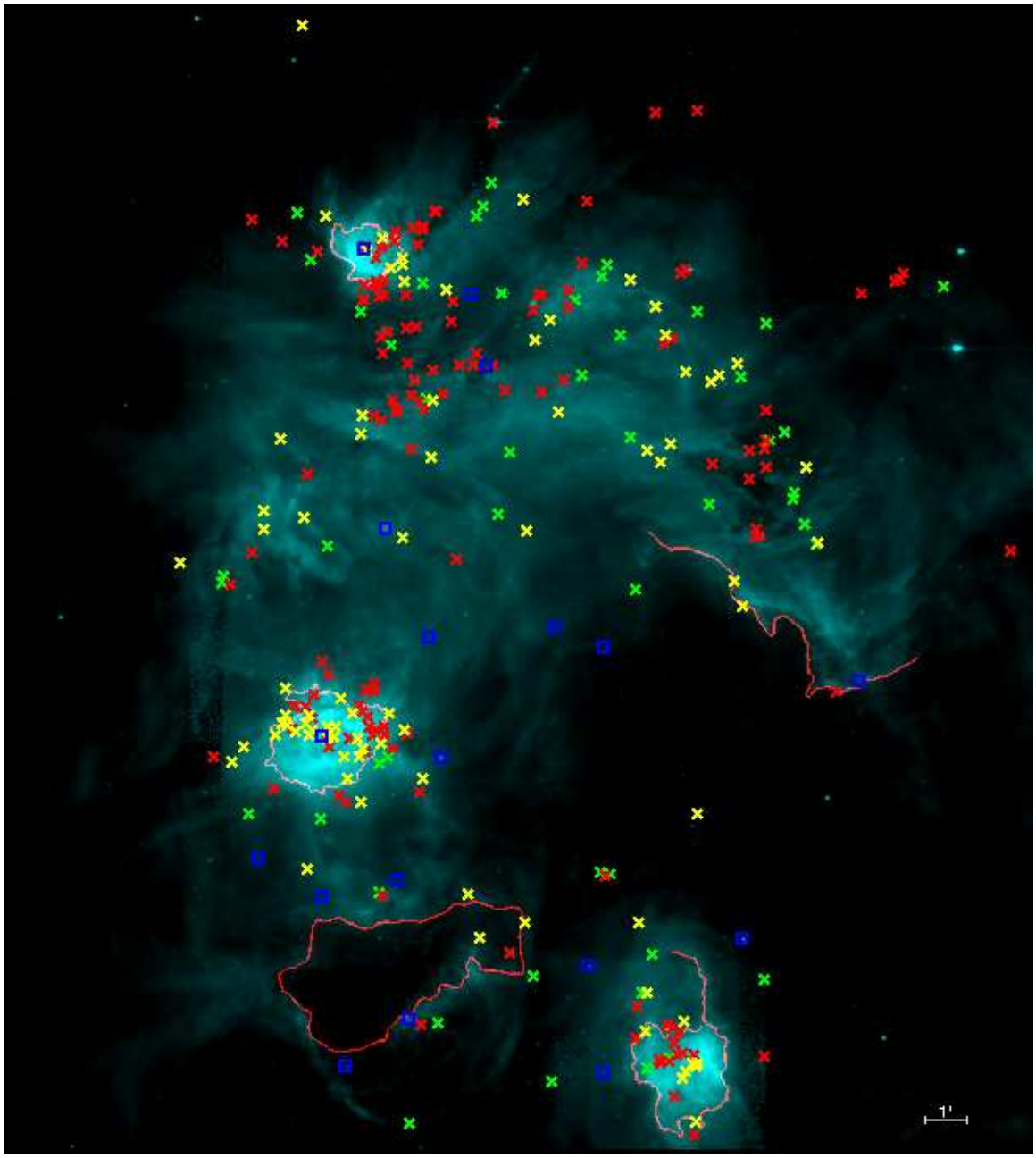

FIG. 21.—Locations of identified ionization fronts in NGC 2175, with the same scale as in Figure 16. Identified ionization fronts are outlined in red and are over-plotted on the IRAC 8.0 μm image. Red, yellow, and green Xs show locations of Class 0/I, Class I/II, and Class II protostars, and blue squares mark the locations of known OB stars in the region.

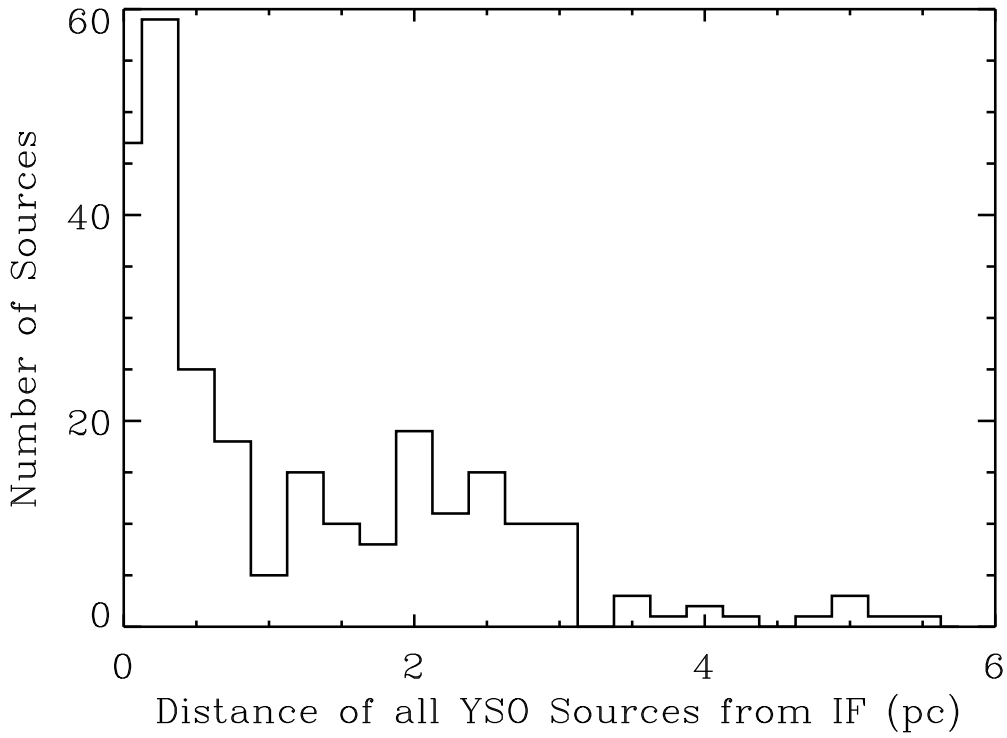

FIG. 22.—Distance distribution of YSOs in NGC 2175 from the nearest ionization front.

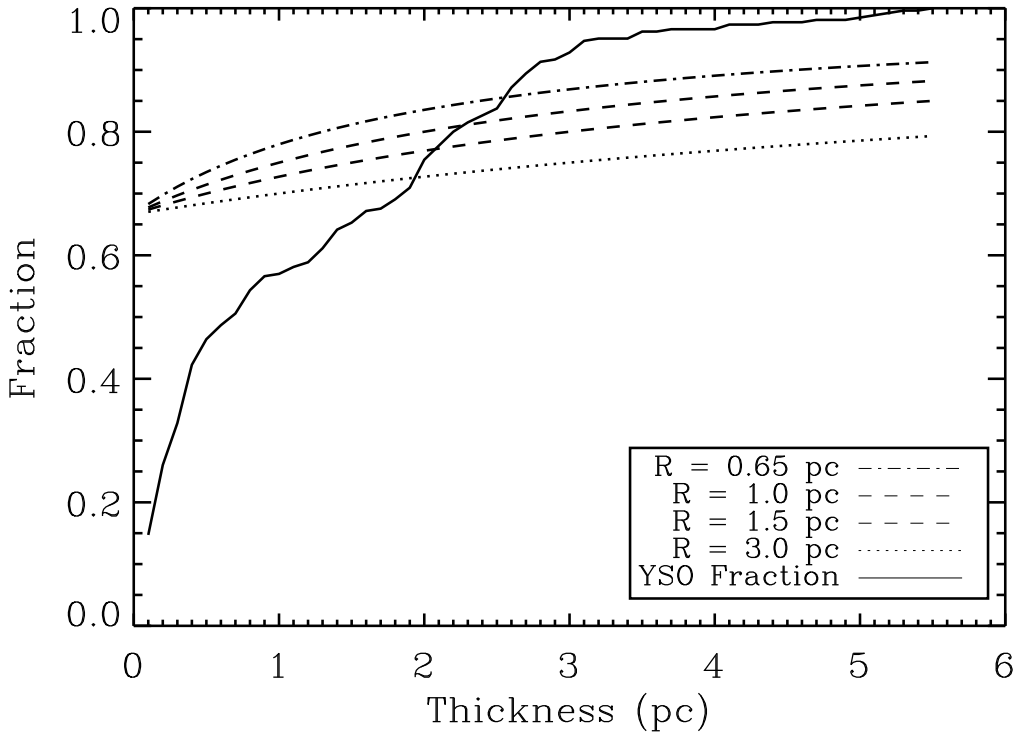

FIG. 23. —A simplified 3D hemispherical model of an ionization front is used to determine the expected number of observed sources that would be seen within a given layer thickness when viewed in projection. The fraction of expected sources observed within a given thickness distribution from an ionization front, with ionization fronts centered at 0.65, 1.0, 1.5, and 3 pc away from an OB star, are shown by dashed lines. The measured distribution of YSOs in NGC 2175 is shown by the solid line. The expected distributions and the observed distribution cross between 2 - 2.6 pc, indicating that the actual distribution of YSOs in NGC 2175 is a population of sources that is concentrated within a layer 2.6 pc or less from the nearest ionization front.

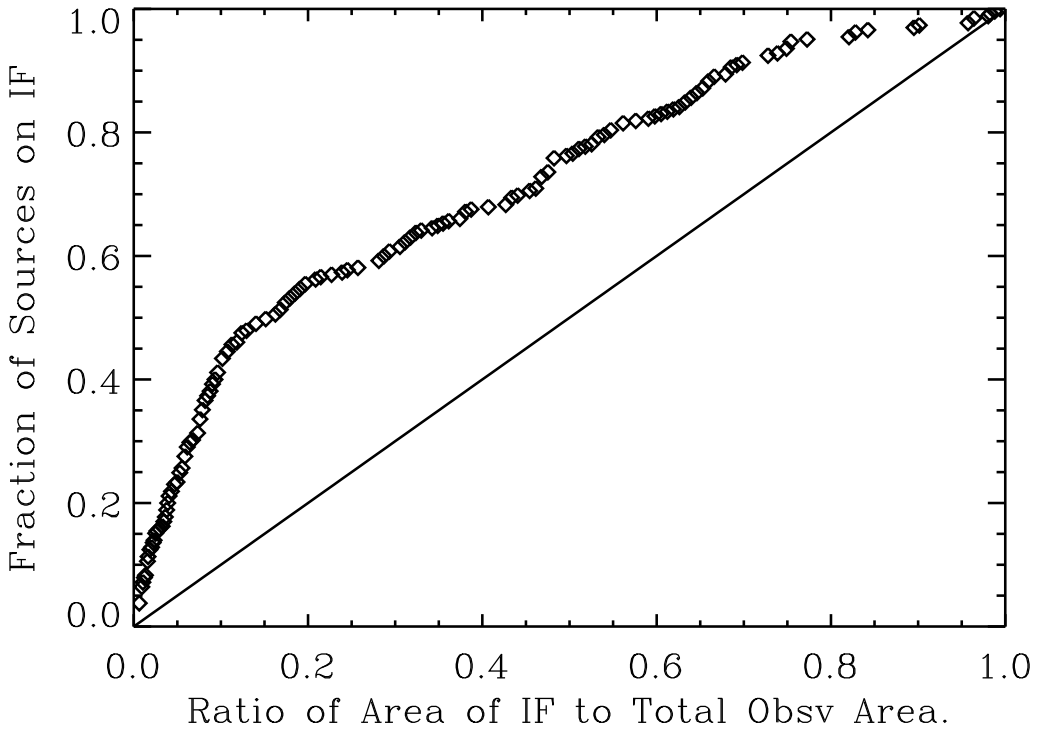

FIG. 24.—Cummulative fractional number of YSO sources in NGC 2175 located on the edge of an ionization front (IF) vs fractional area of the edges, compared to the total observational area. The fraction of the survey area around the ionization front edges is measured at different distances, and the number of YSOs located within that distance were counted. A line with slope equal to one is overplotted. For a random distribution of sources we would expect to see a one-to-one relation between fraction of YSOs on within a given distance distribution of an IF and the fraction of the total survey area within that distance of an IF. However, the fraction of YSOs is always greater (above the line) than the fractional area, therefore this is not a random distribution of sources.

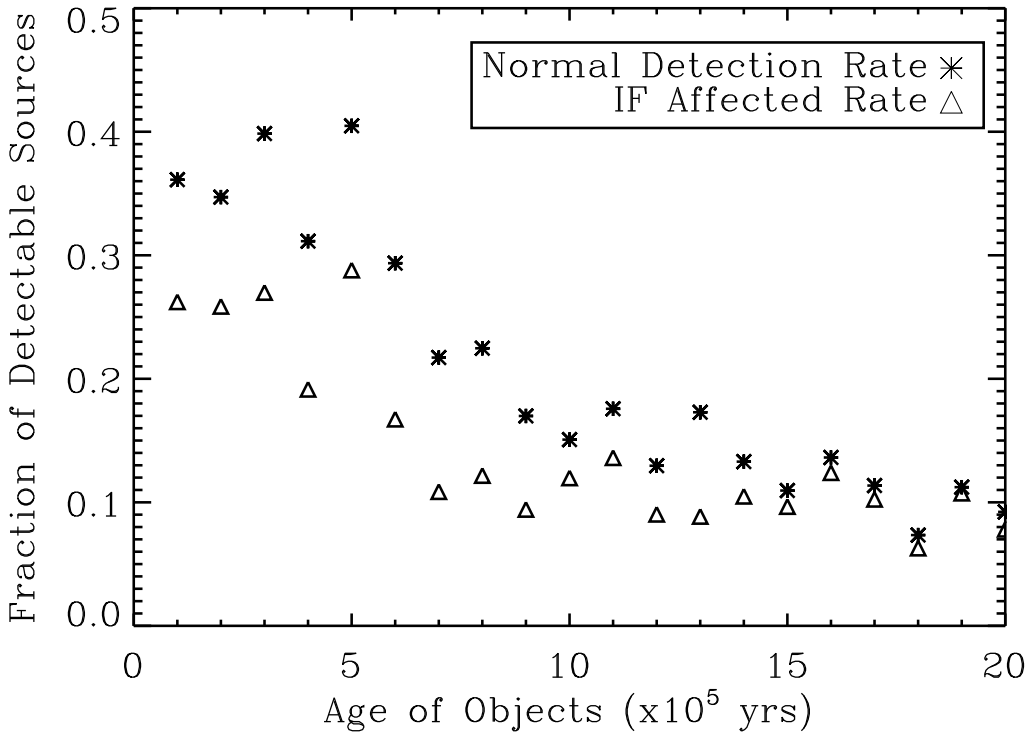

FIG. 25.—The fraction of detectable YSOs vs. age of the object in NGC 2175. A population of stars given by the MF from Equation 8 and a constant SFR (value equal to the calculated SFR from Equation 11) was aged over timesteps of 10^5 yr. The fraction of detectable sources based on our flux limits was calculated at each timestep, the normal detection rate is shown by the asterisk symbols. The detection rate was also calculated for sources uncovered by a passing ionization front. Disk erosion was assumed using models from Johnstone et al. (1998). The ionization front affected detection rate with object age is shown by the triangles. The data show that the best age range to detect the YSOs is around a few$\times 10^5$ yr.

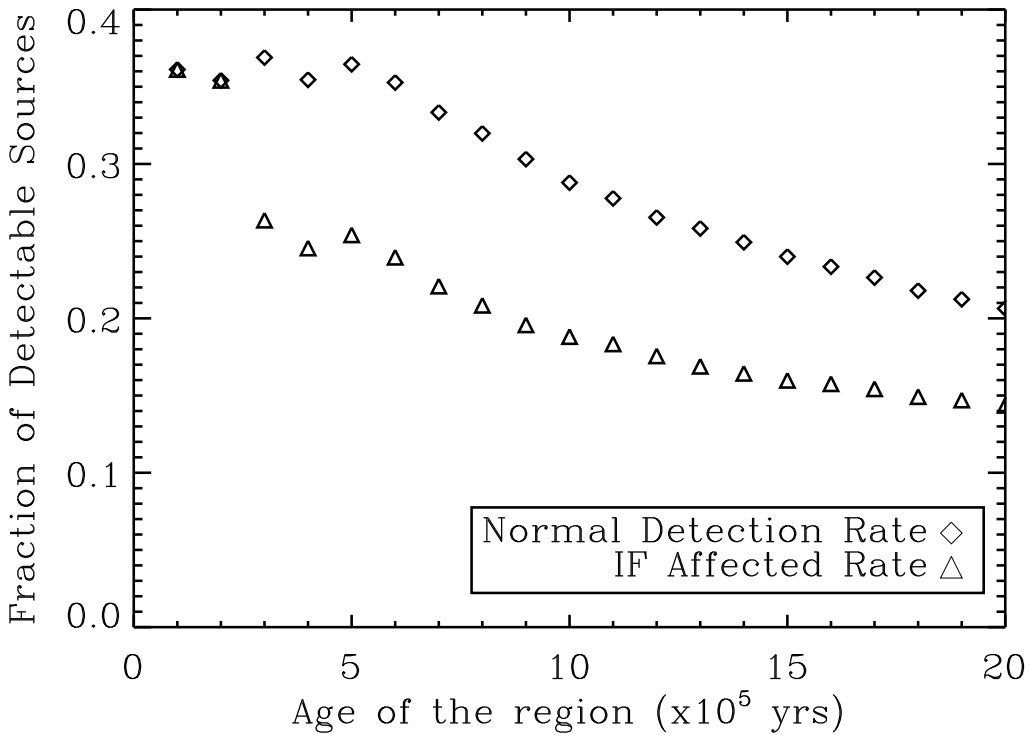

FIG. 26.—The fraction of detectable sources vs. age of the region, using the same methods as described for Figure 25. The normal detection fraction is shown by the asterisk symbols and the ionization affected fractions are shown by the triangles. The detection rate drops to between 15 - 20% by 2 Myr.

4. *SPITZER* OBSERVATIONS OF THE H II REGION NGC 3324

4.1. Outline

In this chapter we continue our analysis of star formation in individual H II region environments using *Spitzer* mid-IR data for NGC 3324. We present IRAC (3.6, 4.5, 5.8, and 8.0 μm) and MIPS 24 μm maps. In this region, 77 sources were identified to have a color excess in their mid-IR colors, and these sources were confirmed as likely protostellar objects by using a YSO SED fitter from Robitaille et al. (2007). The distribution of these YSOs was studied in multiple ways, and from the distribution of the YSOs and best-fit physical parameters we conclude that triggered low-mass star formation is occurring at a rate of 34 - 57% in NGC 3324.

4.2. Introduction

As previously discussed in Chapters 1, 2 and 3, there is ongoing debate about how low-mass star formation proceeds in regions dominated by massive stars. Using *Spitzer* data from two other H II regions (NGC 2467 and NGC 2175), we have shown that there does appear to be differences in where and how low-mass stars form in these types of environments as opposed to smaller isolated regions like Taurus-Auriga. We continue this type of analysis on the cluster of stars, NGC 3324, and its associated H II region.

NGC 3324 is a cluster of stars dominated by two O stars, HD 92206AB (O6.5 Vn) and HD 92206C (O8.5 Vp; Maiz-Apellaniz et al. 2004). It is surrounded by the H II region GUM 31, which has been created by the massive OB stars of the cluster. NGC 3324 was first studied by Moffat & Vogt (1975), and they identified 12 stars located within $1'$ of the cluster core as cluster members. They also noted strong H II emission in the region as evidence of the youth of the cluster. Moffat & Vogt

(1975) derived a distance of 3.3 kpc to the cluster. A further analysis of the cluster by Claria (1977) revealed even more cluster members using UBV photometry of the inner 6′ of the cluster. Claria (1977) gives a distance of 3.1 kpc to the cluster, in good agreement with Moffat & Vogt. An approximate age of 2.2 Myr and an average color excess of E(B-V) equal to 0.47 ± 0.08 were determined by Claria.

A more recent study of the region by Carraro et al. (2001) used UBVRI photometry on ∼1000 stars in the region. They determined an age of the cluster to be between 2 - 3 Myr, which could be an upper limit due to the possibility of the A0 I star, HD 92207, not being a cluster member. They also quote a distance of 3.0 ± 0.1 kpc, which we use in our further analysis of the region. Carraro et al. (2001) identify a number of pre-MS stars, and cite these as more evidence of the youth of the region. De Marco et al. (2006) used archival *HST* data to study a number of H II regions, including NGC 2467 and NGC 3324. However, in NGC 3324, the cavity walls of the H II region appear very smooth as seen in both optical DSS images, and *HST* WFPC-2 and ACS images. They comment that they only see a very few small protrusions and state that the space immediately behind the ionization front is very smooth with no discernible features found. They do not see any evidence of fragments being associated with the ionization front as was the case with NGC 2467.

Finally, Cappa et al. (2008) have done a very recent study of NGC 3324 using a number of different observations: neutral H I 21-cm line data, radio continuum images at 0.84, 2.4, and 4.9 GHz, ^{12}CO observations, and infrared data using IRAS and MSX. The H I 21-cm line image reveals a H I shell that surrounds the H II region.

This H I shell has a radius of approximately 10 pc and a neutral mass was derived by Cappa et al. (2008) of 1500 $M_{\odot}$. They also claim that the mass of the associated molecular gas is 1.1×10^{5} $M_{\odot}$, from CO data. The CO contours can be seen right along the edge of the cavity, tracing out the molecular gas. Using the 4.9 GHz radio data, Cappa et al. (2008) derive an electron density in the region of 33 ± 3 cm^{-3}. They have also identified ∼47 candidate protostellar objects using 2MASS, Midcourse Space Experiment (MSX), and IRAS infrared data. These objects appear to be projected onto the molecular envelope, and they conclude that it is probable that H II region expansion is responsible for triggered star formation in the identified molecular shell.

Using the *Spitzer* data we attempt to identify even more YSOs in order to determine the total distribution of these objects in NGC 3324. Cappa et al. (2008) claim that the H II region expansion is leading to the "Collect and Collapse" method of triggered star formation in NGC 3324. However, we are interested in also testing whether or not triggering is occurring right along the edge of the molecular cloud due to input of the large amount of UV flux from the OB stars. Although the cavity and the ionization fronts appear to be very smooth as evidenced by the *HST* observations, this does provide for a very useful identification of the ionization front edge along with the photodissociation region (PDR). NGC 3324 is another excellent candidate for study of low-mass star formation, as the region is very young and at a relatively nearby distance. We will compare our results with those of other studies,

specifically recent work done by Cappa et al. (2008), and to our own studies of other H II regions presented in this dissertation.

4.3. Observations and Data Reduction

The data for NGC 3324 were obtained by the *Spitzer Space Telescope* with IRAC (Fazio et al. 2004) and MIPS (Rieke et al. 2004) during Cycle #2 as part of the *Spitzer* program PID 20726. We obtained data in all four IRAC wavelength bands and the MIPS 24 μm band. The total mosaicked image size for NGC 3324 is $\sim$26.′8 $\times$ 29.′5 for IRAC and $\sim$30.′9 $\times$ 31.′4 for MIPS. The IRAC data for each frame were exposed for 12 seconds, and the field was dithered five times resulting in a total exposure time of 60 seconds per pixel. For the 24 μm data, each frame was 10 seconds long with 2 cycles, resulting in a total exposure time of 280 seconds. The MIPS data were calibrated by the *Spitzer* Science Center (SSC) pipeline version S14.4.0, and the IRAC data were calibrated with the SSC pipeline version S14.0.0.

IRAC mosaicked images were re-made in each band from the BCD images, using the MOPEX software program, version 030106, in order to reject cosmic rays and remove other detector artifacts. The SSC pipeline version of the MIPS 24 μm data was used in our analysis. Point sources were extracted in each band using the same methods as described in §2.3 and §3.3. The same aperture sizes were used in the IDL task *aper.pro*, in order to extract the sources and measure the flux of each source. Aperture corrections and zero-magnitude flux values were applied in order to convert fluxes into magnitudes (see §2.3 and §3.3 for specific correction values in each band).

4.4 Results

410 point sources were identified in all four IRAC bands, along with 43 MIPS 24 μm point sources. Two *Spitzer* color-color plots were generated along with a 2MASS and *Spitzer* near-IR color-color plot in order to identify candidate YSOs. Initially, 85 YSOs were selected in the IRAC color-color plot, and 32 objects had a color excess in the MIPS and IRAC color-color plot. However, once these sources were checked against contamination from AGB stars and extragalactic sources that could have the same colors, 10 IRAC Class II and two MIPS Class II YSOs were discarded as possible AGB stars, along with one MIPS class I/0 object thrown out as a possible extragalactic source. Table 2 lists the color criteria used for both the selection of the protostellar candidates and the criteria for the contaminant sources. The only difference in the selection of objects for NGC 3324 from Table 2 is that the MIPS color criteria for both Class I and Class II extends from 1.8 - 12.0 in the [8.0]-[24] color. After removal of the possible contaminants, 75 IRAC YSOs and 29 MIPS YSOs remained, with all but two MIPS YSOs overlapping with an IRAC YSO. This resulted in a total of 77 possible protostellar candidates identified in NGC 3324; 34 Class I/0, 16 Class I/II, and 27 Class II YSOs. The position, classification, and *Spitzer* magnitudes and errors for the 77 candidate YSOs in NGC 3324 are listed in Table 7.

Figure 27 is a three-color *Spitzer* image of the region with the 77 identified YSOs overplotted along with the two ionizing O stars marked by X's; the IRAC 4.5 μm channel is in blue, the IRAC 8.0 μm channel is in green, and the MIPS 24 μm

channel is in red. The IRAC YSOs are marked with red, yellow, and green squares for the Class I/O, Class I/II, and Class II YSOs, respectively. The MIPS Class I/0 and Class II YSOs are marked by red and green X's. Bright emission can be seen in the 24μm band in the interior of the H II region cavity, which is likely due to thermal dust emission.

Figures 28 and 29 are plots of the *Spitzer* IRAC and IRAC/MIPS color-color diagrams. In Figure 28, the 75 candidate IRAC YSOs are labeled by the same color scheme as in Figure 26. The 32 objects with an excess in their [8.0]-[24] color are shown in Figure 29, with red and green asterisks corresponding to the Class I/0 and Class II sources respectively. The IRAC color criteria are taken from Megeath et al. (2004) and are based on models from Allen et al. (2004) and Whitney et al. (2003a & 2004b), and the MIPS 24 μm candidate YSO sources are based on color criteria from Reach et al. (2004). See §2.4 for more details on the models that make up each of these types of objects.

The final color-color plot presented here is a 2MASS and *Spitzer* color-color diagram shown in Figure 30. We used the 2MASS PSC to find 2MASS counterparts to the *Spitzer* detected sources. A majority of the *Spitzer* sources had a 2MASS counterpart. In Figure 30, the H-K color is plotted vs. K-[3.6] color, with the reddening vector due to interstellar extinction overplotted. This line has slope of 1.3 as defined by Tapia (1981). 45 2MASS point sources are located to the right of this line with a near-IR color excess, indicating likely protostellar objects. Of these 45 sources with a 2MASS color excess, 37 overlap with a *Spitzer* YSO. It is also interesting to note that

again we see that the *Spitzer* Class I/0 YSOs generally have the reddest colors in the 2MASS color plane and all of the Class I/0 YSOs with a detected 2MASS counterpart show an excess in both their near-IR and mid-IR colors. In contrast, about half of both the *Spitzer* Class I/II and Class II YSOs overlap with a 2MASS source that has a measured near-IR color excess.

4.5. Discussion

4.5.1. *SED Model Fitting of YSOs*

As in both §2.5.1 and §3.5.1, we are interested in determining the physical properties of the candidate YSOs and at the same time helping to confirm the likelihood of the sources being actual protostellar objects. The YSO online SED fitter by Robitaille et al. (2007) was used for all 77 candidate YSOs. The IRAC, 2MASS, and MIPS 24μm band magnitudes, when available, were used as input into the SED fitter. A distance estimate of 3.0 kpc and an average extinction to the region of A_V equal to 1.5 mag, taken from Carraro et al. (2001), were used. If a candidate YSO has a better stellar photospheric fit than any YSO SED fit, then it was thrown out as possible YSO. We also discarded any candidate YSOs that have a large χ^2 value (total χ^2 greater than 100 or χ^2 per data point greater than 12). None of the 77 candidate YSOs were best-fit by a stellar photospheric model alone. The best-fit masses range from 0.4 - 7.0 $M_\odot$, and the best-fit ages range from 10^3 - 2×10^6 yr. Nine YSOs had a best-fit mass less than 1 $M_\odot$ and another 12 objects had a best-fit mass between 1 - 2 $M_\odot$. This represents more than one-quarter of the YSO sample, and while this is a smaller fraction than was found in NGC 2175, it still demonstrates that we are

detecting newly forming low-mass stars in NGC 3324. The best-fit model parameters for the YSOs in NGC 3324 are listed in Table 8.

4.5.2. *Mass Distribution of YSOs and Completeness*

In NGC 3324, the 77 YSOs were grouped into seven mass bins, and each mass bin is equally spaced having a range in mass of 1 $M_{\odot}$. The seven mass bins are centered at 0.5, 1.5, 2.5, 3.5, 4.5, 5.5, and 6.5 $M_{\odot}$. A least squares fit was performed on the data running through the two highest mass bins, and a line of best-fit was derived. The mass function for the YSOs in NGC 3324 has the same form as shown by Equation 1. Figure 31 is a plot of log N versus log Best-Fit Mass for the 77 YSOs. The best-fit line in Figure 31 has a slope of 1.2, as compared with a Salpeter (1955) slope of 1.35. The data here show a shallower slope than that fit by a Salpeter mass distribution. This mass distribution is also shallower than those measured for either NGC 2467 or NGC 2175. Given the best-fit slope of 1.2, the MF spectral index, Γ, is 2.2. Therefore the YSO mass distribution function for NGC 3324 has the following form:

$$\frac{dN}{dM} \propto M^{-2.2} \; or \; \frac{dN}{d(\log M)} \propto M^{-1.2}. \tag{13}$$

There are two known O stars as well as 12 known B8-B9 stars in the cluster. We used these stars to estimate the MF normalization constant. The constant calculated from the number of O stars and the constant from the number of B8/B9 stars were in good agreement, resulting in an average value of 230. Therefore the MF for NGC 3324 becomes:

$$N_{tot} = A \int_{M_1}^{M_2} M^{-2.2} dM = 2.3 \times 10^2 \int_{0.1M_\odot}^{40M_\odot} M^{-2.2} dM. \quad (14)$$

This results in a total of 3.0 $\pm$ 0.8 $\times 10^3$ stars (assuming Poisson statistics on the 14 stars used to calculate the normalization constant) between the mass range of 0.1-40 $M_\odot$ in NGC 3324.

Finally, we want to address completeness. From Figure 31, it is obvious that we are not detecting the total population of YSOs in this region. Therefore, we attempt to estimate how complete we are by using the derived IRAC flux limits for this data set and compare this to the number of YSO SED models we should be able to detect. A similar analysis was performed for NGC 2467 and NGC 2175. The three-σ magnitude limits in the IRAC bands for these observations are: 14.4. 13.8, 12.0, and 11.3 for IRAC 3.6, 4.5, 5.8, and 8.0 μm, respectively. We used the model fluxes from Robitaille et al. (2006) and scaled these fluxes to a distance of 3.0 kpc (the assumed distance to NGC 3324). We also used the estimated foreground extinction to the region of A_V equal to 1.5 mag from Carraro et al. (2001) and applied that to the detectable flux limits of the models. We then calculated what fraction of the models we would be able to detect above this limit; this resulted in 45% of the models, therefore we assume that we are approximately 45% complete.

4.5.3. *Spatial Distribution of YSOs in NGC 3324*

We have shown in Chapters 2 and 3 that YSOs are likely to form at the edges of H II regions in compressed molecular gas. Cappa et al. (2008) have also specifically shown that there is a population of young protostars found in the molecular shell of

gas surrounding the H II region in NGC 3324. Figure 32 is an image of the *Spitzer* 8.0 μm band with the detected ionization fronts overplotted in red, along with the candidate YSOs (red, yellow, and green squares and X's) and two O stars (blue X's) overplotted. We identified five possible ionization fronts in this region using the same method of smoothing the IRAC ch3 and ch4 images and running an edge detection routine; see §2.5.4.1 for more details. In Figure 32, the main ionization front surrounding the H II region cavity can easily be seen. We have identified it as two separate ionization fronts, although there may likely be an ionization front running around the entire circumference of the cavity. However, in some parts on the edge of the cavity the emission from the PDR, as seen in the 8.0 μm emission, is more patchy and a clear edge is not as easily defined. We also detected a few other edges in this image, one which appears to be surrounding a small column of gas and is reminiscent of a small elephant trunk, similar to those seen in M16 (Hester et al. 1996), but on a smaller scale. Two others are around other dense clumps of gas that are more embedded in the molecular shell of material. A large fraction of YSOs appear to be located very near to the edge of the molecular gas and H II region cavity, while only a few YSOs appear to be located in the interior of the H II region. Other YSOs appear to be located farther out in the molecular material, but as we will later discuss, some of them may be located closer to an ionization front than they appear to be.

In Figure 33, we plot the distribution of the distance of YSOs from the nearest ionization front. There is a peak in the histogram of sources at a distance of approximately 0.2 - 0.5 pc, which would correspond to time from the ionization front of

approximately 1 - 2.5×10^5 yr, assuming an ionization front speed of 2 km s^{-1} (Osterbrock 1989). In total, there are 31 YSOs that are measured to be within a projected distance of 1 pc or less from an ionization front. While this only amounts to 40% of the total number of detected YSOs, we will show in the next section that this is likely to be a larger percentage due to some YSOs being located on the back of the ionization front (that is, viewed face-on to our line of sight).

We now want to compare the distribution of our detected YSOs to that seen by Cappa et al. (2008). Cappa et al. (2008) use 2MASS, MSX, and IRAS point source catalogs to identify possible sources with infrared excesses in NGC 3324. They found 47 candidate YSOs in their survey region; 38 of these YSOs fall within the *Spitzer* FOV and 13 of them correspond to a *Spitzer* candidate YSO. In Figure 34 the IRAC 5.8 μm band is shown along with the locations of the candidate YSOs detected in the *Spitzer* survey (red, green, and yellow squares) and the Cappa candidate YSOs (blue X's). A similar overall distribution can be seen between the two datasets, although the overlap between the two is not extremely well correlated. This is likely due to differences in selection criteria and resolution between all of the different source catalogs. Cappa et al. note that most of the objects detected with MSX are likely massive YSOs, as well as three YSOs that are sources of known compact H II regions. In a few bright emission areas, Cappa et al. detect some sources that we do not, and this is likely due to the nebular emission being too high in the 5.8 and 8.0 μm bands for us to accurately detect any true point sources there. They could detect some YSO candidates in these locations from the 2MASS catalog, which at shorter wavelengths

will have less bright nebular emission than in the longer wavelength IRAC channels, or they are the compact H II regions detected with their MSX criteria. Another difference between the two distributions is that Cappa et al. detect a few more candidates in the middle to the H II region as compared to us. They also do not detect as many as we do right along the main sharp ionization front edge. Even with these differences, and the small number of overlapping sources, the overall distributions appear somewhat similar, showing evidence of the youth of the region, and evidence of clustering of YSOs around the compressed edges of the molecular gas.

4.5.4 *Statistical Distribution Tests*

The two known O stars in this region are located at the center of the H II region cavity. They are estimated to be at an average distance of 5 pc from the edge of the ionization fronts. As has been discussed in chapters 2 and 3, we cannot detect ionization fronts that are located face-on to our line of sight, but it is expected that the main ionization front would moving outwards into a volume of space and a simplified model of this ionization front is a spherical bowl. The base of the bowl is the part of the ionization front we are unable to detect. Therefore, we attempt to determine what fraction of YSOs may still be located within 1 pc or less of an ionization front, by calculating the ratio of the detectable volume of the ionization front to the total volume the ionization front encompasses. More details of this process are in explained in §2.5.4.2 an §3.5.3.2.

Figure 35 is a plot of the predicted distribution of YSOs from an ionization volume that is 4 - 6 pc away from the ionizing sources, along with the measured

distance distribution of YSOs in NGC 3324. On the x-axis we plot the thickness of the distribution from the ionization front edge. On the y-axis we plot the fraction of measured YSOs (solid line) and predicted fractions (dashed lines) falling within the given distance to an ionization front. The measured YSO fraction crosses the model predictions at a thickness slightly greater than 2.5 pc. Therefore, we conclude that the YSO population in NGC 3324 is a population of sources that is concentrated within a layer that is 2.5 pc or less from the ionization front. This is a similar result that was seen for NGC 2175, where the YSOs appeared to be concentrated within a layer 2.6 pc or less from the nearest ionization front. Assuming that this is an accurate representation of the distribution of YSOs in NGC 3324, we can also determine from Figure 34 that approximately two-thirds (67%) of the YSOs are likely to be located within 1 pc or less from an ionization front, as compared to our measured value of 40%.

In Figure 36, we show the results of the Poisson probability function for the YSOs being randomly distributed using Equation 4. If this is a random distribution of sources then we would expect that the fraction of YSOs falling on the ionization fronts should equal the ratio of the area of the ionization fronts to the total survey area. However, this is not a random distribution, as Figure 36 shows that the probability of a random distribution of YSOs averages to $\sim 10^{-3}$ (0.1% chance). By the time all of the 77 YSOs fall on an ionization front, the probability of this being a random distribution has increased, however this is expected as there are a handful of detected YSOs that are located at larger distances from an ionization front, and by the time

they are all included in the area of an ionization front this area has grown to encompass a good fraction of the total survey area. Thus, Figure 36 shows that the distribution of YSOs is likely not a random distribution, similar to what has been shown for the other H II regions in this thesis.

4.5.5. *Estimates of Triggering and Star Formation Rates*

In order to calculate a rate of triggering in NGC 3324, we need to first estimate the total star formation rate in this region. A few assumptions go into this calculation, including the use of the calculated mass function from the mass distribution plot of the YSOs in Figure 31. This mass function is shallower than a Salpeter (1955) mass function and it is also shallower than the two previous mass functions we calculated for NGC 2467 and NGC 2175 in Chapters 2 and 3. However, the mass function calculated here is similar to other studies of star forming regions and young clusters where the mass distribution is typically shallower than the Salpeter (1955) IMF. Another assumption implicit in the mass function calculation is the calculation of the normalization constant. We use known numbers of massive OB stars to determine the normalization constant, and there is an uncertainty in this constant as was discussed in §4.5.2. Taking all of this into account, we estimate a mass in stars of ∼1300 $M_\odot$, as shown in Equation 15. The assumed age of the region, 2 Myr, is then used to determine the average SFR in NGC 3324, shown by Equation 16.

$$M_{tot} = \int_0^N M dN = A \int_{M_1}^{M_2} M^{-1.2} dM = 2.3 \times 10^2 \int_{0.1M_\odot}^{40M_\odot} M^{-1.2} dM \sim 1300\,\mathrm{M}_\odot \tag{15}$$

$$Average\ SFR = \frac{1300\,\mathrm{M}_\odot}{2Myr} = 6.5 \times 10^{-4}\ \mathrm{M}_\odot\,\mathrm{yr}^{-1} \quad (16)$$

The average SFR calculated in NGC 3324 is slightly lower than the rates calculated for NGC 2467 and NGC 2175 (1.75×10^{-3} and 2.0×10^{-3} $M_\odot$ yr^{-1}, respectively). This lower SFR is due to assuming a shallower mass function than in the other two regions, resulting in a smaller total mass calculated for the region, but again this mass function is similar to what has been calculated in other star forming regions. In order to estimate a triggered star formation rate, a total number of triggered stars needs to be determined. Figure 31 clearly shows that we are missing a large portion of the lowest mass YSOs in our detections, therefore to estimate what the detection ability is for NGC 3324 we use the same method as was shown in §2.5.5 and §3.5.4. For NGC 2467 and NGC 2175, we have shown that the detection rate of protostellar objects changes with age of the individual object and elapsed age of the region. For the two previous regions in this study, the detection rate falls to as low as 15 - 20%. Using the same analysis, we calculate the fraction of YSO SED models that will be detected in an evolving population with a constant SFR given by Equation 16. Figure 37 shows the results of the YSO detection probabilities versus age of the object using the characteristics of the NGC 3324 region. Figure 37 shows that there is a clear peak at 3×10^5 yr for the best age to be able to detect the protostellar objects. This age also corresponds to the average age of the YSOs from the model SED fitting. Figure 38 shows the detection rate versus elapsed age of the region, the rate falls to about 21% by 2 Myr, the approximate age of NGC 3324. We have also calculated how erosion

of protostellar disks due to passing ionization fronts would affect the detectability of individual YSOs. These data are also shown in Figures 37 and 38, and the detection ability falls to about 16% when this effect is included.

Using the data from Figures 37 and 38, we can estimate a triggered star formation rate. Figure 37 along with the SED model fitting has shown that the YSOs have average ages of 3×10^5 yr and the data from Figure 38 have shown that the current detection rate of YSOs in NGC 3324 is at the 20% level. We have also shown that while not all of the YSOs are within 1 pc or less of an ionization front, we detected 40% of the YSOs within a projected distance of 1 pc, and it is likely that as much as 67% are actually within this distance and will be influenced by H II region expansion. Therefore, as shown in Equation 17, 40 - 67% (31 - 51) of the detected YSOs are within 1 pc or less of an ionization front, and have an average age of 3 $\times10^5$ yr. This results in 5.2 - 8.5×10^{-4} stars formed per yr that are triggered.

$$\frac{\#\ YSOs}{Avg.Age \times DetectionRate} = \frac{31-51}{(3\times10^5\ \text{yr})\times 0.2} = 5.2-8.5\times10^{-4}\ \text{stars}\,\text{yr}^{-1} \quad (17)$$

Using the calculated MF from Equation 13, this results in a triggered SFR of $\sim$2.2 - 3.7×10^{-4} $M_\odot$ yr^{-1}. Comparing that to our average total SFR in the region, the triggered SFR accounts for 34 - 57% of all of the star formation in NGC 3324. This is an even higher amount than was calculated in NGC 2467 (25-50%), but very similar to the amount calculated for NGC 2175 (38-58%). Again, we are showing that while not all of the low-mass star formation is triggered, triggering does appear to be occurring in NGC 3324 and at a significant rate. It is also interesting to note that

while we have calculated different mass functions for the YSOs in all three H II regions, we are still finding relatively similar rates of triggered star formation.

TABLE 7

SPITZER PHOTOMETRY FOR YSOs IN NGC 3324

Source #	IRAC Class	R.A. J2000	Decl. J2000	[3.6]	[4.5]	[5.8]	[8.0]	[24]
1	I/0	10 36 39.35	-58 27 35.34	11.43 ± 0.03	10.28 ± 0.02	9.40 ± 0.05	8.43 ± 0.04	5.01 ± 0.03
2	I/0	10 36 59.29	-58 24 29.60	11.56 ± 0.03	10.35 ± 0.02	9.61 ± 0.06	8.85 ± 0.06	
3	I/0	10 36 52.17	-58 31 29.80	10.73 ± 0.02	8.60 ± 0.01	7.22 ± 0.01	6.36 ± 0.01	2.67 ± 0.02
4	I/0	10 37 00.62	-58 32 41.21	10.97 ± 0.02	9.68 ± 0.01	8.07 ± 0.02	6.83 ± 0.01	3.13 ± 0.01
5	I/0	10 36 53.76	-58 36 31.19	8.81 ± 0.01	7.96 ± 0.00	6.74 ± 0.01	5.31 ± 0.00	1.23 ± 0.01
6	I/0	10 37 36.32	-58 26 54.68	9.71 ± 0.01	8.77 ± 0.01	7.96 ± 0.02	7.06 ± 0.01	3.74 ± 0.02
7	I/0	10 37 00.17	-58 35 33.95	8.82 ± 0.00	8.03 ± 0.00	7.06 ± 0.01	5.92 ± 0.01	3.35 ± 0.02
8	I/0	10 36 54.03	-58 37 19.63	10.95 ± 0.03	10.15 ± 0.02	8.90 ± 0.05	7.53 ± 0.03	3.83 ± 0.01
9	I/0	10 37 37.16	-58 27 39.73	10.77 ± 0.02	9.83 ± 0.01	8.99 ± 0.04	8.08 ± 0.03	4.94 ± 0.03
10	I/0	10 36 52.40	-58 38 08.93	10.35 ± 0.01	9.27 ± 0.01	7.91 ± 0.02	6.63 ± 0.01	
11	I/0	10 36 53.37	-58 37 55.10	10.41 ± 0.02	9.86 ± 0.02	8.57 ± 0.03	7.18 ± 0.02	
12	I/0	10 36 53.91	-58 37 48.08	11.21 ± 0.03	10.51 ± 0.03	9.17 ± 0.06	7.83 ± 0.03	
13	I/0	10 36 48.93	-58 40 07.23	10.64 ± 0.02	9.99 ± 0.02	8.15 ± 0.03	6.56 ± 0.01	2.02 ± 0.01
14	I/0	10 37 35.74	-58 29 40.28	9.83 ± 0.01	8.76 ± 0.01	7.87 ± 0.02	7.00 ± 0.01	4.19 ± 0.03
15	I/0	10 37 28.26	-58 35 49.05	9.11 ± 0.01	8.57 ± 0.01	7.91 ± 0.01	6.46 ± 0.01	2.91 ± 0.02
16	I/0	10 37 41.00	-58 35 44.05	11.82 ± 0.04	10.97 ± 0.03	10.08 ± 0.08	8.62 ± 0.04	
17	I/0	10 38 06.56	-58 39 59.99	11.45 ± 0.03	10.73 ± 0.03	9.57 ± 0.06	8.31 ± 0.04	
18	I/0	10 37 37.43	-58 47 01.93	12.71 ± 0.17	10.89 ± 0.04	9.66 ± 0.14	8.62 ± 0.11	4.33 ± 0.03
19	I/0	10 37 53.80	-58 46 15.37	11.47 ± 0.06	9.08 ± 0.01	7.65 ± 0.03	6.98 ± 0.03	2.53 ± 0.02
20	I/0	10 37 49.30	-58 47 22.47	11.05 ± 0.04	10.16 ± 0.02	9.08 ± 0.08	8.05 ± 0.06	
21	I/0	10 38 06.98	-58 45 13.31	8.88 ± 0.01	8.02 ± 0.01	6.54 ± 0.01	5.51 ± 0.01	2.01 ± 0.02
22	I/0	10 38 10.07	-58 45 28.24	9.60 ± 0.01	7.93 ± 0.00	6.28 ± 0.01	5.61 ± 0.01	1.75 ± 0.01
23	I/0	10 38 15.19	-58 45 36.93	12.79 ± 0.13	10.99 ± 0.04	9.69 ± 0.11	8.77 ± 0.09	4.27 ± 0.02
24	I/0	10 37 49.81	-58 51 36.30	11.39 ± 0.03	10.43 ± 0.02	9.31 ± 0.07	8.18 ± 0.04	4.91 ± 0.03

Continued on next page...

TABLE 7 – Continued

Source #	IRAC Class	R.A. J2000	Decl. J2000	[3.6]	[4.5]	[5.8]	[8.0]	[24]
25	I/0	10 38 35.27	-58 44 15.31	11.58 ± 0.05	10.92 ± 0.04	8.00 ± 0.03	6.23 ± 0.01	3.95 ± 0.02
26	I/0	10 38 25.41	-58 47 41.49	11.33 ± 0.03	10.86 ± 0.03	9.25 ± 0.07	7.63 ± 0.03	5.57 ± 0.03
27	I/0	10 38 41.84	-58 44 37.88	9.02 ± 0.01	8.08 ± 0.00	7.09 ± 0.01	6.19 ± 0.01	3.09 ± 0.02
28	I/0	10 38 03.62	-58 54 41.10	11.33 ± 0.02	10.38 ± 0.02	8.60 ± 0.03	6.94 ± 0.01	
29	I/0	10 38 02.40	-58 55 10.47	11.33 ± 0.03	10.75 ± 0.03	9.67 ± 0.08	8.50 ± 0.05	
30	I/0	10 38 02.70	-58 55 30.95	10.80 ± 0.02	9.87 ± 0.01	8.95 ± 0.04	7.83 ± 0.03	
31	I/0	10 38 04.05	-58 55 14.81	10.10 ± 0.01	9.27 ± 0.01	8.86 ± 0.04	8.05 ± 0.04	
32	I/0	10 38 04.72	-58 55 32.56	9.37 ± 0.01	7.82 ± 0.00	6.51 ± 0.01	5.85 ± 0.01	
33	I/0	10 37 13.13	-58 26 30.63	8.63 ± 0.00	8.02 ± 0.00	6.48 ± 0.01	6.12 ± 0.01	4.05 ± 0.02
34	I/0	10 37 34.78	-58 35 20.63	7.93 ± 0.00	7.24 ± 0.00	6.17 ± 0.00	5.99 ± 0.00	3.66 ± 0.02
35	I/II	10 36 56.38	-58 24 47.17	11.61 ± 0.03	11.28 ± 0.04	9.26 ± 0.05	7.42 ± 0.02	
36	I/II	10 35 30.02	-58 46 18.79	10.39 ± 0.01	10.03 ± 0.02	9.35 ± 0.06	7.76 ± 0.02	
37	I/II	10 37 07.39	-58 28 48.79	10.23 ± 0.02	9.88 ± 0.02	9.04 ± 0.05	7.81 ± 0.03	2.77 ± 0.02
38	I/II	10 36 54.69	-58 37 31.02	11.60 ± 0.04	11.22 ± 0.05	8.90 ± 0.04	7.51 ± 0.02	
39	I/II	10 36 53.12	-58 40 28.61	10.76 ± 0.02	10.54 ± 0.02	8.71 ± 0.02	7.00 ± 0.01	
40	I/II	10 37 45.09	-58 28 52.18	9.89 ± 0.01	9.82 ± 0.01	9.28 ± 0.06	8.17 ± 0.04	
41	I/II	10 37 14.14	-58 36 43.51	9.92 ± 0.01	9.83 ± 0.01	9.28 ± 0.05	7.60 ± 0.02	
42	I/II	10 37 44.16	-58 29 45.03	10.02 ± 0.01	9.77 ± 0.01	9.19 ± 0.05	7.53 ± 0.02	
43	I/II	10 37 23.51	-58 35 28.18	10.20 ± 0.01	10.08 ± 0.02	9.61 ± 0.06	7.80 ± 0.02	
44	I/II	10 36 57.44	-58 44 05.48	9.62 ± 0.01	9.40 ± 0.01	6.73 ± 0.01	5.02 ± 0.00	1.63 ± 0.01
45	I/II	10 37 23.03	-58 43 45.64	10.26 ± 0.01	10.24 ± 0.02	9.13 ± 0.05	7.53 ± 0.02	
46	I/II	10 37 15.97	-58 45 55.45	10.45 ± 0.02	10.42 ± 0.03	9.40 ± 0.10	7.98 ± 0.05	
47	I/II	10 37 24.55	-58 45 26.69	10.06 ± 0.01	9.99 ± 0.02	8.83 ± 0.05	7.17 ± 0.02	
48	I/II	10 38 14.24	-58 37 19.29	10.74 ± 0.02	10.40 ± 0.02	9.94 ± 0.08	8.78 ± 0.05	5.88 ± 0.05
49	I/II	10 38 08.50	-58 47 08.53	10.29 ± 0.02	10.19 ± 0.02	9.31 ± 0.08	8.13 ± 0.05	
50	I/II	10 38 43.25	-58 44 18.53	10.74 ± 0.03	10.47 ± 0.03	9.81 ± 0.15	8.68 ± 0.11	
51	II	10 36 28.31	-58 34 17.25	10.28 ± 0.01	10.21 ± 0.02	9.86 ± 0.10	9.30 ± 0.12	

Continued on next page...

TABLE 7 – Continued

Source #	IRAC Class	R.A. J2000	Decl. J2000	[3.6]	[4.5]	[5.8]	[8.0]	[24]
52	II	10 36 41.69	-58 31 26.39	9.31 ± 0.01	9.28 ± 0.01	8.84 ± 0.04	8.20 ± 0.04	
53	II	10 36 49.50	-58 30 10.25	11.18 ± 0.03	10.80 ± 0.03	10.05 ± 0.12	9.28 ± 0.11	
54	II	10 36 46.24	-58 35 09.85	9.56 ± 0.01	9.53 ± 0.01	9.02 ± 0.07	8.13 ± 0.06	
55	II	10 37 25.22	-58 26 21.47	7.87 ± 0.00	7.43 ± 0.00	6.81 ± 0.01	6.19 ± 0.01	
56	II	10 37 03.51	-58 31 43.42	9.29 ± 0.01	8.55 ± 0.01	6.94 ± 0.01	6.42 ± 0.01	
57	II	10 36 09.07	-58 45 22.50	10.06 ± 0.01	10.04 ± 0.01	9.66 ± 0.08	9.20 ± 0.10	
58	II	10 37 06.08	-58 33 03.81	10.84 ± 0.03	10.45 ± 0.03	9.70 ± 0.13	8.63 ± 0.09	
59	II	10 37 34.05	-58 26 54.15	9.77 ± 0.01	9.27 ± 0.01	8.86 ± 0.03	8.05 ± 0.03	5.37 ± 0.03
60	II	10 36 33.86	-58 41 02.23	10.51 ± 0.01	10.43 ± 0.02	10.27 ± 0.13	9.85 ± 0.17	
61	II	10 36 48.88	-58 38 04.42	10.64 ± 0.02	10.23 ± 0.02	9.74 ± 0.10	8.72 ± 0.07	
62	II	10 37 05.72	-58 34 18.53	10.58 ± 0.02	10.01 ± 0.02	9.28 ± 0.05	8.25 ± 0.04	
63	II	10 37 03.94	-58 34 48.90	8.12 ± 0.00	7.45 ± 0.00	6.53 ± 0.01	5.88 ± 0.01	3.71 ± 0.02
64	II	10 36 57.46	-58 36 36.65	10.74 ± 0.02	10.23 ± 0.02	9.84 ± 0.08	9.08 ± 0.08	
65	II	10 36 51.65	-58 41 00.40	9.76 ± 0.01	9.68 ± 0.01	8.98 ± 0.04	7.96 ± 0.03	
66	II	10 37 46.81	-58 32 19.02	9.70 ± 0.01	9.52 ± 0.01	8.62 ± 0.03	7.76 ± 0.02	
67	II	10 36 36.64	-58 48 55.74	10.46 ± 0.02	10.42 ± 0.02	9.83 ± 0.11	8.85 ± 0.09	
68	II	10 37 00.23	-58 44 36.81	10.17 ± 0.01	10.15 ± 0.02	9.66 ± 0.11	8.64 ± 0.08	
69	II	10 38 19.34	-58 31 26.52	10.40 ± 0.01	9.65 ± 0.01	9.26 ± 0.04	8.65 ± 0.04	
70	II	10 37 13.30	-58 47 11.73	9.91 ± 0.01	9.77 ± 0.02	9.23 ± 0.08	8.35 ± 0.07	
71	II	10 37 40.63	-58 49 10.68	9.25 ± 0.01	9.24 ± 0.01	8.75 ± 0.05	7.96 ± 0.05	
72	II	10 38 07.37	-58 50 24.02	9.47 ± 0.01	8.94 ± 0.01	8.30 ± 0.03	7.26 ± 0.02	4.59 ± 0.03
73	II	10 38 33.14	-58 46 47.36	10.02 ± 0.01	9.79 ± 0.02	9.51 ± 0.10	8.45 ± 0.07	3.33 ± 0.02
74	II	10 38 45.36	-58 43 57.96	8.62 ± 0.00	8.45 ± 0.01	8.03 ± 0.03	7.21 ± 0.02	
75	II	10 38 33.33	-58 46 49.95	9.36 ± 0.01	9.28 ± 0.01	9.07 ± 0.07	8.18 ± 0.06	
76	II	10 38 03.22	-58 55 26.12	10.71 ± 0.02	10.11 ± 0.02	9.29 ± 0.06	8.30 ± 0.04	
77	II	10 38 12.87	-58 56 54.29	11.35 ± 0.03	10.87 ± 0.03	10.24 ± 0.13	9.30 ± 0.11	

TABLE 8

NGC 3324 YSO BEST-FIT PARAMETERS

Source #	Model #	χ^2	Mass ($M_\odot$)	Age ($\times 10^5$ yr)	Temp (K)	Radius ($R_\odot$)	Log(d) (kpc)
1	3002197	106.0	1.16±0.73	0.01	4002	12.09	0.49
2	3002121	13.1	5.37±1.98	0.29	4430	24.60	0.48
3	3010029	78.8	4.29±1.43	0.04	4189	32.23	0.49
4	3001523	46.9	2.18±0.62	0.01	4088	20.49	0.49
5	3007484	72.9	0.92±0.15	0.13	3987	8.40	0.47
6	3016220	103.3	2.01±1.12	0.02	4116	17.66	0.48
7	3000152	87.3	3.53±0.63	0.01	4222	25.12	0.47
8	3005805	77.9	1.14±0.55	0.01	4019	11.31	0.49
9	3012118	82.6	0.98±0.72	0.02	3903	11.90	0.49
10	3005512	81.6	4.35±1.69	0.18	4361	23.07	0.48
11	3019160	43.6	5.79±1.33	0.91	4604	20.89	0.49
12	3017991	83.9	1.89±0.33	0.13	4224	12.75	0.47
13	3006513	88.7	1.22±0.75	0.06	4019	12.03	0.46
14	3016220	62.9	2.01±0.72	0.02	4116	17.66	0.49
15	3004854	92.0	4.86±0.59	0.84	4494	19.83	0.46
16	3010607	87.2	0.56±0.43	0.02	3731	7.25	0.49
17	3008311	115.2	2.08±1.05	0.42	4311	11.66	0.49
18	3005388	12.3	0.59±0.46	0.04	3764	7.43	0.49
19	3012672	42.6	1.63±0.49	0.02	4104	14.23	0.49
20	3007368	8.0	4.40±1.74	2.28	4773	11.46	0.47
21	3007294	55.6	6.23±0.55	0.01	4128	50.58	0.48
22	3010566	102.9	0.38±0.12	0.02	3497	6.05	0.46
23	3018223	5.8	0.60±0.49	0.02	3762	7.75	0.49
24	3016181	20.7	1.46±0.87	0.02	4117	11.97	0.49
25	3016872	62.4	4.57±1.34	8.24	10410	6.04	0.49
26	3016796	84.0	0.98±0.21	0.02	3892	12.40	0.49
27	3006124	83.1	2.60±0.15	0.01	4108	23.44	0.46
28	3008620	110.8	6.04±0.85	7.50	18620	2.96	0.46
29	3018048	23.1	2.81±1.07	0.44	4365	14.50	0.46
30	3002049	29.5	4.35±1.25	1.50	4631	13.88	0.47
31	3004145	50.1	2.61±1.14	0.62	4361	13.45	0.46
32	3010454	31.9	5.77±1.79	0.02	4167	43.91	0.46
33	3017954	51.5	1.05±0.55	0.02	3972	11.34	0.49
34	3015484	70.1	6.98±0.69	13.73	20480	3.21	0.48
35	3002183	105.6	1.63±0.28	1.09	4281	9.08	0.46
36	3000951	22.2	2.24±0.74	0.38	4320	12.45	0.48
37	3009533	78.4	4.41±1.38	1.51	4638	13.93	0.49

Continued on next page...

TABLE 8 – Continued

Source #	Model #	χ^2	Mass ($M_\odot$)	Age ($\times 10^5$ yr)	Temp (K)	Radius ($R_\odot$)	Log(d) (kpc)
38	3001043	114.1	7.03±1.41	0.01	4135	55.99	0.46
39	3015400	113.0	1.93±1.08	0.10	4200	13.86	0.46
40	3019477	35.3	4.07±1.20	0.66	4433	18.55	0.46
41	3015462	56.8	4.81±1.10	1.16	4577	16.96	0.49
42	3010308	21.7	5.29±1.39	1.24	4648	17.44	0.46
43	3013656	66.9	5.08±0.55	1.85	4772	14.40	0.48
44	3015949	70.8	1.94±0.67	0.04	4147	15.70	0.46
45	3009767	97.8	3.57±0.73	0.65	4416	16.78	0.48
46	3000773	27.7	3.47±0.65	0.45	4400	16.88	0.47
47	3010760	68.7	3.82±0.97	0.74	4436	17.40	0.47
48	3016530	32.7	3.34±1.06	13.25	5604	6.44	0.46
49	3004050	20.4	2.64±0.87	0.88	4377	13.19	0.48
50	3014791	24.1	6.39±1.90	0.34	4481	26.76	0.49
51	3004832	11.8	5.08±0.64	1.03	4561	18.36	0.48
52	3006426	75.7	5.07±0.69	27.90	16600	2.69	0.46
53	3017090	9.3	0.72±0.61	0.14	3887	7.06	0.48
54	3014791	89.5	6.39±0.97	0.34	4481	26.76	0.48
55	3006415	98.8	5.89±0.92	18.56	18250	2.92	0.47
56	3013121	68.4	4.42±0.99	0.01	4125	37.82	0.49
57	3014481	107.5	2.62±1.08	0.34	4341	14.19	0.48
58	3015193	2.4	1.77±1.05	0.22	4245	11.18	0.47
59	3004551	27.1	3.56±0.28	14.97	7982	5.59	0.47
60	3009744	41.9	2.43±1.02	1.86	4494	9.16	0.48
61	3002944	15.1	3.14±0.87	27.13	11040	2.49	0.47
62	3003571	17.1	2.15±0.52	0.36	4309	12.18	0.46
63	3016710	71.0	5.48±0.29	11.85	17500	2.80	0.49
64	3015067	8.9	3.17±0.88	18.33	6500	5.72	0.48
65	3014791	55.7	6.39±0.96	0.34	4481	26.76	0.49
66	3000278	108.5	3.65±0.89	0.16	4345	20.14	0.47
67	3017774	55.0	3.03±0.86	26.95	11000	2.90	0.47
68	3004022	7.5	3.58±0.74	0.25	4380	18.23	0.48
69	3012951	73.4	3.59±0.93	4.51	4881	7.19	0.47
70	3007451	73.9	6.03±1.12	1.16	4685	22.43	0.48
71	3014791	102.3	6.39±0.98	0.34	4481	26.76	0.48
72	3000969	22.3	4.13±0.21	10.72	9602	5.70	0.49
73	3007400	10.6	2.23±1.00	0.65	4334	11.93	0.48
74	3018286	116.7	5.56±0.63	0.39	4461	24.04	0.48
75	3008264	125.4	5.64±0.74	0.96	4605	20.10	0.46
76	3004730	9.3	1.83±0.81	0.27	4266	11.07	0.49
77	3005176	2.6	0.97±0.60	1.83	4128	6.01	0.48

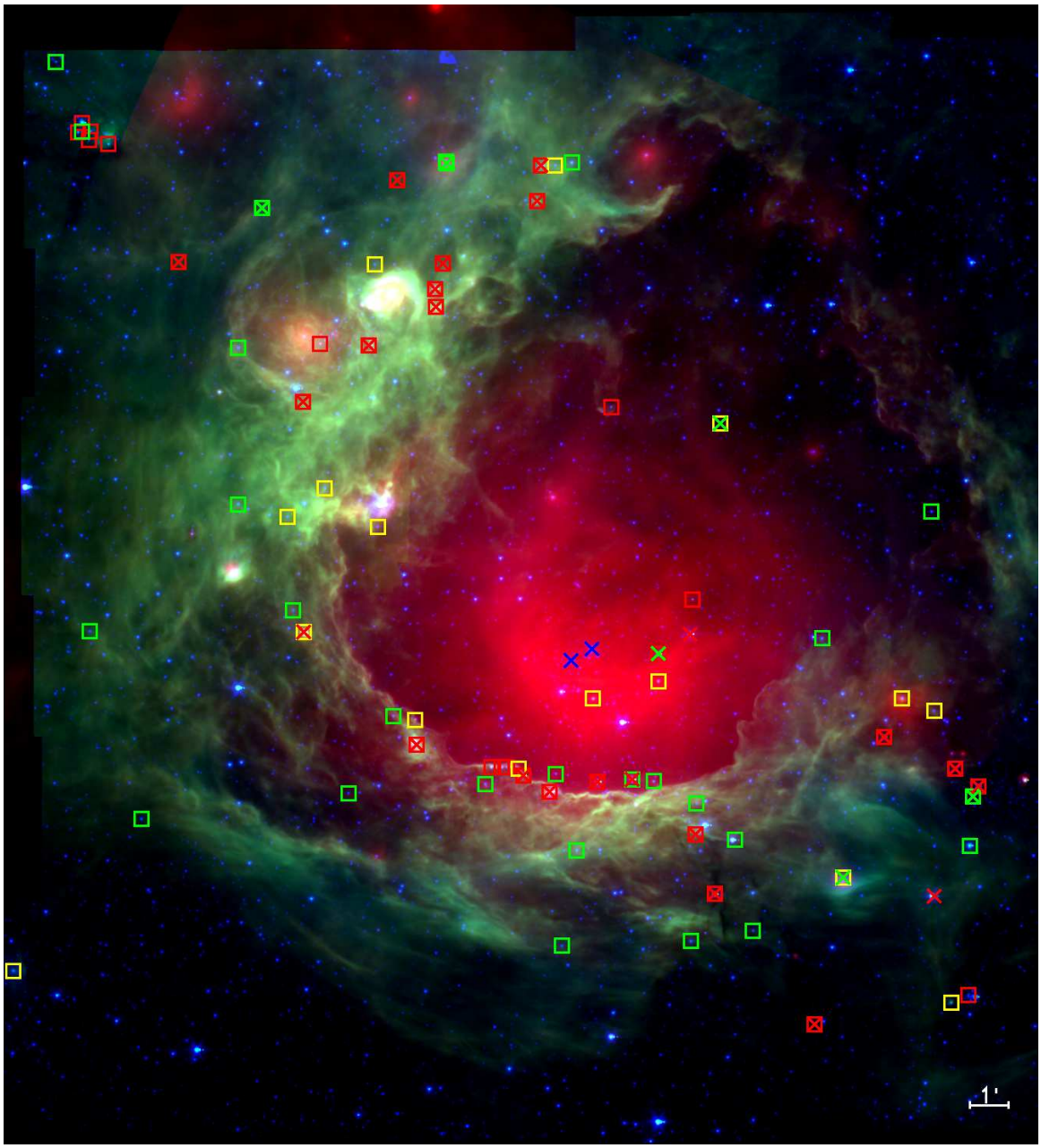

FIG. 27.—3-color *Spitzer* image of NGC 3324: Red is MIPS 24 μm, green is IRAC 8.0 μm, and blue is IRAC 4.5 μm. Red, yellow, and green squares (X's) show locations of the IRAC (MIPS) Class I/0, Class I/II, and Class II protostars. Blue X's mark the locations of the two massive O stars (O6.5 Vn and O8.5 Vp) in the region. The scale bar showing a distance of $1'$ in the image represents a length of $\sim$0.9 pc, given a distance of 3 kpc to the region.

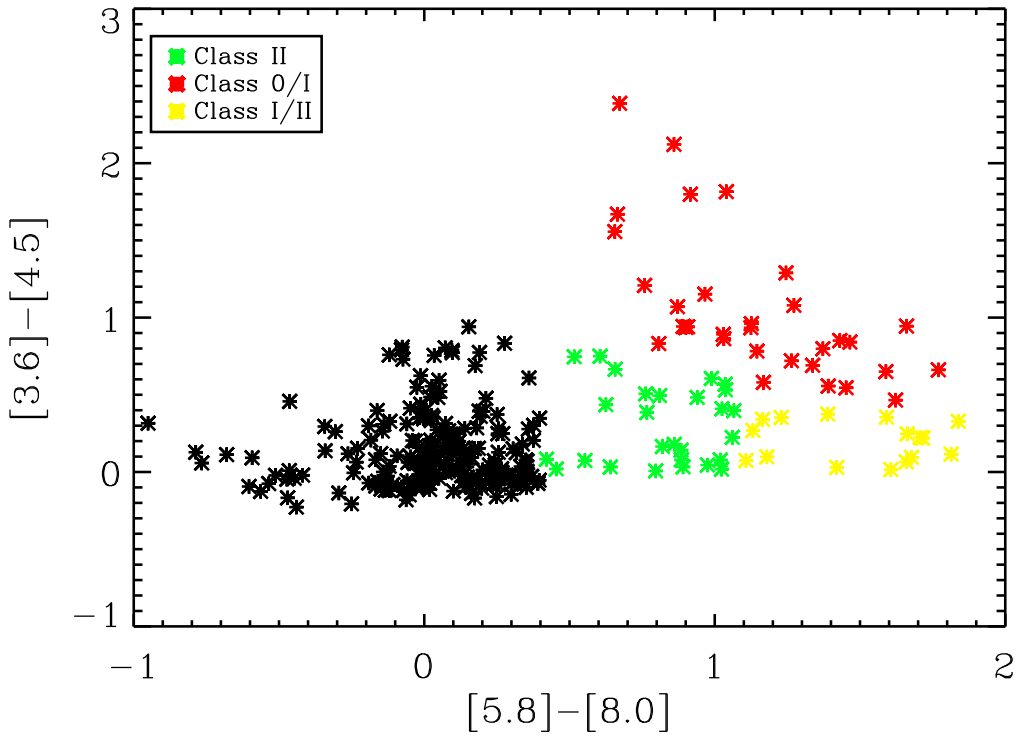

FIG. 28.—IRAC color-color diagram for NGC 3324, showing YSO classification of IRAC detected sources. Color criteria taken from Allen et al. (2004), and Whitney et al. (2003 & 2004b).

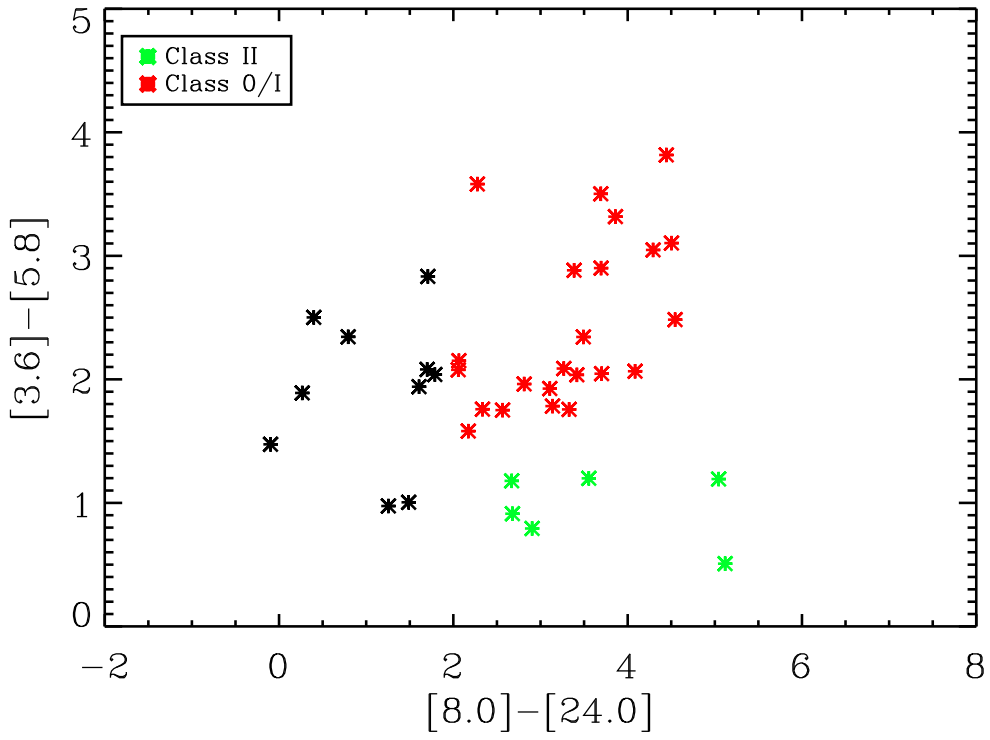

FIG. 29.—IRAC and MIPS color-color diagram for NGC 3324, showing YSO classification of the MIPS 24 μm detected sources. Color criteria taken from Whitney et al. (2003 & 2004b) and Reach et al. (2004).

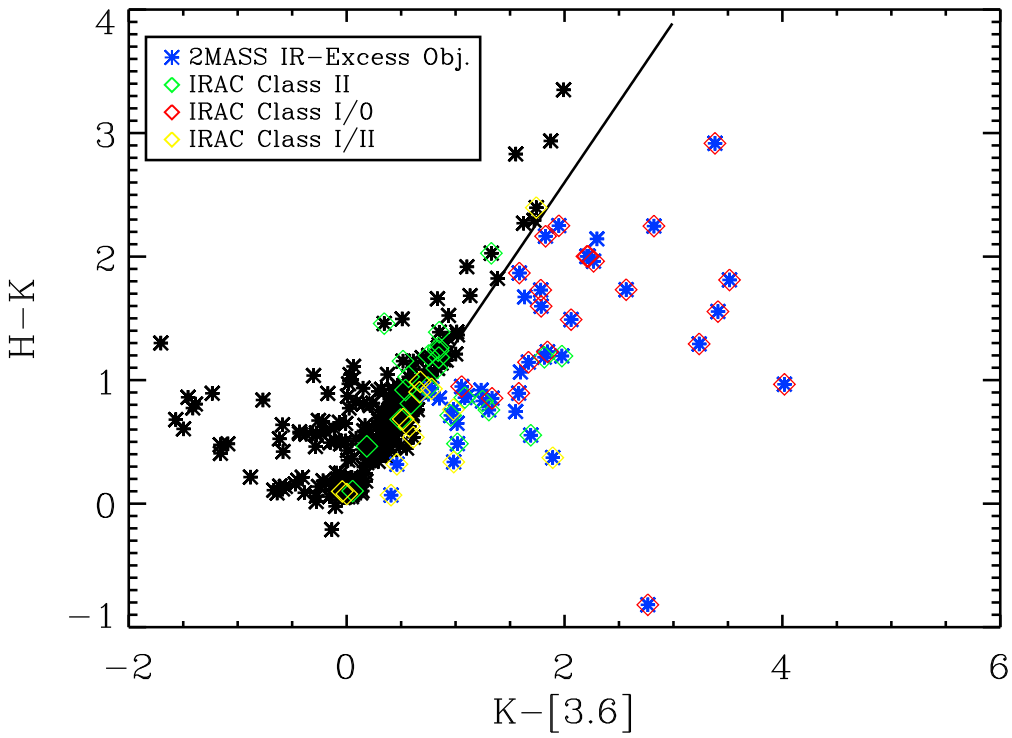

FIG. 30.—2MASS & *Spitzer* color-color diagram of the detected 2MASS sources in NGC 3324. Sources to the right of the reddening vector, with slope equal to 1.3, are sources with an infrared excess in the NIR. 37 out of the 45 sources with a 2MASS NIR-excess correspond to a *Spitzer* selected YSO candidate.

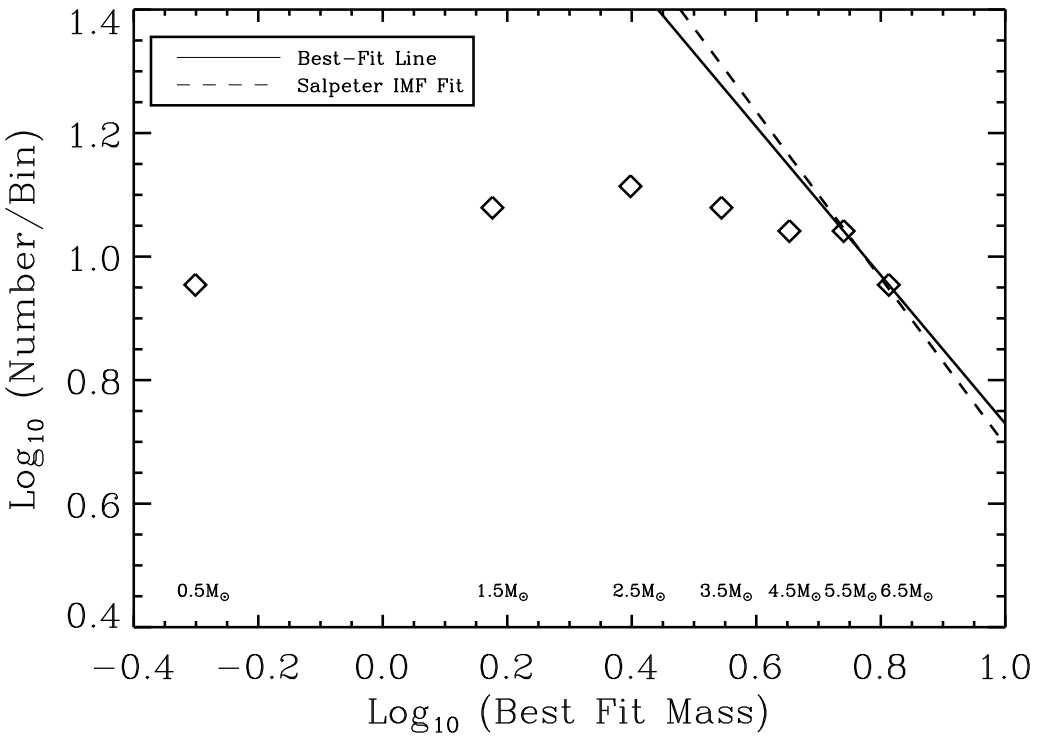

FIG. 31.—Mass distribution function for YSOs in NGC 3324. The solid line is the best-fit to our data, and corresponds to a slope of -1.2. The dashed line is for a Salpeter (1955) IMF with a slope of -1.35. Both lines were fit to the higher mass bins, where our sample is assumed to be complete.

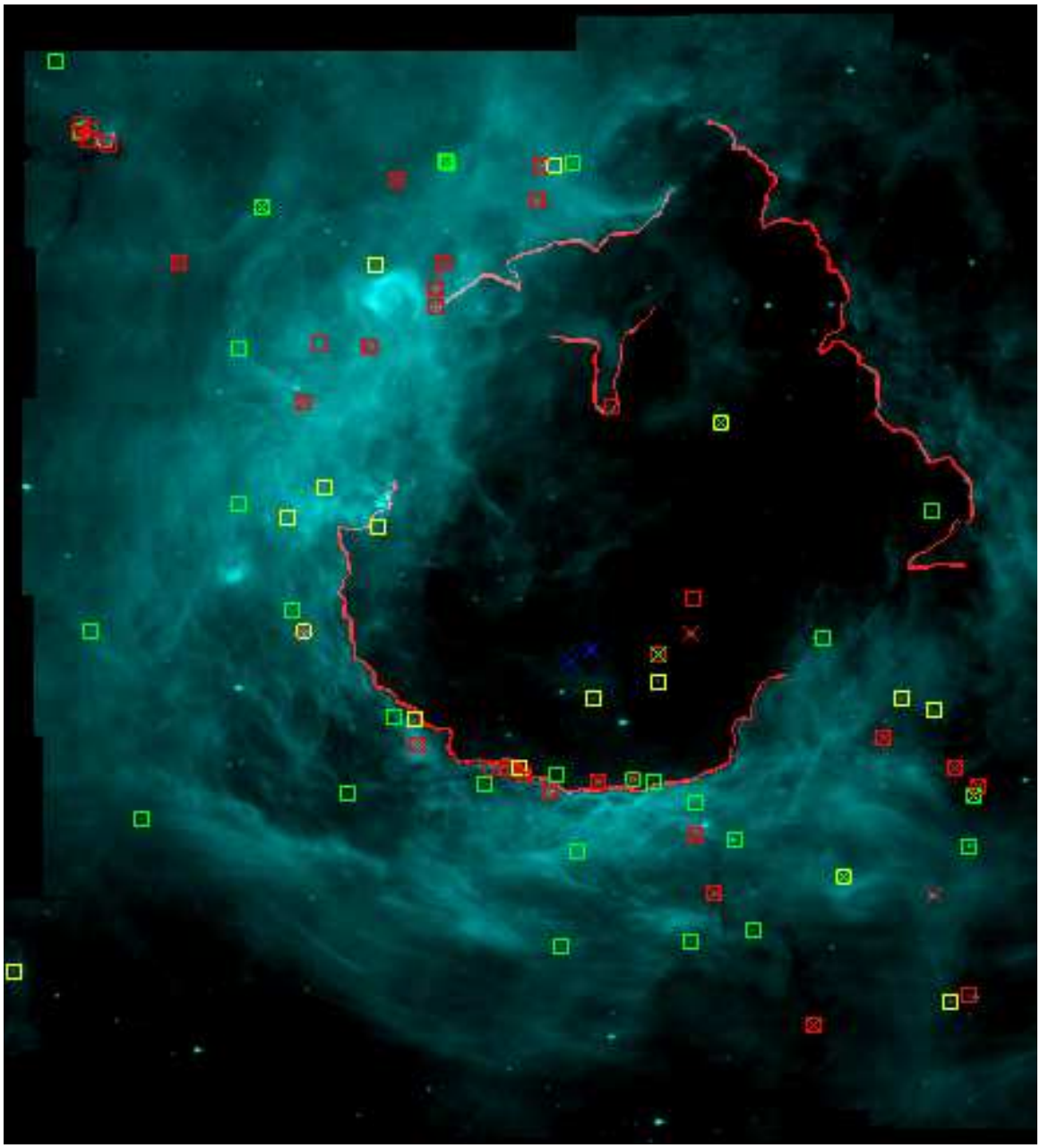

FIG. 32.—Locations of identified ionization fronts in NGC 3324, same scale as in Figure 27. Identified ionization fronts are outlined in red and are over-plotted on the IRAC 8.0 μm image. Red, yellow, and green squares and Xs show locations of Class 0/I, Class I/II, and Class II protostars, blue Xs mark the locations of known OB stars in the region.

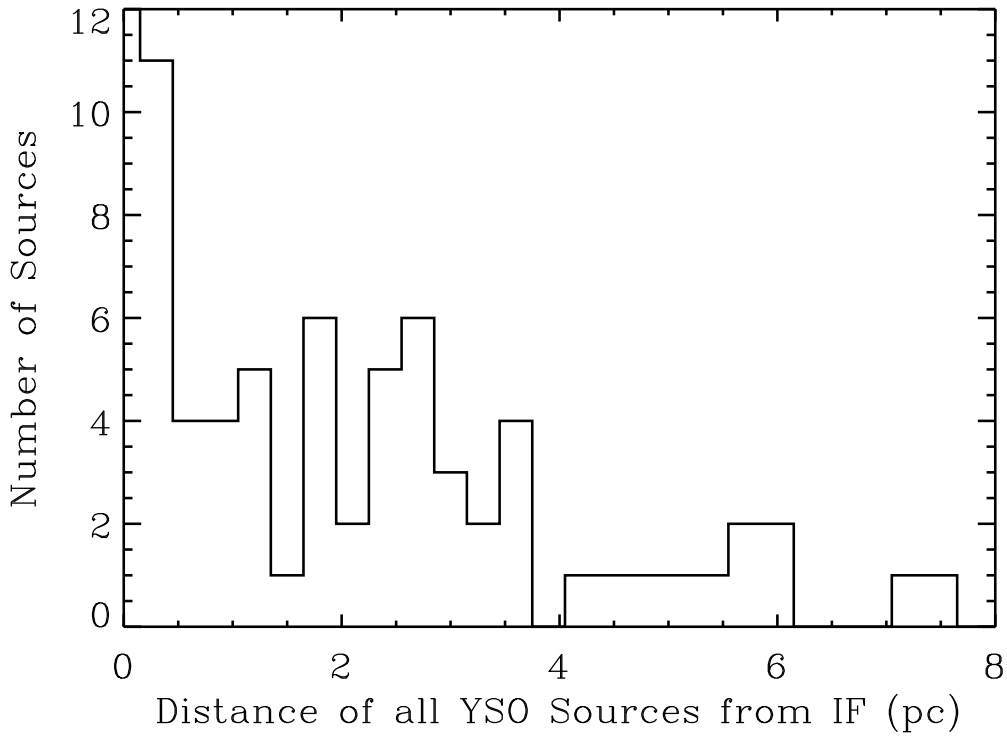

FIG. 33.—Distance distribution of YSOs in NGC 3324 from the nearest ionization front.

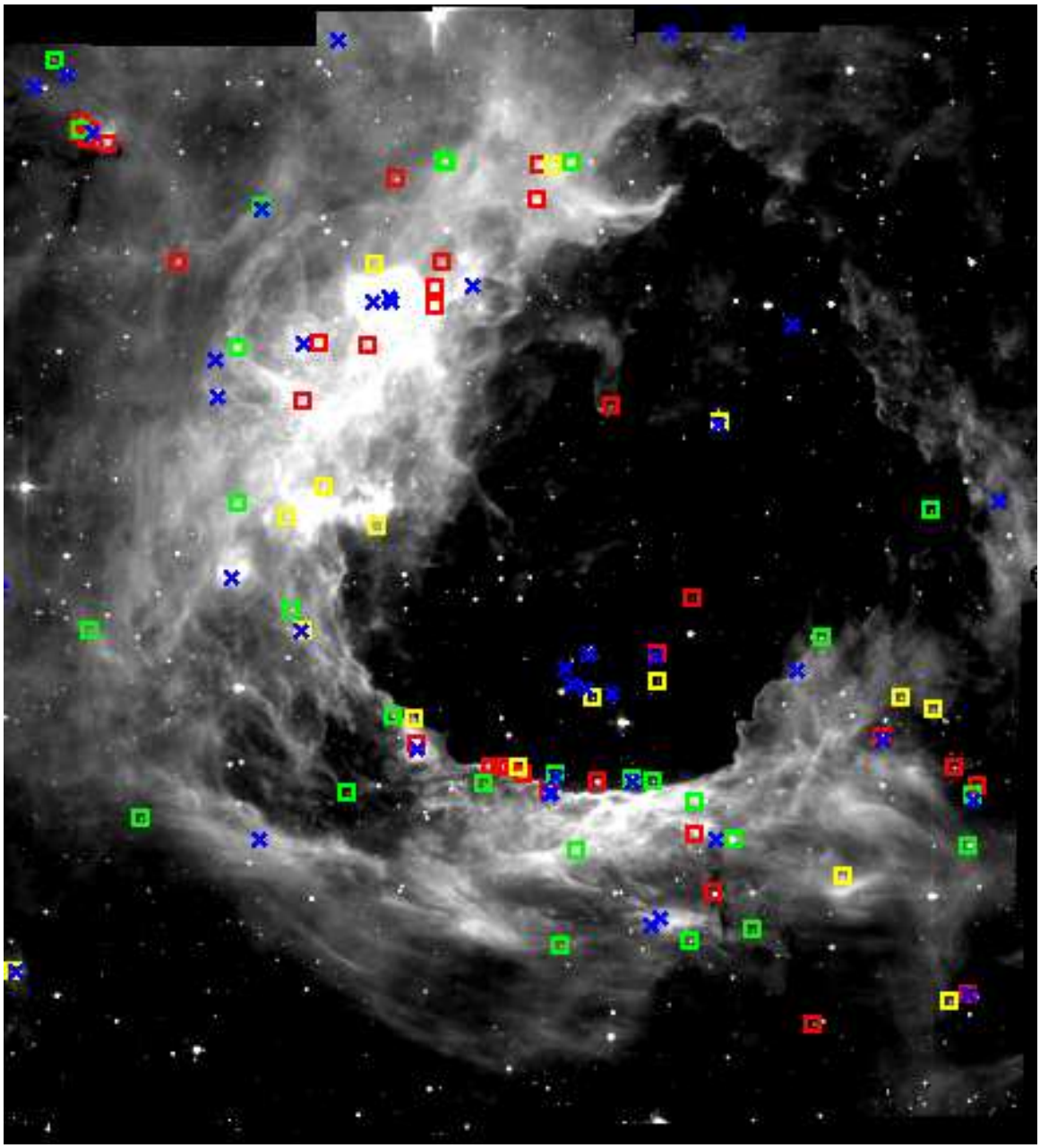

FIG. 34.—*Spitzer* 5.8 μm band image of NGC 3324 with candidate YSOs from two surverys overplotted. Blue X's show the locations of candidate YSOs from Cappa et al. (2008) using 2MASS, MSX, and IRAS archival data. Red, green, and yellow squares show the locations of YSOs detected in this paper using *Spitzer* data. Only 13 of the Cappa et al. candidate YSOs overlap with our candidate YSOs, however a similar overall distribution of the YSOs can be seen between the two surverys.

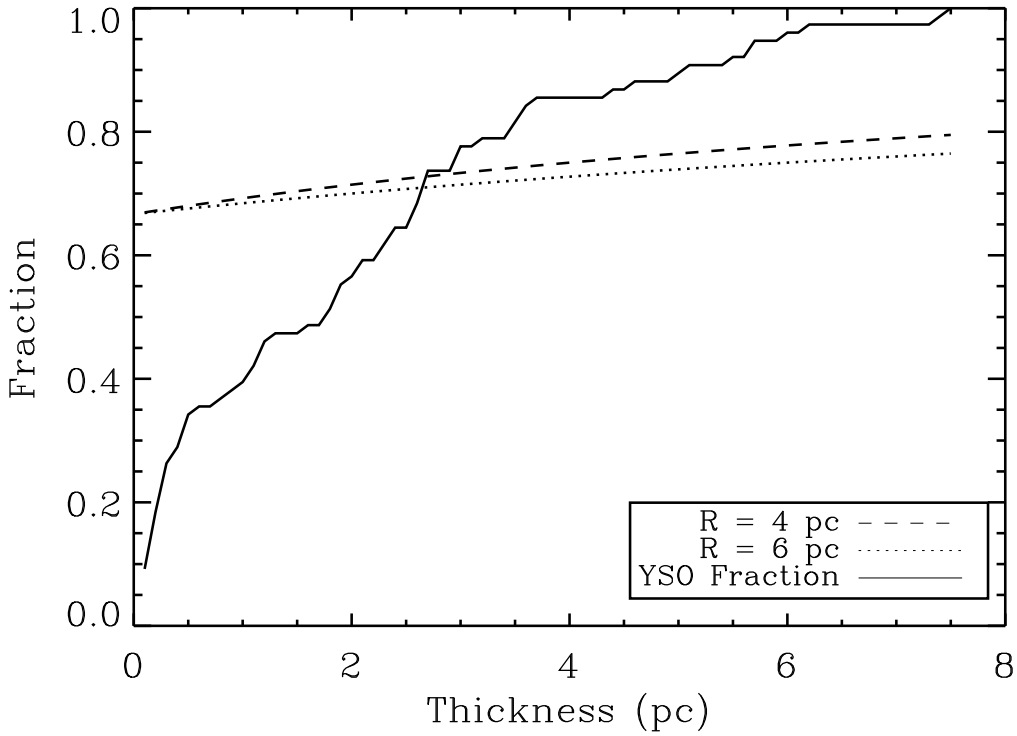

FIG. 35. —A simplified 3D hemispherical model of an ionization front is used to determine the expected number of observed sources that would be seen within a given layer thickness when viewed in projection. The fraction of expected sources observed within a given thickness distribution from an ionization front, with ionization fronts centered at 4 and 6 pc away from an OB star, are shown by dashed lines. The measured distribution of YSOs in NGC 3324 is shown by the solid line. The expected distributions and the observed distribution cross around 2.6 pc, indicating that the actual distribution of YSOs in NGC 3324 is a population of sources that is concentrated within a layer 2.6 pc or less from the nearest ionization front.

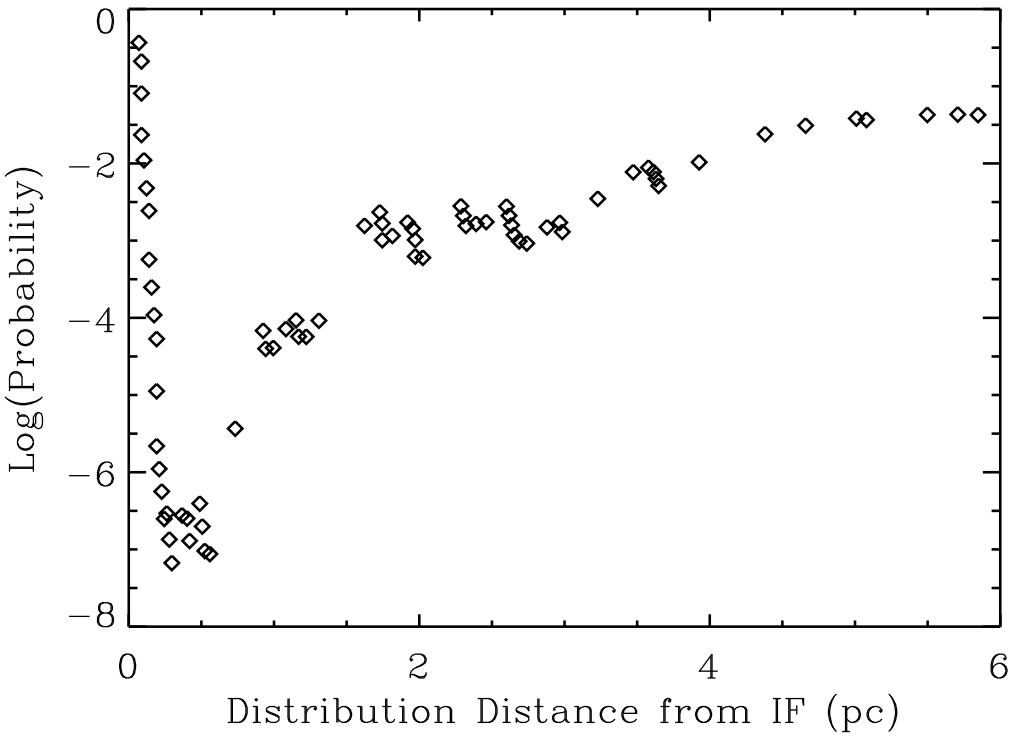

FIG. 36.—The probability of the distribution of YSOs being a random distribution is plotted versus distance. Using the Poisson Probability function, the likelihood that the given distribution of YSOs is positioned within a given distance of an ionization front by chance is calculated. On average, the chance of this distribution occurring randomly is 10^{-3}.

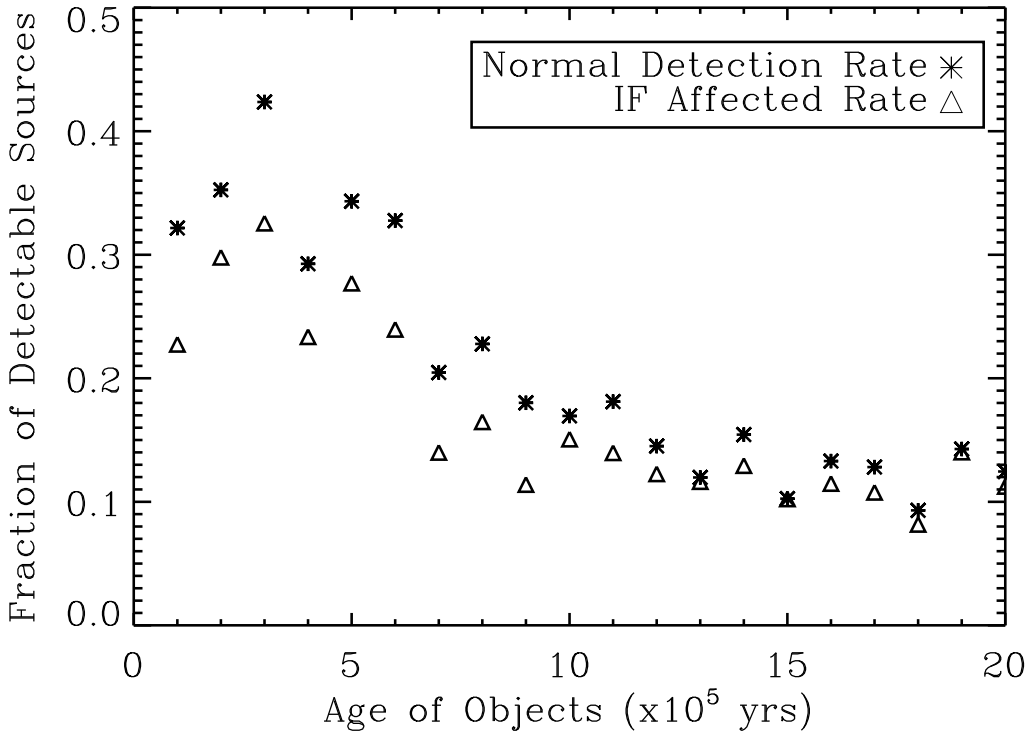

FIG. 37.—The fraction of detectable YSOs vs. age of the object in NGC 3324. A population of stars given by the MF from Equation 13 and a constant SFR (value equal to the calculated SFR from Equation 16) was aged over timesteps of 10^5 yr. The fraction of detectable sources based on our flux limits was calculated at each timestep, the normal detection rate is shown by the asterisk symbols. The detection rate was also calculated for sources uncovered by a passing ionization front. Disk erosion was assumed using models from Johnstone et al. (1998). The ionization front affected detection rate with object age is shown by the triangles. The data show that the best age range to detect the YSOs is around a few$\times 10^5$ yr, with a peak at 3×10^5 yr.

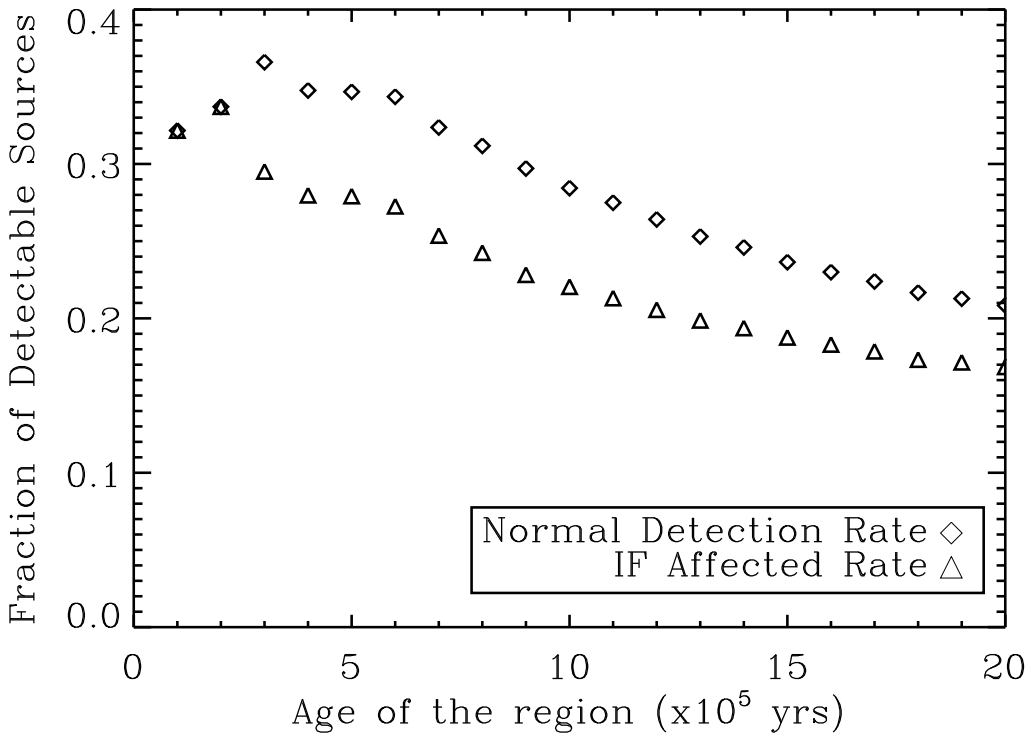

FIG. 38.—The fraction of detectable sources vs. age of the region, using the same methods as described for Figure 37. The normal detection fraction is shown by the asterisk symbols and the ionization affected fractions are shown by the triangles. The detection rate drops to between 16 - 21% by 2 Myr.

5. *SPITZER* OBSERVATIONS OF THE H II REGION M16

5.1. Outline

We present *Spitzer Space Telescope* observations of the H II region M16. For this region, we present new MIPS (24 μm) data and use IRAC (3.6, 4.5, 5.8, and 8.0 μm) observations from the *Spitzer* GLIMPSE legacy survey. The MIPS 24 μm field of view covers approximately 970 square arcminutes. M16 is a well studied star formation region, and past *HST*, *Spitzer*, and *Chandra* observations are compared to the results presented here. Using the *Spitzer* data we have identified over 200 candidate Young Stellar Objects (YSOs), and a large fraction are low-mass protostellar objects. We present color-color diagrams of these objects, as well as look at the spatial distribution of the YSOs in this region. Based on best-fit ages and the spatial distribution of the YSOs, we conclude that triggered star formation due to H II region expansion is occurring at a calculated rate of approximately 14-37% in M16.

5.2. Introduction

The ongoing debate of how low-mass star formation takes place in H II region environments has been discussed in previous chapters. In regions where both massive stars and low-mass stars exist, there are questions of whether or not the high-mass stars will have an effect on the formation of further generations of stars. Or are the low-mass stars forming spontaneously throughout these regions with little influence from their massive nearby neighbors? Does star formation occur as a burst in these regions, resulting in all the stars being formed at the same time, and therefore no low-mass stars are formed later to be affected by the massive stars? Or is the star formation process ongoing in these young regions? These are the types of questions that we are attempting to shed some light on. We have shown that in three H II re-

gions, analyzed using *Spitzer Space Telescope* observations, some amount of low-mass triggered star formation appears to be occurring. Calculations presented in the previous chapters have shown that in these three regions triggering is the dominant force behind 24 - 58% of the total star formation.

M16, also known as the Eagle Nebula, is one of the most famous and well studied star forming regions. M16 is located at a distance of 2.0 ± 0.1 kpc based on spectroscopic parallaxes from Hillenbrand et al. (1993). There are a number of massive O stars in the region, the main ionizing source is the O4 V star, HD 168076, and three other O6 - O7 stars also provide a fraction of the ionizing radiation in the region (Maiz-Apellaniz et al. 2004). Many intermediate and low-mass pre-main sequence stars have been identified in M16 with ages ranging from 0.25 - 1 Myr, and an age estimate for the massive stars in the region is about 2 Myr (Hillenbrand et al. 1993). This leads to the conclusion that star formation has been ongoing over the lifetime of the region, approximately 2 Myr. The work of Hester et al. (1996) using *HST* WFPC2 observations of M16 produced one of the most famous *HST* images, the "Pillars of Creation". In the three pillars centered in the WFPC2 FOV, Hester et al. identified 73 Evaporating Gaseous Globules ("EGGs"). The EGGs appear as small cometary structures that are being photoevaporated by nearby massive stars. The EGGs are thought to be areas of dense gas which are being photoevaporated more slowly than their surroundings. Most of the EGGs have elongated shapes which point directly away from the massive ionizing stars, and they are not being evaporated away as quickly because of the denser clump of material at the head of the structure.

A majority of the EGGs are sitting right at the edges of the pillars, at the interface between the molecular gas and the ionization front.

A JHK_s near-IR survey by Sugitani et al. (2002) centered on the three main pillars in M16 identified a population of low-mass stellar sources. They found that a majority of the youngest objects in the region, the low-mass protostars and T Tauri stars, are seen near the tips and edges of the three pillars. Two very bright, massive YSOs were detected at the tips of pillars 1 and 2, M16 ES-1 and M16 ES-2, respectively. In order to determine if the "EGGs" detected in the pillars actually contain YSOs, McCaughrean & Andersen (2002) obtained Very Large Telescope (VLT) observations of M16 with the ISAAC near-IR camera/spectrograph. Only 11 of the 73 EGGs showed definite evidence of an associated point source. The YSOs at the tips of pillars 1 and 2 were also observed. The mass of M16 ES-1 is estimated to be 5 - 10 $M_\odot$, and M16 ES-2 is estimated to have a mass of 2 - 5 $M_\odot$. Among the EGGs that do contain YSOs, there is a cluster of sources at the tip of column #1. Four of the EGG infrared point sources were determined to have masses ranging from 0.3 - 1.0 $M_\odot$, and the other seven point sources have substellar masses ranging from 0.02 - 0.07 $M_\odot$. Therefore, McCaughrean & Andersen conclude that many of the EGGs may not contain YSOs, however the 15% that do can be considered a lower limit because some of the EGGs remain opaque even at near-IR wavelengths.

Work by Healy et al. (2004a) using the Very Large Array (VLA) detected the presence of water maser emission from eight sources in M16. Water maser emission is known to be associated with protostars, and is a signpost for the earliest stages of star

formation. Recently, M16 has been studied with both *Chandra* and *Spitzer*. Linsky et al. (2007) have observed M16 around the *HST* WFPC2 FOV and the ACS FOV of pillar 5 with the Advanced CCD Imaging Spectrometer (ACIS) on *Chandra*. YSOs typically have high X-ray luminosities, and can be detected through large column densities. 40 X-ray sources were detected near pillars 1, 2, and 3, however no X-ray sources were found to match up with any of the EGGs in the WFPC2 FOV to within a 3-σ position uncertainty of the *Chandra* sources. X-ray point sources were detected at the locations of the two massive YSOs, M16 ES-1 and M16 ES-2, at the tips of pillars 1 and 2. M16 ES-1 was one of the brightest X-ray sources in the field, with an X-ray luminosity of $\sim 10^{32}$ erg s^{-1}, leading Linsky et al. to conclude that it is likely a high-mass YSO. The YSO at the tip of pillar 2 had a much lower measured X-ray flux of $\sim 10^{30}$ erg s^{-1}, which implies in a 2 - 6 $M_{\odot}$ pre-MS star. Indebetouw et al. (2007) used data from the *Spitzer* GLIMPSE Legacy survey to study M16 and the associated cluster NGC 6611. They looked at a larger distribution of YSOs in the region. They find that the distribution of YSOs appears to be somewhat clustered, and conclude that the distribution shows evidence of moderate distributed star formation but not a large amount of evidence for triggered star formation by the cluster NGC 6611.

Using the wealth of data and studies made on M16, we wish to compare the *Spitzer* observations that are a part of this study to what has been done in the past. We are interested in determining if any of the YSOs identified with *Spitzer* correspond to detected YSOs from the VLT and *Chandra* surveys, as well as with locations of "EGGs" and known water maser emission.

5.3. Observations and Data Reduction

The data for M16 were obtained by the *Spitzer Space Telescope* with the Multiband Imaging Photometer for *Spitzer* (MIPS; Rieke et al. 2004) during Cycle #2 as part of the *Spitzer* program PID 20726, and with the Infrared Array Camera (IRAC; Fazio et al. 2004) as part of the Galactic Legacy Infrared Mid-Plane Survey Extraordinaire (GLIMPSE; Benjamin et al. 2003). We have data in all four IRAC wavelength bands and the MIPS 24 μm band. The total mosaicked image size in the 24 μm band is $30\farcm9 \times 31\farcm4$, and we took the corresponding region of overlap in GLIMPSE for the four IRAC bands. For the MIPS 24 μm data, each frame was exposed for three seconds with two cycles, this resulted in a total exposure time of 84 seconds. The IRAC GLIMPSE data for NGC 2175 had a total exposure time of 12 seconds. The MIPS data were calibrated by the *Spitzer* Science Center (SSC) pipeline version S13.2.0, and the IRAC data were calibrated with the SSC pipeline version S14.0.0.

For the IRAC data, images were downloaded from the publicly available GLIMPSE archive along with the point source catalog of sources identified in each band in the field. The SSC pipeline version of the MIPS 24 μm band was used in our analysis. The GLIMPSE point source catalog for the M16 region was cut down to include only point sources in the overlap with the MIPS 24 μm field. We also set a signal-to-noise ratio (SNR) of greater than seven for IRAC point sources to include in our analysis. Point sources were then extracted separately from the 24 μm band using aperture photometry. We used the same aperture size of $6''$, and applied the same aperture

correction and zero-magnitude flux of 7.14 Jy that was used in previous chapters to the extracted point sources in the MIPS 24 μm band.

5.4 Results

Approximately 5000 point sources were identified from the GLIMPSE point source catalog to be within the MIPS 24μm FOV. This number was reduced to 3000 sources that had a SNR $\geq$ 7. Of these 3000 IRAC point sources, 242 were initially identified to have an IRAC color excess, using the [3.6]-[4.5] vs [5.8]-[8.0] color-color diagram. The IRAC point sources with color excesses were also screened against possible AGB and extragalactic contaminants by using color criteria given in Table 2. Only three IRAC selected YSOs had a color matching the criteria for an AGB star, therefore this left us with 239 candidate YSOs selected from the IRAC color-color plane. 50 point sources were identified in the MIPS 24 μm image, and from the MIPS data 29 objects were selected as candidate YSOs. 20 out of the 29 MIPS selected YSOs overlapped with an IRAC selected YSO. This therefore resulted in a total of 248 candidate YSOs; 68 Class I/0, 8 Class I/II, and 172 Class II YSOs.

Figure 39 is a three-color *Spitzer* image of M16 with the Class I/0 candidate YSOs overplotted as yellow squares, and the ionizing O stars labeled by blue squares. The IRAC 4.5 μm band is in blue, IRAC 8.0 μm band is in green, and the MIPS 24 μm band is in red. Due to the larger numbers of Class II YSOs detected in this region, we only show the Class I/0 sources in Figure 39. The locations of the two main *HST* FOV's are outlined in white in Figure 39. The distribution of the Class I/0 YSOs appears to be the most clustered of all of the candidate YSOs. We see

Class I/0 YSOs located in pillars 1 and 2 of the *HST* WFPC2 FOV, as well as in the ACS FOV of pillar 5 located to the middle right of the image.

Figures 40 and 41 are the *Spitzer* color-color diagrams showing the selection of YSO candidates. The IRAC and MIPS selected Class I/0 YSOs are located in the upper right of both plots and are labeled by red squares and red diamonds respectively. These sources have larger (redder) excesses in both colors in each plot. The Class II YSOs in Figure 40 typically have intermediate color excesses in both IRAC colors, whereas the MIPS Class II YSOs, shown as green triangles in Figure 41, have smaller [3.6]-[5.8] color excesses compared to the [8.0]-[24] color excess. The Class I/II YSOs in Figure 40 fall in between the two color regimes. Figure 42 is a 2MASS and *Spitzer* color-color diagram. Approximately 150 of the *Spitzer* YSOs have a corresponding 2MASS point source, and of these 150 2MASS sources 120 have a measured near-IR excess as shown in Figure 42. Another 100 2MASS point sources also had a measured near-IR excess but do not correspond to a *Spitzer* detected YSO.

5.5. Discussion

5.5.1. *SED Model Fitting of YSOs*

The next step in the YSO identification process was to run the 248 YSOs through the SED fitter of Robitaille et al. (2007). This process is described in more detail in §2.5.1 and §3.5.1. For the initial candidate YSOs in M16, 11 sources were discarded as possible protostellar objects after the SED fitter was run. All 11 of these objects were better fit by a purely stellar photosphere SED model, and therefore are unlikely to be YSOs. The rest of the candidate YSOs had good fits, with a majority

having low χ^2 values. More than 200 sources had a total $\chi^2 \leq 20$, and only 14 sources had a $\chi^2 \geq 50$. Considering the quality of the YSO SED fits, we are confident that the rest of the sample represents a population of protostellar objects in M16. After the SED fitting, we were left with 64 Class I/0 objects, 8 Class I/II objects, and 165 Class II objects, resulting in a total of 237 detected YSOs in M16. The positions, YSO classification, *Spitzer* magnitudes, and associated magnitude errors for the 237 candidate YSOs are listed in Table 9. Best-fit physical parameters for each YSO were determined, using the method described in §2.5.2 of finding the average mass among models within 3-σ of the best-fit, and using the model with the lowest χ^2 value and closest model mass to the calculated average mass. The best-fit SED model parameters for each YSO are listed in Table 10. These results show that a large fraction of low-mass YSOs were detected in M16. Out of the 237 YSOs, 55 have a best-fit mass less than 1 $M_\odot$, and another 57 YSOs have a best-fit mass between 1 - 2 $M_\odot$.

5.5.2. *Mass Distribution of YSOs and Completeness*

For M16, the 237 YSOs were grouped into eight mass bins of equal spacing. The eight mass bins are centered at 0.5, 1.5, 2.5, 3.5, 4.5, 5.5, 6.5, and 7.5 $M_\odot$. Performing a least squares fit on three of the higher mass bins (4.5, 5.5, and 6.5 $M_\odot$) results in a best-fit slope equal to 1.53. Figure 43 is a plot of log N vs log Best-Fit Mass for the 237 YSOs. The best-fit line, with slope equal to 1.53, is overplotted as the solid line and the Salpeter (1955) mass distribution with slope equal to 1.35 is overplotted as the dashed line. The data appear to have a slightly steeper slope than

a Salpeter mass distribution, which results in more stars at the lower-mass end. The YSO mass distribution for M16 is similar to what was measured for NGC 2467 in Chapter 2, however it is still very comparable to a Salpeter mass distribution. Given the best-fit slope of 1.53, the MF spectral index, Γ, is 2.53. Therefore, the YSO mass distribution function for M16 has the following form:

$$\frac{dN}{dM} \propto M^{-2.53} \; or \; \frac{dN}{d(\log M)} \propto M^{-1.53}. \tag{18}$$

In M16 there are four known massive O stars ranging from O4-O7 (Maiz-Apellaniz et al. 2004), as well as five O stars ranging in mass from O8-O9.5 V (Cruz-Gonzalez et al. 1974). Using these objects, we estimated a MF normalization constant of 960 for the best-fit mass distribution, and a normalization constant equal to 720 for a Salpeter mass distribution. Using the best-fit MF spectral index, the mass distribution function for M16 becomes:

$$N_{tot} = A \int_{M_1}^{M_2} M^{-2.53} dM = 9.6 \times 10^2 \int_{0.1M_\odot}^{60M_\odot} M^{-2.53} dM. \tag{19}$$

This results in a total of 2.1 $\pm$ 0.7 $\times 10^4$ stars (assuming Poisson statistics on the 9 stars used to calculate the normalization constant) between the mass range of 0.1-60 $M_\odot$ in M16. If we assume a Salpeter mass distribution, then the total number of stars is 1.2 $\pm$ 0.4 $\times 10^4$.

The completeness of the YSO sample in M16 was calculated using the three-σ magnitude limits in the IRAC bands. The magnitude limits were converted into flux limits and then compared to the model fluxes of the SEDs from Robitaille et al. (2006).

The model fluxes were scaled to a distance of 2 kpc, the assumed distance to M16 and an assumed average foreground extinction of A_V equal to 2.5 mag (Hillenbrand 1993) was also accounted for in the model flux limits. The calculated IRAC three-σ magnitude limits for these observations are: 14.7, 13.9, 12.7, and 12.0 for IRAC 3.6, 4.5, 5.8, and 8.0μm, respectively. The fraction of detectable models we should detect assuming these flux limits is 60% for M16, therefore we assume we are approximately 60% complete. This completeness limit is higher than any of the other previous datasets. This is likely due to using the GLIMPSE point source catalog which has higher total magnitude limits in the IRAC bands and different methods of point source extraction compared to our own point source extraction in the previous three datasets.

5.5.3. *Comparison to HST Images*

We are interested in comparing the *HST* WFPC2 images of M16 (Hester et al. 1996) to the *Spitzer* images of the region, as well as looking at the distribution of candidate YSOs that are located in the *HST* FOV. McCaughrean & Andersen (2002) found that only 11 of the 73 "EGGs" contained possible YSOs; the rest may be starless cores. In Figure 44, we show the famous three-color WFPC2 image of M16 (Hester et al. 1996) along with the locations of detected YSOs from the *Spitzer* selected sources. Hα emission is shown in red, [S II] emission is in green, and [O III] emission is in blue. Three Class I/0 YSOs are located in pillar #1 (left-most pillar) as shown by the red squares. Three more Class I/0's are in pillar #2, and two Class II YSOs are located in pillar #3. Another Class II YSO is located just off the tip of pillar #2. The majority

of these nine candidate YSOs are located right at the edges of the columns in the compressed gas that is being photoevaporated due to the nearby massive O stars.

One YSO is located in the tip of pillar 1, near the location of the massive YSO M16 ES-1. This candidate YSO is also very near to the locations of "EGGs" #'s 15 and 16, but does not appear to be exactly coincident with either. This YSO, also known as P1 (Sugitani et al. 2002; Indebetouw et al. 2007), was classified as a Class I object with a best-fit mass of 4.5 $M_{\odot}$ using SED fitting by Indebetouw et al. (2007), however models with masses ranging from 1.6 to 6.4 $M_{\odot}$ also had good fits to the Indebetouw et al. data. The YSO SED fitting performed in this analysis also classifies it as a Class I/0 object (#62), but with a higher mass of 7.9 $M_{\odot}$, agreeing more with the mass estimate of 5 - 10 $M_{\odot}$ by McCaughrean & Andersen (2002). The second Class I/0 YSO from the top of pillar #1, source #18, is coincident with EGG #25 and has a best-fit mass from the SED fitting of 2.3 $M_{\odot}$. The Class I/0 YSO located at the tip of the small protruding finger in pillar #1 (Source #17) is coincident with the location of EGG #31. This object has a best-fit mass of 5.7 $M_{\odot}$. In pillar #2, the Class I/0 YSO near the top of the column is coincident with EGG #73. This YSO (Source #61) is also nearby to water maser emission detected by Healy et al. (2004a) at the tip of pillar 2, however it is not coincident with this source and therefore we conclude the water maser emission is not from the YSO we detected at the tip of pillar 2. Healy et al. note that this water maser emission is also nearby to M16 ES-2, but is separated by a distance of $2\farcs7$, and they therefore rule out M16 ES-2 as the source of the water maser emission. Healy et al. conclude that this emission is due to

an unseen protostellar object. The Class I/0 source near the right-hand edge of pillar 2, source #14, overlaps with a detected X-ray source from Linsky et al. (2007), and appears to be a lower-mass object with a SED best-fit mass of 1.2 $M_{\odot}$. The Class II YSO just above pillar #2, source #236, also appears to overlap with a detected X-ray source and has a best-fit mass of 2.8 $M_{\odot}$. The remaining Class I/0 YSO in pillar 2 and the two Class II YSOs in pillar 3 do not overlap with any EGGs or X-ray sources.

Another note of interest is the location of four other Class II YSOs that can be seen in Figure 44, but just fall out of the WFPC2 batwing FOV. These sources are no longer in the dense compressed gas of the pillars but appear to have recently been uncovered by the passing ionization front. We can see a progression of sources by evolutionary class in Figure 44. The Class I/0 YSOs are all located in the columns of dense molecular gas, most still embedded but located right at the edges where the gas would be the most compressed, whereas a majority of the Class II YSOs are located just off the tips of the columns and have already been uncovered by the passing ionization front. Indebetouw et al. (2007) have a different conclusion based on the YSOs they identified in the M16 trunks. They too find that there are several very young sources in the trunks that possibly may have been triggered by compression of the columns from the nearby massive stars in NGC 6611, however they also see older Class II sources, with ages closer to 1 Myr, in some of the pillar tips. They also claim to see no noticeable pattern in evolutionary state with the younger sources farther from the NGC 6611 cluster, as might be expected for triggered star

formation. Our analysis shows a more noticeable trend in the youngest sources being located in the compressed gas of the columns and the older Class II's located outside the columns, having already been uncovered. Therefore as discussed above, contrary to the conclusions of Indebetouw et al. (2007), we still see evidence for triggered star formation particularly in the M16 elephant trunks.

The *HST* ACS image centered on pillar #5, which is located below and to the right of the WFPC2 FOV as seen in the orientation of Figure 39, also contains a number of detected YSOs. We found six Class I/0 YSOs located along this column of gas and they can be seen in Figure 39. One bright embedded Class I/0 YSO is located right at the tip of pillar 5. There are also a number of Class II and Class I/0 YSOs that are just above the top of column 5 and appear to have recently been uncovered. The ACS FOV cuts off right before the top of this column of gas, so these YSOs are not seen in the ACS image, therefore the ACS image is not shown, but the YSOs can be seen in the *Spitzer* image of Figure 39. Looking at the distribution of YSOs seen in all four main columns, we see a clustering of sources located right along the column edges in compressed molecular gas. While we do not see a candidate YSO at every X-ray and "EGG" location, we do see YSOs forming in these columns of very dense gas that are being exposed to the ionizing radiation. We see a general trend of the more evolved Class II YSOs located in the interior of the H II region, already uncovered by the passing ionization front, and the younger Class I/0's embedded in the columns of molecular gas, but many right at the edges.

5.5.4. *Spatial Distribution of YSOs in M16*

In the previous section we have focused on the distribution of YSOs in the *HST* FOVs, but to analyze the total YSO spatial distribution we mapped the location of the ionization front edges created by the massive O stars in M16. This was done using the method of smoothing the IRAC ch3 and ch4 images and running an edge detection routine, as described in §2.5.4.1. Three main ionization fronts were identified in M16: one surrounding the *HST* WFPC2 pillars (#'s 1, 2, and 3), another ionization front can be seen around the column of gas in the ACS image, column #5, and the third ionization front borders the north edge of the H II region cavity, below the three main columns in M16. The detected ionization fronts are shown in Figure 45, along with the locations of the four main ionizing stars (blue squares), and the locations of all 237 candidate YSOs: red, yellow, and green squares, representing Class I/0, I/II, and II YSOs, respectively.

In Figure 46, we plot the distribution of the distance of YSOs from the nearest ionization front. There is a peak in the histogram of sources at a distance of about 0.75 pc, which would correspond to time from the ionization front of approximately 3.8×10^5 yr, assuming an ionization front speed of 2 km s^{-1} (Osterbrock 1989). In total, there are approximately 100 YSOs that are measured to be within a projected distance of 1 pc or less from an ionization front; this accounts for almost half of the detected YSO sample.

In order to determine what total fraction of the YSOs in M16 is likely to be within 1 pc or less of an ionization front, we looked at a 3D model of the region

projected onto the 2D plane of the sky. The same procedure as was done in §2.5.4.2 was followed here. For M16, the four main ionizing O stars are located at distances ranging from ∼0.5 - 4 pc away from the actual ionization fronts, with average distances to the fronts on the order of 1 - 3 pc. In Figure 47, we show the predicted distribution of YSOs vs. the measured distribution of YSOs in M16. We have plotted three different hemispherical distributions (1.0, 2.0, and 3.0 pc). Figure 47 shows that if all of the 237 YSOs are actually within 1 pc of an ionization front, then we should expect to measure between 68 - 75% of the sources within this distance. However, for M16 only 43% of the YSOs were found within 1 pc or less of an ionization front. In Figure 47, the lines of the predicted distributions cross the measured distribution of YSOs at values of 2.5, 2.8, and 4.5 pc. The larger distribution distance of 4.5 pc corresponds to the OB stars being only 1 pc from the ionization fronts, and while some of the O stars in this field are that close to the ionization fronts in places, on average the O stars are 2 - 3 pc from the ionization fronts. Therefore, we conclude that the YSOs in M16 are a population of sources that is concentrated within a layer that is 2.5 - 2.8 pc from the nearest ionization fronts, and approximately 70% of these sources are likely within 1 pc or less from the nearest front.

Figure 48 shows the results of the likelihood of the measured distribution of YSOs to be a random distribution. A Poisson probability function was used for this calculation, following the formulation of Equation #4. Within the first 0.5 pc, the likelihood of this distribution occurring by chance is only 10^{-3} or 0.1%. Between a distance of 1 - 2 pc, the probability of a random distribution falls off dramatically,

but then begins to increase as more of the survey area is included. Overall, Figure 48 shows that this distribution of sources is likely not random, with the average probability of a random distribution being approximately 10^{-5} for the YSOs in M16.

5.5.5. *Estimates of Triggering and Star Formation Rates*

The same approach for determining triggered star formation rates in the previous chapters is applied to M16. We first want to estimate an average star formation rate for the region. The calculated MF ($\Gamma = 2.53$) from the candidate YSOs in M16 is slightly steeper than a Salpeter MF, but falls in between the mass functions calculated for other H II regions in this study. Using the MF calculated shown in Equation 18, we can estimate the total mass in stars and then using the assumed age of the region, 2 Myr, calculate the average SFR for M16:

$$M_{tot} = \int_0^N M dN = A \int_{M_1}^{M_2} M^{-1.53} dM = 9.6 \times 10^2 \int_{0.1M_\odot}^{60M_\odot} M^{-1.53} dM \sim 6000\,\mathrm{M}_\odot \tag{20}$$

$$Average\ SFR = \frac{6000\,\mathrm{M}_\odot}{2Myr} = 3.0 \times 10^{-3}\ \mathrm{M}_\odot\,\mathrm{yr}^{-1} \tag{21}$$

The total mass and average SFR using a Salpeter MF is shown below in Equations 22 and 23:

$$M_{tot} = \int_0^N M dN = A \int_{M_1}^{M_2} M^{-1.35} dM = 7.2 \times 10^2 \int_{0.1M_\odot}^{60M_\odot} M^{-1.35} dM \sim 4000\,\mathrm{M}_\odot \tag{22}$$

$$Average\ SFR = \frac{4000\,\mathrm{M}_\odot}{2Myr} = 2.0 \times 10^{-3}\ \mathrm{M}_\odot\,\mathrm{yr}^{-1} \quad (23)$$

This SFR for M16 with $\Gamma = 2.53$ mass distribution is slightly larger than those calculated for the other three regions, but within the error estimates of the other three regions. However, the calculated SFR using the Salpeter MF is approximately the same as the calculated SFRs for NGC 2467 and NGC 2175 (1.75 and 2.0×10^{-3} $\mathrm{M}_\odot$ yr^{-1}, respectively). It is also not surprising that M16 would have a slightly higher star formation rate since it is a more massive region and contains more massive O stars than the other regions.

In order to estimate a triggered star formation rate in M16 we need to estimate what fraction of YSOs are actually being affected by H II region expansion and therefore are possibly triggered. In §5.5.4, we clearly showed that the current distribution of YSOs does not appear to be random, and as many as 70% of the YSOs are expected to be within 1 pc or less of the nearest ionization front. In order to determine what fraction of YSOs we are missing in M16, we use the SED models and calculate what fraction will be detected with an evolving population based on the MF and SFR previously calculated for M16 (equations 18 and 21, respectively). The results of this analysis are shown in Figures 49 and 50. Figure 49 shows the fraction of YSOs that will be detected for a given age of a protostellar object. The detection fraction drops off as the YSO population ages, however not as fast as it did in a few of the other regions. This is likely due to using deeper IRAC magnitude data in the M16 dataset, therefore it is likely that more of the older YSO population is detected

in M16 as compared with the previous regions. For the normal unaffected detection rate, the peak age to best detect sources is at 5×10^5 yr and for the ionization front affected rate the peak age is 2×10^5 yr. Therefore, while a slightly longer age span is seen for good detection in M16, the likely average age of the YSOs is still around a few$\times10^5$ yr.

Figure 50 shows the detection fraction vs. elapsed age of the region. This rate starts off at about 60%, comparable to the completeness estimates found for M16 in §5.5.2, but then falls to ∼40% by 2 Myr. Again, these rates are slightly higher than in the other three regions, owing to the higher flux limits of this dataset. Looking at the ionization front affected detection rate shows that the fraction of detectable YSOs can fall to as low as 20%. The detection fractions shown in Figure 50 were also calculated for a Salpeter MF ($\Gamma = 2.35$). Using a Salpeter mass distribution produced slightly higher detection fractions as is shown in Figure 50. For the Salpeter mass distribution, the unaffected detection fraction dropped to 0.45 by 2 Myr, as compared with 0.4, and the ionization front affected rate fell to 0.25 by 2 Myr.

From the SED fitting, the 237 candidate YSOs have a likely average age of 3×10^5 yr, and from the analysis shown in Figure 49 it is likely that the best age range to detect the YSOs is also at a few$\times10^5$ yr. In order to estimate what fraction of YSOs are likely triggered, we look at the fraction that are found within a distance of 1 pc or less from the front. Over 40% were shown to be within a projected distance of 1 pc or less, and from the analysis of §5.5.4 we demonstrated that it is likely approximately 70% are within this distance. This would result in 166 of the 237

current YSOs being triggered by the expansion of the H II region. We have also just shown that we are only detecting a certain fraction of the current YSO population, between 20 - 45%. Therefore this results in 1.2 - 2.8$\times10^{-3}$ stars formed per yr that are triggered in M16.

$$\frac{\#\ YSOs}{Avg.Age \times DetectionRate} = \frac{166}{(3 \times 10^5\ \text{yr}) \times (0.45 - 0.2)} = 1.2{-}2.8{\times}10^{-3}\ \text{stars}\,\text{yr}^{-1} \tag{24}$$

Using the calculated MF from Equation 18, this results in a triggered SFR of 4 - 8$\times10^{-4}$ $M_\odot$ yr^{-1}, giving 14 - 27% of the total SFR. Using the Salpeter MF results in a triggered SFR of 4 - 7.3$\times10^{-4}$ $M_\odot$ yr^{-1}, giving of 20 - 37% of the total SFR. Therefore, there is a possible range of triggering in M16 of 14 - 37%. This is the lowest triggered SFR as compared with the other previous H II regions. This result might demonstrate that triggered star formation is not as significant in M16 as perhaps in other H II regions, however we are still estimating that triggered star formation is occurring here. One-fifth to over one-third of the stars formed here are likely to have been triggered by the expansion of the H II region and the effects of the massive O stars.

TABLE 9

SPITZER PHOTOMETRY FOR YSOs IN M16

Source #	IRAC Class	R.A. J2000	Decl. J2000	[3.6]	[4.5]	[5.8]	[8.0]	[24]
1	I/0	18 18 41.34	-14 00 03.86	11.92 ± 0.06	11.02 ± 0.06	10.40 ± 0.07	9.58 ± 0.04	
2	I/0	18 18 25.95	-13 55 37.95	8.80 ± 0.03	6.88 ± 0.05	5.21 ± 0.02	4.12 ± 0.03	1.05 ± 0.04
3	I/0	18 18 28.60	-13 55 42.31	12.02 ± 0.07	10.89 ± 0.10	10.09 ± 0.07	9.28 ± 0.08	
4	I/0	18 18 13.50	-13 50 17.25	10.11 ± 0.06	9.14 ± 0.05	8.27 ± 0.04	7.48 ± 0.03	
5	I/0	18 18 40.73	-13 53 11.32	12.66 ± 0.06	11.85 ± 0.09	11.30 ± 0.13	10.40 ± 0.08	
6	I/0	18 19 21.68	-13 57 35.17	13.19 ± 0.10	12.38 ± 0.11	11.73 ± 0.14	10.82 ± 0.10	
7	I/0	18 18 12.28	-13 47 43.82	9.45 ± 0.07	9.02 ± 0.05	8.42 ± 0.04	7.14 ± 0.03	
8	I/0	18 18 40.82	-13 50 23.52	11.70 ± 0.06	10.67 ± 0.06	9.64 ± 0.05	8.91 ± 0.06	
9	I/0	18 18 41.54	-13 50 18.36	11.99 ± 0.07	11.13 ± 0.06	10.39 ± 0.06	9.67 ± 0.05	
10	I/0	18 19 17.08	-13 54 50.55	9.71 ± 0.04	9.11 ± 0.04	8.46 ± 0.04	7.02 ± 0.02	
11	I/0	18 18 11.84	-13 46 16.78	12.79 ± 0.06	12.00 ± 0.13	10.55 ± 0.08	9.04 ± 0.06	
12	I/0	18 18 05.76	-13 45 28.67	12.75 ± 0.13	11.81 ± 0.14	10.47 ± 0.14	9.32 ± 0.15	
13	I/0	18 18 10.95	-13 45 24.76	13.06 ± 0.06	11.26 ± 0.06	10.06 ± 0.07	9.13 ± 0.05	
14	I/0	18 18 49.87	-13 50 14.37	11.07 ± 0.07	10.58 ± 0.08	10.03 ± 0.10	8.66 ± 0.10	
15	I/0	18 18 52.37	-13 50 28.42	11.00 ± 0.09	10.19 ± 0.07	9.51 ± 0.08	8.67 ± 0.09	
16	I/0	18 17 53.16	-13 42 42.13	7.93 ± 0.04	6.91 ± 0.05	6.00 ± 0.03	5.28 ± 0.04	1.92 ± 0.03
17	I/0	18 18 52.99	-13 49 38.06	11.74 ± 0.05	9.95 ± 0.06	8.35 ± 0.04	6.94 ± 0.04	3.75 ± 0.51
18	I/0	18 18 51.55	-13 49 12.28	11.89 ± 0.07	11.15 ± 0.08	9.85 ± 0.11	8.61 ± 0.13	
19	I/0	18 18 40.22	-13 47 41.54	12.25 ± 0.08	11.40 ± 0.07	10.64 ± 0.10	9.37 ± 0.04	4.44 ± 0.23
20	I/0	18 18 47.96	-13 48 36.23	11.29 ± 0.05	10.80 ± 0.07	10.22 ± 0.05	9.09 ± 0.08	
21	I/0	18 18 44.63	-13 48 00.42	11.70 ± 0.07	10.89 ± 0.07	10.33 ± 0.06	9.52 ± 0.06	
22	I/0	18 18 40.84	-13 47 27.84	12.31 ± 0.08	11.89 ± 0.09	11.57 ± 0.15	10.10 ± 0.12	
23	I/0	18 18 45.77	-13 47 57.73	12.56 ± 0.09	12.05 ± 0.11	11.44 ± 0.13	10.28 ± 0.07	
24	I/0	18 18 45.84	-13 46 53.77	11.04 ± 0.10	10.23 ± 0.11	9.78 ± 0.09	8.89 ± 0.07	

Continued on next page...

TABLE 9 – Continued

Source #	IRAC Class	R.A. J2000	Decl. J2000	[3.6]	[4.5]	[5.8]	[8.0]	[24]
25	I/0	18 18 45.19	-13 46 27.61	13.10 ± 0.10	12.25 ± 0.10	11.30 ± 0.12	9.94 ± 0.07	
26	I/0	18 19 27.07	-13 51 28.86	13.83 ± 0.12	11.68 ± 0.09	10.35 ± 0.06	9.63 ± 0.06	
27	I/0	18 18 28.23	-13 43 34.91	12.06 ± 0.07	11.53 ± 0.07	10.76 ± 0.10	9.64 ± 0.12	
28	I/0	18 18 51.72	-13 45 08.22	11.35 ± 0.09	10.88 ± 0.08	10.23 ± 0.09	9.06 ± 0.14	
29	I/0	18 18 38.63	-13 41 57.33	10.14 ± 0.13	9.28 ± 0.05	8.35 ± 0.10	7.48 ± 0.14	
30	I/0	18 19 05.18	-13 45 19.32	9.38 ± 0.08	8.22 ± 0.06	7.17 ± 0.05	6.32 ± 0.08	2.60 ± 0.06
31	I/0	18 19 04.57	-13 45 13.89	12.00 ± 0.08	11.11 ± 0.09	10.51 ± 0.09	9.71 ± 0.05	
32	I/0	18 19 07.33	-13 45 23.62	9.53 ± 0.09	7.54 ± 0.10	6.30 ± 0.03	5.39 ± 0.07	1.04 ± 0.07
33	I/0	18 19 31.04	-13 45 28.90	11.18 ± 0.06	10.33 ± 0.07	9.44 ± 0.05	8.60 ± 0.07	
34	I/0	18 18 45.05	-13 39 12.61	9.67 ± 0.04	8.24 ± 0.04	7.15 ± 0.03	6.34 ± 0.03	3.79 ± 0.15
35	I/0	18 19 35.83	-13 45 15.11	12.29 ± 0.07	11.43 ± 0.07	10.89 ± 0.10	10.15 ± 0.07	
36	I/0	18 19 11.71	-13 39 57.53	13.88 ± 0.10	12.85 ± 0.14	11.48 ± 0.10	10.24 ± 0.08	
37	I/0	18 19 38.60	-13 42 40.84	11.40 ± 0.05	9.89 ± 0.05	8.69 ± 0.04	7.49 ± 0.03	
38	I/0	18 19 03.91	-13 36 47.82	8.51 ± 0.04	7.33 ± 0.03	6.26 ± 0.04	5.27 ± 0.02	2.89 ± 0.04
39	I/0	18 18 32.85	-13 32 39.21	10.20 ± 0.04	8.64 ± 0.05	7.46 ± 0.04	6.53 ± 0.03	
40	I/0	18 19 07.73	-13 36 45.48	11.47 ± 0.05	10.63 ± 0.04	9.99 ± 0.07	9.36 ± 0.05	
41	I/0	18 19 08.58	-13 36 45.57	12.57 ± 0.07	11.52 ± 0.05	10.77 ± 0.08	9.91 ± 0.08	
42	I/0	18 19 07.44	-13 36 29.49	11.78 ± 0.06	10.90 ± 0.06	10.18 ± 0.06	9.78 ± 0.08	
43	I/0	18 19 08.64	-13 36 24.89	8.56 ± 0.10	7.68 ± 0.07	6.71 ± 0.03	6.00 ± 0.03	3.05 ± 0.04
44	I/0	18 19 11.24	-13 35 45.95	10.78 ± 0.04	9.77 ± 0.05	8.97 ± 0.05	8.32 ± 0.03	
45	I/0	18 19 21.11	-13 36 28.81	13.14 ± 0.06	12.66 ± 0.11	11.98 ± 0.14	10.45 ± 0.14	
46	I/0	18 19 09.48	-13 34 27.44	9.83 ± 0.04	8.76 ± 0.05	7.76 ± 0.03	6.76 ± 0.03	3.50 ± 0.05
47	I/0	18 19 35.92	-13 37 21.13	8.43 ± 0.04	7.52 ± 0.04	6.56 ± 0.03	5.86 ± 0.03	
48	I/0	18 19 07.42	-13 33 12.97	11.95 ± 0.05	11.04 ± 0.07	10.62 ± 0.07	9.85 ± 0.07	
49	I/0	18 19 14.69	-13 34 08.84	11.43 ± 0.05	10.45 ± 0.06	9.71 ± 0.06	8.69 ± 0.09	
50	I/0	18 19 12.95	-13 33 43.64	9.99 ± 0.05	7.66 ± 0.06	6.26 ± 0.03	5.48 ± 0.03	1.66 ± 0.03
51	I/0	18 19 11.95	-13 33 26.52	11.69 ± 0.06	10.21 ± 0.07	9.19 ± 0.05	8.25 ± 0.05	

Continued on next page...

TABLE 9 – Continued

Source #	IRAC Class	R.A. J2000	Decl. J2000	[3.6]	[4.5]	[5.8]	[8.0]	[24]
52	I/0	18 19 14.74	-13 33 43.41	12.45 ± 0.05	11.50 ± 0.07	10.88 ± 0.08	9.97 ± 0.09	
53	I/0	18 19 16.87	-13 33 40.13	13.93 ± 0.09	11.57 ± 0.08	9.93 ± 0.06	8.97 ± 0.07	
54	I/0	18 19 15.69	-13 33 30.21	11.90 ± 0.07	11.05 ± 0.09	10.69 ± 0.05	10.11 ± 0.08	
55	I/0	18 19 10.95	-13 32 27.66	11.66 ± 0.05	10.28 ± 0.04	9.27 ± 0.05	8.59 ± 0.03	
56	I/0	18 19 25.92	-13 33 00.01	12.23 ± 0.06	11.37 ± 0.10	11.24 ± 0.13	10.30 ± 0.08	
57	I/0	18 19 23.98	-13 31 00.07	12.31 ± 0.12	11.67 ± 0.10	11.35 ± 0.11	10.17 ± 0.06	
58	I/0	18 18 11.43	-13 41 18.82	7.53 ± 0.04	6.50 ± 0.02	5.37 ± 0.03	4.72 ± 0.04	2.56 ± 0.12
59	I/0	18 19 16.21	-13 45 04.33	7.13 ± 0.03	6.27 ± 0.03	5.41 ± 0.03	4.93 ± 0.03	
60	I/0	18 19 25.34	-13 45 35.71	7.85 ± 0.07	6.31 ± 0.02	5.26 ± 0.03	4.41 ± 0.03	0.95 ± 0.06
61	I/0	18 18 48.66	-13 49 55.24	9.79 ± 0.05	9.39 ± 0.06	7.99 ± 0.03	8.18 ± 0.05	3.77 ± 0.14
62	I/0	18 18 50.07	-13 48 58.23	8.97 ± 0.04	8.40 ± 0.04	6.53 ± 0.03	7.18 ± 0.03	0.59 ± 0.04
63	I/0	18 19 15.29	-13 39 41.00	11.59 ± 0.07	9.79 ± 0.06	8.27 ± 0.05	7.36 ± 0.03	3.92 ± 0.22
64	I/0	18 19 26.57	-13 45 39.00	10.49 ± 0.06	9.99 ± 0.05	8.37 ± 0.04	8.77 ± 0.05	2.96 ± 0.23
65	I/II	18 18 41.59	-13 56 43.60	12.20 ± 0.06	12.14 ± 0.12	11.37 ± 0.11	9.93 ± 0.13	
66	I/II	18 17 53.85	-13 50 10.41	12.24 ± 0.06	12.13 ± 0.06	11.61 ± 0.13	10.42 ± 0.08	
67	I/II	18 17 53.57	-13 44 23.15	12.74 ± 0.06	12.64 ± 0.09	11.94 ± 0.14	10.82 ± 0.11	
68	I/II	18 18 47.97	-13 47 13.65	11.62 ± 0.06	11.28 ± 0.07	9.70 ± 0.06	8.44 ± 0.05	
69	I/II	18 18 55.54	-13 48 02.00	10.82 ± 0.04	10.65 ± 0.06	10.38 ± 0.07	9.22 ± 0.04	
70	I/II	18 18 36.05	-13 44 57.89	11.24 ± 0.08	10.84 ± 0.07	10.30 ± 0.09	8.99 ± 0.04	
71	I/II	18 19 06.19	-13 44 28.74	11.70 ± 0.06	11.53 ± 0.07	11.39 ± 0.10	10.15 ± 0.06	
72	I/II	18 19 27.20	-13 35 17.59	11.51 ± 0.05	11.60 ± 0.07	11.43 ± 0.12	10.33 ± 0.14	
73	II	18 18 39.49	-14 00 34.12	11.26 ± 0.04	10.83 ± 0.06	10.44 ± 0.07	9.58 ± 0.04	
74	II	18 18 10.98	-13 56 42.43	12.04 ± 0.05	12.03 ± 0.08	12.01 ± 0.12	11.29 ± 0.12	
75	II	18 18 26.30	-13 58 13.47	12.48 ± 0.09	11.97 ± 0.11	11.55 ± 0.10	10.70 ± 0.10	
76	II	18 18 14.98	-13 55 12.51	11.66 ± 0.09	11.76 ± 0.08	11.58 ± 0.12	10.79 ± 0.14	
77	II	18 18 54.25	-13 59 39.47	12.05 ± 0.06	11.95 ± 0.08	11.54 ± 0.10	10.79 ± 0.10	
78	II	18 19 05.80	-14 00 49.34	11.16 ± 0.05	10.79 ± 0.06	10.63 ± 0.07	9.79 ± 0.08	

Continued on next page...

TABLE 9 – Continued

Source #	IRAC Class	R.A. J2000	Decl. J2000	[3.6]	[4.5]	[5.8]	[8.0]	[24]
79	II	18 18 43.03	-13 55 21.10	7.50 ± 0.04	6.98 ± 0.04	6.24 ± 0.03	5.66 ± 0.03	
80	II	18 18 07.74	-13 50 28.25	9.71 ± 0.04	9.41 ± 0.05	8.95 ± 0.04	7.93 ± 0.03	
81	II	18 19 13.83	-13 58 44.93	8.92 ± 0.03	8.60 ± 0.05	8.12 ± 0.04	7.28 ± 0.03	
82	II	18 18 37.38	-13 53 49.74	11.09 ± 0.04	10.82 ± 0.07	10.33 ± 0.07	9.56 ± 0.09	
83	II	18 18 11.82	-13 50 05.58	12.11 ± 0.05	11.97 ± 0.08	11.94 ± 0.13	11.15 ± 0.14	
84	II	18 17 40.17	-13 45 56.39	11.18 ± 0.04	11.12 ± 0.06	10.59 ± 0.09	9.70 ± 0.14	
85	II	18 18 29.97	-13 52 15.95	12.87 ± 0.09	12.27 ± 0.09	11.92 ± 0.15	11.09 ± 0.13	
86	II	18 17 41.27	-13 45 33.42	12.04 ± 0.07	11.92 ± 0.09	11.57 ± 0.12	10.48 ± 0.15	
87	II	18 18 40.61	-13 53 02.40	11.08 ± 0.10	10.32 ± 0.10	9.72 ± 0.09	9.11 ± 0.07	
88	II	18 18 41.22	-13 53 06.95	11.42 ± 0.07	10.96 ± 0.09	10.37 ± 0.09	9.52 ± 0.14	
89	II	18 18 32.04	-13 51 50.35	11.69 ± 0.06	11.04 ± 0.05	10.45 ± 0.08	9.64 ± 0.03	
90	II	18 18 02.37	-13 47 31.24	11.59 ± 0.05	11.05 ± 0.07	10.56 ± 0.08	9.81 ± 0.04	
91	II	18 17 32.85	-13 43 25.16	12.16 ± 0.06	12.05 ± 0.09	11.97 ± 0.14	11.10 ± 0.13	
92	II	18 18 08.86	-13 47 39.84	11.42 ± 0.05	10.81 ± 0.06	10.32 ± 0.06	9.70 ± 0.08	
93	II	18 18 38.22	-13 51 16.95	12.28 ± 0.07	11.79 ± 0.09	11.21 ± 0.10	10.29 ± 0.07	
94	II	18 18 26.60	-13 48 50.36	11.86 ± 0.06	11.07 ± 0.07	10.54 ± 0.05	9.87 ± 0.04	
95	II	18 17 47.40	-13 43 20.79	7.33 ± 0.04	6.82 ± 0.04	6.13 ± 0.04	5.45 ± 0.02	
96	II	18 18 32.78	-13 49 10.10	12.23 ± 0.08	11.74 ± 0.11	11.01 ± 0.11	10.25 ± 0.09	
97	II	18 18 23.21	-13 47 49.82	9.68 ± 0.04	9.29 ± 0.08	8.83 ± 0.04	7.97 ± 0.03	
98	II	18 18 41.61	-13 50 13.31	11.62 ± 0.07	10.98 ± 0.06	10.33 ± 0.06	9.29 ± 0.03	
99	II	18 18 44.59	-13 50 34.79	11.86 ± 0.07	11.40 ± 0.07	11.05 ± 0.10	10.38 ± 0.06	
100	II	18 18 39.01	-13 49 50.07	12.06 ± 0.06	11.76 ± 0.07	11.31 ± 0.09	10.50 ± 0.07	
101	II	18 17 47.13	-13 42 59.80	11.47 ± 0.08	11.40 ± 0.11	11.32 ± 0.12	10.28 ± 0.15	2.87 ± 0.04
102	II	18 18 33.80	-13 49 03.96	12.74 ± 0.08	12.15 ± 0.07	11.52 ± 0.11	10.54 ± 0.05	
103	II	18 18 51.07	-13 51 13.55	11.84 ± 0.05	11.78 ± 0.08	11.35 ± 0.13	10.30 ± 0.13	
104	II	18 18 12.62	-13 46 09.16	11.99 ± 0.06	11.46 ± 0.08	11.25 ± 0.11	10.65 ± 0.11	
105	II	18 18 33.21	-13 48 47.76	12.54 ± 0.05	12.13 ± 0.09	11.68 ± 0.10	11.10 ± 0.11	

Continued on next page...

TABLE 9 – Continued

Source #	IRAC Class	R.A. J2000	Decl. J2000	[3.6]	[4.5]	[5.8]	[8.0]	[24]
106	II	18 18 31.32	-13 48 32.28	11.77 ± 0.07	11.40 ± 0.10	11.03 ± 0.09	10.37 ± 0.06	
107	II	18 18 43.27	-13 50 03.53	12.36 ± 0.08	11.95 ± 0.11	11.34 ± 0.11	10.50 ± 0.07	
108	II	18 18 48.97	-13 50 47.98	11.45 ± 0.07	11.01 ± 0.08	9.92 ± 0.08	9.13 ± 0.15	
109	II	18 18 42.31	-13 49 54.33	11.84 ± 0.06	11.50 ± 0.08	11.09 ± 0.08	10.41 ± 0.07	
110	II	18 18 42.00	-13 49 42.37	10.94 ± 0.05	10.46 ± 0.06	10.05 ± 0.06	9.32 ± 0.04	
111	II	18 17 42.43	-13 41 44.37	12.03 ± 0.06	11.38 ± 0.07	10.76 ± 0.07	10.16 ± 0.06	
112	II	18 18 35.39	-13 48 30.23	12.26 ± 0.07	11.84 ± 0.09	11.13 ± 0.09	10.35 ± 0.06	
113	II	18 18 37.08	-13 48 40.53	12.97 ± 0.08	12.53 ± 0.10	11.92 ± 0.11	11.14 ± 0.10	
114	II	18 18 35.76	-13 48 20.43	12.68 ± 0.07	11.98 ± 0.09	11.29 ± 0.10	10.70 ± 0.08	
115	II	18 18 12.35	-13 45 02.92	11.90 ± 0.05	11.22 ± 0.09	10.69 ± 0.09	10.11 ± 0.06	
116	II	18 18 44.44	-13 49 12.78	12.53 ± 0.07	12.10 ± 0.09	11.33 ± 0.10	10.55 ± 0.08	
117	II	18 18 46.31	-13 49 26.82	12.26 ± 0.07	11.76 ± 0.08	11.14 ± 0.09	10.11 ± 0.10	
118	II	18 18 35.31	-13 47 59.02	12.41 ± 0.10	11.97 ± 0.08	11.83 ± 0.14	11.08 ± 0.11	
119	II	18 18 47.01	-13 49 29.14	11.54 ± 0.06	11.13 ± 0.07	10.78 ± 0.09	9.97 ± 0.07	
120	II	18 18 40.96	-13 48 39.39	12.53 ± 0.05	11.89 ± 0.09	11.27 ± 0.07	10.44 ± 0.07	
121	II	18 18 46.86	-13 49 16.46	10.68 ± 0.05	10.22 ± 0.05	9.78 ± 0.05	8.87 ± 0.03	
122	II	18 18 37.93	-13 48 05.90	12.39 ± 0.06	11.90 ± 0.08	11.52 ± 0.11	10.53 ± 0.06	
123	II	18 18 36.31	-13 47 52.07	12.65 ± 0.11	12.40 ± 0.14	11.80 ± 0.14	11.00 ± 0.14	
124	II	18 18 31.40	-13 47 06.12	11.75 ± 0.14	11.37 ± 0.15	11.09 ± 0.11	10.45 ± 0.12	
125	II	18 18 39.39	-13 48 08.35	12.43 ± 0.06	11.99 ± 0.09	11.76 ± 0.12	11.15 ± 0.11	
126	II	18 18 16.85	-13 45 11.31	11.26 ± 0.06	10.70 ± 0.08	10.21 ± 0.06	9.61 ± 0.08	
127	II	18 18 58.29	-13 50 29.85	10.72 ± 0.05	10.14 ± 0.05	9.51 ± 0.07	8.78 ± 0.13	
128	II	18 18 45.17	-13 48 37.35	10.77 ± 0.05	10.17 ± 0.06	9.68 ± 0.04	8.88 ± 0.04	
129	II	18 18 42.51	-13 48 08.57	12.69 ± 0.10	12.21 ± 0.15	11.84 ± 0.13	11.14 ± 0.11	
130	II	18 18 42.00	-13 48 03.60	10.91 ± 0.07	10.40 ± 0.07	9.79 ± 0.06	9.06 ± 0.04	
131	II	18 18 39.77	-13 47 43.79	8.60 ± 0.05	8.04 ± 0.04	7.46 ± 0.03	6.46 ± 0.02	4.44 ± 0.23
132	II	18 18 37.19	-13 47 20.63	11.69 ± 0.06	11.14 ± 0.08	10.67 ± 0.07	9.92 ± 0.06	

Continued on next page...

TABLE 9 – Continued

Source #	IRAC Class	R.A. J2000	Decl. J2000	[3.6]	[4.5]	[5.8]	[8.0]	[24]
133	II	18 18 41.08	-13 47 49.29	12.78 ± 0.10	12.27 ± 0.13	11.54 ± 0.14	10.76 ± 0.08	
134	II	18 18 45.21	-13 48 13.08	12.50 ± 0.06	11.88 ± 0.07	11.64 ± 0.10	10.73 ± 0.09	
135	II	18 18 30.56	-13 46 13.49	12.69 ± 0.08	12.13 ± 0.09	11.59 ± 0.11	10.71 ± 0.14	
136	II	18 18 48.92	-13 48 32.16	12.03 ± 0.05	11.55 ± 0.08	10.88 ± 0.08	9.80 ± 0.11	
137	II	18 18 38.70	-13 47 10.27	11.37 ± 0.08	10.93 ± 0.07	10.71 ± 0.09	10.12 ± 0.07	
138	II	18 18 46.28	-13 48 08.82	12.03 ± 0.05	11.77 ± 0.09	11.50 ± 0.13	10.73 ± 0.09	
139	II	18 18 42.49	-13 47 35.26	11.86 ± 0.05	11.53 ± 0.07	11.36 ± 0.10	10.67 ± 0.09	
140	II	18 18 45.45	-13 47 57.36	12.02 ± 0.07	11.33 ± 0.08	10.90 ± 0.09	10.34 ± 0.08	
141	II	18 18 45.02	-13 47 52.16	12.01 ± 0.07	11.36 ± 0.08	10.84 ± 0.09	10.04 ± 0.15	
142	II	18 18 18.37	-13 44 22.02	11.36 ± 0.05	10.80 ± 0.06	10.26 ± 0.06	9.49 ± 0.07	
143	II	18 19 00.92	-13 49 52.82	12.16 ± 0.05	11.90 ± 0.10	11.51 ± 0.10	10.63 ± 0.10	
144	II	18 18 42.80	-13 47 27.96	12.11 ± 0.07	11.62 ± 0.12	10.94 ± 0.09	9.98 ± 0.07	
145	II	18 18 45.38	-13 47 46.57	11.48 ± 0.04	10.79 ± 0.06	10.15 ± 0.07	9.42 ± 0.06	
146	II	18 18 40.54	-13 47 00.56	11.23 ± 0.06	10.67 ± 0.05	10.08 ± 0.08	9.15 ± 0.04	
147	II	18 18 40.07	-13 46 52.77	10.92 ± 0.05	10.49 ± 0.05	9.99 ± 0.06	9.19 ± 0.03	
148	II	18 18 43.00	-13 47 15.27	11.19 ± 0.06	10.52 ± 0.07	10.04 ± 0.07	9.52 ± 0.07	
149	II	18 19 09.39	-13 50 41.14	7.74 ± 0.03	7.15 ± 0.06	6.43 ± 0.03	5.46 ± 0.03	3.31 ± 0.04
150	II	18 18 45.12	-13 47 23.54	9.32 ± 0.05	8.87 ± 0.05	8.19 ± 0.05	7.49 ± 0.08	
151	II	18 18 48.64	-13 47 49.56	11.14 ± 0.08	10.75 ± 0.07	10.36 ± 0.06	9.70 ± 0.10	
152	II	18 18 31.74	-13 45 35.81	11.44 ± 0.05	10.97 ± 0.06	10.54 ± 0.06	9.90 ± 0.08	
153	II	18 19 03.92	-13 49 45.40	12.18 ± 0.06	11.75 ± 0.09	11.26 ± 0.10	10.45 ± 0.13	
154	II	18 18 35.34	-13 45 57.28	11.55 ± 0.06	11.00 ± 0.06	10.49 ± 0.09	9.96 ± 0.07	
155	II	18 18 40.08	-13 46 31.46	10.81 ± 0.06	10.39 ± 0.06	10.09 ± 0.06	9.55 ± 0.05	
156	II	18 18 40.86	-13 46 36.15	10.84 ± 0.07	10.38 ± 0.05	9.88 ± 0.07	8.99 ± 0.05	
157	II	18 18 35.34	-13 45 48.23	10.70 ± 0.04	10.39 ± 0.08	9.93 ± 0.06	9.03 ± 0.06	
158	II	18 18 41.56	-13 46 31.13	8.53 ± 0.05	8.23 ± 0.04	7.81 ± 0.03	6.96 ± 0.03	
159	II	18 18 37.29	-13 45 57.35	11.31 ± 0.08	10.97 ± 0.10	10.49 ± 0.09	9.74 ± 0.05	

Continued on next page...

TABLE 9 – Continued

Source #	IRAC Class	R.A. J2000	Decl. J2000	[3.6]	[4.5]	[5.8]	[8.0]	[24]
160	II	18 18 40.50	-13 46 19.53	11.71 ± 0.06	11.13 ± 0.07	10.77 ± 0.09	10.04 ± 0.11	
161	II	18 18 43.20	-13 46 39.45	10.70 ± 0.07	10.41 ± 0.07	10.00 ± 0.06	9.22 ± 0.04	
162	II	18 18 42.48	-13 46 27.22	12.26 ± 0.06	11.73 ± 0.10	11.00 ± 0.09	10.40 ± 0.15	
163	II	18 18 39.72	-13 45 51.88	10.98 ± 0.05	10.70 ± 0.07	10.16 ± 0.07	9.41 ± 0.05	
164	II	18 18 42.40	-13 46 11.22	11.40 ± 0.05	10.83 ± 0.08	10.23 ± 0.07	9.71 ± 0.10	
165	II	18 18 43.23	-13 46 15.01	12.19 ± 0.07	11.66 ± 0.08	11.17 ± 0.11	10.09 ± 0.09	
166	II	18 18 49.87	-13 46 59.55	9.73 ± 0.04	9.23 ± 0.05	8.67 ± 0.04	8.10 ± 0.06	
167	II	18 18 43.75	-13 46 09.26	10.25 ± 0.07	9.66 ± 0.10	9.13 ± 0.05	8.35 ± 0.08	
168	II	18 18 55.44	-13 47 36.69	11.99 ± 0.13	11.75 ± 0.14	11.33 ± 0.14	10.55 ± 0.11	
169	II	18 18 41.31	-13 45 45.22	11.17 ± 0.06	10.79 ± 0.07	10.57 ± 0.08	9.87 ± 0.11	
170	II	18 18 43.75	-13 45 59.09	11.13 ± 0.05	10.72 ± 0.07	10.16 ± 0.06	9.34 ± 0.06	
171	II	18 19 04.72	-13 48 38.28	12.17 ± 0.06	11.70 ± 0.09	10.94 ± 0.06	10.14 ± 0.07	
172	II	18 18 39.25	-13 44 58.73	12.50 ± 0.10	11.97 ± 0.08	11.32 ± 0.13	10.29 ± 0.09	6.19 ± 0.11
173	II	18 18 52.24	-13 46 39.15	10.80 ± 0.05	10.30 ± 0.05	10.07 ± 0.06	9.36 ± 0.04	
174	II	18 19 20.75	-13 50 14.55	9.29 ± 0.04	8.76 ± 0.04	8.34 ± 0.04	7.52 ± 0.04	
175	II	18 18 55.04	-13 46 44.44	10.98 ± 0.05	10.61 ± 0.06	10.29 ± 0.06	9.59 ± 0.05	
176	II	18 18 19.96	-13 41 51.15	11.03 ± 0.05	10.60 ± 0.07	10.17 ± 0.07	9.56 ± 0.14	
177	II	18 19 24.36	-13 50 10.24	10.87 ± 0.10	10.23 ± 0.06	9.61 ± 0.07	8.87 ± 0.14	
178	II	18 18 47.93	-13 45 20.02	11.04 ± 0.05	10.55 ± 0.07	10.04 ± 0.10	9.28 ± 0.15	
179	II	18 19 12.97	-13 48 30.10	12.35 ± 0.07	11.88 ± 0.09	11.53 ± 0.13	10.50 ± 0.11	
180	II	18 18 50.24	-13 45 31.92	11.64 ± 0.07	11.07 ± 0.06	10.77 ± 0.11	10.01 ± 0.09	
181	II	18 19 20.02	-13 49 12.80	10.96 ± 0.05	10.58 ± 0.06	10.19 ± 0.07	9.54 ± 0.05	
182	II	18 18 52.64	-13 45 22.98	12.52 ± 0.06	12.04 ± 0.09	11.80 ± 0.15	11.01 ± 0.15	
183	II	18 18 58.56	-13 45 34.56	10.44 ± 0.04	10.06 ± 0.05	9.65 ± 0.06	8.56 ± 0.04	
184	II	18 18 29.79	-13 41 48.81	10.68 ± 0.07	9.96 ± 0.06	9.29 ± 0.06	8.53 ± 0.13	
185	II	18 19 22.65	-13 48 40.24	11.57 ± 0.05	10.97 ± 0.06	10.70 ± 0.08	9.73 ± 0.09	
186	II	18 19 20.10	-13 48 06.20	11.82 ± 0.08	11.31 ± 0.10	10.90 ± 0.06	10.29 ± 0.09	

Continued on next page...

TABLE 9 – Continued

Source #	IRAC Class	R.A. J2000	Decl. J2000	[3.6]	[4.5]	[5.8]	[8.0]	[24]
187	II	18 18 45.00	-13 43 19.37	7.88 ± 0.05	7.13 ± 0.04	6.52 ± 0.03	5.94 ± 0.04	
188	II	18 19 03.20	-13 45 39.43	11.41 ± 0.05	10.85 ± 0.06	10.38 ± 0.06	9.66 ± 0.05	
189	II	18 19 01.60	-13 45 16.20	9.76 ± 0.06	9.34 ± 0.05	8.85 ± 0.04	7.88 ± 0.03	
190	II	18 19 02.34	-13 45 18.41	11.51 ± 0.08	11.37 ± 0.08	10.90 ± 0.10	10.19 ± 0.07	
191	II	18 18 57.76	-13 44 42.44	10.60 ± 0.05	10.20 ± 0.06	9.81 ± 0.06	9.17 ± 0.04	
192	II	18 19 17.66	-13 47 17.30	11.74 ± 0.04	11.28 ± 0.08	10.89 ± 0.09	10.30 ± 0.08	
193	II	18 19 04.36	-13 45 23.12	12.13 ± 0.06	11.55 ± 0.08	10.90 ± 0.10	10.09 ± 0.09	
194	II	18 19 15.00	-13 46 43.52	12.13 ± 0.06	11.65 ± 0.08	11.08 ± 0.09	10.23 ± 0.07	
195	II	18 19 01.74	-13 44 31.88	10.02 ± 0.05	9.40 ± 0.05	8.92 ± 0.04	8.33 ± 0.04	
196	II	18 19 20.93	-13 46 58.94	12.32 ± 0.06	11.80 ± 0.08	11.42 ± 0.13	10.63 ± 0.12	
197	II	18 19 05.67	-13 44 44.85	11.06 ± 0.06	10.70 ± 0.07	10.43 ± 0.07	9.75 ± 0.09	
198	II	18 18 47.43	-13 42 03.66	11.69 ± 0.06	11.34 ± 0.08	10.90 ± 0.12	10.02 ± 0.09	
199	II	18 18 27.85	-13 39 11.30	11.77 ± 0.05	11.28 ± 0.09	10.96 ± 0.12	10.41 ± 0.14	
200	II	18 19 04.56	-13 43 58.31	9.61 ± 0.07	9.16 ± 0.08	8.77 ± 0.09	7.87 ± 0.06	
201	II	18 18 59.57	-13 43 13.10	12.36 ± 0.05	12.02 ± 0.08	11.69 ± 0.15	10.99 ± 0.15	
202	II	18 19 01.75	-13 43 24.64	12.32 ± 0.08	11.64 ± 0.09	11.18 ± 0.07	10.33 ± 0.08	
203	II	18 18 53.46	-13 42 10.05	11.86 ± 0.06	11.24 ± 0.07	10.27 ± 0.07	9.36 ± 0.13	
204	II	18 19 08.54	-13 44 02.76	10.94 ± 0.05	10.52 ± 0.05	10.18 ± 0.05	9.47 ± 0.04	
205	II	18 18 39.38	-13 39 23.23	12.15 ± 0.07	11.60 ± 0.07	10.94 ± 0.09	10.24 ± 0.10	
206	II	18 18 48.52	-13 39 42.02	12.28 ± 0.05	11.84 ± 0.10	11.18 ± 0.09	10.54 ± 0.13	
207	II	18 18 31.60	-13 37 15.45	11.67 ± 0.04	11.07 ± 0.04	10.50 ± 0.08	9.75 ± 0.04	
208	II	18 19 33.91	-13 44 20.91	11.92 ± 0.06	11.45 ± 0.07	10.99 ± 0.10	10.31 ± 0.12	
209	II	18 19 20.88	-13 42 04.20	8.85 ± 0.04	8.41 ± 0.04	7.86 ± 0.03	6.86 ± 0.03	4.44 ± 0.06
210	II	18 19 13.27	-13 38 08.86	13.24 ± 0.07	12.68 ± 0.11	11.87 ± 0.13	11.31 ± 0.14	
211	II	18 18 47.05	-13 34 43.12	10.95 ± 0.06	10.41 ± 0.07	9.55 ± 0.04	8.98 ± 0.09	
212	II	18 19 17.87	-13 38 32.61	11.98 ± 0.05	11.29 ± 0.06	10.72 ± 0.10	9.93 ± 0.13	
213	II	18 18 35.53	-13 32 59.59	11.29 ± 0.05	10.88 ± 0.06	10.32 ± 0.07	9.64 ± 0.06	

Continued on next page...

TABLE 9 – Continued

Source #	IRAC Class	R.A. J2000	Decl. J2000	[3.6]	[4.5]	[5.8]	[8.0]	[24]
214	II	18 18 36.05	-13 32 55.24	10.95 ± 0.05	11.05 ± 0.10	10.61 ± 0.09	9.87 ± 0.12	
215	II	18 18 36.82	-13 32 47.65	11.78 ± 0.06	11.24 ± 0.07	10.86 ± 0.14	9.91 ± 0.12	
216	II	18 19 06.49	-13 36 31.01	12.26 ± 0.05	11.58 ± 0.07	10.88 ± 0.08	9.89 ± 0.06	
217	II	18 19 07.87	-13 36 16.42	11.80 ± 0.08	11.13 ± 0.12	10.30 ± 0.08	9.46 ± 0.08	
218	II	18 19 08.88	-13 36 19.17	11.83 ± 0.07	11.25 ± 0.07	10.84 ± 0.09	10.32 ± 0.10	
219	II	18 19 06.12	-13 35 52.68	10.65 ± 0.04	10.03 ± 0.06	9.50 ± 0.05	8.87 ± 0.05	
220	II	18 19 22.14	-13 37 34.21	12.10 ± 0.09	11.54 ± 0.07	10.98 ± 0.11	9.96 ± 0.12	
221	II	18 18 42.58	-13 31 30.82	12.93 ± 0.08	12.54 ± 0.13	11.55 ± 0.11	10.74 ± 0.12	
222	II	18 19 19.20	-13 35 41.90	12.05 ± 0.06	11.36 ± 0.07	10.96 ± 0.09	10.34 ± 0.10	
223	II	18 19 10.04	-13 33 39.42	12.42 ± 0.05	11.70 ± 0.07	10.94 ± 0.05	10.30 ± 0.08	
224	II	18 19 14.19	-13 33 55.55	9.44 ± 0.03	8.77 ± 0.05	8.11 ± 0.03	7.38 ± 0.04	
225	II	18 19 26.22	-13 35 12.20	10.09 ± 0.04	9.70 ± 0.04	9.28 ± 0.04	8.50 ± 0.03	
226	II	18 19 18.07	-13 33 55.33	11.88 ± 0.06	11.10 ± 0.07	10.23 ± 0.08	9.59 ± 0.14	
227	II	18 19 13.20	-13 33 08.17	12.69 ± 0.05	11.96 ± 0.09	11.57 ± 0.11	11.02 ± 0.15	
228	II	18 19 20.37	-13 31 02.86	12.39 ± 0.06	12.07 ± 0.07	11.80 ± 0.13	11.06 ± 0.10	
229	II	18 18 02.88	-13 43 40.50	6.84 ± 0.02	6.07 ± 0.01	5.16 ± 0.03	4.55 ± 0.02	2.19 ± 0.05
230	II	18 18 47.26	-13 54 12.84	6.41 ± 0.01	5.89 ± 0.01	4.93 ± 0.03	4.29 ± 0.02	
231	II	18 18 59.41	-13 57 01.59	9.31 ± 0.05	9.29 ± 0.05	8.74 ± 0.06	7.96 ± 0.06	4.53 ± 0.10
232	II	18 19 04.87	-13 48 20.62	9.28 ± 0.04	9.12 ± 0.10	8.74 ± 0.06	7.93 ± 0.06	2.50 ± 0.17
233	II	18 18 31.90	-13 51 41.16	7.45 ± 0.03	7.18 ± 0.05	6.70 ± 0.03	6.18 ± 0.03	4.14 ± 0.70
234	II	18 18 35.00	-13 53 14.22	6.71 ± 0.02	6.15 ± 0.01	5.41 ± 0.03	4.94 ± 0.02	3.04 ± 0.09
235	II	18 18 45.72	-13 46 36.38	8.00 ± 0.04	7.93 ± 0.04	7.88 ± 0.04	7.28 ± 0.06	1.66 ± 0.04
236	II	18 18 49.08	-13 49 39.03	9.99 ± 0.05	9.97 ± 0.06	9.59 ± 0.05	9.64 ± 0.12	6.19 ± 0.11
237	II	18 19 00.32	-13 42 46.05	9.65 ± 0.04	9.67 ± 0.05	9.46 ± 0.05	9.09 ± 0.10	3.10 ± 0.14

TABLE 10

M16 YSO BEST-FIT PARAMETERS

Source #	Model #	χ^2	Mass ($M_\odot$)	Age ($\times 10^5$ yr)	Temp (K)	Radius ($R_\odot$)	Log(d) (kpc)
1	3016851	2.5	0.96±0.33	2.50	4139	5.63	0.29
2	3010566	58.2	0.38±0.16	0.02	3497	6.05	0.28
3	3015140	1.6	1.53±0.76	1.29	4274	8.53	0.28
4	3009218	7.4	5.17±0.75	1.36	4668	16.35	0.31
5	3003150	1.4	0.43±0.24	0.12	3619	5.54	0.32
6	3005974	0.4	0.29±0.07	0.14	3338	4.42	0.29
7	3015029	10.0	2.79±1.15	1.08	4411	13.16	0.28
8	3005132	66.0	5.60±2.07	0.19	4398	27.33	0.28
9	3017233	2.1	1.18±0.42	0.70	4178	7.41	0.28
10	3007611	20.8	4.31±1.30	7.00	6028	9.20	0.31
11	3007376	2.1	1.19±0.94	0.19	4100	9.40	0.28
12	3015114	0.3	2.17±1.13	0.26	4284	12.98	0.32
13	3012495	11.9	1.45±0.89	0.69	4241	8.54	0.29
14	3006440	6.7	1.22±0.89	0.78	4190	7.55	0.28
15	3006995	0.5	2.10±0.97	1.08	4344	10.91	0.32
16	3006570	68.4	6.04±0.97	0.02	4169	45.45	0.32
17	3005674	58.4	5.73±1.06	2.86	6109	14.27	0.28
18	3005857	11.7	2.33±1.47	3.35	4617	6.36	0.32
19	3004946	4.7	0.82±0.63	0.45	4022	5.99	0.28
20	3006818	12.5	1.92±0.64	3.61	4548	5.53	0.30
21	3016751	7.3	0.89±0.40	2.71	4111	5.26	0.32
22	3007177	0.6	1.62±0.87	1.73	4317	8.29	0.32
23	3019025	8.3	0.44±0.11	0.69	3666	3.94	0.31
24	3012552	1.8	1.65±0.99	1.22	4293	9.05	0.28
25	3014129	4.7	0.73±0.46	0.70	3981	5.26	0.29
26	3020034	9.5	6.77±3.16	0.04	4217	45.75	0.28
27	3010738	6.1	0.85±0.62	0.28	4004	6.70	0.28
28	3008244	4.2	1.11±0.58	2.20	4198	6.25	0.32
29	3014974	11.7	2.88±1.46	1.73	4542	10.10	0.32
30	3012655	10.5	1.33±0.55	0.03	4024	13.36	0.28
31	3008491	16.7	2.56±1.58	0.34	4340	13.90	0.31
32	3014813	15.5	2.13±0.41	0.01	4094	19.80	0.32
33	3010466	1.0	2.13±1.18	1.08	4347	11.01	0.31
34	3005923	34.0	2.88±0.03	0.02	4175	22.48	0.32
35	3013474	4.0	1.10±0.31	0.76	4157	6.95	0.31
36	3011970	1.0	0.78±0.76	0.02	3882	8.51	0.28
37	3015171	9.1	1.67±0.74	0.09	4180	12.15	0.28

Continued on next page...

TABLE 10 – Continued

Source #	Model #	χ^2	Mass ($M_\odot$)	Age ($\times 10^5$ yr)	Temp (K)	Radius ($R_\odot$)	Log(d) (kpc)
38	3011198	129.0	4.31±0.79	9.53	9877	5.90	0.29
39	3011507	13.3	3.02±1.93	0.04	4245	20.33	0.28
40	3013492	1.3	1.75±1.03	1.83	4359	8.21	0.29
41	3017892	3.7	0.95±0.36	0.22	4025	7.94	0.32
42	3017426	5.3	2.31±1.33	1.22	4376	11.36	0.30
43	3007278	44.1	7.78±1.86	16.65	22120	3.43	0.32
44	3012138	22.3	5.03±0.01	1.29	4636	16.20	0.28
45	3019810	1.5	0.52±0.18	3.10	3791	3.75	0.29
46	3006727	42.2	1.58±0.77	0.07	4128	12.87	0.28
47	3014857	86.1	6.95±0.70	0.24	4454	30.70	0.28
48	3018268	15.4	0.74±0.34	1.97	4007	5.01	0.30
49	3001942	7.4	1.88±1.02	0.39	4292	10.79	0.31
50	3005335	106.5	2.03±1.15	0.02	4108	18.11	0.32
51	3014730	6.3	2.28±1.52	0.91	4354	11.83	0.32
52	3009191	2.4	0.77±0.33	0.54	4000	5.60	0.31
53	3002429	8.5	1.61±0.37	0.06	4123	13.30	0.31
54	3004728	5.2	1.15±0.53	0.95	4173	7.12	0.32
55	3009806	5.1	4.56±1.92	2.79	4874	11.22	0.28
56	3019761	9.2	0.63±0.26	3.44	3922	4.19	0.32
57	3009868	4.6	0.83±0.58	2.17	4064	5.30	0.32
58	3006037	81.1	5.78±2.85	0.02	4169	43.82	0.28
59	3010363	28.6	7.80±0.66	1.18	9119	16.97	0.30
60	3008014	103.8	5.94±1.84	0.01	4122	48.92	0.32
61	3017917	113.4	6.36±1.24	0.97	4656	24.67	0.32
62	3004811	116.3	7.93±0.19	0.32	4720	39.83	0.31
63	3018731	48.9	0.73±0.46	0.02	3836	8.51	0.28
64	3011384	105.8	5.84±0.25	1.87	5068	20.96	0.29
65	3006837	12.0	1.11±0.65	4.70	4312	3.87	0.32
66	3011682	7.8	0.89±0.19	1.24	4086	5.83	0.29
67	3012314	3.4	1.48±0.83	4.08	4449	4.62	0.28
68	3010695	18.4	3.77±1.16	0.08	4264	24.46	0.32
69	3008790	11.4	3.58±0.97	5.83	4966	6.68	0.32
70	3018574	7.1	3.15±0.86	2.76	4698	8.09	0.32
71	3002983	7.1	1.54±0.78	3.32	4433	5.28	0.32
72	3013720	10.3	3.07±0.09	6.82	4900	5.49	0.32
73	3011834	8.1	1.75±0.88	4.27	4534	4.86	0.28
74	3006167	4.6	1.17±0.35	2.62	4247	5.91	0.32
75	3006225	4.4	0.64±0.46	6.75	3955	3.14	0.30
76	3000437	10.1	2.11±0.81	2.71	4530	6.81	0.32
77	3008427	15.5	2.25±0.93	3.04	4584	6.56	0.30

Continued on next page...

TABLE 10 – Continued

Source #	Model #	χ^2	Mass ($M_\odot$)	Age ($\times 10^5$ yr)	Temp (K)	Radius ($R_\odot$)	Log(d) (kpc)
78	3013412	8.8	3.17±0.42	6.21	4895	5.83	0.32
79	3009478	47.1	6.40±0.95	1.13	4737	26.40	0.29
80	3006319	5.7	3.42±0.77	16.80	8083	5.24	0.28
81	3007857	12.2	4.23±0.67	8.94	7759	7.29	0.32
82	3013153	11.4	2.44±0.74	5.39	4721	5.18	0.28
83	3006167	2.5	1.17±0.39	2.62	4247	5.91	0.31
84	3003580	10.5	1.83±0.24	1.41	4327	9.43	0.31
85	3000105	3.8	0.91±0.89	4.96	4195	3.55	0.31
86	3006386	12.1	1.01±0.25	1.05	4127	6.45	0.31
87	3002486	1.7	3.06±0.90	1.65	4556	10.64	0.30
88	3001254	2.2	1.64±1.09	2.42	4401	6.58	0.31
89	3017434	7.8	1.09±0.17	2.05	4187	6.33	0.29
90	3008369	4.5	2.12±0.75	7.79	4709	4.11	0.31
91	3003201	0.9	1.80±0.87	4.50	4554	4.80	0.29
92	3002749	4.4	1.49±0.70	2.43	4356	6.38	0.31
93	3007922	2.7	0.97±0.67	5.39	4239	3.47	0.28
94	3001093	2.4	2.06±1.05	2.77	4527	6.64	0.32
95	3004677	47.0	7.15±0.93	0.15	4415	35.21	0.28
96	3009949	1.0	1.25±0.65	6.50	4400	3.47	0.28
97	3018235	7.0	3.41±0.79	13.76	5935	6.69	0.28
98	3017469	6.0	2.13±0.93	25.57	4977	2.84	0.30
99	3013707	2.7	0.96±0.31	4.03	4207	4.14	0.32
100	3002760	1.2	1.50±0.66	8.59	4528	3.31	0.28
101	3012927	33.4	0.98±0.05	0.18	4012	8.84	0.28
102	3003812	2.1	0.59±0.47	5.99	3907	2.98	0.31
103	3000437	9.3	2.11±1.01	2.71	4530	6.81	0.31
104	3012746	4.4	2.52±1.44	3.21	4638	6.69	0.32
105	3017773	0.0	0.87±0.85	3.65	4138	4.37	0.32
106	3019806	8.2	2.10±0.86	6.49	4682	4.42	0.31
107	3008064	5.3	1.36±0.71	5.69	4436	3.79	0.32
108	3015644	4.2	4.10±2.52	0.58	4429	18.92	0.29
109	3009949	0.1	1.25±0.66	6.50	4400	3.47	0.28
110	3018604	12.8	3.07±0.87	4.30	4788	6.50	0.30
111	3011834	9.0	1.75±1.31	4.27	4534	4.86	0.32
112	3006968	5.6	2.55±1.16	2.92	4624	7.08	0.29
113	3016571	8.7	1.31±0.96	1.39	4225	7.65	0.28
114	3017076	0.1	0.64±0.29	0.36	3868	5.57	0.31
115	3010776	0.4	2.16±0.91	3.93	4613	5.63	0.28
116	3001003	8.0	0.77±0.70	7.17	4089	2.87	0.28
117	3016510	4.5	1.11±0.87	10.13	4344	2.70	0.30

Continued on next page...

TABLE 10 – Continued

Source #	Model #	χ^2	Mass ($M_\odot$)	Age ($\times 10^5$ yr)	Temp (K)	Radius ($R_\odot$)	Log(d) (kpc)
118	3019770	1.8	2.29±0.65	21.03	4988	3.17	0.29
119	3008369	1.8	2.12±0.79	7.79	4709	4.11	0.32
120	3007545	13.7	0.40±0.74	2.45	3607	3.21	0.30
121	3012237	1.9	3.05±0.65	5.06	4819	6.06	0.31
122	3003282	12.3	2.27±0.91	0.58	4336	12.20	0.28
123	3006970	0.5	0.66±0.45	6.87	3966	3.18	0.28
124	3006184	0.1	3.06±0.56	9.61	5008	5.00	0.32
125	3005725	5.3	2.13±0.86	1.83	4434	8.95	0.28
126	3008329	0.5	1.33±0.65	1.93	4256	7.23	0.28
127	3001928	0.7	2.82±1.07	1.87	4555	9.58	0.32
128	3004958	2.7	3.48±0.97	16.98	9262	4.67	0.29
129	3002376	0.1	2.94±1.22	3.72	4736	6.73	0.30
130	3002486	3.2	3.06±0.80	1.65	4556	10.64	0.31
131	3016287	15.6	4.49±0.75	22.13	15450	2.51	0.32
132	3018851	0.2	2.52±0.96	19.03	5091	3.60	0.28
133	3014740	0.1	0.48±0.14	1.94	3740	3.69	0.31
134	3013016	3.6	2.82±0.52	22.40	5789	5.07	0.32
135	3007545	0.3	0.40±0.12	2.45	3607	3.21	0.31
136	3006199	8.4	1.77±0.83	8.27	4622	3.64	0.30
137	3001774	1.9	2.41±0.65	5.03	4705	5.31	0.29
138	3005323	0.1	2.08±0.48	7.43	4693	4.15	0.30
139	3000461	1.3	2.34±0.51	10.76	4820	3.88	0.28
140	3000786	0.8	3.83±0.84	7.14	5208	7.60	0.28
141	3015341	1.3	1.42±0.85	0.67	4237	8.43	0.28
142	3015037	6.2	2.14±0.60	6.46	4691	4.47	0.31
143	3018426	4.2	0.67±0.17	3.72	3965	4.31	0.29
144	3017345	1.3	0.90±0.45	2.19	4104	5.57	0.31
145	3013615	2.5	2.55±0.93	2.05	4540	8.70	0.28
146	3019806	3.8	2.10±0.90	6.49	4682	4.42	0.28
147	3002516	7.1	2.62±0.76	4.71	4731	5.71	0.28
148	3012212	5.0	2.01±0.88	1.47	4358	9.87	0.32
149	3004170	9.9	5.10±0.89	13.84	16720	2.69	0.32
150	3000562	4.4	4.14±1.04	2.62	4792	10.11	0.28
151	3018998	1.7	2.32±0.88	2.79	4577	7.00	0.30
152	3018138	4.8	2.07±0.83	5.04	4636	4.91	0.30
153	3010283	4.1	1.41±0.97	1.20	4247	8.08	0.31
154	3003577	0.1	1.63±0.91	2.33	4389	6.77	0.32
155	3006309	3.5	2.57±0.79	3.87	4686	6.17	0.32
156	3011617	7.8	2.87±0.74	5.31	4800	5.73	0.28
157	3008437	1.3	2.67±0.88	3.69	4691	6.45	0.32

Continued on next page...

TABLE 10 – Continued

Source #	Model #	χ^2	Mass ($M_\odot$)	Age ($\times 10^5$ yr)	Temp (K)	Radius ($R_\odot$)	Log(d) (kpc)
158	3006105	7.0	4.61±0.69	6.04	6401	9.70	0.28
159	3011676	6.0	2.13±0.85	3.51	4588	5.93	0.32
160	3000390	0.6	3.27±0.46	16.33	6294	6.12	0.30
161	3018604	2.2	3.07±1.02	4.30	4788	6.50	0.31
162	3012349	0.7	4.08±1.59	0.49	4420	19.11	0.30
163	3001774	3.7	2.41±0.82	5.03	4705	5.31	0.31
164	3004671	3.8	1.85±0.85	1.44	4332	9.43	0.29
165	3006968	16.6	2.55±1.14	2.92	4624	7.08	0.28
166	3012951	8.4	3.59±0.66	4.51	4881	7.19	0.32
167	3014833	4.7	2.23±0.99	1.06	4357	11.40	0.32
168	3002159	0.2	1.61±0.23	9.62	4581	3.28	0.31
169	3014444	1.5	2.92±0.21	7.83	4901	5.03	0.32
170	3016751	5.0	0.89±0.46	2.71	4111	5.26	0.32
171	3013461	15.6	0.62±0.53	1.02	3901	4.58	0.32
172	3011046	3.3	0.49±0.21	0.48	3736	4.45	0.30
173	3018883	6.5	3.01±0.40	12.38	5113	4.76	0.30
174	3012951	1.2	3.59±0.84	4.51	4881	7.19	0.28
175	3001155	1.9	3.26±0.22	8.33	5019	5.59	0.29
176	3011399	0.0	1.60±0.89	2.35	4380	6.75	0.31
177	3016852	3.8	1.75±0.94	0.30	4266	10.51	0.28
178	3000579	0.7	2.51±0.66	5.60	4739	5.16	0.32
179	3005982	11.8	0.53±0.30	3.45	3808	3.77	0.28
180	3008369	2.5	2.12±0.88	7.79	4709	4.11	0.31
181	3009938	7.2	2.35±0.81	4.32	4666	5.63	0.32
182	3018685	4.2	1.27±0.63	3.04	4318	5.36	0.32
183	3017850	6.3	2.50±0.59	4.40	4700	5.73	0.29
184	3010466	3.3	2.13±0.36	1.08	4347	11.01	0.32
185	3001923	12.2	0.89±0.34	1.24	4087	5.84	0.31
186	3000921	3.4	1.60±0.81	5.62	4526	4.12	0.28
187	3005727	4.2	6.71±0.68	1.41	5460	24.54	0.30
188	3008369	11.0	2.12±0.62	7.79	4709	4.11	0.28
189	3006569	13.8	3.20±0.91	1.83	4602	10.21	0.31
190	3014461	3.0	0.97±0.51	3.21	4175	4.96	0.29
191	3018604	10.4	3.07±0.59	4.30	4788	6.50	0.28
192	3000755	11.2	1.46±0.94	5.13	4467	4.10	0.32
193	3015197	2.9	0.80±0.37	10.51	4123	2.34	0.32
194	3007913	0.1	0.98±0.58	3.49	4200	4.64	0.31
195	3016740	7.2	3.14±0.76	1.44	4520	11.83	0.29
196	3008000	2.1	0.55±0.46	2.08	3828	4.02	0.32
197	3002342	2.8	2.62±0.77	6.58	4794	4.97	0.28

Continued on next page...

TABLE 10 – Continued

Source #	Model #	χ^2	Mass ($M_\odot$)	Age ($\times 10^5$ yr)	Temp (K)	Radius ($R_\odot$)	Log(d) (kpc)
198	3006990	26.2	5.06±1.23	0.15	4352	26.98	0.28
199	3002548	1.7	0.87±0.26	3.31	4115	4.70	0.28
200	3014528	5.5	3.42±0.93	14.90	6513	6.32	0.32
201	3002202	1.0	1.52±0.69	6.01	4508	3.89	0.32
202	3019005	6.8	1.21±0.84	9.05	4405	2.96	0.30
203	3014129	4.1	0.73±0.53	0.70	3981	5.26	0.32
204	3004916	7.1	1.80±0.92	3.00	4491	5.96	0.28
205	3010381	1.9	0.74±0.26	0.86	3989	5.19	0.32
206	3006920	6.3	0.61±0.41	2.75	3900	4.23	0.32
207	3014230	3.9	1.06±0.46	1.32	4154	6.61	0.32
208	3014271	3.6	1.15±0.43	2.76	4249	5.63	0.32
209	3015556	24.5	3.89±0.34	15.23	12940	3.01	0.32
210	3016413	0.8	0.51±0.38	2.57	3789	3.80	0.28
211	3016101	10.4	1.70±0.69	2.34	4417	6.72	0.28
212	3000836	6.2	0.95±0.27	2.65	4140	5.49	0.30
213	3010776	17.2	2.16±0.87	3.93	4613	5.63	0.32
214	3005393	30.1	3.78±0.58	2.06	4685	10.50	0.28
215	3008369	4.7	2.12±0.70	7.79	4709	4.11	0.32
216	3012069	14.4	0.72±0.32	2.44	3995	4.84	0.32
217	3003816	6.1	0.87±0.56	2.55	4091	5.28	0.28
218	3013707	2.1	0.96±0.28	4.03	4207	4.14	0.28
219	3012341	6.8	2.33±0.84	2.07	4504	8.43	0.31
220	3003499	5.5	0.84±0.37	1.88	4068	5.45	0.28
221	3010925	9.4	0.57±0.49	1.27	3846	4.22	0.28
222	3014626	8.0	0.74±0.27	2.08	4006	4.98	0.30
223	3008244	4.7	1.11±0.62	2.20	4198	6.25	0.32
224	3008007	10.7	3.34±0.97	0.83	4423	15.44	0.28
225	3013998	10.4	2.31±0.87	1.68	4441	9.75	0.32
226	3007835	7.2	1.10±0.46	0.95	4159	6.87	0.28
227	3013982	6.3	0.49±0.13	1.50	3743	3.74	0.28
228	3011092	1.0	1.08±0.65	7.45	4317	3.06	0.28
229	3015030	44.4	7.46±0.42	14.00	21500	3.34	0.32
230	3002366	94.8	6.56±0.78	6.14	19700	3.10	0.29
231	3003237	86.9	4.14±0.67	8.18	6218	8.55	0.28
232	3015795	71.6	3.81±0.70	2.02	4683	10.64	0.28
233	3003965	17.4	4.28±0.03	24.99	14980	2.44	0.28
234	3012453	12.5	5.77±0.96	18.93	18020	2.89	0.31
235	3008702	61.7	4.39±0.15	0.87	4483	18.37	0.30
236	3008944	19.5	2.83±0.95	2.33	4616	8.39	0.29
237	3012482	44.2	4.44±1.16	6.75	6385	9.23	0.31

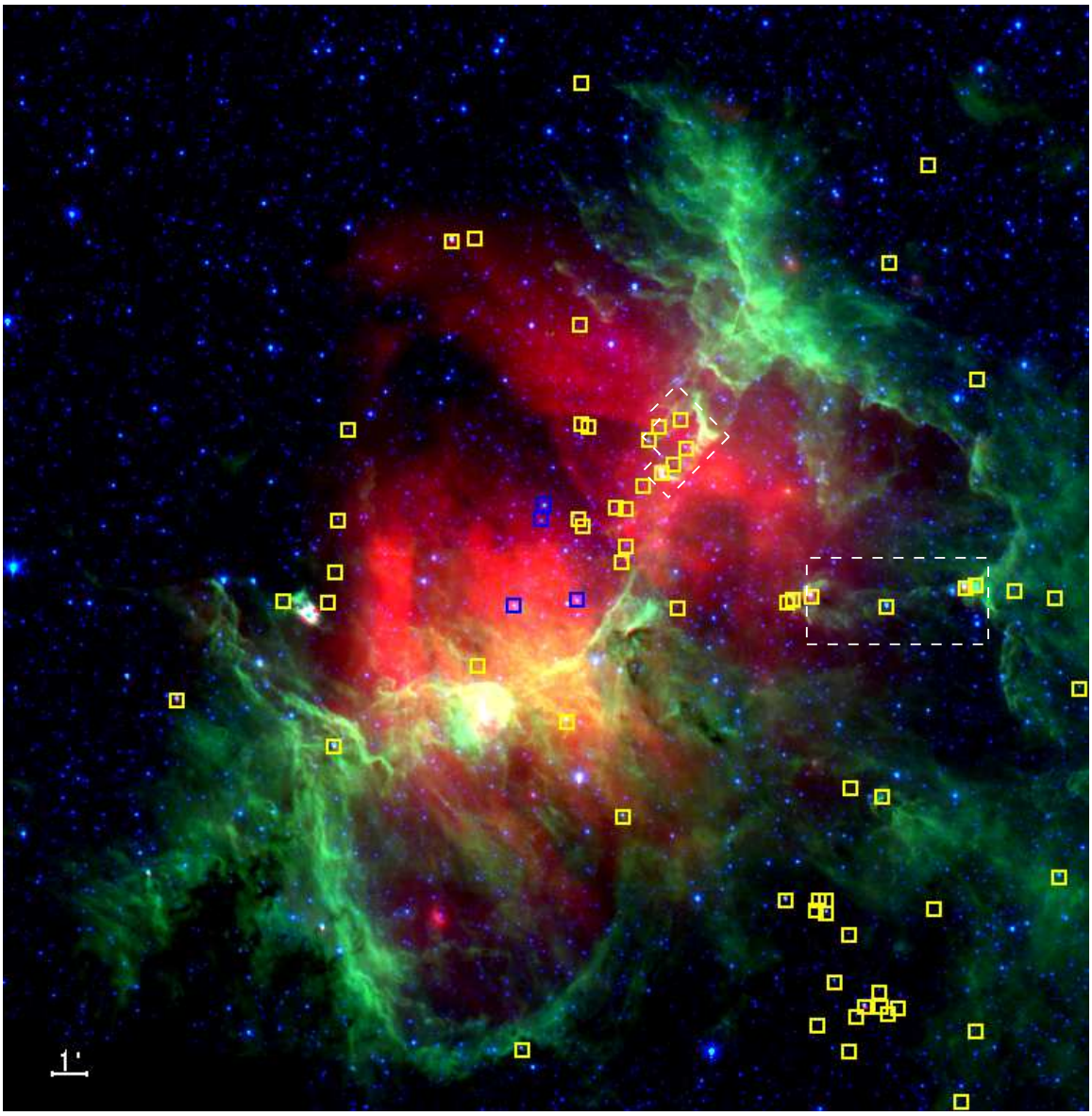

FIG. 39.—3-color *Spitzer* image of M16: Red is MIPS 24 μm, green is IRAC 8.0 μm, and blue is IRAC 4.5 μm. Yellow squares show the locations of the IRAC and MIPS Class I/0 protostars, and blue squares mark the locations of the four ionizing O stars (O4 V, O6V, O6V, and O7 Ib) in the region. The *HST* WFPC2 and ACS FOV's are outlined in white. The scale bar showing a distance of $1'$ in the image represents a length of $\sim$0.6 pc, given a distance of 2 kpc to the region.

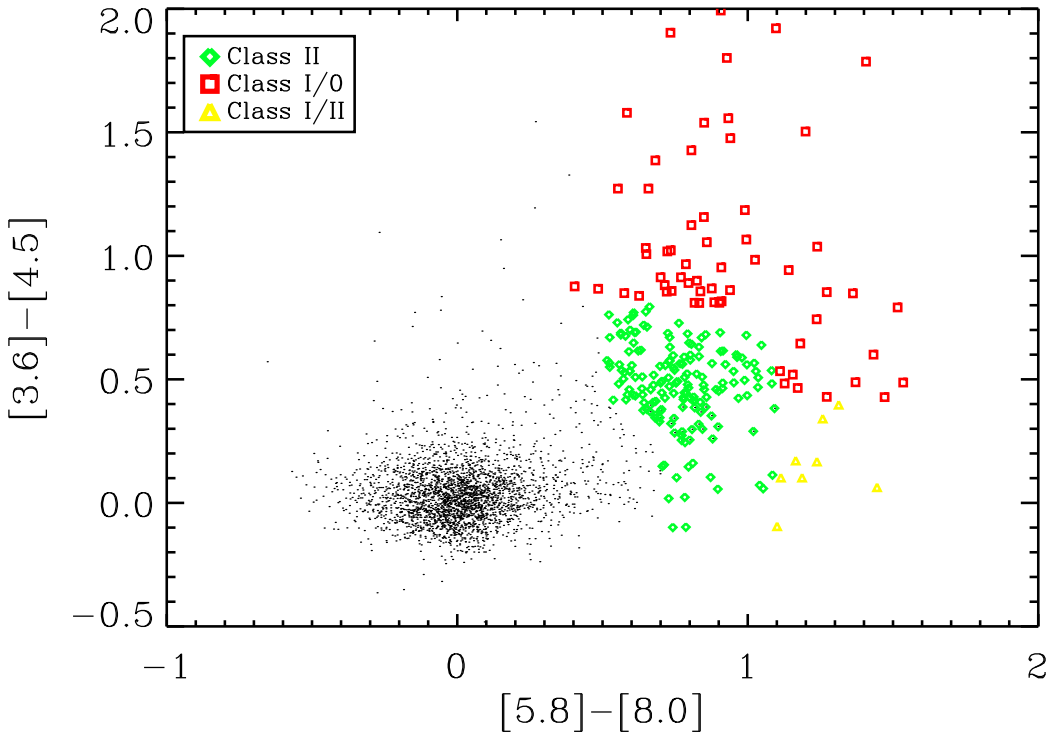

FIG. 40.—IRAC color-color diagram for M16, showing YSO classification of IRAC detected sources. Color criteria taken from Allen et al. (2004), and Whitney et al. (2003 & 2004b).

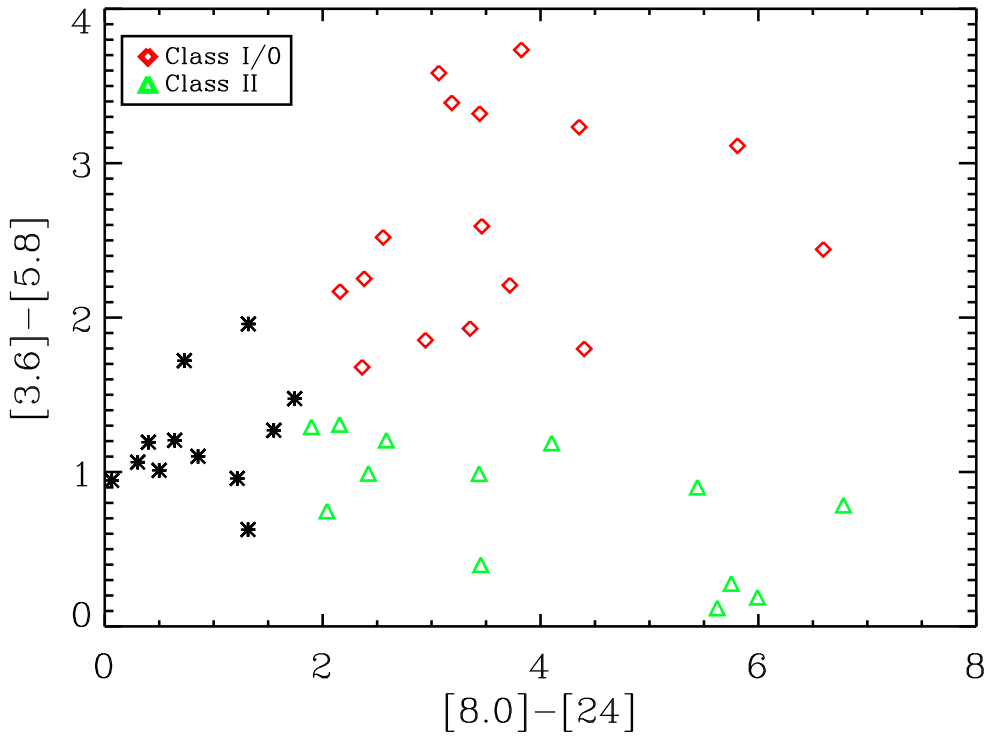

FIG. 41.—IRAC and MIPS color-color diagram for M16, showing YSO classification of the MIPS 24 μm detected sources. Color criteria taken from Whitney et al. (2003 & 2004b) and Reach et al. (2004).

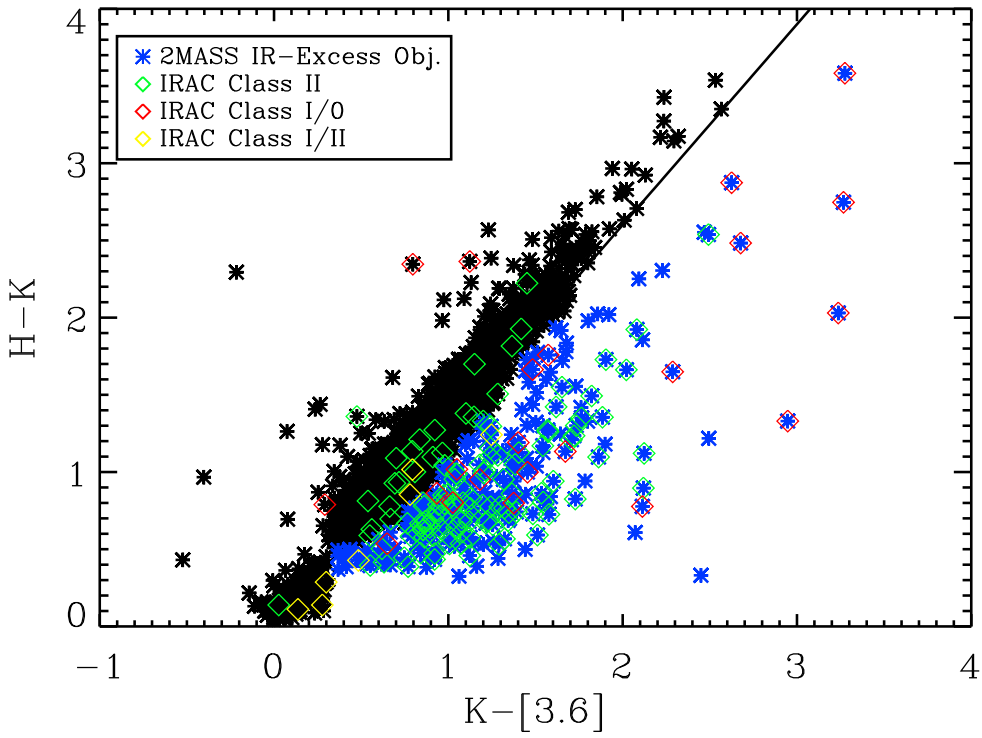

FIG. 42. —2MASS & *Spitzer* color-color diagram of the detected 2MASS sources in M16. Sources to the right of the reddening vector, with a slope equal to 1.3, are sources with an infrared excess in the NIR. 120 out of the 150 2MASS sources corresponding to a *Spitzer* selected YSO have a near-IR color excess in their 2MASS colors. Another 100 2MASS point sources also have a near-IR color excess, but do not have a mid-IR color excess from their *Spitzer* colors.

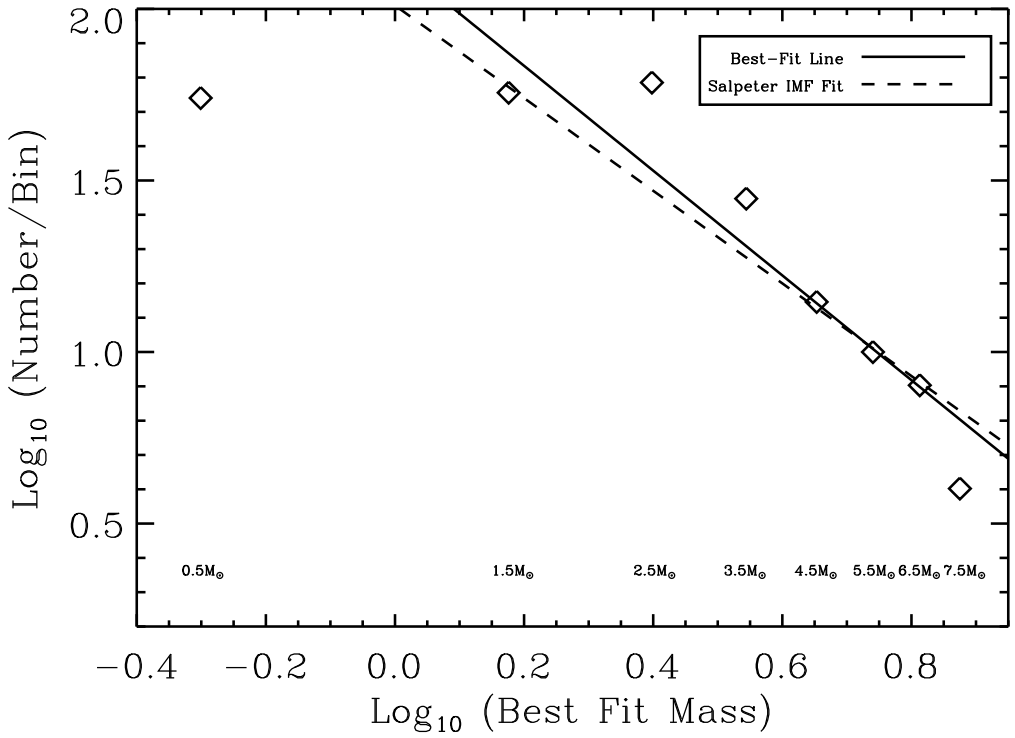

FIG. 43.—Mass distribution function for YSOs in M16. The solid line is the best-fit to our data, and corresponds to a slope of -1.53. The dashed line is for a Salpeter IMF with a slope of -1.35. Both lines were fit to the higher mass bins, 4.5, 5.5, and 6.5 $M_{\odot}$.

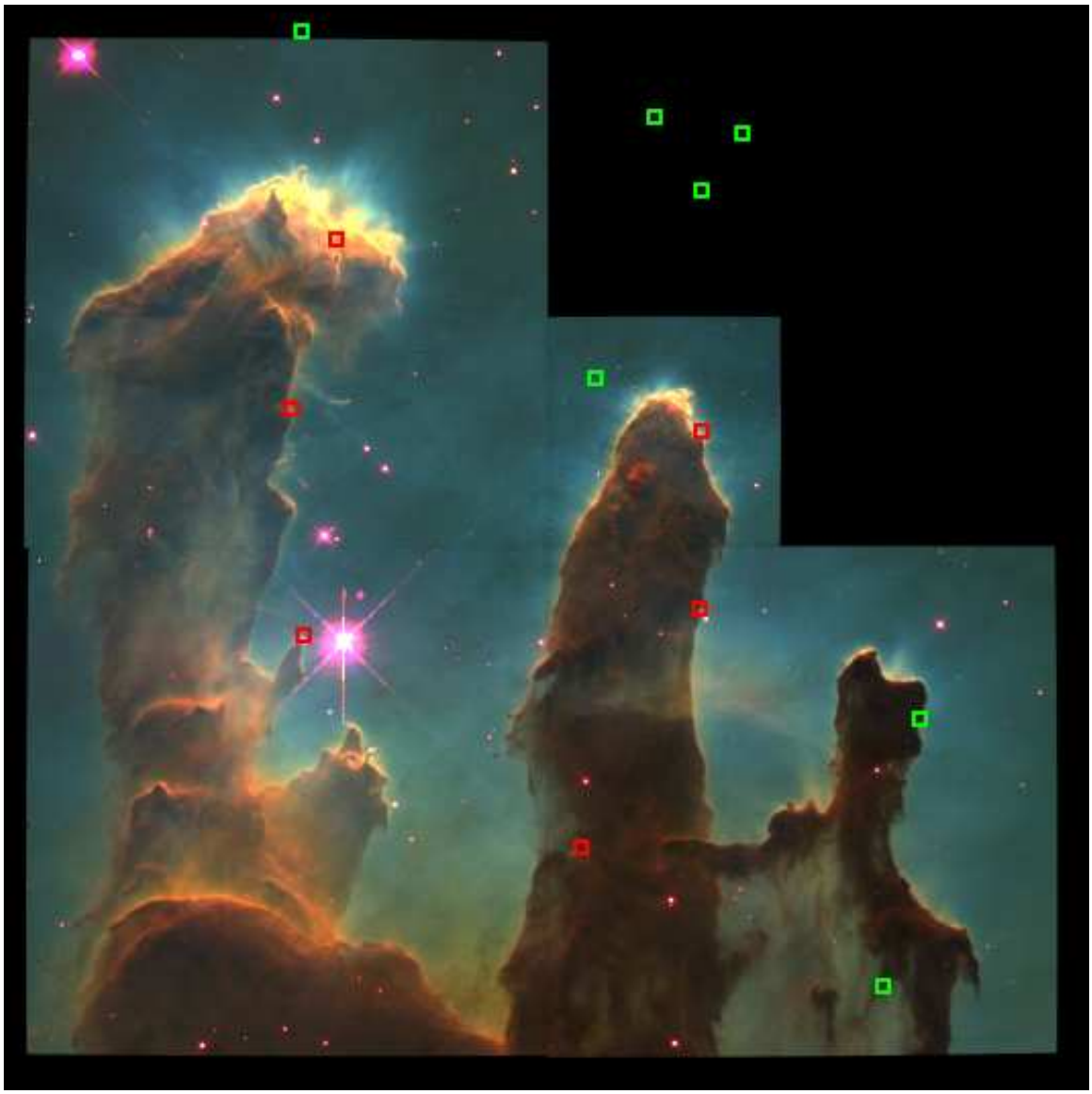

FIG. 44.—*HST* WFPC2 image of M16: Hα emission is in red, [S II] emission is green, and [O III] emission is in blue. Detected YSOs in this image are labeled by red and green squares for Class I/0 and Class II YSOs, respectively. Three of the sources correspond to the location of an "EGG" from Hester et al. (1996), and two YSOs are coincident with the location of X-ray sources from Linsky et al. (2007).

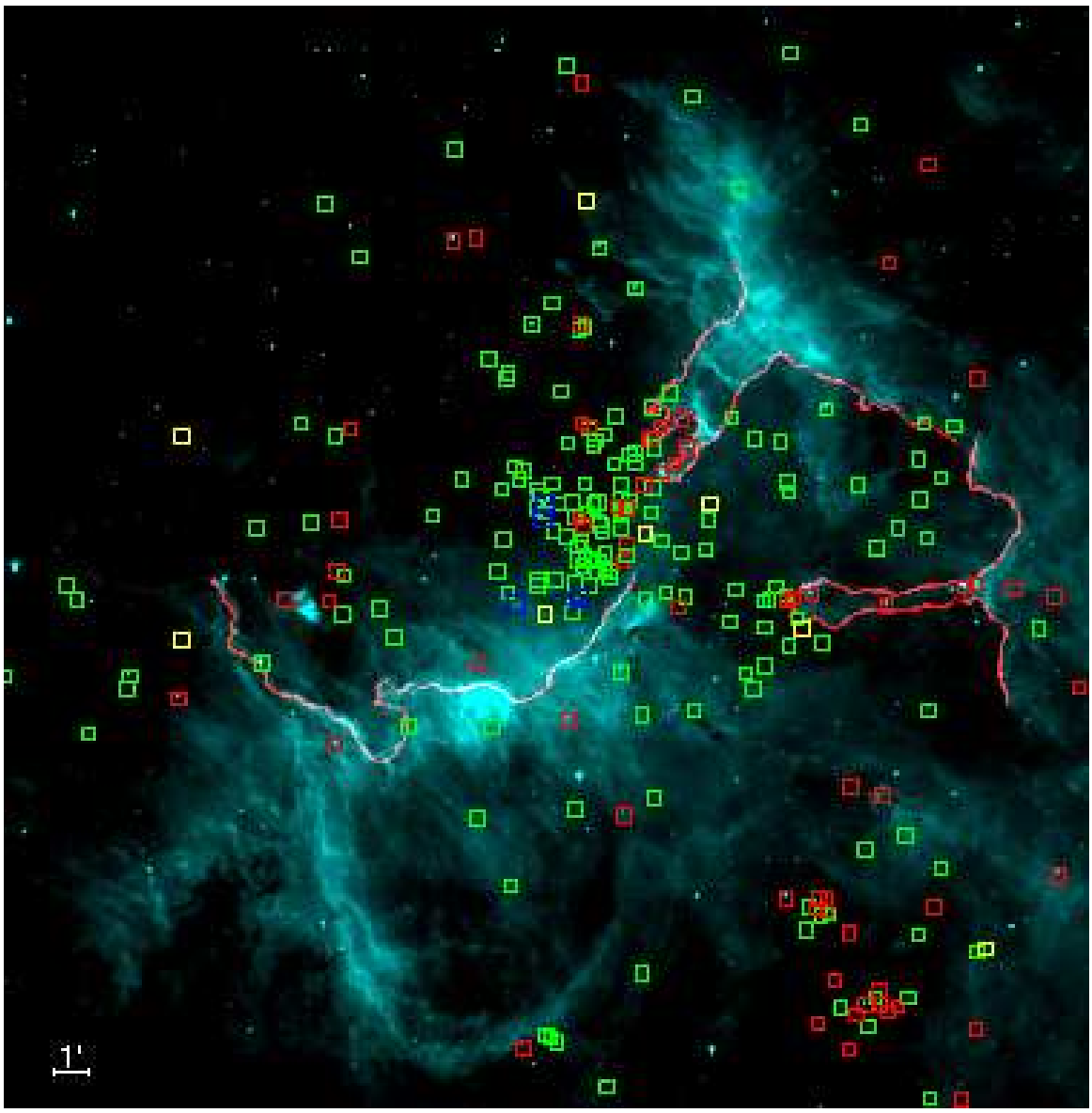

FIG. 45.—Locations of identified ionization fronts in M16, with the same scale as in Figure 39. Identified ionization fronts are outlined in red and are over-plotted on the IRAC 8.0 μm image. Red, yellow, and green squares show locations of Class 0/I, Class I/II, and Class II protostars, blue squares mark the locations of the ionizing 0 stars in the region.

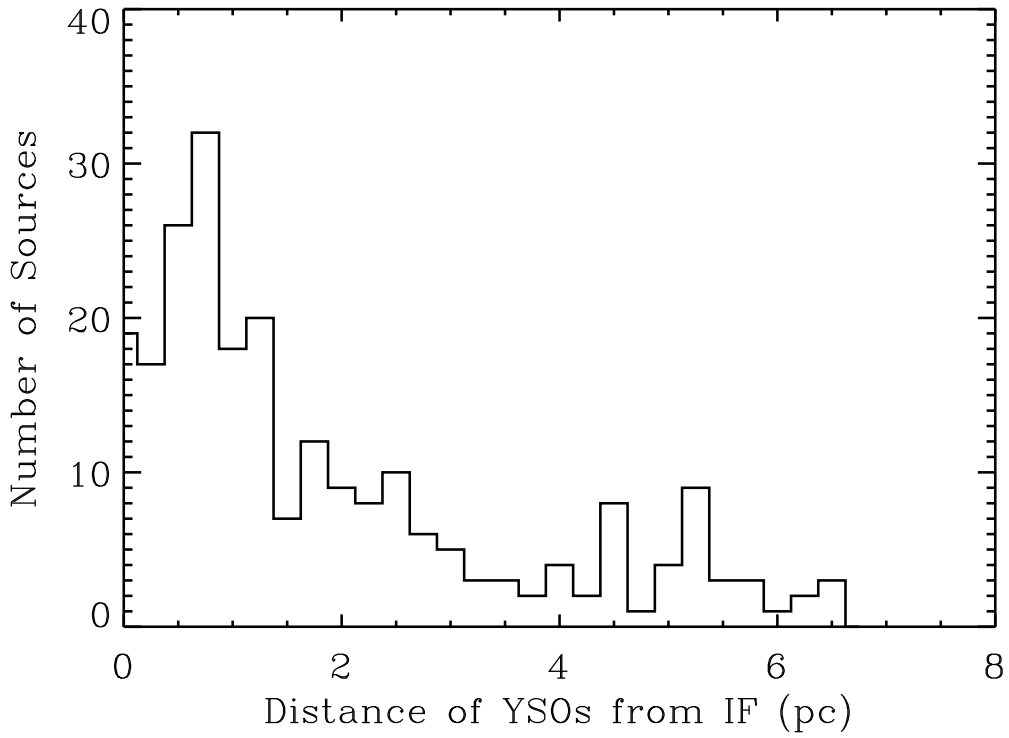

FIG. 46.—Distance distribution of the 237 candidate YSOs in M16 from the nearest ionization front.

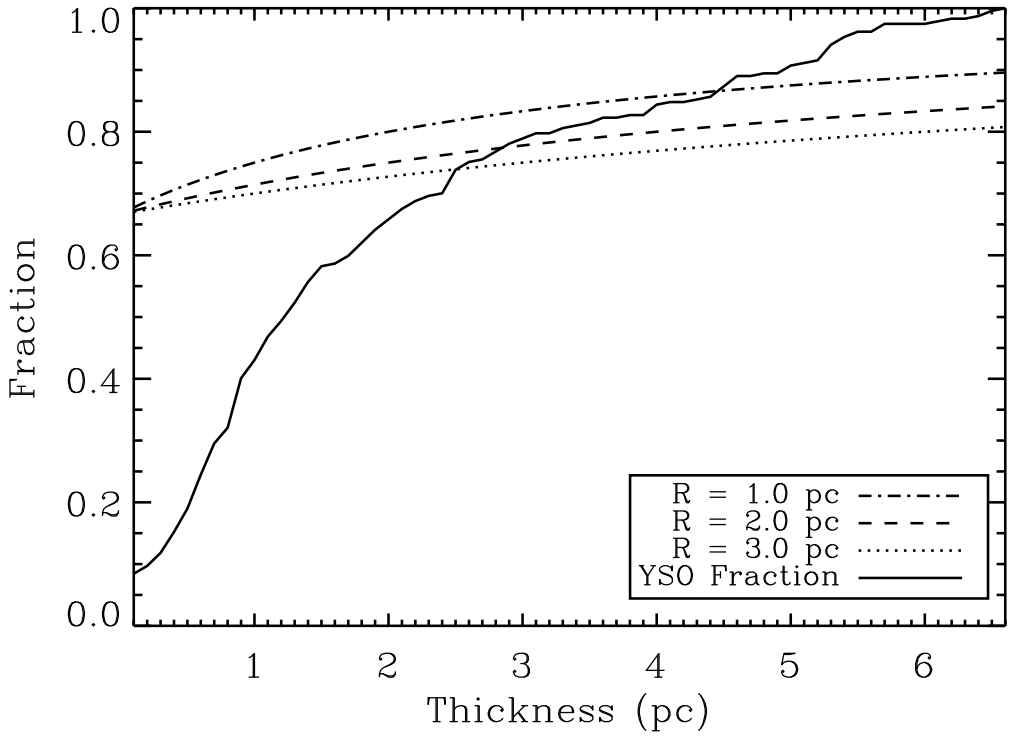

FIG. 47. —A simplified 3D hemispherical model of an ionization front is used to determine the expected number of observed sources that would be seen within a given layer thickness when viewed in projection. The fraction of expected sources observed within a given thickness distribution from an ionization front, with ionization fronts centered at 1, 2, and 3 pc away from an OB star, are shown by dashed lines. The measured distribution of YSOs in M16 is shown by the solid line. The expected distributions and the observed distribution cross between 2.5 - 4.5 pc, indicating that the actual distribution of YSOs in M16 is a population of sources that is concentrated within a layer $\sim$2.5 pc from the nearest ionization front.

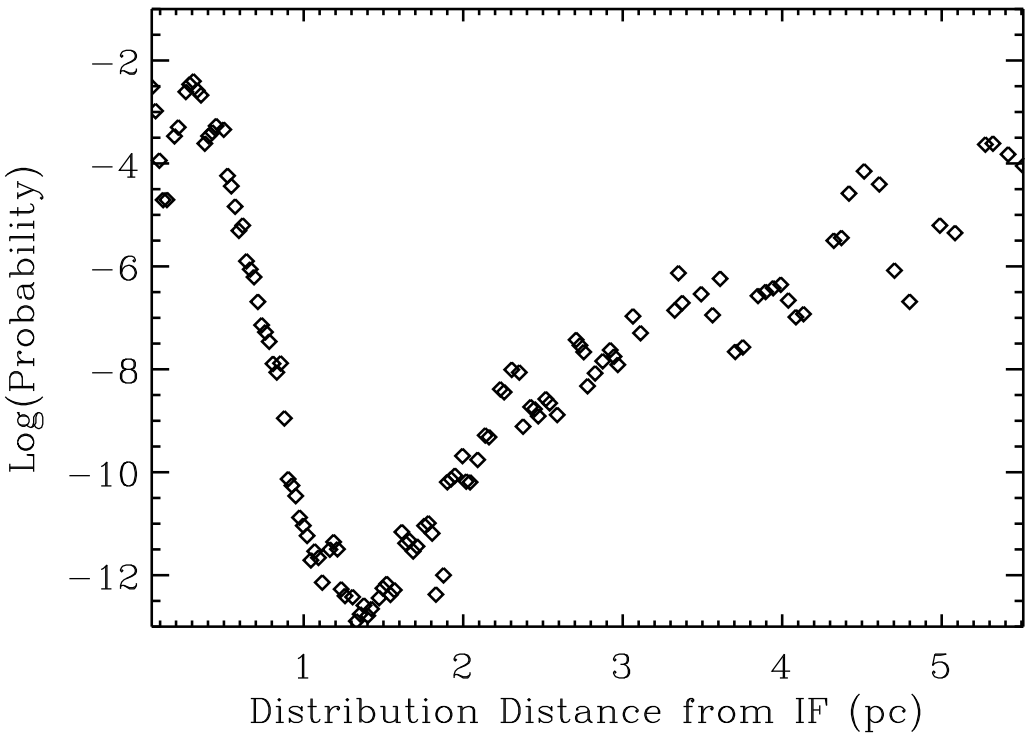

FIG. 48.—The probability of the distribution of YSOs being a random distribution is plotted versus distance. Using the Poisson Probability function, the likelihood that the given distribution of YSOs is positioned within a given distance of an ionization front by chance is calculated. On average, the chance of this distribution occurring randomly is 10^{-5}.

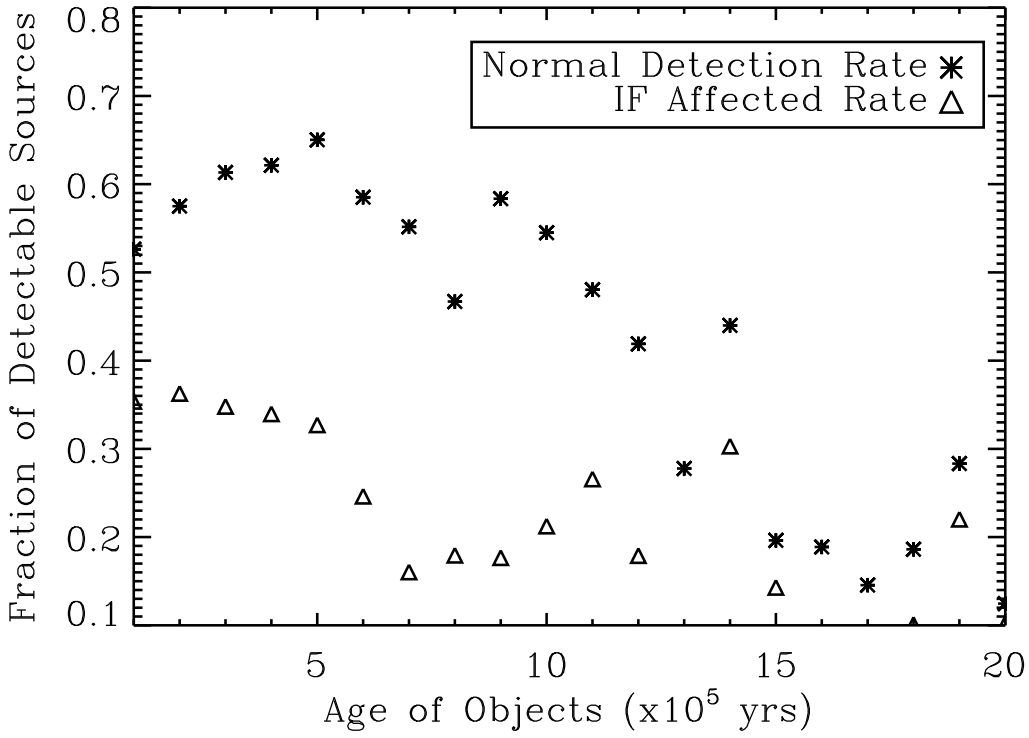

FIG. 49.—The fraction of detectable YSOs vs. age of the object in M16. A population of stars given by the MF from Equation 18 and a constant SFR (value equal to the calculated SFR from Equation 21) was aged over timesteps of 10^5 yr. The fraction of detectable sources based on our flux limits was calculated at each timestep, the normal detection rate is shown by the asterisk symbols. The detection rate was also calculated for sources uncovered by a passing ionization front. Disk erosion was assumed using models from Johnstone et al. (1998). The ionization front affected detection rate with object age is shown by the triangles. The data show that the best age range to detect the YSOs is around a few$\times 10^5$ yr, with a peak at 5×10^5 yr for the normal rate and a peak around 2×10^5 yr for the ionzation affected rate.

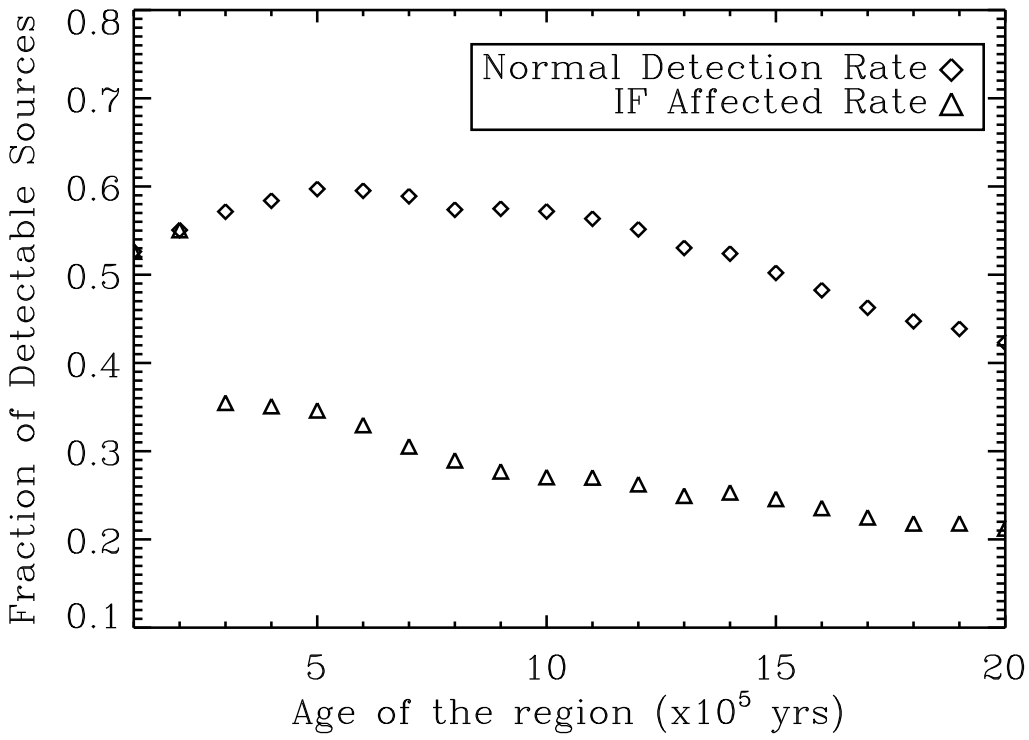

FIG. 50.—The fraction of detectable sources vs. age of the region, using the same methods as described for Figure 49. The normal detection fraction is shown by the diamonds and the ionization affected fractions are shown by the triangles. The detection rate drops to between 40 - 20% by 2 Myr. Using a Salpeter (1955) mass function produces similar results (not shown here), but slightly higher detection fractions of 0.45 and 0.25 for the unaffected rate and ionization affected rate.

6. AN ANALYSIS OF YSO CLUSTERING ACROSS THE GALACTIC MID-PLANE USING GLIMPSE

6.1. Introduction

The Galactic Legacy Infrared Mid-Plane Survey Extraordinaire (GLIMPSE) is a *Spitzer* legacy survey designed to map the mid-plane of the inner Milky Way Galaxy in the four *Spitzer* IRAC bands (3.6, 4.5, 5.8, and 8.0 μm). The GLIMPSE survey covers galactic longitudes from $\pm$ 0 - 65, and galactic latitude from $\pm$ 1. Images are generated in $3^\circ \times 2^\circ$ in each passband. There are approximately 30 of these fields in the entire GLIMPSE survey area. A combined mosaicked image of the entire GLIMPSE region made by the GLIMPSE team can be seen in Figure 51. Reliable point source catalogs have also been generated for the entire survey by the GLIMPSE team, with over 72 million point sources identified in the entire GLIMPSE field.

Strong Polycyclic Aromatic Hydrocarbon (PAH) emission can easily be seen in the GLIMPSE images. The PAH molecules form in molecular clouds, and PAH emission exists in an area known as the Photodissociation Region (PDR), where UV radiation from nearby massive stars is penetrating the surface layers of the molecular cloud and exciting the PAH molecules. PAH emission is seen in the 8.0 μm IRAC band, where the excited PAH molecules are emitting at wavelengths of 7.7 and 8.8 μm. The PDR is the layer of molecular gas that is immediately exterior to the H II region and the ionization front. Therefore, PAH emission is a signpost of high-mass star formation and the location of the PDR.

Thermal emission from dust at various temperatures can be seen in all of the IRAC bands. The dust typically has temperatures ranging from 30 - 1600 K, and the cooler the dust, the longer the wavelength at which it radiates. The dust is heated by

visible and UV light from stellar sources and then radiates in the infrared. As has been previously discussed in the other chapters, YSOs are identified due to this process of heated dust. For YSOs, the circumstellar dust in the proto-planetary disk is heated by radiation from the central source and the dust then re-radiates in the infrared. Figure 52 demonstrates this effect, where we see the combined spectral energy distributions produced from the central star and from the black body of the dust emission. Four different stellar sources are shown in Figure 52, ranging in temperature from 30,000 - 3500 K. In all four models, the combined SED is above that produced solely by the central star, thereby producing the measured excesses seen in the infrared.

The main advantage of using the GLIMPSE survey is to be able to use a well-characterized dataset that covers a statistically significant sample of the Milky Way Galaxy. The GLIMPSE survey has been used for a number of very interesting studies; developing the YSO SED models and radiative transfer codes (Robitaille et al. 2006, 2007; Whitney et al. 2003a, 2003b, & 2004b), identifying PAH bubbles (Churchwell et al. 2006, 2007), and studying outflows from newly forming massive stars (Cyganowski et al. 2008) among others. In this study, we use archival data from the GLIMPSE survey to first identify YSOs in each GLIMPSE region, and then to look at the surface distribution of the YSOs across the Milky Way. We are specifically interested in studying the concentration of YSOs in compressed gas from H II region expansion. The locations of massive stars and H II regions are compared with the overall surface density of the YSOs.

6.2. Data Analysis

From the GLIMPSE archive we used the GLIMPSE Highly Reliable Catalog (GLMIC) of point sources, along with 3° × 2° images of all four IRAC bands for each of the 30 mini regions in the GLIMPSE dataset. From the GLMIC for each region, we first selected sources that were detected in all four IRAC bands. Candidate YSOs were then selected in each region by using the same color criteria as given by Table 2. However, because of the large numbers of point sources within each region, typically on the order of 10^5 sources detected in each IRAC band, the generated color-color diagrams are analyzed by eye and the criteria are adjusted for each specific region if needed, in order to ensure that only the "red" sources are being selected as YSOs and not sources that are part of the main sequence area of the color-color diagram. Figure 53 is a sample of a few of the IRAC color-color diagrams created for four different regions; from galactic longitude l=10-13°, l=13-16°, l=16-19°, and l=19-22°. The selected sources were also screened against background extragalactic contaminants and AGB stars, again using the color and magnitude criteria for these sources that is also listed in Table 2. In each 3° × 2° region, we typically find a few thousand candidate YSOs.

The next step in the analysis process was to measure the surface distribution of YSOs in each region. This was done by using a median-distance-to-neighbors algorithm (Healy 2004b) in order to construct surface density contours showing the distribution of YSOs. Essentially, for each YSO point source, the nearest-neighbor code calculates the distance to all other point sources and then medians the distance

to the 14 closest neighbors. A value of 14 nearest neighbors was chosen in order to adequately represent a small group or clustering of YSOs. This median distance for each point source is used to estimate the density at that location. A density map is created that is equal to calculated density at each YSO location, and is equal to zero everywhere else. A mask of pixel locations is also made, with a value of one at each YSO location and a value of zero everywhere else. The density map and mask are smoothed using a Gaussian smoothing kernel. The resulting surface density map comes from dividing the smoothed density map by the smoothed mask.

The surface density map is overplotted on each image as a contour plot, with each contour level representing a factor of two increase in YSO source density. These surface density maps were made for all of the GLIMPSE regions. Examples of these maps can be seen for the majority of the GLIMPSE survey in Figures 54 - 58. Each figure contains two images and each image is a strip running in nine degrees of galactic longitude made from three separate regions that were mosaicked together. The figures show 3-color images made using the IRAC bands 3.6, 5.8, and 8.0 μm. The YSO contours are overplotted on each image. When the contour images are lined up from region to region, the contours overlap and are continuous across the regions. There are however, edge effects of the contours seen at each end of the image. The individual contour images for the $3^\circ \times 2^\circ$ FOVs do not show these effects, and when more images are mosaicked together the contours overlap perfectly in the middle of the combined images.

6.3. Discussion

6.3.1 *Clustering of YSO Sources*

The overall results of the surface density contours, as shown in Figures 54 - 58, show that, in general, the YSOs are concentrated in gas along the mid-plane of the galaxy. Clusters of YSO sources can been seen in almost every image. In order to better analyze the amount of clustering, we have also plotted the surface density contours over the locations of the individual YSO point sources. Examples of these types of plots can be seen in Figures 59, 60, and 61 for the regions l=13-16°, l=16-19°, and l=19-22°. The surface density contours are shown in red and the source locations are in white. The green asterisks represent H II region locations, which we discuss in the following section.

These three figures visually show the concentration of YSOs by two methods, the surface density contours and the actual pixel locations of individual sources. Just by looking at the images by eye, one can pick out clusters of sources and see how they are grouped together. In Figure 59, where the H II region M17 is located in the lower left part of the image, it is clear that this is where the majority of YSOs in this region are located. The surface density of YSOs in other parts of this image is noticeably less as compared with the area surrounding M17. The same thing can be seen in Figure 60, where M16 is located in the upper right. This part of the region has the highest level of surface density contours, it is also one of the highest concentrations of YSOs throughout the entire GLIMPSE survey. Whereas, in Figure 61, for the region l=19-22°, there are fewer total numbers of YSOs than compared

with either the M17 or M16 regions, ∼700 less YSOs in this region. This can also be seen in the smaller surface density contour levels, and while there are a few clusters of YSOs, some near H II regions, overall the YSO surface density appears lower and more uniformly distributed in this region than in others. One other note of interest is that there are also slightly fewer H II regions in this part of the sky than in other regions. The difference in H II regions between the l=19-22° and other regions is argueably small (five versus seven or eight H II regions), but this difference may also account for a smaller overall rate of star formation occurring here. Therefore, if the star formation rate is lower overall and there are fewer massive stars forming as well, than we are likely to see fewer low-mass YSOs forming and being triggered from the influences of massive stars. This scenario can explain the more uniform distribution of the surface density of YSOs seen in Figure 61.

6.3.2 *Correlation of YSO Sources with other Tracers of Star Formation*

As part of our analysis, we also want to look at how the clustering of YSOs compares to the location of other signposts of recent star formation, such as known locations of H II regions. Archival databases and catalogs were searched for each region in order to map the locations of all known H II regions out to a given distance. We limited the surveyed H II regions to have known distances within 7 kpc of the Sun. This was done in order to insure that we are comparing a sample of YSOs to a similar sample of H II regions. It is unlikely that many low-mass YSOs would be detected in the GLIMPSE survey past this distance due to the flux limits of the survey. Higher mass YSOs can be detected out to greater distances, but based on model simulations

(Whitney et al. 2003a, 2003b, & 2004b) assuming GLIMPSE sensitivities of 1, 3, 12, and 25 mJy at 3.6, 4.5, 5.8, and 8.0 μm respectively, Class 0 YSOs with M $\leq$ 1 $M_{\odot}$ can only be observed out to a distance of $\sim$4 kpc and Class 0 YSOs with M $\leq$ 3 $M_{\odot}$ can only be observed out to 7 kpc.

Once a known list of H II regions was made, the locations of the H II regions were compared with the YSO surface density plots. In Figures 62, 63, 64, and 65, we show the YSO contour maps overplotted on a 3-color image of four separate regions, along with the locations of known H II regions shown by green asterisks. In all of these regions, (l=13-16 centered near M17, l=16-19 centered near M16, l=49-52 near W51, and l=52-55 centered near Sharpless 82), it is clear that the majority of the H II region locations trace areas of higher YSO concentrations.

Comparing all of the GLIMPSE contour images with the locations of H II regions, we find that $\sim$43% of the H II regions are located in close proximity to a large concentration of YSOs. H II regions located within a contour level of three or more were considered nearby to a cluster of YSOs. Taking a slightly less conservative approach, $\sim$84% of the H II regions are located within a contour level of two or greater. While not all of the high concentrations are located in close proximity to an H II region, a large fraction appear to be. We are also limited by the H II region studies, and to only those H II regions with known distances and radial velocity measurements. When looking at the largest clusters (contour levels of 4 or higher) independently, we find that roughly two-thirds are located in close proximity to a known H II region.

Again, this shows that the two seem to be correlated, but we are limited by the sample of known H II regions within a given distance.

Overall, the GLIMPSE images along with the YSO surface density maps show the distribution of YSOs across the galactic mid-plane. This distribution appears to be clustered in many areas, and the overall surface density of YSOs does not appear to be random. We see a correlation of newly forming protostars with the locations of known H II regions, adding support to the idea of triggered star formation from H II region expansion. The global picture that this dataset gives to a better understanding of star formation in our galaxy is very important. It allows for a larger view of the star formation picture, and along with the more detailed observations and analysis of specific H II region environments it can help in answering many of the ongoing questions about the significance of triggered star formation in H II region environments. This dataset and the analysis shown here clearly demonstrate that a majority of YSOs are forming in crowded, clustered environments, and not in relative isolation.

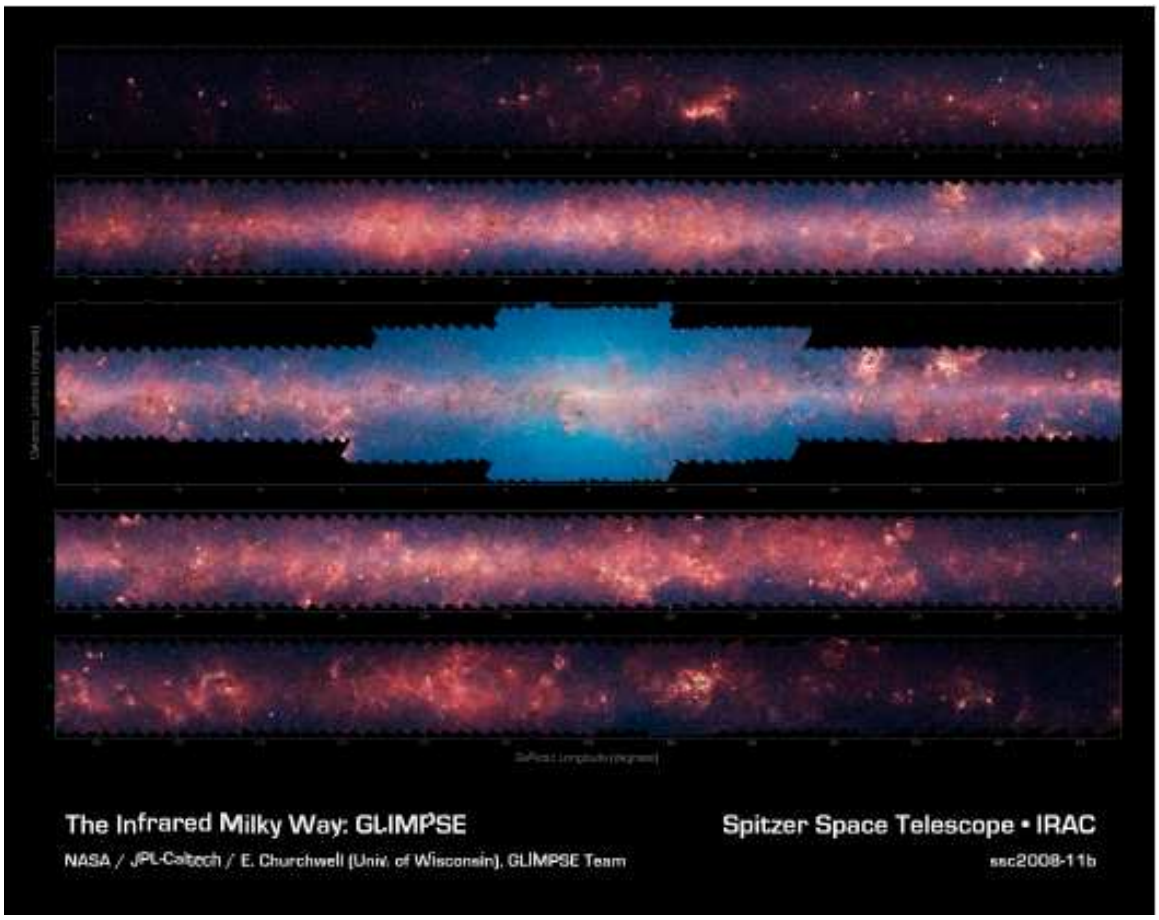

FIG. 51.—A mosaicked image of the Galactic Mid-Plane from the GLIMPSE survey. All four IRAC bands were used to make this image, with the shorter wavelengths (3.6 and 4.5 μm) in blue and the longer wavelength bands in green (5.8 μm) and red (8.0 μm). Credit GLIMPSE Team, http://www.astro.wisc.edu/sirtf/

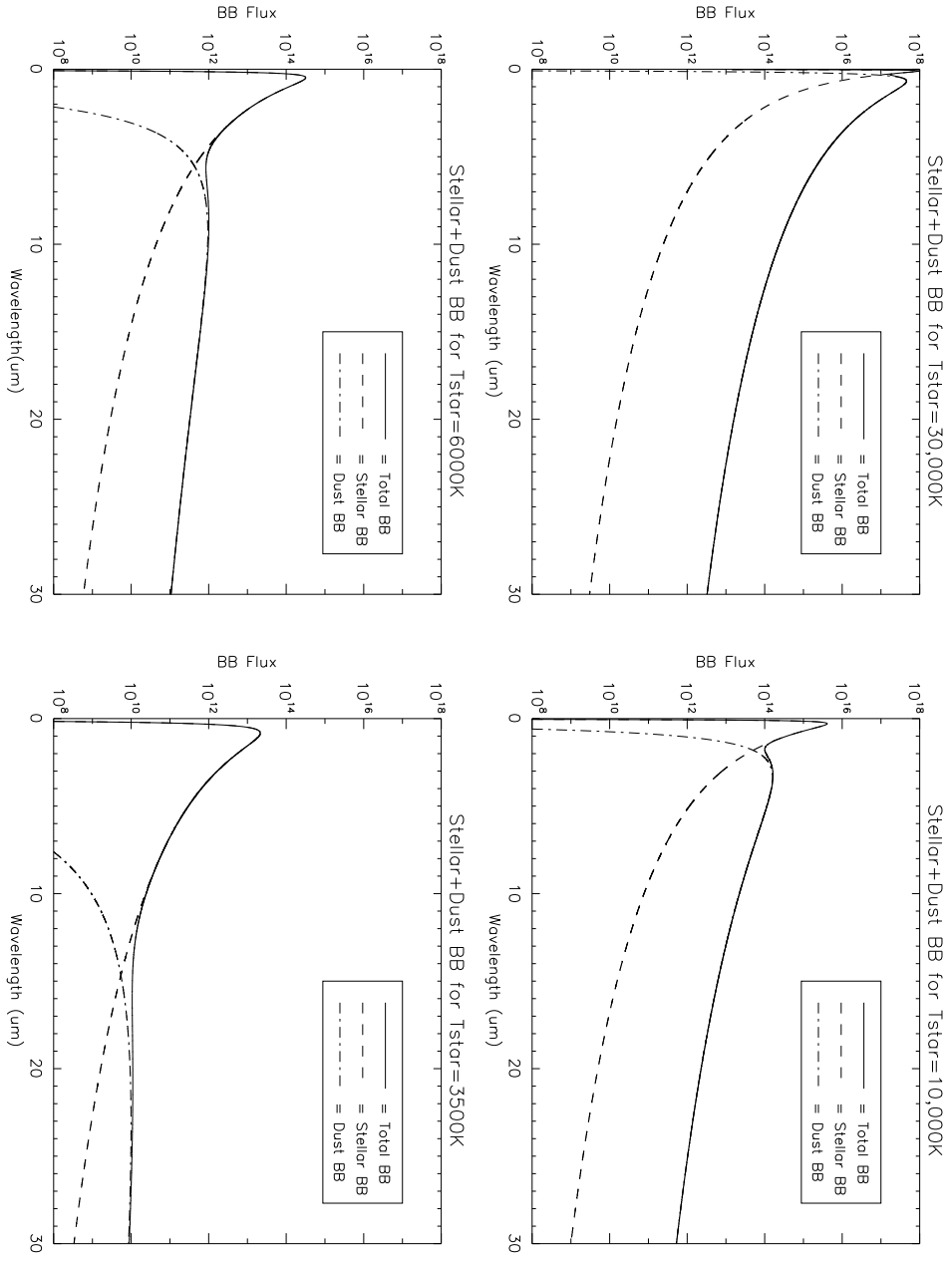

FIG. 52.—Model SEDs produced from central stellar sources of varying temperature and from dust emission surrounding the star.

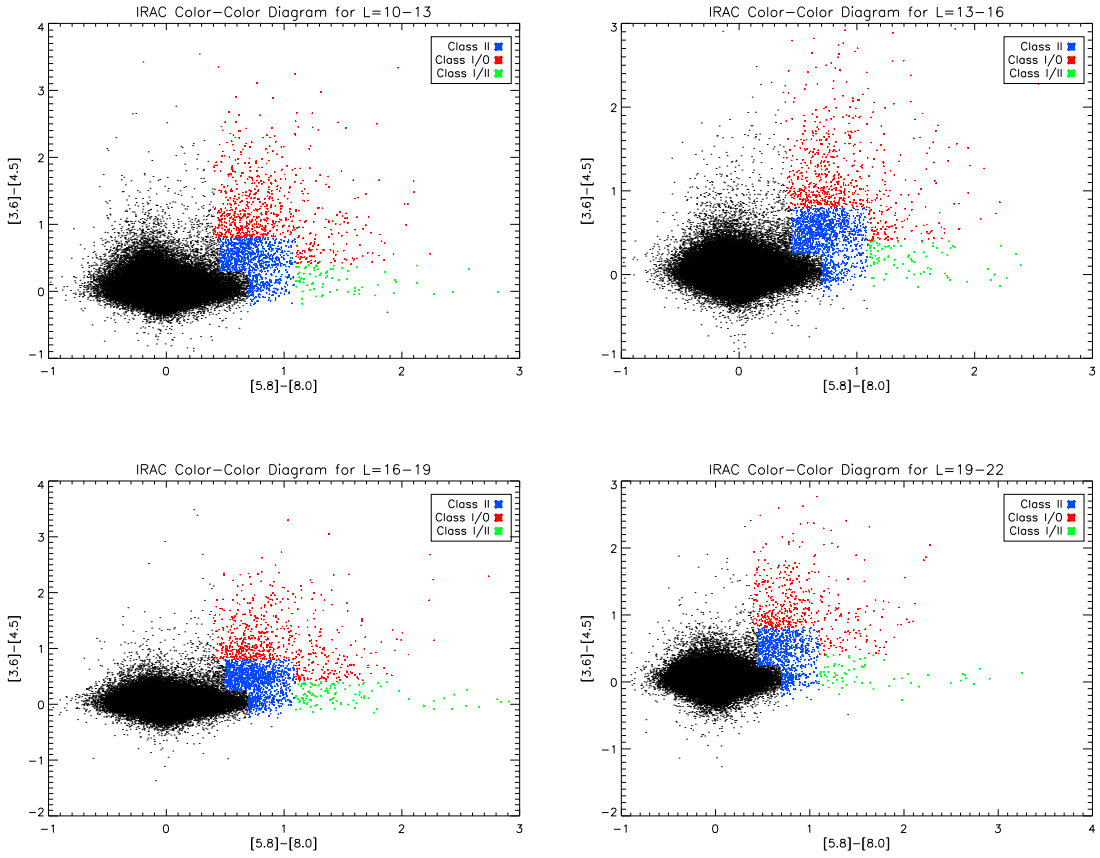

FIG. 53.—IRAC color-color plots from four different regions within the GLIMPSE dataset, l=10-13, l=13-16, l=16-19, and l=19-22. Classes of YSOs are shown in blue, green, and red.

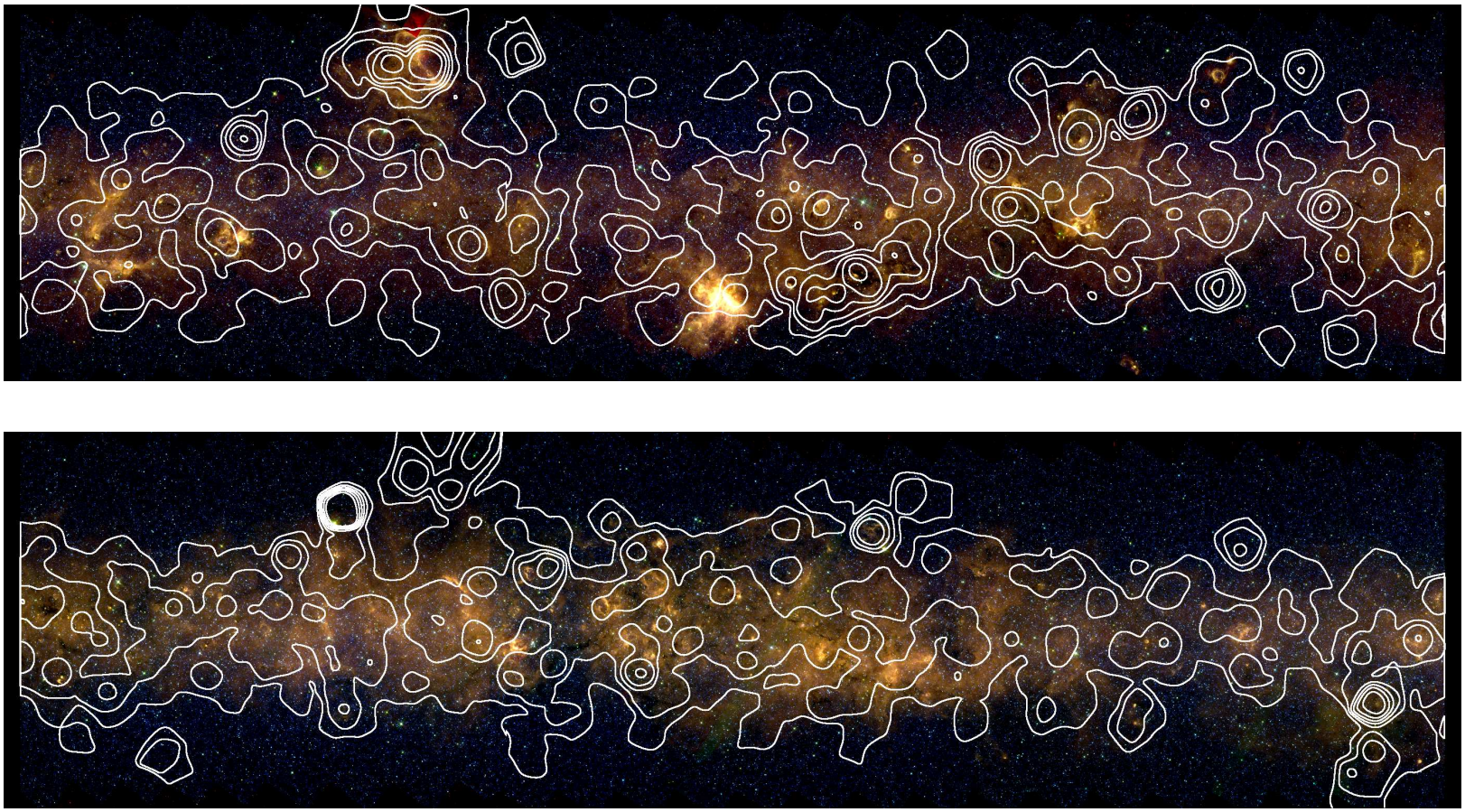

FIG. 54.—3-color GLIMPSE images of the region l=10-37; top: l=10-19, bottom: l=19-28. IRAC bands 3.6, 5.8, and 8.0 μm are shown in blue, green, and red, respectively. The contours show the surface density of candidate YSOs in the region, each contour level represents a factor of two increase.

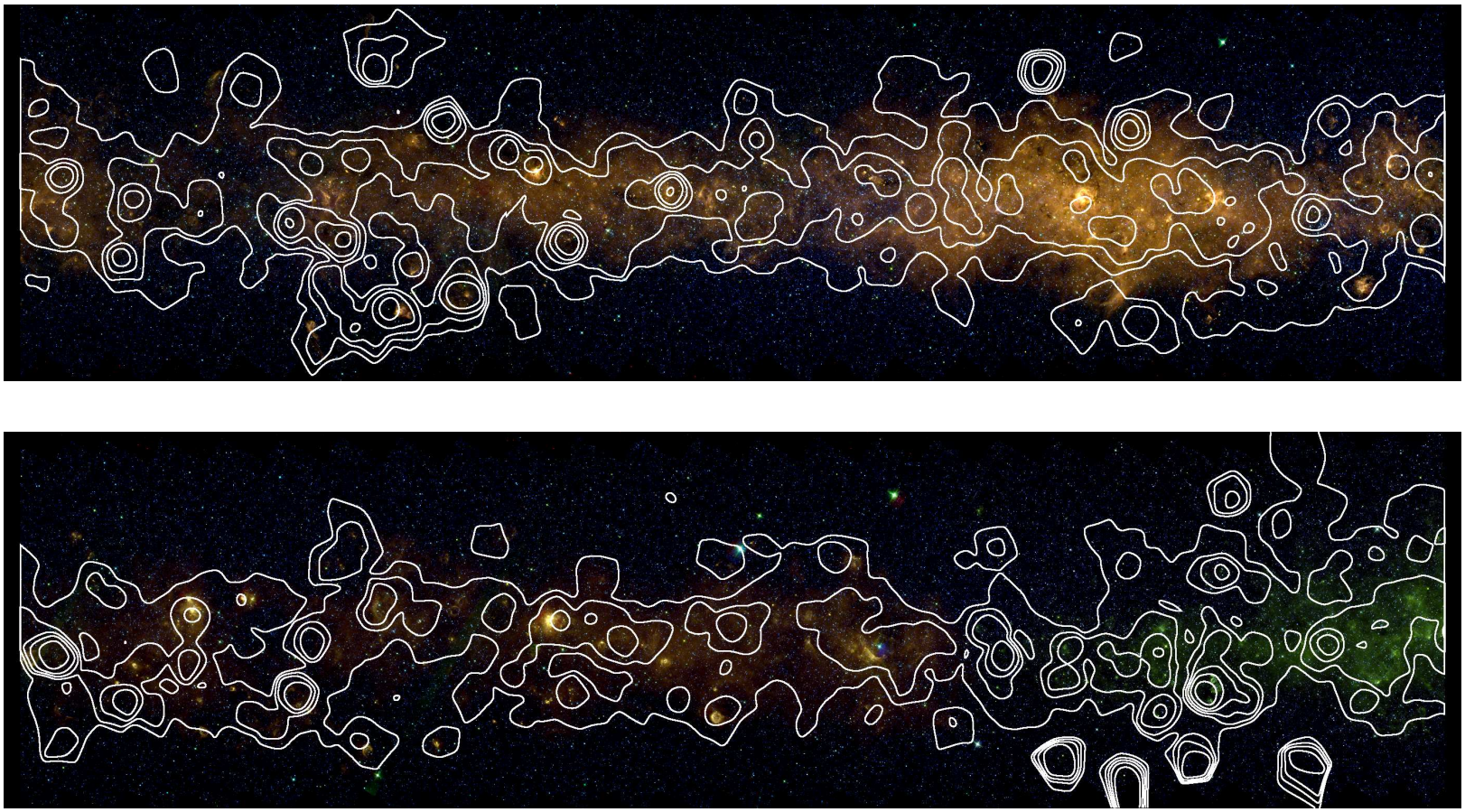

FIG. 55.—3-color GLIMPSE images of the region l=28-46; top: l=28-37, bottom: l=37-46. IRAC bands 3.6, 5.8, and 8.0 μm are shown in blue, green, and red, respectively. The contours show the surface density of candidate YSOs in the region, each contour level represents a factor of two increase.

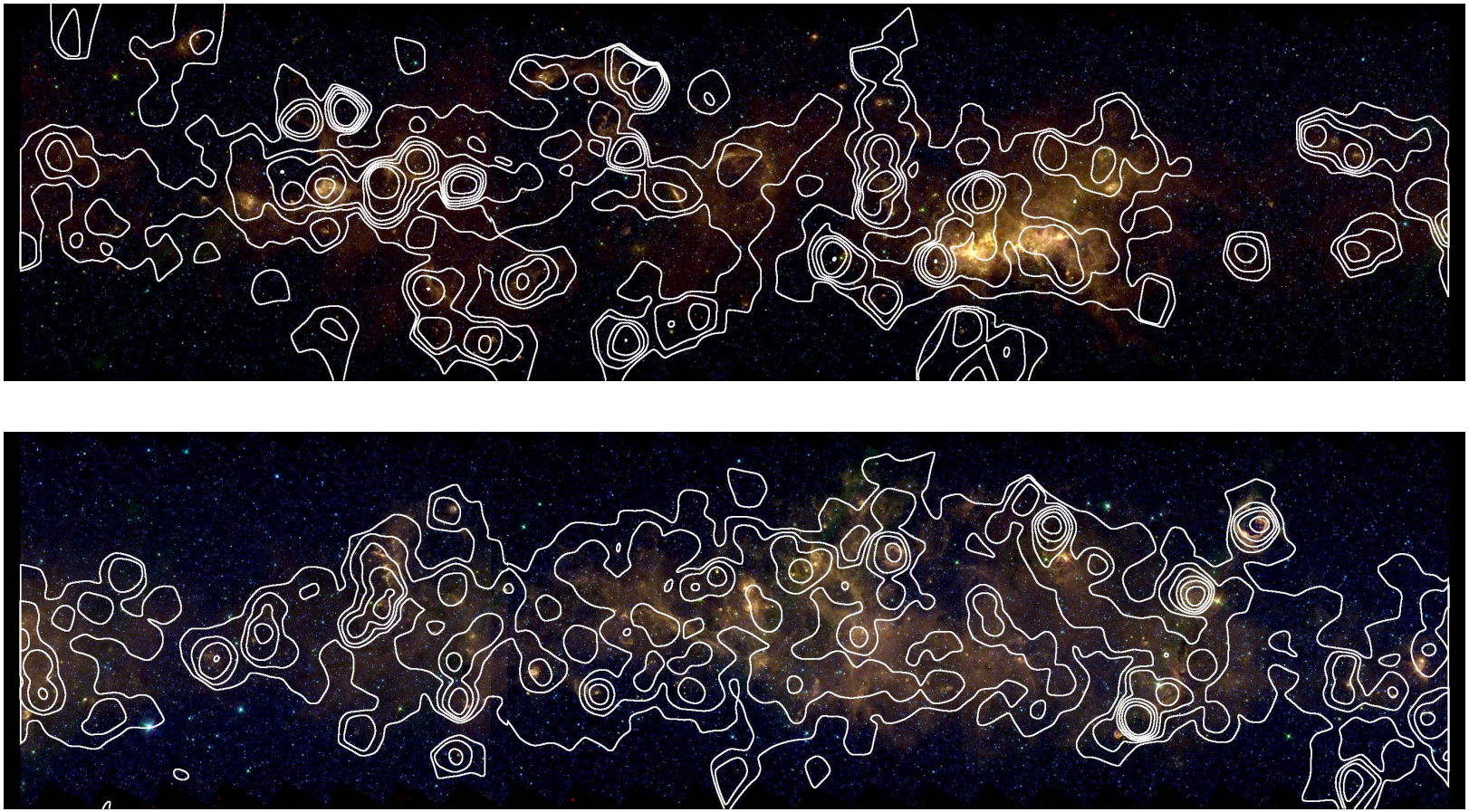

FIG. 56.—3-color GLIMPSE images of the region l=46-55 & l=307-316; top: l=46-55, bottom: l=307-316. IRAC bands 3.6, 5.8, and 8.0 μm are shown in blue, green, and red, respectively. The contours show the surface density of candidate YSOs in the region, each contour level represents a factor of two increase.

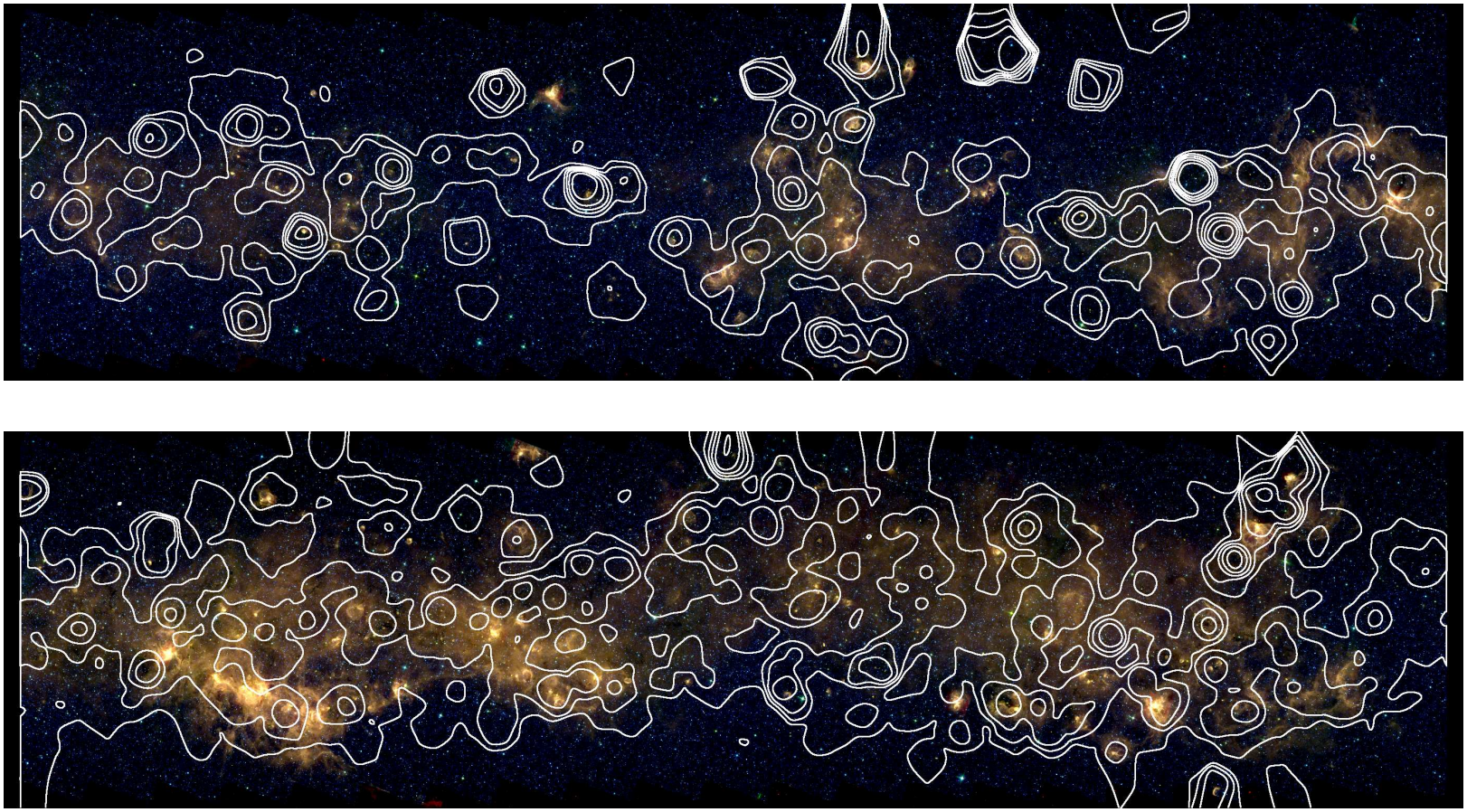

FIG. 57.—3-color GLIMPSE images of the region l=316-334; top: l=316-325, bottom: l=325-334. IRAC bands 3.6, 5.8, and 8.0 μm are shown in blue, green, and red, respectively. The contours show the surface density of candidate YSOs in the region, each contour level represents a factor of two increase.

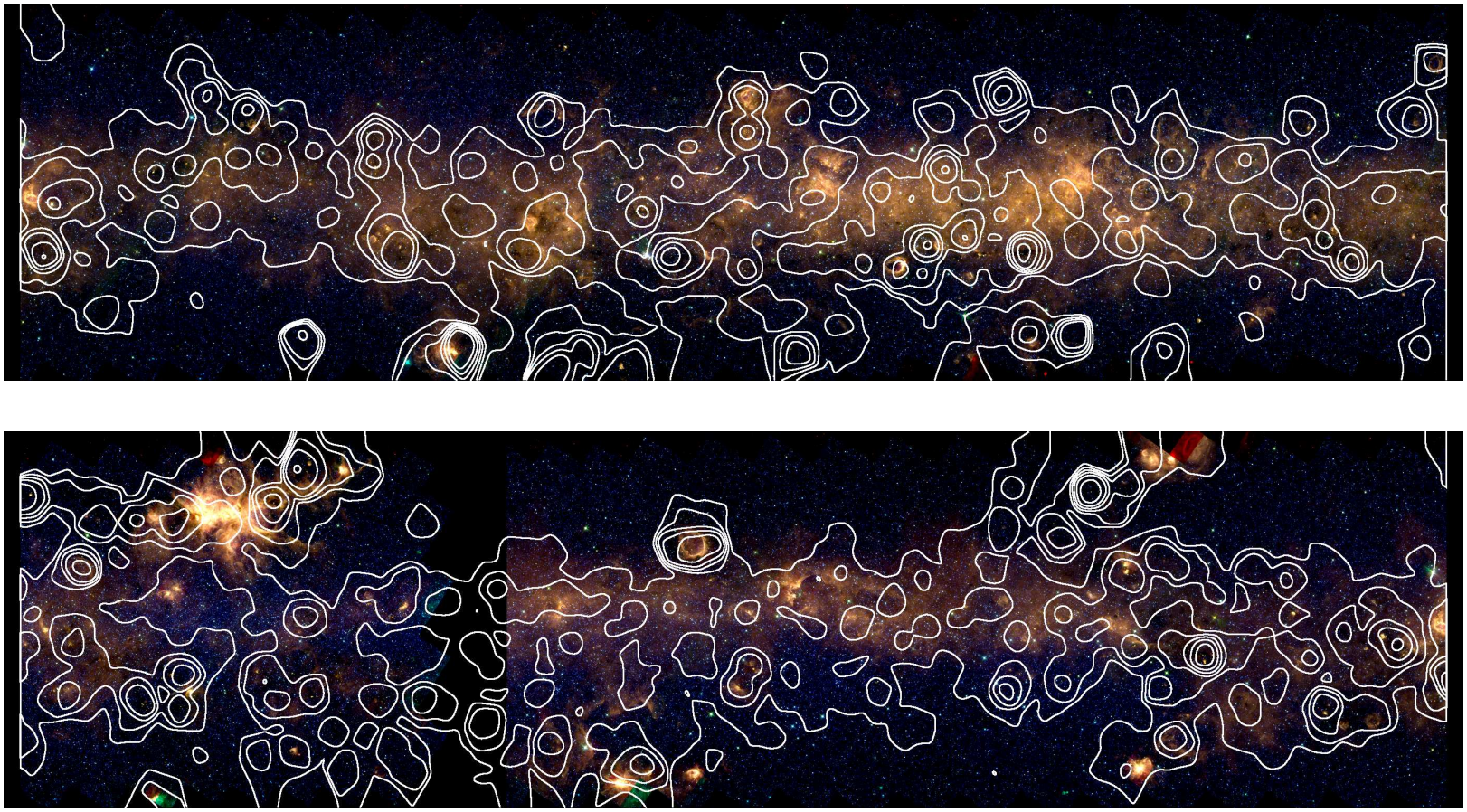

FIG. 58.—3-color GLIMPSE images of the region l=334-352; top: l=334-343, bottom: l=343-352. IRAC bands 3.6, 5.8, and 8.0 μm are shown in blue, green, and red, respectively. The contours show the surface density of candidate YSOs in the region, each contour level represents a factor of two increase.

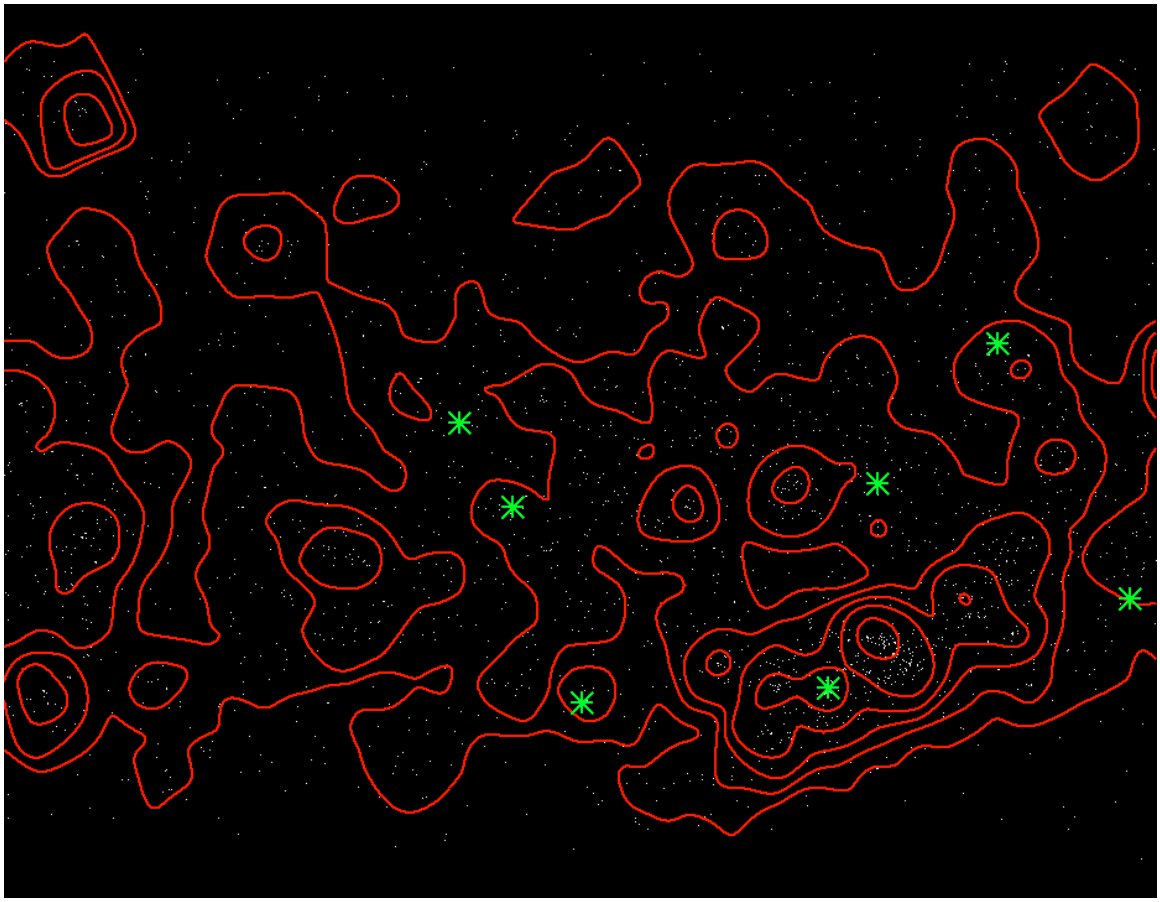

FIG. 59. —The location of individual YSO candidates for the region l=13-16 are marked by the white points. The surface density contours are overplotted in red, with each contour level representing a factor of two increase. Locations of known H II regions are marked by green asterisks. M17 is loacted in the lower middle part of the image, where a strong concentration of sources is located.

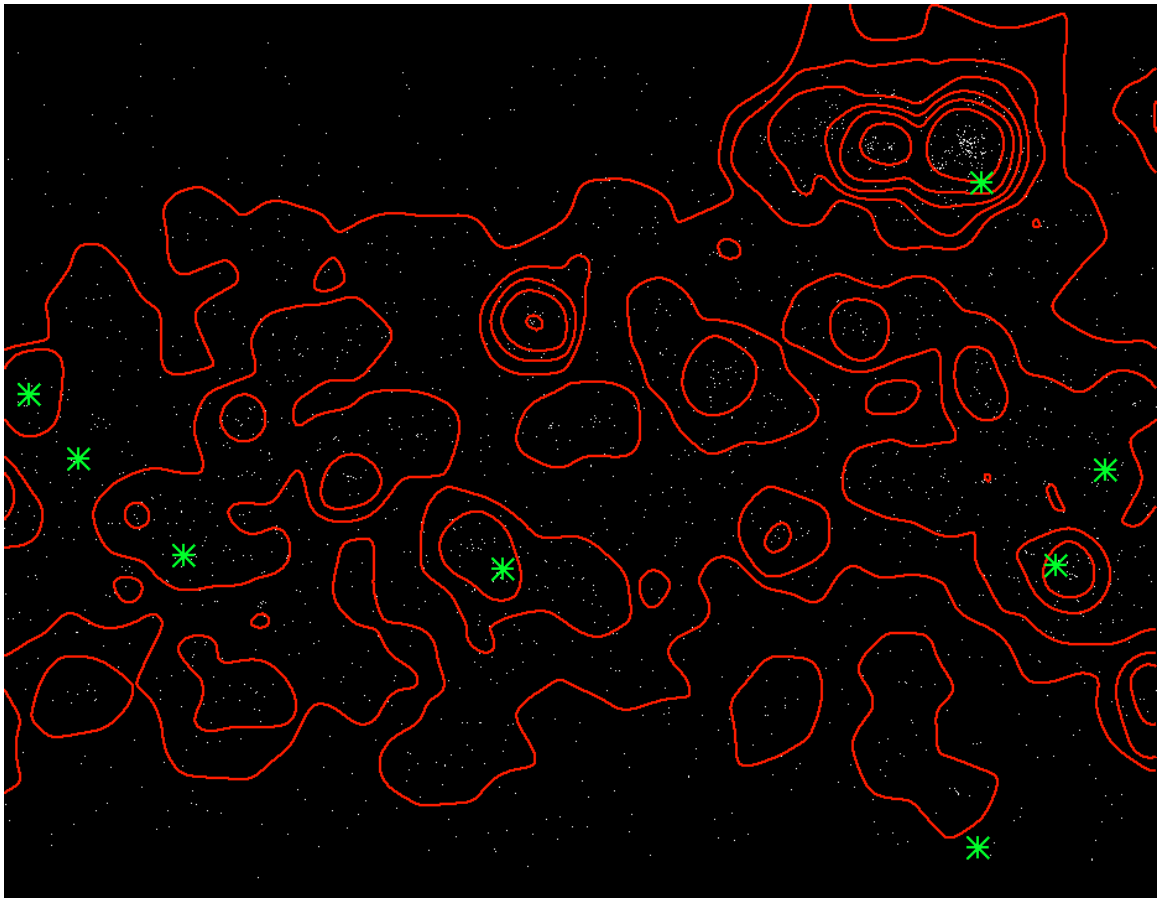

FIG. 60. —The location of individual YSO candidates for the region l=16-19 are marked by the white points. The surface density contours are overplotted in red, with each contour level representing a factor of two increase. Locations of known H II regions are marked by green asterisks. M16 is loacted to the upper right, where a strong concentration of sources is located.

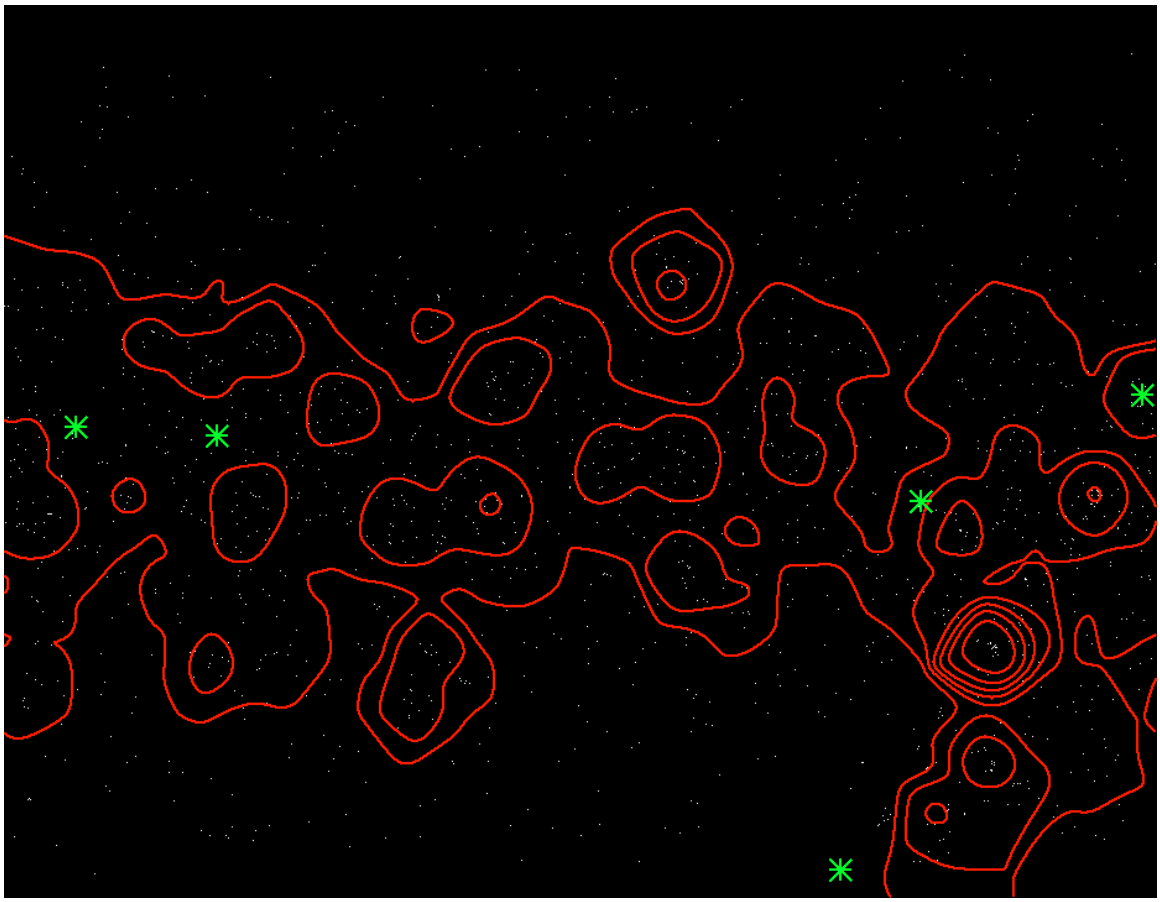

FIG. 61. —The location of individual YSO candidates for the region l=19-22 are marked by the white points. The surface density contours are overplotted in red, with each contour level representing a factor of two increase. Locations of known H II regions are marked by green asterisks.

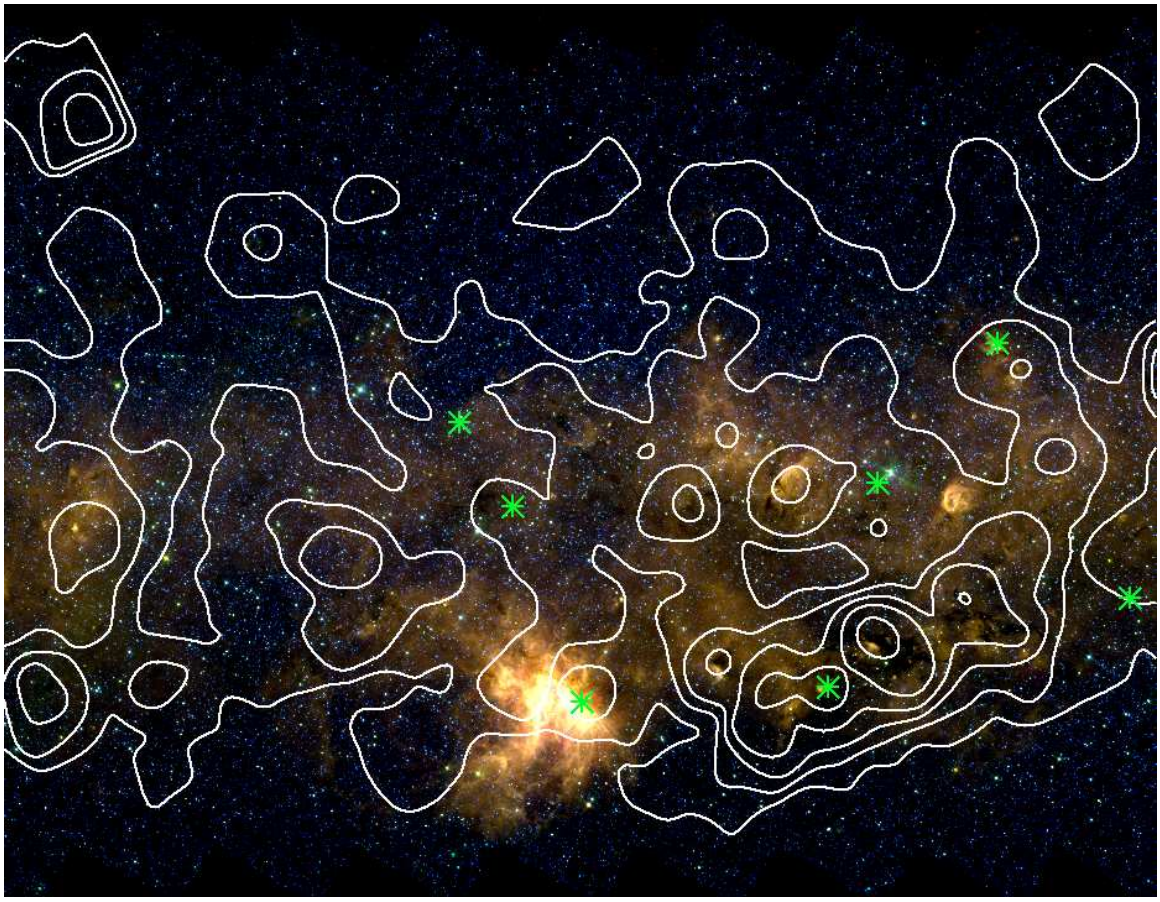

FIG. 62.—3-Color GLIMPSE image of the region l=13-16. IRAC bands 3.6, 5.8, and 8.0 μm are shown in blue, green, and red, respectively. The contours show the surface density of candidate YSOs in the region, with each contour level representing a factor of two increase. Locations of known H II regions are marked by green asterisks. The H II region M17 is the very bright region in the lower middle part of the image. The locations of high concentrations of YSOs and H II regions appear to be correlated.

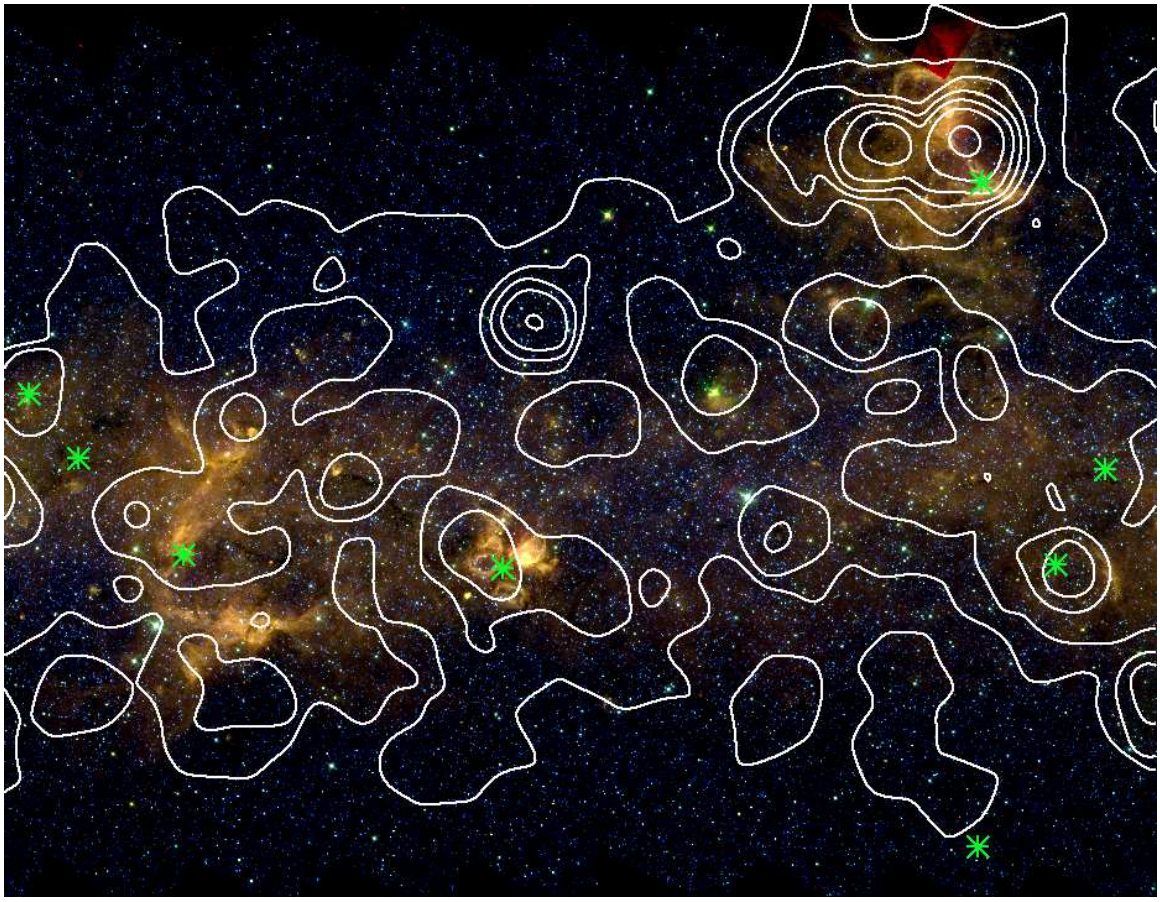

FIG. 63. —3-Color GLIMPSE image of the region l=16-19. IRAC bands 3.6, 5.8, and 8.0 μm are shown in blue, green, and red, respectively. The contours show the surface density of candidate YSOs in the region, with each contour level representing a factor of two increase. Locations of known H II regions are marked by green asterisks. The H II region M16 is the bright region in the upper right. The locations of high concentrations of YSOs and H II regions appear to be correlated.

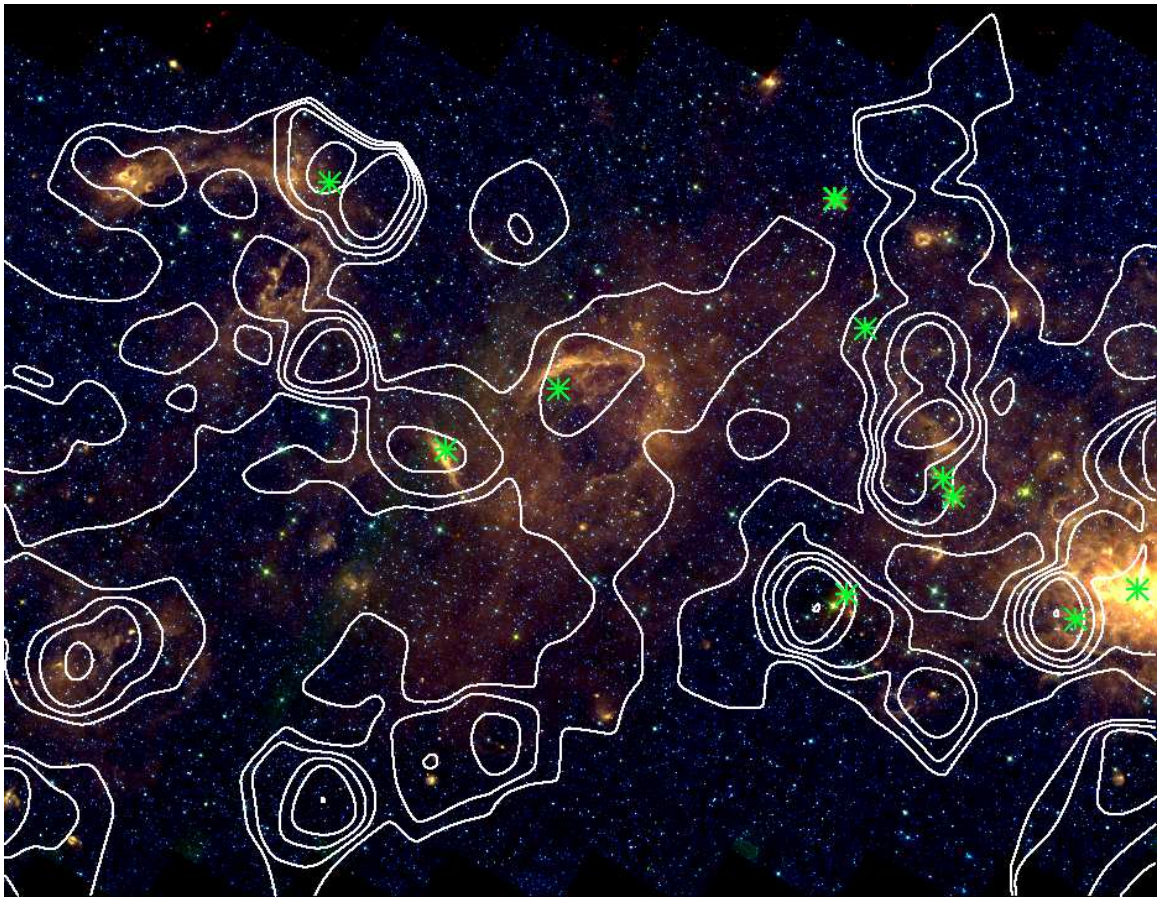

FIG. 64.—3-Color GLIMPSE image of the region l=49-52. IRAC bands 3.6, 5.8, and 8.0 μm are shown in blue, green, and red, respectively. The contours show the surface density of candidate YSOs in the region, with each contour level representing a factor of two increase. Locations of known H II regions are marked by green asterisks. The H II region W51 is the bright region on the right-hand side. The locations of high concentrations of YSOs and H II regions appear to be correlated.

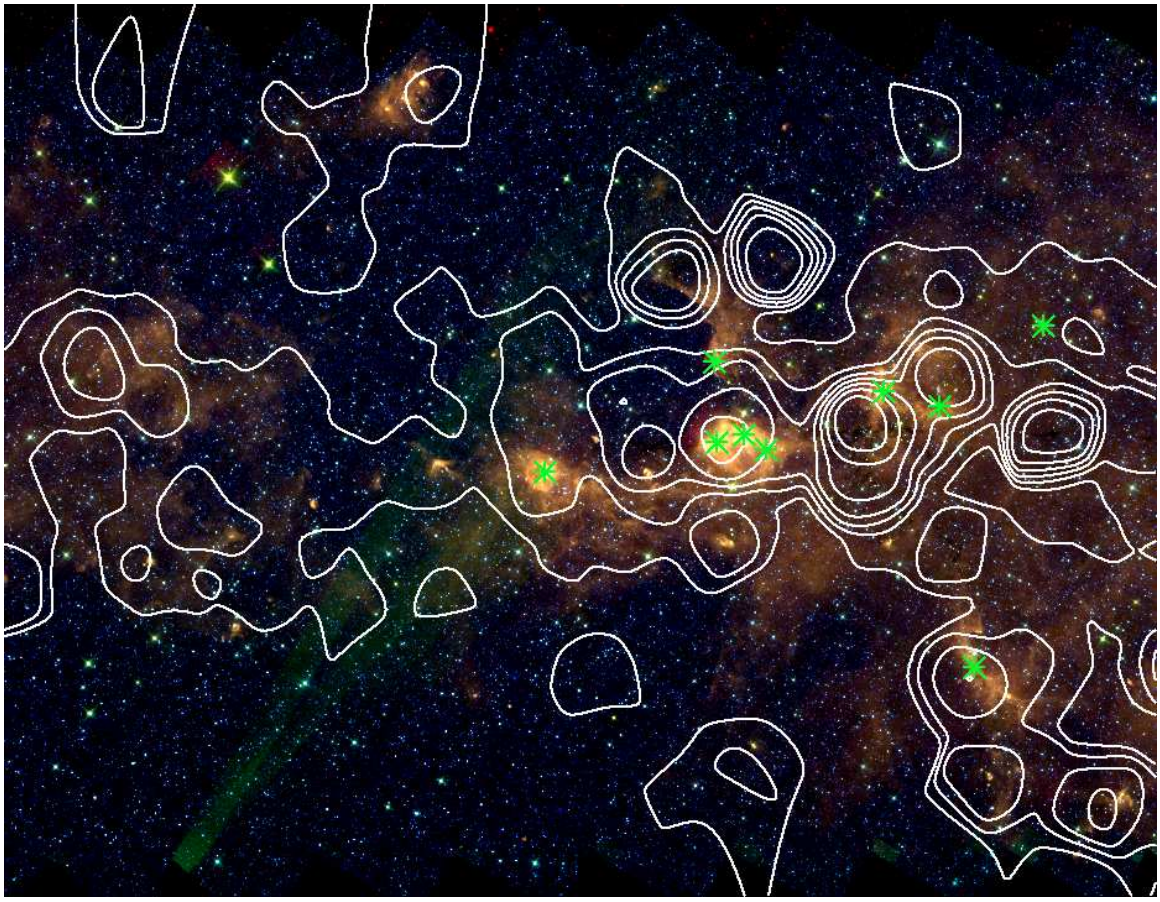

FIG. 65. —3-Color GLIMPSE image of the region l=52-55. IRAC bands 3.6, 5.8, and 8.0 μm are shown in blue, green, and red, respectively. The contours show the surface density of candidate YSOs in the region, with each contour level representing a factor of two increase. Locations of known H II regions are marked by green asterisks. The H II region Sh-82 is located in the middle of the image. The locations of high concentrations of YSOs and H II regions appear to be correlated.

7. CONCLUSION

This dissertation has focused on the study of star formation in H II region environments in order to better understand the differences between star formation in these environments and in small isolated regions. This dissertation specifically studied the role of triggered star formation due to H II region expansion and attempts to quantify the amount of triggering in four specific H II region environments. We also looked at a global view of star formation in the Milky Way Galaxy by using the *Spitzer* GLIMPSE survey to map the surface density of YSOs across the galactic mid-plane. The density of YSOs in the GLIMPSE survey was also compared to known locations of H II regions in order to look at the correlation of YSOs with other tracers of massive star formation.

In Chapter 2, we used new *Spitzer* mid-IR observations of the H II region NGC 2467, along with archival *HST* and 2MASS data, to identify YSOs in this region and to study the distribution of these sources. In this first study we developed a method to accurately select point sources that were in the cluster, and from the point source selection, we detected 45 candidate YSOs based on their mid-IR color excesses. Model YSO SEDs were used to help confirm the candidate YSOs and to determine best-fit properties of these sources. The best-fit physical parameters were then used to determine a mass function for the current YSO population in NGC 2467. The interaction of the massive stars in the cluster with the newly forming protostars was studied by mapping the locations of ionization fronts in the region and comparing the distribution of candidate YSOs to ionization front locations. The statistical significance of the distribution of YSOs was also studied in a number of ways, leading to the conclusion that the population of YSOs is not a random distribution and that they

are highly correlated with the locations of ionization fronts. The second main result from Chapter 2 was an estimate of the triggered star formation rate for this region. We found that triggered star formation is occurring in NGC 2467 at a rate of 4.2 - 9×10^{-4} $M_{\odot}$ yr^{-1}, which is equal to 24 - 52% of the total estimated star formation.

The methods developed in Chapter 2 were applied to three more H II regions in Chapters 3 - 5. We also had new *Spitzer* observations for each of these three regions, NGC 2175, NGC 3324, and M16. For NGC 2175, we detected 265 candidate YSOs. The selected 265 sources were confirmed as probable YSOs by using a SED fitter from Robitaille et al. (2007). The SED fitter and color-criteria of other contaminant objects (AGB stars and extragalactic sources) allowed us to discard an additional 75 initial YSO candidates as unlikely protostellar objects. 191 of the 265 YSOs also showed an excess in their near-IR colors from 2MASS photometry.

We then mapped out the location of detectable ionization fronts and calculated the distance of each YSO from the nearest ionization front. From our initial calculations, we determined that over half of the YSOs were located within a projected distance of 1 pc or less from an ionization front, and we concluded that these objects were likely triggered due to the expanding H II regions. Further analysis showed that due to some of the ionization fronts moving face-on to our line of sight, it is likely that as much as 70% of the YSOs are within 1 pc from an ionization front. The distribution of YSOs also shows that they are strongly clustered in the regions of compressed gas. Many YSOs are located near the ridge of compressed molecular gas created by the ionizing effects from the O6.5 V star. As well as many more YSOs

that are clustered around the smaller compact H II regions in the area. It seems likely that if the main ionizing star has led to triggering of more massive stars, as has been shown by previous studies (Lada & Wooden 1979), then the compact H II regions created by the newer OB stars is leading to triggering of many more low-mass stars. We definitely see clustering of YSOs in NGC 2175, mostly centered around three of these compact H II regions. Finally, we estimated the total current rate of star formation and a possible triggered star formation rate in NGC 2175. The estimated current total star formation rate is 2×10^{-3} $M_{\odot}$ yr^{-1}, with a triggered star formation rate equal to 0.75 - 1.15×10^{-3} $M_{\odot}$ yr^{-1}. This results in 38 - 58% of the YSOs in this region being formed by triggering due to H II region expansion.

In Chapter 4, we have identified 77 candidate YSOs in NGC 3324 based on *Spitzer* mid-IR excesses; 37 of the 77 sources also had a 2MASS measured near-IR color excess, helping to confirm them as YSO candidates. When the sample of *Spitzer* selected YSOs was compared to a selection of 47 YSOs by Cappa et al. (2008) using IRAS, MSX, and 2MASS data, we found that 13 of these sources matched up.

The two main O stars, located at the center of NGC 3324, have created an ionized cavity and the main ionization front created by these stars is clearly visible in the images presented in this chapter. Looking at the distribution of YSOs shows that a significant fraction are located very near to the edge of the ionization front. Some have already been uncovered by the passing ionization front, and are currently sitting right inside the H II region. Whereas even more YSOs appear to still be located in compressed molecular gas near the ionization fronts. The last piece of analysis for this

region was to estimate the rate of triggered star formation. The estimated current total star formation rate is 6.5×10^{-4} $M_\odot$ yr^{-1}, with a triggered star formation rate equal to 2.2 - 3.7×10^{-4} $M_\odot$ yr^{-1}. This results in 34 - 57% of the YSOs in this region being formed by triggering due to H II region expansion.

In Chapter 5, we performed the same analysis on M16 as had been done in the other three regions. In M16, 237 candidate YSOs were identified. Due to the wealth of data on M16, we wanted to compare our results to the many previous studies done on M16. We detected a few of the previously well known YSOs in M16, two located at the tips of famous columns in the *HST* WFPC-2 FOV. We also detected three YSOs that overlap with three of the "EGGs" from Hester et al. (1996), along with a few YSOs that overlapped with known X-ray sources from Linsky et al. (2007). From our analysis, there does appear to be a number of very young Class I/0 YSOs embedded in the molecular gas of the M16 columns, whereas there are a number of older Class II YSOs already uncovered but very close to the columns, suggesting that we are seeing a progression in terms of evolutionary class within the columns. This is evidence for some triggered star formation occurring in M16, especially within the elephant trunks. However, M16 had the lowest calculated triggered star formation rate as compared to the other three regions. The calculated triggered star formation rate ranged from 4 - 8×10^{-4} $M_\odot$ yr^{-1} for M16, which equals 14 - 37% of the total SFR for this region. Therefore, it is probable that there is some triggering occurring in M16, but that there is also distributed star formation occurring in this region. This agrees with the overall conclusions of Indebetouw et al. (2007) on their analysis

of M16 with *Spitzer* data. The one difference we see when comparing to their study is that we see stronger evidence for triggered star formation having occurred in the elephant trunks of M16.

In Chapter 6, we present the results of a global study of star formation across the galactic plane. We used the GLIMPSE survey to select tens of thousands of YSOs in the Milky Way and to look at their overall surface distribution. The surface density maps of YSOs showed that there are strong clusterings of YSOs forming in the Galaxy. We also showed that there appears to be a correlation between these strong clusterings and the locations of known H II regions. Overall, we concluded that as many as 67% of the strong concentrations of YSOs are located in close proximity to a known H II region. This leads to the conclusion that new protostars are often formed in clusters, and many are formed very nearby to massive stars and the H II regions created by the massive stars. Therefore, it seems likely that triggered star formation from H II region expansion is occurring on a large scale across the Milky Way Galaxy.

This dissertation set out to test a number of predictions about the different scenarios of star formation in H II region environments. The difference between the two main scenarios (coveal star formation vs. ongoing triggered star formation) is dependent on the age spread within a given cluster. Hillenbrand et al. often suggest most star formation in H II region enviroments is coeval, claiming that age spreads that are seen in the HR diagrams of young clusters, such as NGC 6611 in M16, can be negated if there is an error of one spectral subtype in classification of cluster members. They also claim that the ages of low-mass stars pre-main sequence stars are

often underestimated and ages of massive stars are overestimated. In the NGC 6611 cluster, Hillenbrand et al. (1993) show evidence that the star formation is relatively coeval for the high-mass stars (cluster age of ∼2 Myr with an age spread of ∼1 Myr). However, Hillenbrand et al. (1993) also detect a younger, low-mass pre-MS population, with ages ranging from 0.25 - 1 Myr, agreeing with the data presented in this dissertation for M16. Hillenbrand et al. (1993) conclude that an age spread of 1 Myr is relatively small; therefore the star formation in M16 can be considered coeval. However, we have shown that triggering occurs on short timescales of order a few$\times 10^5$ yr.

If coeval star formation is the dominant scenario for star formation in rich clusters, then one would expect the spatial distribution of pre-main sequence stars, in a given region, to be randomly distributed and uncorrelated to the compressed gas around the H II regions. Another prediction for this scenario is that we would expect to see clusters of young low-mass stars located in the extended areas around H II regions. Finally, we would expect to see that the ages of low-mass stars are greater than the ages of the massive ionizing stars. Whereas, if triggering from H II region expansion is a dominant mode, then we expect to see YSOs that are found concentrated in the compressed gas from the H II region expansion. We would also expect the low-mass stars to have an age spread ranging from very young up to the age of the massive stars. Again, these are all testable predictions. The results presented in this dissertation do not show a random spatial distribution of low-mass stars. Instead, the spatial distribution of YSOs in the four H II regions shows that

the majority (60-100%) of the young population of protostars is correlated with the locations of ionization fronts and the compressed molecular gas. Also, the average age (few$\times 10^5$ yr) of the protostellar objects in these regions is younger than age of the massive ionizing stars, with typically a few YSOs in each region having ages closer to the age of the massive ionizing stars, on order a Myr. We do not see a population of old low-mass and intermediate-mass stars.

Another point about the spatial distribution of YSOs in these regions is that in a few areas we do see clusters of YSOs that are not in close proximity to an ionization front. But one might speculate that these clusters of YSOs were closer to the ionization front at one time, and were still triggered by the expansion of the H II region. One such cluster can be in seen in M16, located in the lower right of Figure 39. This cluster of YSOs appears to not be embedded in compressed molecular gas and it is farther awawy from the four main ionizing O stars. But given an expanding H II region, we expect to see clusters of low-mass YSOs that have already been uncovered by the ionization fronts, and are now sitting in the exposed interior of the H II region; therefore, this cluster could likely still have been triggered by the expanding H II region. A cluster like this would not have been included in the total fraction of YSOs that is used to estimate the amount of triggering in M16, however if at one point this cluster was closer to the ionization front, and was likely triggered, then the estimated amount of triggered star formation in M16 would be higher.

A few other past results can be compared with the results presented in this dissertation, including the study by Haisch et al. (2001) on the survival of disks with

age in a cluster. Haisch et al. using JHKL infrared excesses calculated the fraction of sources with disks within a given cluster, and compared clusters of various ages. They found a trend in the fraction of sources with disks versus cluster age; demonstrating that the youngest clusters have the highest fraction of sources with disks. The clusters ranged in age from 0.3 - 30 Myr, and the disk fraction ranged from 85 - 3%. By the time one looks at a cluster that is 3 Myr, the disk fraction has fallen to 50% and by the time the cluster is 5 Myr, the disk fraction is as low as 12%. This seems to suggest that the star formation rate is decreasing rather quickly, even within the first few Myr. On the other hand, our results showed a similar result for the detection fraction of YSOs with cluster age, but we assumed a constant star formation rate. The detection fraction decreases with age, even with a constant star formation rate. This is likely due to the lowest mass protostars being undetectable after the first 0.5 Myr of their formation. Even though a new population of low-mass protostars was assumed to be continuously forming, the total detection fraction will still decrease with time. Our results showed that within the first 0.5 Myr, we could on average detect 40-50% of the YSOs, but after 0.5 Myr the detection fraction dropped fairly rapidly and falls to 15-30% by 2 Myr, agreeing with the decrease in disk fraction measured by Haisch et al. (2001).

Gounelle and Meibom (2008) have used the Haisch et al. results to suggest that star formation substantially decreases with time in cluster environments. Our results can serve as post-diction to those of Haisch et al. suggesting that star formation can be ongoing in a rich cluster, and not decreasing with time. Star formation in

the immediate vicinity of the massive ionizing star will decrease due to the molecular material being photoionized as well as being dissipated by winds from the massive star, but star formation should still continue in the nearby compressed molecular gas. Gounelle and Meibom (2008) interpret the Haisch et al. result as evidence that it is unlikely that a number of protoplanetary disks will be injected with SLRs from a nearby massive star once it goes supernova. However, we have shown that it is highly plausible that star formation is still ongoing in young clusters within the first few Myr, and not decreasing as dramatically as Gounelle and Meibom claim. Even with a constant star formation rate, we have shown that the detection fraction of YSOs will decrease with time in a young cluster. Typically by the time the region is 2 Myr, the detection fraction is between 15 - 30%, and it can be lower than one-third of what it was during the first 0.5 Myr, agreeing with the results of Haisch et al. (2001). Our results have also shown that there is ongoing star formation in these clusters within distances of only a few tenths of a pc - 5 pc from the massive star. Gounelle and Meibom (2008) also conclude that a protoplanetary disk has to be within a maximum distance of 0.4 pc away from the massive star when it goes supernovae in order to be injected with SLRs. At least 10% of the protostars in each of the four H II regions presented here are within a projected distance of 0.4 pc or less from the massive ionizing stars. While this is a small fraction, this could be considered as a lower limit, given the fact that some YSOs will not be detected. We have shown that star formation is likely not decreasing at the substantial rate that Gounelle and Meibom cite, rather the detection fraction of YSOs decreases with time. Therefore, this could

still result in a number or protostellar objects being injected by SLRs from the nearby supernovae in each region.

Overall, the studies presented in this dissertation have shown that triggered star formation is occurring in many regions, and that it is a dominant mode of low-mass star formation, rather than the isolated star formation seen in Taurus-Auriga. We have calculated that the triggered star formation rate accounts for at least 14 - 58% of the total star formation in these regions. As was shown in Chapter 2, given the fact that as many as 70-90% of all low-mass stars form in rich clusters also containing massive stars (Lada & Lada 2003), then as many as 10 - 52% of all low-mass stars may be formed by triggering from H II region expansion. It is probable that some of the low-mass stars in these regions have formed spontaneously throughout the lifetime of the region, but we are also seeing populations of very young objects that are currently forming in compressed gas from the H II region expansion. While the data do not suggest that triggering is the only mode of low-mass star formation in these regions, it does suggest that triggering is occurring and has contributed a substantial fraction to the overall star formation rate.

REFERENCES

Adams, F.C., Lada, C.J., & Shu, F.H. 1987, ApJ, 312, 788

Allen, L.E., et al. 2004, ApJS, 154, 363

Andre, P., Ward-Thompson, D., & Barsony, M. 1993, ApJ, 406, 122

Bally, J., O'Dell, C.R., & McCaughrean, M.J. 2000, AJ, 119, 2919

Balog, Z., et al. 2007, ApJ, 660, 1532

Benjamin, R.A., et al. 2003, PASP, 115, 953

Bertoldi, F. 1989, ApJ, 346, 735

Bertoldi, F. & McKee, C.F. 1990, ApJ, 354, 529

Blaauw, A. 1964, ARA&A, 2, 213

Cappa, C. et al. 2008, A&A, 477, 173

Carraro, G., Patat, F., & Baumgardt, H. 2001, A&A, 371, 107

Cernicharo, J., et al. 1998, Science, 282, 462

Cernicharo, J., et al. 1992, A&A, 261, 589

Chabrier, G. 2003, PASP, 115, 763

Churchwell, E. et al. 2007, ApJ, 670, 428

Churchwell, E. et al. 2006, ApJ, 649, 759

Claria, J.J. 1977, A&A, 27, 145

Cruz-Gonzalez, C. et al. 1974, Rev. Mexicana Astron. Astrofis., 1, 211

Cyganowski, C.J. et al. 2008, Accepted to AJ, astroph/0810.0530

Dahm, S.E. & Hillenbrand, L.A. 2007, AJ, 133, 2072

de Geus, E.J., de Zeeuw, P.T., & Lub, J. 1989, A&A, 216, 44

De Marco, O., et al. 2006, AJ, 131, 2580

de Zeeuw, P.T., et al. 1999, AJ, 117, 354

Deharveng, L., Zavagano, A., & Caplan, J. 2005, A&A, 433, 565

Elmegreen, B.G. & Lada, C.J. 1977, ApJ, 214, 725

Elmegreen, B.G. 2008, 4th *Spitzer* Science Center Conference, "The Evolving ISM in the Milky Way and Nearby Galaxies: Recycling in the Nearby Universe;", http://ssc.spitzer.caltech.edu/mtgs/ismevol/

Everett, M.E. & Howell, S.B. 2001, PASP, 113, 1428

Fazio, G.G., et al. 2004, ApJS, 154, 10

Feinstein, A. & Vazquez, R.A. 1989, A&A, 77, 321

Felli, M., Habing, H.J., & Israel, F.P. 1977, A&A, 59, 43

Fitzgerald, M.P. & Moffat, A.F.J. 1974, AJ, 79, 876

Fountain, W.F., Gary, G.A., & Odell, C.R. 1983, ApJ, 273, 639

Gounelle, M. & Meibom, A. 2008, ApJ, 680, 781

Grasdalen, G.L. & Carrasco, L. 1975, A&A, 43, 259

Haikala, L.K. 1995, A&A, 294, 89

Haisch, K.E., Lada, E.A., & Lada, C.J. 2001, ApJ, 553, L153

Harvey, P.M., et al. 2006, ApJ, 644, 307

Healy, K.R., Hester, J.J., & Claussen, M.J. 2004a, ApJ, 610, 835

Healy, K.R. 2004b, PhD Thesis, Arizona State University

Hester, J.J., et al. 1996, AJ, 111, 2349

Hester, J.J., Scowen, P.A., Stapelfeldt, K.R., Krist, J., & WFPC2 IDT Team 1999, BAAS, 31, 932

Hester, J.J. & Desch, S.J. 2005, in ASP Conf. Ser. 341, "Chondrites and the Protoplanetary Disk", 107

Hillenbrand, L.A., Bauermeister, A., & White, R.J. 2007, in ASP Conf. Ser. 384, "Cool Stars 14", 200

Hillenbrand, L.A. 1997, AJ, 113, 1733

Hillenbrand, L.A. et al. 1993, AJ, 106, 1906

Ikeda, H. et al. 2008, AJ, 135, 2323

Indebetouw, R. et al. 2007, ApJ, 666,321

Johnstone, D., Hollenbach, D. & Bally, J. 1998, ApJ, 499, 758

Kerton, C.R. et al. 2008, MNRAS, 385, 995

Koempe, C. et al. 1989, A&A, 221, 295

Lada, C.J. & Lada, E.A. 2003, ARA&A, 41, 57

Lada, C.J. & Wooden, D. 1979, ApJ, 232, 158

Larosa, T.N. 1983, ApJ, 274, 815

Lee, H.-T. & Chen, W.P. 2007, ApJ, 657, 884

Lee, H.-T. et al. 2005, ApJ, 624, 808

Lee, T. et al. 1998, ApJ, 506, 898

Linsky, J.L. et al. 2007, ApJ, 654, 347

Maiz-Apellaniz, J. et al. 2004, ApJS, 151, 103

McCaughrean, M.J. & Andersen, M. 2002, A&A, 389, 513

Megeath, S.T., et al. 2004, ApJS, 154, 367

Moffat, A.F.J. & Vogt, N. 1975, ApJS, 20, 125

Moreno-Corral, M.A., Chavarria-K., C., & de Lara, E. 2002, Rev. Mexicana Astron. Astrofis., 38, 141

Munari, U. & Carraro, G. 1996, MNRAS, 283, 905

Munari, U., Carraro, G., & Barbon, R. 1998, MNRAS, 297, 867

O'Dell, C.R., Wen, Z., & Hu, X. 1993, ApJ, 410, 696

Oey, M.S., Watson, A.M., Kern, K., & Walth, G.L. 2005, AJ, 129, 393

Padgett, D.L., et al. 1999, AJ, 117, 1490

Palla, F. 1999, in "The Origin of Stars and Planetary Systems", ed. C.J. Lada & N.D. Kylafis (NATO ASI Ser. C, 540: Dordrecht: Kluwer), 375

Pismis, P. & Moreno, M.A. 1974, Rev. Mexicana Astron. Astrofis., 1, 373

Poulton, C. et al. 2008, MNRAS, 384, 1249

Preibisch, T. & Zinnecker, H. 2001, in ASP Conf. Ser. 243, 791

Preibisch, T. & Zinnecker, H. 1999, AJ, 117, 238

Reach, W.T., et al. 2004, ApJS, 154, 385

Rho, J., Reach, W.T., Lefloch, B. & Fazio, G.G. 2006, ApJ, 643, 965

Rieke, G.H. et al. 2004, ApJS, 154, 25

Robitaille, T.P., et al. 2006, ApJS, 167, 256

Robitaille, T.P., et al. 2007, ApJS, 169, 328

Salpeter, E.E. 1955, ApJ, 121, 161

Seale, J.P. & Looney, L.W. 2008, ApJ, 675, 427

Simon, J.D. et al. 2007, ApJ, 669, 327

Slesnick, C.L., Hillenbrand, L.A., & Carpenter, J.M. 2008, Accepted to ApJ, astroph/0809.1436

Smith, M.D. 1998, Ap&SS, 261, 169

Stacy, J.G. & Jackson, P.D. 1982, A&AS, 50, 377

Stahler, S.W. 1988, PASP, 100, 1474

Strom, K.M. et al. 1989, ApJS, 71, 183

Sugitani, K. et al. 2002, ApJ, 565, 25

Sugitani, K., Fukui, Y., & Ogura, K. 1991, IAUS, 147, 498

Sugitani, K. et al. 1989, ApJ, 342, 87

Tapia, M. 1981, MNRAS, 197, 949

Wadhwa, M. et al. 2007, in "Protostars and Planets V", eds. B. Reipurth, D. Jewitt, and K. Keil, University of Arizona Press, Tucson, 951, 835

White, R.J. & Hillenbrand, L.A. 2004, ApJ, 616, 998

Whitney, B.A., et al. 2003a, ApJ, 598, 1079

Whitney, B.A., et al. 2003b, ApJ, 591, 1049

Whitney, B.A., et al. 2004a, ApJS, 154, 315

Whitney, B.A., et al. 2004b, ApJ, 617, 1177

Zavagno, A. et al. 2006, A&A, 446, 171